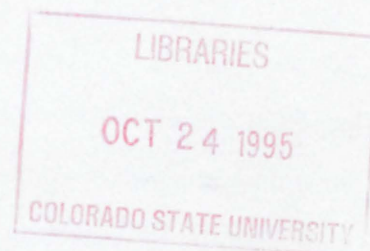


0CS054  
0-104  
110.583  
ARCHIVE

# A PARAMETERIZATION OF CUMULUS CONVECTION WITH MULTIPLE CLOUD BASE LEVELS

by Ping Ding

David A. Randall, Principal Investigator



**Colorado  
State  
University**

**DEPARTMENT OF  
ATMOSPHERIC SCIENCE**

PAPER NO. 583

# A PARAMETERIZATION OF CUMULUS CONVECTION WITH MULTIPLE CLOUD BASE LEVELS

by

Ping Ding

Research supported by the  
National Science Foundation  
under grant number ATM-9121629

Department of Atmospheric Science  
Colorado State University  
Fort Collins, CO

August 1995

Atmospheric Science Paper No. 583



018401 0089349

## ABSTRACT

The Arakawa-Schubert cumulus parameterization allows a spectrum of cloud types with many different cloud-top heights. All cumulus clouds are assumed to have their bases in the PBL, however. Convection can and does, in reality, originate above the boundary layer. Observations and numerical studies suggest that cumulus clouds originating from the free atmosphere have important influences on the large-scale circulation and the Earth's radiation budget. We have therefore developed a generalized cumulus parameterization which can represent moist convection originating in the free atmosphere.

We begin by simplifying the Arakawa-Schubert parameterization through the use of a linear mass flux profile in the cloud model which is used to determine the in-cloud properties. For a given height above cloud base, linear relationships between the entrainment rate and the in-cloud moist static energy and in-cloud moisture are demonstrated mathematically. A greatly simplified approach to obtain the entrainment parameter is derived. Cloud-top entrainment is included in the cloud model and a method to add the ice phase is constructed. Five criteria are introduced for cloud existence. The simplified parameterization is tested in the CSU GCM. The results show that the simplified parameterization can produce cumulus activity and a simulated climate similar to those obtained with the original, more complex version of the Arakawa-Schubert parameterization.

Next, a generalized cumulus parameterization with multiple cloud base levels is developed starting from the simplified single cloud-base parameterization. A cloud model is constructed in which the cloud base level as a second "cloud type" index. The generalized parameterization is implemented in the CSU GCM. The results indicate that deep penetrative convection is reduced because altocumulus clouds compete for the CAPE. With more cloud types and less deep convection, a wider and smoother cumulus precipitation pattern is produced. This makes the simulated total precipitation pattern agree better with observations, e.g., the unrealistically strong precipitation rate over the Western

Pacific is reduced. Due to the weaker deep convection and more vigorous shallow clouds, the lower and middle troposphere is moistened. With the weaker penetrative cumulus convection in the tropics compared with the control run, in conjunction with the decreased cumulus precipitation and latent heating, the new parameterization produces a weaker Hadley cell and a well defined Ferrel circulation in the Southern Hemisphere, in much better agreement with observations. In active altocumulus regions, a warmer middle and upper troposphere, and cooler lower troposphere are produced. The modifications of the simulated radiation budget by the multiple cloud base parameterization are not significant.

Since most of the altocumulus clouds produced by the model have relatively low cloud bases, the efficiency of evaporation of altocumulus precipitation below cloud base is small. Experiments also show that cumulus activity is sensitive to cloud base conditions. More realistic cloud base conditions can improve the cumulus parameterization.

## Acknowledgments

I would like to thank my advisor, professor David A. Randall, for his tremendous help, invaluable guidance, encouragement and instruction throughout the course of this research and my term as a graduate student in the past four years. I am very grateful to professors Wayne H. Schubert, Richard H. Johnson, Michael Kirby, and Graeme Stephens for their interest in my work, their constructive comments and their valuable time in serving on my dissertation committee.

Thanks to Don Dazlich, the guru of the CSU GCM, for his expert help on using the CSU GCM. I am grateful to Dr. A. Scott Denning for his invaluable help in many aspects. I thank Drs. Laura D. Fowler and Kuanman Xu for their many constructive discussions and suggestions about this work. Cindy Carrick and Kelley Ann Wittmeyer gave their generous help to me and to all Randall's rabbits. Their efforts make Randall's rabbits to be a great group. Thanks are extended to Drs. Junyi Wang, Dzong-Ming Pan; Ms. Ching-Hsuan Chen, Douglas Cripe, and Ross Heikes.

I would like to give my special thanks to my wife Hongxia Li. Her continuous support and patience through the years is so important to me.

This research was supported by the National Science Foundation under grant ATM-9121629. Computing resources were provided by the National Energy Research Computer Center at Lawrence Livermore National Laboratory.

**To my parents  
and  
my wife**

# Table of Contents

<b>Chapter 1 Introduction</b>	1
<b>Chapter 2 A Review of studies in Moist Convection and Cumulus Parameterization</b>	7
2.1 Moist Convection and Large-Scale Motions	7
2.1.1 Cumulus convection and cloud clusters	
2.1.2 Radiative effects of cumulus convection	
2.1.3 Momentum transfer by cumulus convection	
2.2 The Development of the Theory of Cumulus Parameterization	14
2.2.1 The representation of cumulus convection by large-scale variables	
2.2.2 Existing Cumulus Parameterizations	
2.3 Convection Starting from the Free Atmosphere	26
<b>Chapter 3 Arakawa-Schubert Cumulus Parameterization and CSU GCM</b>	32
3.1 The Arakawa-Schubert Cumulus Parameterization	33
3.1.1 Modifications of large-scale fields by cumulus ensembles	
3.1.2 The spectral cumulus ensemble model	
3.2 The Quasi-Equilibrium Closure Hypothesis of the A-S Parameterization	40
3.2.1 The cloud work function	
3.2.2 The quasi-equilibrium hypothesis	

3.3	Observational Tests .....	47
3.3.1	Evaluation of the quasi-equilibrium hypothesis	
3.3.2	Observational tests of the A-S parameterization	
3.4	Modifications of the A-S Parameterization .....	50
3.4.1	The inclusion of convective downdrafts	
3.4.2	Prognostic closure	
3.5	Simulations with the A-S Parameterization in the CSU GCM .....	54
3.5.1	Description of CSU GCM	
3.5.2	Some numerical experiments	
3.6	Effects of the MSTADJ in model simulations .....	69
3.6.1	MSTADJ incidence in the control simulation	
3.6.2	Simulation test without MSTADJ	

## **Chapter 4 The Linear Mass Flux Profile ( I )**

	.....	78
4.1	Entrainment and Cloud Models .....	79
4.1.1	Jet and plume models	
4.1.2	Thermal or bubbles	
4.2	The Linear Mass Flux Profile.....	84
4.2.1	The linear mass flux profile assumption	
4.2.2	The linear relation between the entrainment rate and the in-cloud moist static energy	
4.2.3	The linear relation between the entrainment rate and the in-cloud moisture	
4.3	The Determination of the Entrainment Rate with the Consideration of Virtual Temperature .....	95

## **Chapter 5 The Linear Mass Flux Profile ( II )**

.....	101
5.1 Cloud-top entrainment.....	101
5.1.1 Entrainment processes at cloud top	
5.1.2 The incorporation of cloud-top entrainment into the cloud model	
5.2 The Ice Phase of Cumulus Clouds.....	105
5.2.1 The inclusion of the ice phase	
5.2.2 The Linear Relation between the Entrainment Rate and Cloud Moisture with Ice	
5.3 Criteria for the Existence of Clouds .....	115
5.4 Simulations Using the Cumulus Parameterization with the Linear Mass Flux Profile .....	117
5.4.1 Simulated cumulus activity	
5.4.2 The simulated climate	
5.4.3 Radiation effects of the linear version cumulus parameterization	
5.5 The summary of the L-run results .....	134

## **Chapter 6 A Cumulus Parameterization with Multiple Cloud Base Levels**

.....	138
6.1 A cumulus parameterization with multiple cloud-base levels.....	139
6.1.1 Conditionally unstable layers	
6.1.2 Entrainment rate and cloud properties	
6.1.3 Cloud work function and cumulus kinetic energy	
6.2 Simulation experiments with the multiple cloud base cumulus parameterization.....	144
6.2.1 Cumulus clouds from the generalized parameterization	

6.2.2	Precipitation	
6.2.3	Cumulus mass flux detrainment, cumulus heating and cumulus moistening	
6.3	The simulated climate	163
6.3.1	Simulated 500 mb geopotential height fields	
6.3.2	The temperature and moisture fields	
6.3.3	The atmospheric circulation	
6.4	Effects of altocumulus convection on soundings at some individual locations	174
6.5	Radiation Budget	183
6.5.1	Planetary albedo	
6.5.2	OLR and absorbed solar radiation	

## **Chapter 7 Tests of the MCB-Parameterization with Evaporation of Cumulus Rainfall below Cloud Base**

		190
7.1	A cumulus rainfall evaporation scheme	191
7.2	Simulation test results	194
7.2.1	Total precipitation rate	
7.2.2	Comparisons of the moisture and temperature fields	
7.2.3	Mean meridional circulation	
7.3	Summary	200

## **Chapter 8 An Experiment with Revised Cloud base Conditions**

		202
8.1	Design of the experiment	202
8.2	Results and discussions	203

- 8.2.1 Simulated cumulus activity
- 8.2.2 Precipitation
- 8.2.3 Cumulus detrainment mass flux and specific humidity

## **Chapter 9 Summary and Conclusions**

.....	212
9.1 Summary .....	212
9.2 Conclusions.....	217
9.3 Future work.....	218

## **References**

.....	220
-------	-----

## List of Figures

- Figure 2.1: A schematic figure showing the interaction between large-scale and moist - convective processes (from Arakawa, 1993). p15
- Figure 2.2: The cloud map from Warner et al. (1980). p27
- Figure 2.3: Incidence of cumulus(CUP) and moist convective adjustment (MSTADJ) from CSU GCM for July. p30
- Figure 3.1: A unit horizontal area in the A-S parameterization (based on Arakawa and Schubert, 1974). p33
- Figure 3.2: Typical vertical profiles of  $\bar{h}(p)$ ,  $\bar{h}^*(p)$  (solid lines) and  $hc(p)$ (dashed lines).  $hc(p)$  are labeled with value of in percent per kilometer (from Arakawa and schubert, 1974). p39
- Figure 3.3: A schematic diagram showing a hypothetical equilibrium curve in the -RH space that separates stable and unstable regions. Large-scale forcing (heavy solid arrow), its components (solid arrows), and the corresponding adjustment (dashed arrow) are shown in the diagram (from Arakawa, 1993). p45
- Figure 3.4: A schematic diagram showing updraft with tilting and downdraft. p51
- Figure 3.5: The modified  $\sigma$ -coordinate corresponds to the PBL top and to the surface (from Suarez *et al.*, 1983). p57
- Figure 3.6: July 500 mb geopotential height from the control run (a); and the ECMWF four year mean (b). Units are in meter. Heavy shading corresponds to values greater than 5750m. Contour intervals are every 50 meters. p64

Figure 3.7: Latitude-pressure temperature distributions from the C-run (a); the ECMWF data (b); and ECMWF data minus the C-run (c). Units are in degree K. Contour intervals are 5 K in (a) and (b); and 1 K in (c). p66

Figure 3.8: Total July precipitation from (a) the control run simulation, and (b) observations according to Legates and Willmott (1990). Units are in  $\text{mm day}^{-1}$  and contour intervals are  $2 \text{ mm day}^{-1}$ . Values larger than  $6 \text{ mm day}^{-1}$  are shaded. p67

Figure 3.9: Streamfunction of the control-run simulated (a) and observed (b) mean meridional circulation with units in  $10^9 \text{ kg s}^{-1}$ . Contour intervals are  $20 \times 10^9 \text{ kg s}^{-1}$ . Positive values are heavy shaded and values less than  $-120 \times 10^9 \text{ kg s}^{-1}$  are light shaded. p68

Figure 3.10: Zonally averaged cumulus Incidence (solid line) and MSTADJ incidence (dotted line) from the C-run for July. p70

Figure 3.11: Zonally averaged temperature difference between the C2-run and the C-run for July. Contour intervals are 0.4 K and values larger than zero are shaded. p71

Figure 3.12: Zonally average cumulus precipitation, large-scale precipitation and total precipitation from the C2-run (solid lines) and the C-run (dotted lines). Units are in  $\text{mm day}^{-1}$ . p73

Figure 3.13: OLR (upper panel) and downward solar radiation (lower panel) at the model top from the C-run and the C2-run for July. Units are in  $\text{W m}^{-2}$ . Values larger than  $265 \text{ W m}^{-2}$  are shaded, and contour intervals are  $15 \text{ W m}^{-2}$  in panels (a) and (b); values larger than  $350 \text{ W m}^{-2}$  are shaded and contour intervals are  $25 \text{ W m}^{-2}$  in panels (c) and (d). p74

Figure 3.14: Zonally averaged OLR and downward solar radiation from the C2-run (solid

lines) and the C-run (dotted lines). Unit is  $\text{W m}^{-2}$ . p76

Figure 4.1: A schematic diagram of plume model. p80

Figure 4.2: A schematic diagram of thermal model. A cumulus clouds can consist of several thermals. p83

Figure 4.3: Model layer description (based on Lord *et al.*, 1982). p87

Figure 5.1: July cumulus incidence from the control run (a) and the linear-version run (b). Contour intervals are 0.1. Values larger than 0.5 are shaded. p119

Figure 5.2: Zonal mean cumulus incidence from control run (solid line) and linear version cumulus parameterization run (dotted line). p120

Figure 5.3: Cumulus detrainment mass flux for July from the control run (a) and the linear version run (b). The unit is inverse hours ( $\text{hour}^{-1}$ ) and values larger than 0.05 are shaded. p121

Figure 5.4: July cumulus precipitation maps from control run (upper panel) and linear version run (lower panel). The unit is  $\text{mm day}^{-1}$  and values larger than  $6 \text{ mm day}^{-1}$  are shaded. p122

Figure 5.5: Zonally averaged cumulus heating rates from C-run (a) and L-run (b) for July. Units are in  $\text{K day}^{-1}$ . Contour interval is  $0.2 \text{ K day}^{-1}$ . Values larger than  $1.5 \text{ K day}^{-1}$  are shaded. p124

Figure 5.6: July 500 mb geopotential height fields from the C-run and the L-run. Units are in meter and values larger than 5750 are shaded. p125

Figure 5.7: Zonally averaged temperature distributions from the control run (a); the linear version run (b); and the ECMWF analysis (c). Units are in degree K and contour intervals are 5 K. p127

Figure 5.8: July total precipitation fields from the C-run (a); the L-run (b); and Legates and Willmott (1990). Units are in  $\text{mm day}^{-1}$ . Contour intervals are  $2 \text{ mm day}^{-1}$ . Values larger than  $6 \text{ mm day}^{-1}$  are shaded. p128

Figure 5.9: Zonally averaged specific humidity from the C-run and the L-run. Units are in  $\text{g kg}^{-1}$ . Contour intervals are in  $1 \text{ g kg}^{-1}$  and values larger  $10 \text{ g kg}^{-1}$  are shaded. p129

Figure 5.10: Zonally averaged July mean meridional circulation from the C-run (a); the L-run (b) and observations (c). Units are in  $10^9 \text{ kg s}^{-1}$ . The contour intervals are  $\text{kg s}^{-1}$ . Positive values are heavy shaded and values less than are light shaded. p131

Figure 5.11: Zonally averaged distributions of planetary albedo simulated from control run and linear version, and derived from the ERBE data set for July. Unit is%. p132

Figure 5.12: July absorbed solar radiation for the C-run; the L-run; and the ERBE data set. Units are in  $\text{W m}^{-2}$ . Contour intervals are  $15 \text{ W m}^{-2}$ . Values larger than  $265 \text{ W m}^{-2}$  are shaded. p133

Figure 5.13: Outgoing long-wave radiation from the control run, the linear version run and the ERBE data. Units are in  $\text{W m}^{-2}$  and values larger than  $265 \text{ W m}^{-2}$  are shaded. Contour intervals are  $15 \text{ W m}^{-2}$ . p135

Figure 6.1: July cumulus incidence from control run (a), multiple cloud base run (b) and their difference (c). Values larger than 0.5 are shaded in (a), (b); values larger than 0.1 are shaded in (c). Contour intervals are 0.1 in (a) and (b), and 0.05 in (c). p146

Figure 6.2: July cumulus incidence from MCB simulation. The upper map shows incidence of cumulus clouds which only start from the PBL. The lower map shows

the difference between the total cumulus incidence of MCB-run and the upper map. In (a), values larger than 0.5 are shaded and the contour interval is 0.1. In (b), values larger than 0.15 are shaded and the contour interval is 0.05. p148

Figure 6.3: July MSTADJ incidence for C-run. The contour interval is 0.05. Values larger than 0.4 are shaded. p149

Figure 6.4: Total July precipitation from control simulation (a); MCB simulation (b); Legates and Willmott (1990); and MCB-run minus C-run (d). Units are in  $\text{mm day}^{-1}$ . The contour interval is 2 and values larger than 6 are shaded in (a), (b), and (c); values less than zero are lightly shaded in (d). p154

Figure 6.5: Zonal mean total precipitation rates for July from the C-run, the MCB-run and observations. Unit is  $\text{mm day}^{-1}$ . p156

Figure 6.6: July cumulus precipitation from MCB simulation (a), and the difference between MCB simulation and control simulation (b). Unit is  $\text{mm day}^{-1}$ . Values larger than  $6 \text{ mm day}^{-1}$  are shaded in map (a), and values larger than  $1 \text{ mm day}^{-1}$  are heavy shaded; smaller than  $-1 \text{ mm day}^{-1}$  are light shaded in (b). Contour interval is  $2 \text{ mm day}^{-1}$  in (a), and  $1 \text{ mm day}^{-1}$  in (b). p157

Figure 6.7: July zonal mean cumulus precipitation from the MCB simulation (solid curve), control simulation (dotted curve) and their difference (dashed curve). Unit is  $\text{mm day}^{-1}$ . p160

Figure 6.8: Zonal mean July cumulus detrainment from C-run (a), MCB-run (b) and MCB-run minus C-run (c). Units are in  $\text{hour}^{-1}$ . Values larger than 0.05 are shaded in (a) and (b); values larger than zero are shaded in (c). p162

Figure 6.9: Zonal mean July Cumulus heating rate from C-run (a), MCB-run (b), and MCB-run minus C-run (c). Units are in  $\text{K day}^{-1}$ . Values larger than  $1.5 \text{ K day}^{-1}$  are shaded in (a) and (b). Negative values are shaded in (c). p164

Figure 6.10: Zonal mean July cumulus moistening rate from C-run (a), MCB-run (b), and MCB-run minus C-run (c). Unit is  $\text{g kg}^{-1} \text{ day}^{-1}$ . Values less than  $-0.0005$  are shaded. The contour interval is  $0.00008 \text{ g kg}^{-1} \text{ day}^{-1}$ . p165

Figure 6.11: July 500mb geopotential height fields from the C-run (a), the MCB-run (b), and ECMWF data (c). The unit is in meter and values larger than 5750 are shaded. The contour interval is 50 meters. p167

Figure 6.12: Latitude-pressure temperature distributions from the C-run (a); the MCB-run (b); and the temperature difference with observations (c) and (d). The unit is K. Contour intervals are 5 in (a), (b); and 2 in (c), (d). p168

Figure 6.13: Zonal mean July relative humidity from C-run (a), MCB-run (b), MCB-run minus C-run (c), and ECMWF data (d). Values larger than 80% are dark shaded; and values smaller than 20% are light shaded in panels (a), (b), and (d); Values larger than 2% are dark shaded; and values smaller than -2% are light shaded in the panel (c). p170

Figure 6.14: July zonal mean zonal wind from C-run (a), MCB run (b), and ECMWF data. Unit is  $\text{m s}^{-1}$ . The contour interval is  $5 \text{ m s}^{-1}$ . Heavy shading corresponds to values larger than  $20 \text{ m s}^{-1}$ , and light shading corresponds to values less than zero. p172

Figure 6.15: July streamfunction of the mean meridional circulation from C-run (a), MCB-run (b), and observations. Units are in  $10^9 \text{ kg s}^{-1}$ . The control interval is  $\text{kg s}^{-1}$ . Positive values are heavily shaded and values less than  $\text{kg s}^{-1}$  are lightly shaded. p173

Figure 6.16: July simulated monthly mean temperature vertical profiles from C-run (solid lines) and MCB-run (dashed lines) for SN1 ~ SN4. p176

Figure 6.17: Same as Fig. 6.16, except for specific humidity. p177

Figure 6.18: Temperature and specific humidity difference at SN1 to SN4 between the MCB simulation and the control simulation. The vertical coordinate is pressure in mb. p178

Figure 6.19: Same as Fig. 6.16, except for SN5 ~ SN8. p179

Figure 6.20: Same as Fig. 6.17, except for SN5 ~ SN8. p180

Figure 6.21: Same as Fig. 6.18, except for SN5 ~ SN8. p181

Figure 6.22: July planetary albedo from control simulation (a); MCB simulation (b); and ERBE data (c). Units are in%. Values smaller than 25 are shaded. The contour interval is 5. p184

Figure 6.23: Zonally averaged planetary albedo from the C-run (dashed line); the MCB-run (dotted line); and the ERBE data set for July. Units are in %. p185

Figure 6.24: July outgoing longwave radiation maps from the control simulation (a); the MCB simulation (b); and ERBE data (c). Units are in  $W m^{-2}$ . The contour interval is  $15 W m^{-2}$ . Values larger than  $265 W m^{-2}$  are shaded. p186

Figure 6.25: Zonally averaged outgoing longwave radiation from the C-run (dashed line); the MCB run (dotted line); and the ERBE data set for July. Units are in  $W m^{-2}$ . p187

Figure 6.26: July absorbed solar radiation from control simulation (a); MCB simulation (b); and ERBE data (c). Units are in  $W m^{-2}$  and values larger than  $350 W m^{-2}$  are shaded. p188

Figure 6.27: Zonally averaged absorbed solar radiation from the C-run (dashed line); the MCB run (dotted line); and the ERBE data set for July. Units are in  $W m^{-2}$ . p189

Figure 7.1: Total July precipitation from the MCB simulation (a); the MCBEVP simulation (b); and their difference (c). Units are in  $\text{mm day}^{-1}$ . Contour intervals are 2 in (a) and (b), and 1 in (c). Values larger than 6 are shaded in (a) and (b), and values less than zero are shaded in (c). p195

Figure 7.2: Zonal mean specific humidity from the MCB-run (a); the MCBEVP-run (b); and the MCBEVP-run minus the MCB-run (c). Units are in  $\text{g kg}^{-1}$ . Intervals are 0.5 in the maps (a) and (b) and 0.1 in (c). Values larger than 5 are shaded in (a) and (b). Values larger than zero are shaded in (c). p197

Figure 7.3: Latitude-pressure temperature distributions from the MCB-run (a); the MCBEVP-run (b); and the differences of MCBEVP and the MCB simulations. The units are in degree K. Contour intervals are 5 K in (a) and (b); and 0.2 K in (c). p198

Figure 7.4: July streamfunction of the mean meridional circulation from the MCB-run (a) and the MCBEVP-run (b). Units are in  $10^9 \text{ kg s}^{-1}$ . The control interval is  $\text{kg s}^{-1}$ . Positive values are heavy shaded and values less than are light shaded. p200

Figure 8.1: July zonally averaged cumulus precipitation rates from the MCBRVC run (dashed line) and the MCB run (solid line). Units are  $\text{mm day}^{-1}$ . p208

Figure 8.2: July zonally averaged total precipitation rates from the MCBRVC run (dashed line); the MCB run (solid line); and observations (from Legates and Willmott, 1990) (dotted line). Units are  $\text{mm day}^{-1}$ . p208

Figure 8.3: Latitude-pressure cross section of specific humidity difference between the MCBRVC run and the MCB run. Unit is  $\text{g kg}^{-1}$ . The contour interval is  $0.1 \text{ g kg}^{-1}$ . Positive values are shaded. p209

Figure 8.4: Latitude-pressure cross section of specific humidity difference between the

MCBRVC run and the MCB run. Unit is  $\text{g kg}^{-1}$ . The contour interval is  $0.1 \text{ g kg}^{-1}$ . Positive values are shaded. p210

# Chapter 1

## Introduction

Cumulus convection plays a very important role in the large-scale atmospheric circulation because of its latent heat release, radiative effects, and vertical transports of heat, moisture, and momentum. The importance of cumulus convection in the heat balance of the tropical atmosphere and tropical cyclones has been recognized since 1950s (Riehl and Malkus 1958, 1961; Ooyama 1964; Charney and Eliassen 1964). The detrainment of water vapor, liquid water and ice from deep penetrative cumulus clouds can significantly influence their environment (Yanai et al. 1973; Gray 1973; and Arakawa and Schubert 1974). The optically thick anvil clouds produced by deep convection affect the radiation budgets of the atmosphere and planet's surface, change the atmosphere's thermodynamic structure, and modify the atmosphere general circulation (e.g., Webster and Stephens 1980; Randall et al. 1989; and Harshvardhan et al. 1989).

Simulations of large-scale and mesoscale systems will fail without quantitatively accounting for the effects of cumulus convection. Since the horizontal scale of the individ-

ual cumulus clouds is only a few kilometers, it is totally impractical to resolve them in any numerical model of the large-scale circulation. Therefore, the only way to represent the effects of cumulus convection in a large-scale model is to formulate, or parameterize the collective influence of cumulus clouds within a larger area in terms of the large-scale environmental variables. This is the basic idea of cumulus parameterization. The organization of the individual clouds into clusters and the observed relationships between cloud clusters and synoptic-scale atmospheric structures indicate that cumulus convection is controlled by large-scale dynamical and thermodynamical processes. This suggests that cumulus parameterization is possible. The fact that the time and space scales of cumulus convection are much smaller than those of large-scale disturbances has encouraged attempts at cumulus parameterization.

The key element of a cumulus parameterization is to formulate relations between the effects of the “subgrid-scale” cumulus clouds and the scales of motion resolved by a large-scale model. As Lord (1978) mentioned, “the goal of the so-called cumulus parameterization is formally stated as follows: to predict the changes in the large-scale variables, due to cumulus convection, from the known large-scale variables.” Arakawa and Cheng (1993) defined the goal of the cumulus parameterization as “to formulate the collective effects of subgrid-scale clouds in terms of the prognostic variables of grid scale.” Cumulus parameterizations are discussed in more details in Chapter 2.

Since the importance of cumulus convection on the tropical cyclone was recognized early (Malkus and Riehl 1960), as discussed by Ooyama (1971, 1982), the concept of cumulus parameterization in numerical models originated with studies of tropical

cyclones. The early parameterizations resulted in the successful simulation of some aspects of tropical cyclones, but they were emphasizing on deep convection and its latent heat release. The effects of shallow cumulus clouds and feedbacks of cumulus clouds on the large-scale environment were not taken account adequately. Therefore, the early parameterizations were not designed for more general use in large-scale numerical prediction models.

With the increase of the understanding of the interaction between cumulus clouds and the large-scale environment, a variety of cumulus parameterizations have been proposed for large-scale numerical models in the past three decades. These parameterization schemes include moist convective adjustment scheme (Manabe et al. 1965; Manabe and Smagorinsky 1967; Miyakoda et al. 1969; Krishnamurti and Moxim 1971; Kurihara 1973); Kuo-type schemes (Kuo 1965, 1974; Anthes 1977; Krishnamurti et al. 1976; 1980; 1983; Molinari 1982); the Arakawa-Schubert scheme (Arakawa and Schubert 1974; Lord and Arakawa 1980; Lord 1982; Kao and Ogura 1988; Cheng and Arakawa 1990; Moorthi and Suarez 1992; Randall and Pan 1993); the Betts-Miller scheme (Betts 1986; Betts and Miller 1986); and other schemes (Ooyoma 1971; Kreitzberg and Perkey 1976; Fritsch and Chappell 1980a; Frank and Cohen 1987; Tiedtke 1989; Emanuel 1991).

The Arakawa-Schubert (A-S) parameterization is the most elaborate. The A-S parameterization makes use of a spectrum of cloud types and a quasi-equilibrium hypothesis as its closure assumption. Even though the A-S parameterization is the most physical scheme and has been successfully tested by using observational data, it has its own flaws, e.g., the complicated calculations in the A-S scheme make it very difficult to implement in

large-scale General Circulation Models (GCMs). More importantly, the A-S parameterization assumes that all cumulus clouds start from the Planetary Boundary Layer (PBL) and the spectral cloud model identifies cloud types only by their detrainment levels. Observations and numerical experiments suggest, however, that cumulus convection starting above the PBL has important influences on the large-scale circulation and the Earth's radiation budget. This will be discussed later. The radiative and thermodynamical effects of stratiform clouds produced by cumulus convection starting above the PBL significantly affect large-scale motions (see the discussion in section 2.3). Therefore, it is necessary to have a more realistic cumulus parameterization which can be conveniently implemented in GCMs for studying large-scale atmospheric circulations.

The main purpose of this report is to develop a generalized cumulus parameterization which can represent the effects of cumulus clouds originating not only in the PBL but also in the free atmosphere. In order to avoid further complicating the original A-S parameterization, we begin by simplifying the scheme through the use of a linear mass flux profile, and introduce a much simpler approach to obtain the entrainment parameter. The cloud top entrainment process is also included and a method to include the ice phase is constructed. Finally, the new parameterization is implemented into the Colorado State University GCM (CSU GCM) and the effects of cumulus convection originating in the free atmosphere are studied through analysis of the results.

In Chapter 2, we further review studies of cumulus convection and its interaction with large-scale atmospheric motions. The development of cumulus parameterization theory and existing schemes are introduced. Observational and modeling studies of cumulus

convection starting from the free atmosphere are also reviewed in this Chapter.

Chapter 3 gives a detailed review of the A-S parameterization and its observational tests. The CSU GCM is briefly introduced and some simulation results from CSU GCM are presented.

In Chapter 4, we start to introduce the linear mass flux profile. The relations between the cumulus cloud entrainment parameter and in-cloud moist static energy and in-cloud moisture are formulated corresponding to the linear mass flux profile assumption. A very simple method to determine the cumulus cloud entrainment parameter is proposed.

In Chapter 5, we further modify the cloud model to include the cloud-top entrainment process. Meanwhile, the ice formation process is formulated with the use of the linear mass flux profile assumption. The criteria for the existence of cumulus clouds in the cloud model are discussed. Some simulations with the revised cumulus parameterization are presented and analyzed.

In Chapter 6, a generalized cumulus parameterization representing cumulus clouds starting from the free atmosphere is introduced. The new parameterization is implemented in the CSU GCM. The effects of cumulus convection starting from the free atmosphere are studied through simulations with the GCM.

In order to study the effects of evaporation of altocumulus precipitation when raindrops fall below cloud base, we incorporate a rainfall evaporation scheme developed by Fowler et al. (1994) into the cumulus parameterization in Chapter 7. Simulation results are

presented and discussed.

The cloud base conditions in the A-S parameterization are assumed to be the same as the environmental air of cloud base layers. A simulation experiment with the enhanced cloud base moisture is presented in Chapter 8.

Finally, summary, conclusions and further research plans are given in Chapter 9.

## **Chapter 2**

### **A Review of studies in Moist Convection and Cumulus Parameterization**

Cumulus convection is among the most visible and perplexing phenomena in the Earth's atmosphere. Many attempts have been made to understand the interactions of cumulus convection with large-scale circulations. The importance of cumulus convection for large-scale motions has been demonstrated by many observational, theoretical and modeling studies. Some studies of moist convection and cumulus parameterization in large-scale models are reviewed in this Chapter.

#### **2.1 Moist Convection and Large-Scale Motions**

##### **2.1.1 Cumulus convection and cloud clusters**

Early observational studies recognized that cumulus convection plays an important role in large-scale tropical disturbances. Riehl and Malkus (1958) studied the heat budget of the “equatorial trough zone”, which today is called the Intertropical Convergence Zone (ITCZ), and found that the deep cumulus clouds carry the released latent heat of conden-

sation to the upper troposphere, to balance the energy losses due to radiation and poleward transport. Through studies of the formation of tropical cyclones, it was found that latent heat release in deep cumulus clouds is essential to hurricane formation (Riehl and Malkus, 1961; Yanai, 1961a, b). Early theories of tropical cyclone development were proposed by Charney and Eliassen (1964) and Ooyama (1964). In their classical papers, they argued that cumulus convection and large-scale boundary-layer convergence are coupled, and proposed the concept of conditional instability of the second kind (CISK). In CISK, cumulus clouds act through the release of the latent heat of condensation to maintain a large-scale low pressure system; in turn, the low-level convergence associated with the large-scale depression provides rising motion and moisture to sustain the cumulus clouds. In other words, the cumulus convection and the large-scale motions cooperate to generate and maintain the disturbance.

Based on cloud pictures taken from satellites during 1967, the JOC Study Group on Tropical Disturbances (1970) documented unquestionable evidence of the organization of maritime tropical clouds into "cloud clusters." Meanwhile, cumulus cloud clusters and their relationships with synoptic-scale systems were studied by many people during the 1970's. Using composite satellite images, Chang (1970) showed clear evidence of a systematic westward propagation of cloud clusters. Through a census of the Atlantic tropical systems of 1969, Frank (1970) concluded that the orientation and behavior of cloud clusters are directly related to synoptic systems rather than randomly distributed. Martin and Suomi (1972) studied cloud clusters over the tropical North Atlantic ocean by using satellite images. They found that the displacement of cloud clusters occurs through a complex combination of band and cell movement. Manabe et al. (1970) argued that the eddy avail-

able potential energy generated by the release of the latent heat of condensation is the primarily kinetic energy source of the wave disturbances. Reed and Recker (1971) composited 18 disturbance cases in the equatorial western Pacific during the wet season (July-September) of 1967. They deduced that the synoptic-scale divergence represents the collective outflow from cumulonimbus clusters. The cloud amount is related to the structure of the synoptic-scale system.

Cumulus convection and its interactions with large-scale motions have undergone intensive investigation since their importance was recognized. In order to better understand these complex interactions, the GARP (Global Atmospheric Research Program) Atlantic Tropical Experiment (GATE) was carried out in 1974. Using the GATE data, many studies of cumulus convection and its interactions with large-scale motions and meso-scale systems were carried out. For example, Leary and Houze (1979b) studied the anvil precipitation structure by using GATE data. They presented a schematic diagram of a meso-scale system describing the convective updrafts and downdrafts as well as meso-scale updrafts and downdrafts. The anvil precipitation process was illustrated. A similar diagram was discussed by Houze (1977).

Houze and Betts (1981) summarized the results from many GATE studies. They concluded that convection was dominated by cloud clusters, and that the cloud clusters were divided into two types: rapidly moving squall clusters and slowly moving nonsquall clusters. It was also noted that deep cumulonimbus clouds are always accompanied by a spectrum of smaller convective features ranging from moderate cumulonimbus down to tiny nonprecipitating cumulus. The relatively few large cumulonimbus rain areas, how-

ever, accounted for about 90% of the rainfall in GATE. The anvil clouds associated with the deep convection developed a region of stratiform precipitation adjacent to the active convective cells. A substantial fraction of the total rainfall in GATE fell as stratiform precipitation of this type. Houze and Betts stated that downdrafts, of both convective scale and mesoscale, are very important for the formation of cloud systems. They discussed how convective cloud clusters modify the thermodynamic and dynamic structure of the large-scale environment by various physical processes.

Recently, Cotton and Anthes (1989) summarized studies showing that cumulus convection, especially deep, intense convection, can have an important effect on the dynamics and energetics of larger-scale atmospheric systems in both the tropics and extratropics. For example, cumulus convection always plays a very important role in the development of tropical cyclones, tropical squall lines and tropical cloud clusters. Mesoscale convective complexes, extratropical squall lines, cold fronts, extratropical cyclones and many other phenomena are also strongly affected by the energy released in cumulus clouds and by the vertical convective transports of heat, moisture and momentum. Cotton and Anthes took the development of hurricanes as an example. During the developing and mature stage of a hurricane, very strong cumulus convection occurs in the eye wall region. The vertical transports of heat and moisture by this convection and the latent heat released directly drive the hurricane system.

Studies of cumulus convection and the interactions between cumulus convection and large-scale motions provided the basic knowledge and physical background for parameterizing cumulus effects in General Circulation Models (GCMs). The organized

behavior of cumulus clouds implies that their collective effects can be formulated in terms of their large-scale environment. This is important for cumulus parameterization in which large-scale variables are used to parameterize effects of cumulus clouds because the size of a individual cumulus cloud, usually several kilometers, is too small to be resolved by a GCM grid which is several hundred kilometers.

### 2.1.2 Radiative effects of cumulus convection

The other important role of cumulus convection on the large-scale circulation is its radiative effects, which were ignored until the 1970s. Albrecht and Cox (1975) used a large-scale diagnostic model to determine the radiative heating effects. The model is a single partial differential equation obtained by combining the horizontal momentum equations, hydrostatic equation, continuity equation and thermodynamic equation. The diabatic heating is specified and the atmospheric response is calculated in the model. Albrecht and Cox found that the structures of the forced motions are very sensitive to the phase difference between the convective and radiative heating when the heating is combined. In other words, the radiation effects on the atmospheric motions are closely related to the convective activities.

Stephens and Webster (1979) studied the importance of cloud variability on radiative heating. According to their results, the cloud type and height and the latitude at which the cloud exists exert a profound influence on the radiative state of the atmospheric column.

Herman et al. (1980) estimated the radiative effects of global cloudiness through general circulation model experiments. Their results show that on a global basis clouds

increase the global radiation balance by  $40 \text{ Wm}^{-2}$  by absorbing longwave radiation, but decrease it by  $56 \text{ Wm}^{-2}$  by reflecting solar radiation to space. The net effect of the global cloudiness on the radiation budget is a reduction of the net radiation by  $16 \text{ Wm}^{-2}$ , due to the dominance of the cloud albedo effect. Their experiments also showed that removal of the clouds' infrared absorption cools the atmosphere and causes additional cloudiness to occur, while removal of the clouds' solar radiative properties warms the atmosphere and causes fewer clouds to form.

Webster and Stephens (1980) studied the radiative effects of anvil cloud decks in the tropical atmosphere by using Winter Monsoon Experiment (WMONEX) data. Their study indicates that the existence of vast decks of middle and upper extended clouds have a significant influence on the radiative balance of the tropical atmosphere. Their results also showed that the big difference between the radiative cooling at the cloud top and the radiative heating at the cloud base could destabilize the cloud layer. The large radiative heating at the cloud base makes an important contribution to the total diabatic heating. The role of the radiative effects of the anvil cloud decks is closely related to the development of the convection.

Ramanathan et al. (1983) presented results and analyses from a series of sensitivity experiments based on GCM simulations. Their results showed that a GCM with an improved cloud/radiation model is better able to reproduce many observed features. When the improvements in the cloud/radiation treatment were removed, the simulation of zonal mean winds and temperatures degraded and departed drastically from observations.

Ackerman et al. (1988) addressed the interactions of tropical cirrus anvils with

infrared and solar radiation. They found that the ice water content and its vertical distribution, the depth of the anvil and the underlying atmosphere can all significantly influence the radiative processes. They argued that because the radiative processes can affect the anvil temperature profile, anvil dynamics on a variety of scales, and ice particle microphysics, sophisticated models which can properly simulate the anvil life cycle are strongly needed.

Harshvardhan et al. (1989) obtained somewhat realistic Earth radiation budget and cloudiness simulations by using a general circulation model in which new parameterizations of solar, terrestrial radiation, and cloud optical properties were included. Randall et al. (1989) examined cloud-radiation interactions through numerical simulation experiments. They concluded that while cloudiness modifies the radiation processes, it is also true that radiative effects play a significant role in the generation and development of the clouds. They concluded that more realistic cloud parameterizations are sorely needed.

Beyond any doubt, moist convection plays an important role in the cloud-radiation effects by producing anvil clouds. The cloud radiative effects, in turn, can impact the moist convection and the cloud amount. The interactions between moist convection and cloud radiative effects significantly influence the atmospheric circulation. Hence, it is important to have a realistic representation of cumulus convection in a GCM.

### 2.1.3 Momentum transfer by cumulus convection

The importance of cumulus convection for the transports of momentum and vorticity in tropical wave systems and cloud clusters has also been mentioned in many studies (Cho and Cheng, 1980; Cho et al., 1979; Chu et al., 1981; Esbensen et al. 1982). Stevens

(1979) evaluated the budgets of vorticity, momentum and divergence based on composited GATE data. He showed that there is a significant residual imbalance for each of the large-scale budgets, which suggests that the convective-scale circulations strongly affect the large-scale disturbances and that cumulus transports must be parameterized in the dynamic budgets for a proper treatment of the dynamics and energetics of the wave disturbances. By using GATE data, Tollerud and Esbensen (1983) found that the large cloud cluster scale circulation can not account for most of the development and maintenance of the asymmetric vorticity patterns. They indicated that small-scale circulations are largely responsible for the development of these large-scale flow patterns from the analysis of the budget residuals. They also found that the variations of the tropical upper-level easterlies are associated with cloud clusters.

The importance of moist convection for the large-scale motions has been fully accepted as more and more recent studies focused on this subject (e.g., Kiladis and Weickmann, 1992; Machado et al., 1992; Sheu and Curry, 1992; Keenan and Rutledge, 1993; Mapes, 1993). To represent the effects of moist convection in large- or meso-scale models is among the most challenging tasks in the numerical simulation of the atmosphere. This report is a contribution on this subject.

## **2.2 The Development of the Theory of Cumulus Parameterization**

The concept of cumulus parameterization has been introduced in Chapter 1. The need for a realistic cumulus parameterization in a GCM is obvious from the above reviews. We further discuss the development of the theory of cumulus parameterizations in this section. Some of the most widely used cumulus parameterizations will also be intro-

duced.

### 2.2.1 The representation of cumulus convection by large-scale variables

As suggested by Arakawa (1993), the interactions between cumulus convection and large-scale circulation can be illustrated as shown in Fig. 2.1.

Cumulus convection is controlled by large-scale processes. Large-scale atmospheric circulations, meanwhile, are influenced by cumulus convection. We call the effects of cumulus convection on large-scale fields “feedback” processes; they are shown in the lower part of the loop in Fig. 2.1. The right half of the loop (with heavier arrows) represents the problem of cumulus parameterization. In practical cumulus parameterizations, the most important task is to quantitatively determine the effects of the cumulus convection in terms of large-scale observable variables. This includes two tasks: 1) to formulate control; 2) to formulate feedback. This is fundamental to cumulus parameterization.

Yanai et al. (1973) developed a bulk model of a cumulus cloud ensemble for use in

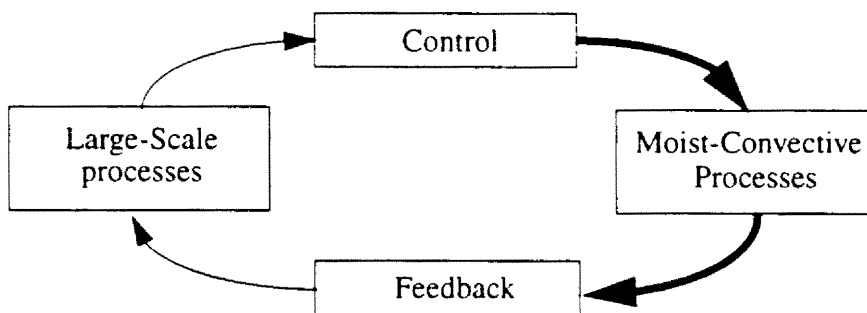


Fig. 2.1. A schematic figure showing the interaction between large-scale and moist-convective processes (from Arakawa, 1993).

a diagnostic study of cumulus effects on the heat and moisture budgets of the Marshall Islands region. Yanai and Johnson (1993) gave a summary of the bulk method. It starts from the conservation of moist static energy under both dry and moist adiabatic processes, and the moisture continuity equation. Yanai et al. (1973) defined  $Q_1$  and  $Q_2$  as apparent heat source and apparent moisture sink, i.e.

$$\begin{aligned} Q_1 &\equiv \frac{\partial \bar{s}}{\partial t} + \bar{\mathbf{v}} \cdot \nabla \bar{s} + \bar{\omega} \frac{\partial \bar{s}}{\partial p} \\ &= Q_R + L(\bar{c} - \bar{e}) - \nabla \cdot \overline{s' \mathbf{v}'} - \frac{\partial \overline{s' \omega'}}{\partial p} \quad , \end{aligned} \quad (2.1)$$

$$\begin{aligned} Q_2 &\equiv -L \left( \frac{\partial \bar{q}}{\partial t} + \bar{\mathbf{v}} \cdot \nabla \bar{q} + \bar{\omega} \frac{\partial \bar{q}}{\partial p} \right) \\ &= L(\bar{c} - \bar{e}) + L \nabla \cdot \overline{q' \mathbf{v}'} + L \frac{\partial \overline{q' \omega'}}{\partial p} \quad . \end{aligned} \quad (2.2)$$

In the above,  $s \equiv c_p + gz$  is the dry static energy,  $q$  is the mixing ratio of water vapor,  $\mathbf{v}$  is the horizontal velocity,  $\omega$  is the vertical  $p$ -velocity,  $Q_R$  is the heating rate due to radiation,  $c$  is the rate of condensation, and  $e$  is the rate of evaporation of cloud water per unit mass of air. A prime denotes deviations from the horizontal average and an overbar denotes the horizontal average. When the horizontal eddy transport terms are neglected, combining (2.1) and (2.2) gives

$$Q_1 - Q_2 - Q_R = -\frac{\partial \overline{h' \omega'}}{\partial p} \quad , \quad (2.3)$$

where  $h = s + Lq$  is the moist static energy. The right hand-side of (2.3) is a measure of the vertical eddy transport of total energy and can be used to measure the activity of cumulus convection. All terms on the left-hand side of (2.3) can be determined from observations of the large-scale environment. This provides a method to measure the activity of cumulus

convection by the use of observations of the large-scale environment.

Yanai et al. classified cumulus clouds according to the heights of their tops, and all sub-ensemble cumulus clouds in a cloud ensemble are assumed to have a common cloud base height. They defined  $M_c$  as the upward mass flux in the active cumulus clouds,  $\bar{M}$  as the average mass flux across a unit horizontal area, and  $\tilde{M}$  as the residual mass flux in the environment. Then the vertical transport of dry static energy by the clouds (the right-hand side of Eq. (2.1)) can be related to  $M_c$  by

$$Q_1 - Q_R = -M_c \frac{\partial \bar{s}}{\partial p} - Le \quad . \quad (2.4)$$

By combining the large-scale heat and moisture budgets and an entraining plume model of a cumulus cloud ensemble, a large amount of information can be obtained about the bulk properties of tropical cloud clusters. After calculating the mass flux in the clouds and the mean large-scale convergence, Yanai et al. found that the cloud mass flux exceeds the mean vertical mass flux required by large-scale convergence. This means that compensating sinking motion exists between the clouds. Therefore, they concluded that cumulus convection modifies the large-scale temperature and moisture fields through detrainment and cumulus-induced subsidence in the environment. The detrainment causes large-scale cooling and moistening due to re-evaporation of liquid water (and ice) detrained from the clouds, and the cumulus-induced subsidence causes large-scale warming and drying due to adiabatic compression. Actually, they obtained the same conclusion given by Gray (1973). This study gives us a clear idea about how cumulus convection affects the large-scale environment, and it also provides a method to quantitatively describe the characteristics of the cumulus clouds. This approach is called the bulk method because we get the

average cloud characteristics of a cloud cluster.

The other approach which is widely used to study cumulus convection is the spectral method. This method was developed by Arakawa (1969), Ogura and Cho (1973), Arakawa and Schubert (1974), and Nitta (1975), and was also summarized by Yanai and Johnson (1993). An equation used in the spectral method is

$$Q_1 - Q_2 - Q_R = -M_c \frac{\partial \bar{h}}{\partial p} + \sum_i \delta_i (h_{Di} - \bar{h}) \quad , \quad (2.5)$$

where  $i$  is used to identify different cloud types;  $\delta_i$  is the rate of mass detrainment by  $i$ th cloud; the subscript  $( )_D$  signifies the value in the detraining air. In this case, cumulus clouds are classified according to their (assumed) constant fractional rate of entrainment. The entrainment mass flux increases exponentially with height and all the mass detrains at the top of clouds. A different entrainment rate,  $\lambda$ , corresponds to different cloud-top height and different cloud type. Because a larger  $\lambda$  corresponds to stronger entrainment which dilutes the cloud air faster and causes them to lose buoyancy sooner, clouds with larger  $\lambda$ 's have lower cloud-top heights. Classification by  $\lambda$  is thus analogous to classification by cloud-top height.

The total mass flux in the clouds is expressed by

$$M_c(p) = \int_0^{\lambda_D(p)} m_B(\lambda) \eta(p, \lambda) d\lambda \quad , \quad (2.6)$$

where  $m_B(\lambda)$  is the sub-ensemble mass flux, at the cloud base  $p_B$ , due to the cloud whose fractional rate of entrainment is  $\lambda$ .  $\eta(p, \lambda)$  is the normalized mass flux and  $\lambda_D(p)$  is the  $\lambda$  of clouds which detrain at pressure  $p$ . The mass detrainment,  $\delta(p)dp$ , in the layer between

$p$  and  $p + dp$ , can be represented as:

$$\delta(p) = m_B[\lambda_D(p)] \eta[p, \lambda_D(p)] \frac{d\lambda_D(p)}{dp} \quad (2.7)$$

Finally, by using (2.6), and (2.7), equation (2.5) can be written as

$$Q_1 - Q_2 - Q_R = (h_D - \bar{h}) m_B[\lambda_D(p)] \eta[p, \lambda_D(p)] \frac{d\lambda_D(p)}{dp} - \frac{\partial \bar{h}}{\partial p} \int_0^{\lambda_D(p)} m_B(\lambda) \eta(p, \lambda) d\lambda \quad (2.8)$$

Equation (2.8) can be used to determine  $m_B(\lambda)$  if  $Q_1 - Q_2 - Q_R$  is known. After  $m_B(\lambda)$  has been obtained, the vertical energy and moisture profiles in the cumulus clouds can be obtained. Because  $M_B(\lambda)$  varies continuously with  $\lambda$ , this approach is called the spectral method. The effects of stratiform cloud precipitation, mesoscale downdrafts and convective-scale downdrafts are neglected in both methods. Moist convection starting from the free atmosphere is not included in either method.

Yanai and Johnson (1993) reviewed the impacts of cumulus convection on the thermodynamic fields, and compared the results of the bulk method and the spectral method. The comparison indicated that even though the two methods share similar physical principles, there are substantial differences in the formulation and the technical detail of the numerical solutions. When they compared the upward mass flux in clouds,  $M_C$ , from the two methods, they found remarkable agreement, except near the cloud base and near the tropopause. The average vertical profiles of the mass detrainment  $\delta\Delta p$  obtained by the two methods was also compared, again with good agreement. They noted that the bulk

method is a useful tool for the determination of the cumulus properties, such as  $M_C$ . However, the important advantage of the spectral model is that the properties of different cloud types (clouds with the same cloud base but different cloud tops) can be obtained.

The spectral method has many advantages over the bulk method. It provides not only the bulk properties of the total ensemble, but also the spectrum of cloud-base mass flux. The properties of individual cloud types can be determined.

The coexistence of shallow clouds and deep clouds is very important. Clouds with different cloud-top heights have different effects on large-scale heat and moisture budgets. For example, if only deep cumulus clouds are considered, an excessively dry lower troposphere results because of the lack of shallower cloud detrainment (Arakawa, 1969). This is the reason that the spectral method was introduced by Arakawa and Schubert (1974) in their parameterization theory.

Of course, cloud-base heights could also be different in the real atmosphere, as discussed in Chapter 1, and clouds with different cloud-base heights can have different effects on the large-scale environment. Solving this problem is a primary goal of this report. Clearly the assumption of a single cloud base is a big deficiency of cumulus parameterizations considering that in the real atmosphere cumulus clouds can start from any altitude in the troposphere. This is further discussed in section 2.3.

Developing methods to determine cloud properties by using large-scale variables, or developing cloud models, is the first step for the generation of a cumulus parameterization. Therefore, the development of the bulk and spectral methods was significant for stud-

ies of cumulus convection and cumulus parameterization.

### 2.2.2 Existing Cumulus Parameterizations

With the increasing recognition of the importance of the effects of cumulus convection on the large-scale environment, many cumulus parameterizations have been proposed in the last two decades. The widely used parameterizations in general circulation models (GCMs) include moist-convective adjustment parameterizations; Kuo-type parameterizations; the Betts-Miller parameterization; and Arakawa-Schubert parameterizations. Some parameterizations have been developed for use in mesoscale numerical models. The following is a brief review of the parameterizations used in GCMs. A more detailed description of the Arakawa-Schubert parameterization is given in Chapter 3 of this report.

Manabe et al. (1965) introduced the “moist convective adjustment” parameterization which is used in the Geophysical Fluid Dynamics Laboratory (GFDL) GCM. It is among the simplest methods for parameterizing the collective effects of cumulus clouds on the large-scale environment. This adjustment parameterization bypasses the detailed physical mechanisms of the interactions between cumulus clouds and the large-scale environment. In this parameterization, whenever the large-scale environmental relative humidity exceeds a specified value (which might be 100%) and the lapse-rate between adjacent model layers exceeds the moist adiabat, the temperature and moisture in each layer are modified so that 1) the total moist enthalpy is conserved, 2) the large-scale environmental relative humidity is unchanged, 3) the lapse rate is moist adiabatic, and 4) all condensed water precipitates immediately.

The moist convective adjustment as originally proposed by Manabe et al. is also called “hard convective adjustment” because the parameterization assumes that the adjustment starts when the grid-scale thermodynamic state becomes saturated. Actually, cumulus convection can occur over an area which is only a small portion of the total grid area. In this case the grid-scale moisture field may not be saturated. In order to remedy this weakness of the hard convective adjustment parameterization, the so called “soft convective adjustment” has been proposed by Miyakoda et al. (1969). The soft scheme assumes that saturation occurs only over a specified fraction of the grid area, with the air between the clouds remaining unsaturated. The grid-scale moisture that is an average over the cloud and environment may not be saturated. This assumption introduces an additional empirical parameter, the fractional cloud area in a unit grid-scale area, but it allows the parameterization to activate before model layers become fully saturated. The earliest soft moist convective adjustment proposed by Miyakoda et al. used 80% relative humidity instead of the saturation condition.

Because the moist convective adjustment parameterization only adjusts two adjacent layers each time, it is assumed that clouds extend only two model layers with tops in the above layer and bases in the below layer.

Shortcomings of convective adjustment were summarized by Frank and Molinari (1993). Because convective adjustment schemes ignore real physical processes of interactions between cumulus convection and large-scale environment, cumulus clouds cannot be represented realistically by these schemes.

Despite the simplicity of the moist convective adjustment, it has been applied with

some success in simulating the time-averaged distributions of tropical precipitation.

Kuo (1965) introduced a cumulus parameterization which is based on the relationship between convective rainfall and large-scale moisture convergence. In this scheme, cumulus convection is assumed to result from the moisture supply due to large-scale convergence and evaporation from the surface. The total large-scale supply of moisture is partitioned into two parts, one for the moistening of the environment and the other for heating the atmosphere by condensation. The ratio of heating to moistening is determined by  $c_p(T_c - T)/L(q_c - q)$ , where the subscript  $c$  refers to values on a moist adiabat which the atmosphere will finally adjust to. The ratio estimated in this way, however, underestimates the convective rainfall (and heating) rates in large-scale tropical applications (Krishnamurti et al., 1976; Anthes, 1977). In order to remove this deficiency of the parameterization, a partitioning parameter,  $b$ , was introduced by Kuo (1974). He assumed that a fraction,  $b$ , of the total water vapor converge is stored and acts to increase the humidity of the column; while the remaining fraction,  $1 - b$ , is condensed and precipitated. The new scheme provided a more reasonable precipitation rate (Krishnamurti et al. 1980), but a further question is how to determine the empirical partitioning parameter,  $b$ .

Since then, many attempts to formulate  $b$  have been proposed (Cho, 1975; Fritsch et al., 1976; Krishnamurti et al., 1976, 1983, 1988; Anthes, 1977). A commonly used formulation of  $b$  was suggested by Anthes (1977), who related the value of  $b$  to the mean saturation deficit of the whole cloud layer. Studies also showed that the partitioning parameter,  $b$ , is spatial scale-dependent and may well vary in time due to mesoscale circulations. In some instances, the precipitation values even exceeded the large-scale moisture supply,

corresponding to a negative value of  $b$  (Cho, 1976; Fritsch et al., 1976; Grell et al., 1990).

There have been many attempts to test and improve the Kuo scheme (e.g., Anthes, 1977; Krishnamurti et al., 1980, 1983; Kuo and Anthes, 1984; Geleyn, 1985; Molinari and Corsetti, 1985; Krishnamurti and Bedi, 1988; Grell et al., 1990). An advantage of the Kuo scheme is that it is simple and provides immediate measures of cumulus heating and drying in terms of measurable large-scale variables, without having to compute cloud dynamical processes and cloud microphysical processes. The basic assumptions of the scheme, however, are highly questionable. For example, it is assumed that the environment is heated by mixing of cloud air with environmental air. Actually, the main cumulus heating mechanism is induced compensating sinking in the environment outside the clouds. Meanwhile, the Kuo scheme only considers the moistening effect by large-scale advective processes, moisture diffuses out of the cloud though. The destabilizing effect on temperature lapse rate was neglected. The simplicity of the Kuo-type scheme makes it impossible to study explicitly the interactions between cumulus clouds and the large-scale motions. Because particular cloud types are not defined in the Kuo-type parameterization, there is no classification of cloud tops and cloud bases. The different effects of different cloud types can not be classified.

Betts (1986) and Betts and Miller (1986) proposed an alternative moist convective adjustment parameterization. They replaced the conditionally neutral saturated equilibrium state by a so called quasi-equilibrium state in which typical tropical observations are used as reference. Two different reference thermodynamical vertical structures are used, corresponding to deep convection and shallow convection. The adjustment of the Betts-

Miller parameterization is applied over an empirically chosen finite time interval, and this is another important difference compared with the traditional moist convective adjustment parameterizations. Some success in numerical simulations has been achieved with this parameterization (Betts and Miller, 1986), although the validity of the empirically chosen quasi-equilibrium state for different synoptic situations is questionable. The parameterization was tested at ECMWF (Heckley et al., 1987) and has been used in theoretical studies of hurricane development (Baik et al., 1990). Betts and Miller (1993) modified the parameterization by explicitly introducing the low-level cooling and drying by a downdraft mass flux.

Since specific physical processes are ignored in the Betts-Miller parameterization, it has limited flexibility and is not optimal for investigating interactions between convection and larger scales. Another limitation of the Betts-Miller parameterization is its definition of the reference profile. It is impossible that the reference profiles are unique. For different synoptic situations and in different regions, the reference profiles must be different. This will cause difficulties in the implementation of the parameterization.

The Arakawa-Schubert cumulus parameterization (Arakawa and Schubert, 1974) is a comprehensive attempt to parameterize cumulus convection in large-scale models. It is a generalization of the moist-convective adjustment parameterizations. The approach is drastically different from others since some basic understanding of the interactions between cumulus clouds and large-scale environment are incorporated into the parameterization. The Arakawa-Schubert cumulus parameterization theory, its observational tests and modifications are reviewed in detail in Chapter 3.

Tiedtke (1989) proposed a cumulus parameterization using a comprehensive mass flux scheme. The cloud ensemble is described by a one-dimensional bulk model in the parameterization. The closure assumptions for determining the bulk cloud mass flux are: penetrative convection and mid-level convection are maintained by large-scale moisture convergence and shallow convection by supply of moisture due to surface evaporation. All clouds are assumed starting in the lowest model layer.

It has been seen that one basic assumption in the AS parameterization, as well as in other parameterizations (except the moist convective adjustment parameterization), is that all cumulus convection starts from the PBL. In the next section, we will show that in the real atmosphere cumulus clouds can have cloud bases at any altitude of the troposphere instead of only the PBL and moist convection starting from the free atmosphere is important in many aspects.

### **2.3 Convection Starting from the Free Atmosphere**

As discussed earlier in this chapter, most of the cumulus parameterizations are based on the assumption that all cumulus clouds originate in PBL. Observations reviewed below indicate that in reality cumulus convection can start from the free atmosphere, above the PBL.

Warner et al. (1980) analyzed a cloud cluster occurred on 18 September 1974 during GATE. They used aircraft, radar, satellite and ship data to construct a cloud map. In their case, cloud coverage over the aircraft box approached 50% and cumulus towers were accompanied by altostratus, altocumulus and cirrus. The cloud maps (see Fig. 2.2) they

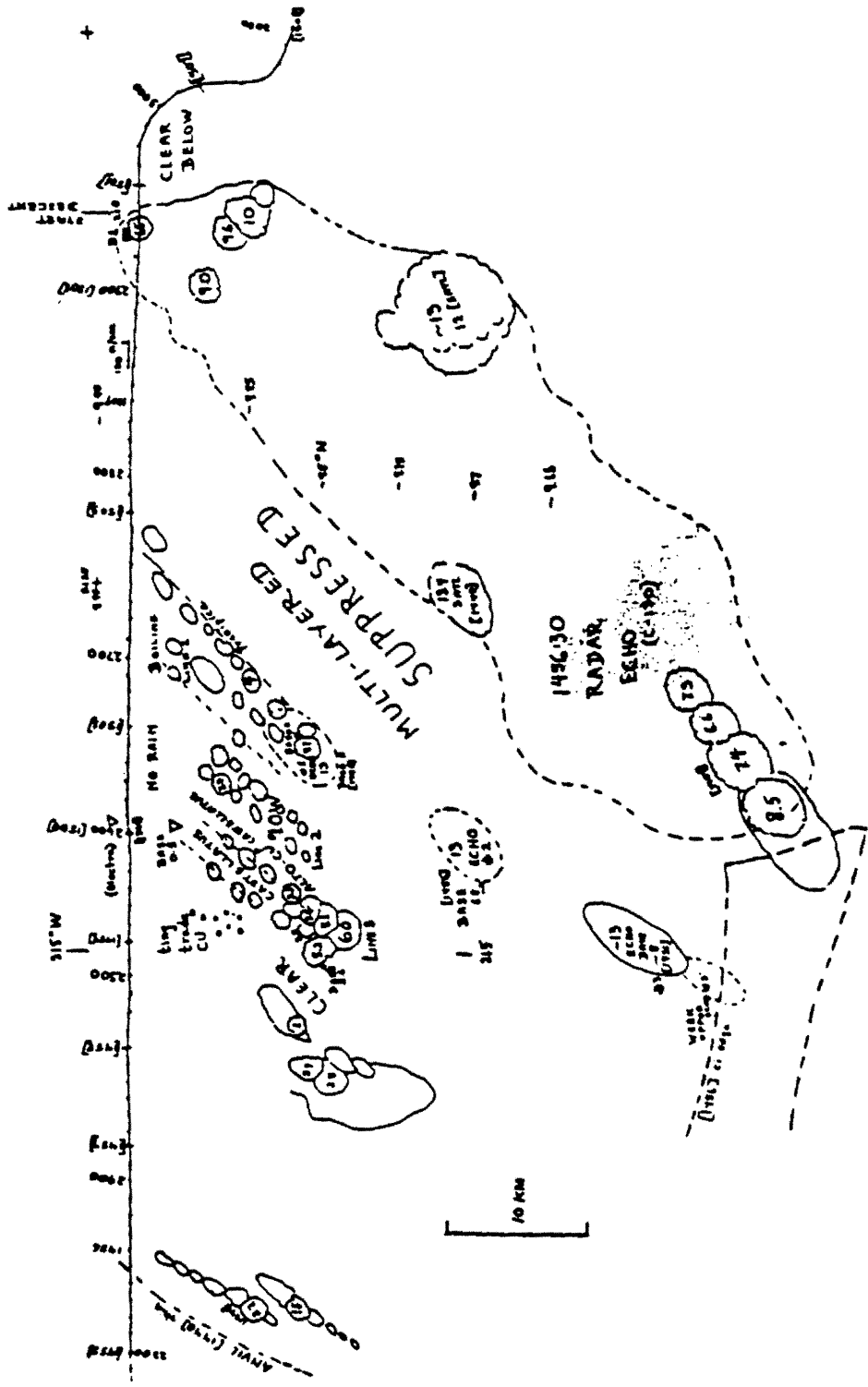


Fig. 2.2 The cloud map from Warner et al. (1980).

constructed show that many clouds have their bases above the PBL. Among them, one of the highest cumulonimbus with a base slanting from 5 to 8 km, and tops reaching 13 km. Warner et al. concluded that these altocumulus castellanus are symptomatic of convective instability released by uplift from below.

Warner and Grumm (1984) studied cloud distributions in a Bay of Bengal monsoon depression on 7 July 1979 by using a variety of observations, including cloud photographs from aircraft. An interesting phenomenon showed by their cloud mapping is that there was much dense high overcast based around 7.5 km with cumulus contiguous with it.

Holle et al. (1979) investigated cloudiness organizations and distributions during GATE. Hourly whole-sky photographs taken aboard four U.S. ships during the daytime hours of the three phases of GATE were used in their studies. Clouds with bases lower than 2 km were defined as low clouds and Clouds with bases higher than 2 km were defined as upper clouds. Their results showed that the GATE area was very cloudy, as expected for a region in the vicinity of the equatorial trough. From their report, the average total cloud cover was 77% and 41% of them were upper clouds (with cloud bases higher than 2 km)!

Colman (1983) did a case study about an intense and persistent outbreak of elevated convection. The selected case was an outbreak of convection which occurred over northeast Texas on March 5, 1982 and continued into March 6, 1982. Colman's analysis indicated that at the mid-levels the convective line was organized ahead of a cyclonic circulation center. The keys for creating the convective instability aloft were temperature and moisture advection. Meanwhile, strong frontogenesis occurred at 850 mb and the associ-

ated frontal circulation most likely provided the forcing needed to trigger the convection. In this type of convection, no inflow air originates in the PBL.

The above discussion shows that observational studies and analysis suggest that convection can start above PBL and that this convection is important in the real atmosphere. The same question, in the meantime, has been raised by modeling studies. Randall et al. (1989) studied interactions among radiation, convection, and large-scale dynamics by using the UCLA / GLA GCM. As in the CSU GCM, the penetrative cumulus convection that originates in the PBL was parameterized by using the AS parameterization, called CUP in the paper. A supplementary parameterization for moist convection which originates above the PBL was included in the GCM. That is Manabe's moist convective adjustment parameterization, called MSTADJ. The model's large-scale precipitation parameterization was called LSP. In this way, simulated cloudiness in the free atmosphere is always associated with CUP, LSP, and / or MSTADJ. Although it was expected that CUP would represent the most important cumulus convection for driving the general circulation, the simulation results for January and July indicated that CUP is only active over 9% of the Earth's surface, while MSTADJ is active over 17% of the Earth, and LSP over about 60%. The zonally averaged frequencies of occurrence showed that even though cumulus incidence and MSTADJ incidence increase and decrease together, MSTADJ is consistently more prevalent, even slightly so in the ITCZ. In other words, MSTADJ is too strong. Randall et al. concluded that the upper tropospheric cloudiness associated with cumulus convection has a powerful influence on both the convection and the large-scale circulation. This implies that we need a more realistic cumulus parameterization which includes physical representations of cumulus convection originating within free atmo-

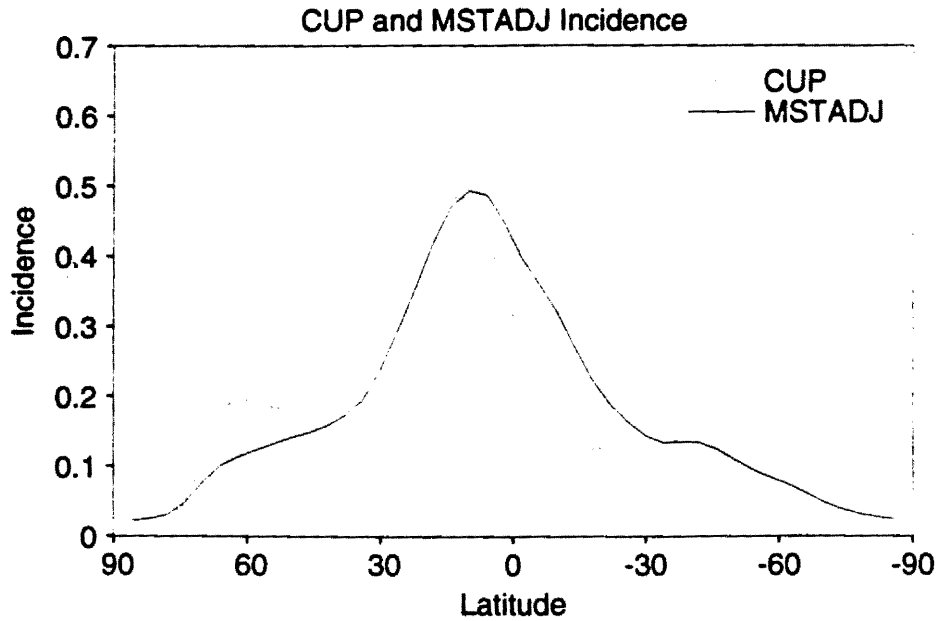


Fig. 2.3 Incidence of cumulus(CUP) and moist convective adjustment (MSTADJ) from CSU GCM for July.

sphere above PBL.

Fig. 2.3 shows the incidence of cumulus and moist convective adjustment from the current CSU GCM for July. With the modification of the AS parameterization in CSU GCM, for example, the implementation of the prognostic equilibrium assumption. MSTADJ and CUP have almost the same magnitudes. It is seen that MSTADJ is quite competitive with CUP even in the tropics. Overall, MSTADJ is much more active than expected. This suggests an important role for cumulus convection originating above the PBL in determining the model's climate.

From the above mentioned observational and model results, we conclude that cumulus convection starting above PBL has an important role on the atmospheric general circulation. In order to improve the model's performance, it is necessary to modify the AS

parameterization to include a representation of cumulus convection starting above the PBL.

## **Chapter 3**

# **Arakawa-Schubert Cumulus Parameterization and CSU GCM**

With the increasing understanding of interactions between moist convection and large-scale motions, many cumulus parameterizations have been proposed and used in general circulation models (GCMs). As indicated in Chapter 2, however, some of these parameterizations are very crude and do not include a theoretical framework which can describe mutual interactions between cumulus convection and its environment. Arakawa and Schubert (1974) developed a physical comprehensive and closed cumulus parameterization (hereafter referred as the A-S parameterization). In Chapter 1 we have stated that the main purpose of this report is to develop a more general parameterization based on the A-S parameterization. Hence, the A-S parameterization theory will be introduced in this Chapter in detail. The cloud model used, the observational tests, performed methods of implementation, and proposed modifications of the A-S parameterization are also reviewed in this chapter. Later this chapter, the Colorado State University (CSU) General Circulation Model (GCM) is briefly described and some simulations with the A-S parame-

terization are presented.

### 3.1 The Arakawa-Schubert Cumulus Parameterization

#### 3.1.1 Modifications of large-scale fields by cumulus ensembles

It is now commonly recognized that cumulus convection modifies large-scale temperature and moisture fields through detrainment and cumulus-induced subsidence in the environment. Due to re-evaporation of detrained cloud water or cloud ice, the detrained air causes large-scale cooling and moistening. Meanwhile, the cumulus-induced subsidence causes large-scale warming and drying. A cumulus parameterization shows how to quantitatively determine the modification of the large-scale fields by cumulus convection.

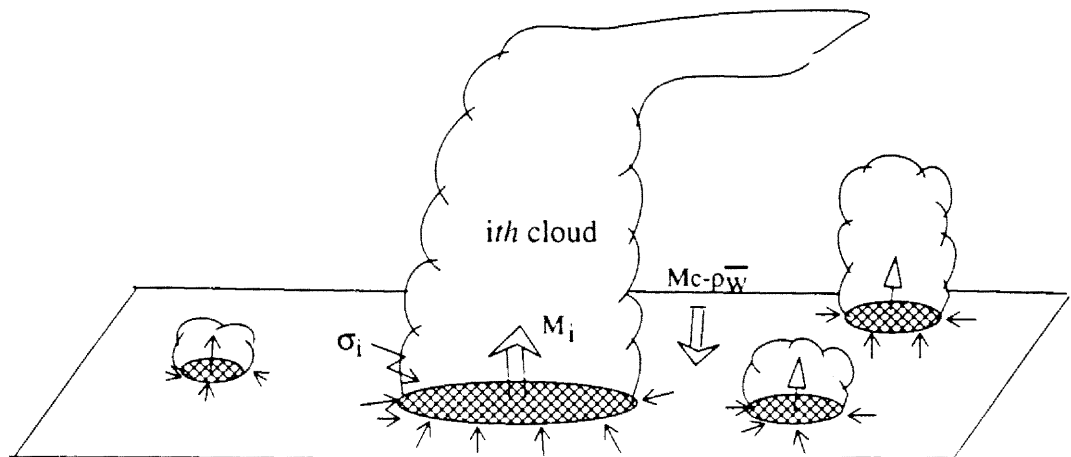


Fig. 3.1 A unit horizontal area in the A-S parameterization (based on Arakawa and Schubert, 1974).

First of all, A-S assumed that there exists an idealized unit area (see Fig. 3.1) which is big enough so that the cloud ensemble can be considered as a statistical entity but small enough so that the environment is approximately uniform horizontally. Using  $\sigma_i$  to

represent the fractional area covered by the  $i$ th subensemble of clouds, the total fractional area covered by the cloud ensemble,  $\sigma_C$ , is

$$\sigma_C = \sum_i \sigma_i \quad , \quad (3.1)$$

and the total vertical mass flux through cloud ensemble,  $M_C$ , is given by

$$M_C = \sum_i M_i \quad , \quad (3.2)$$

where  $M_i$  is the vertical mass flux of the  $i$ th subensemble. If  $\rho \bar{w}$  is used to represent the net vertical mass flux over the large-scale unit horizontal area, then

$$-\tilde{M} = M_C - \rho \bar{w} \quad , \quad (3.3)$$

where  $\tilde{M}$  is the downward compensating mass flux in the environment between the cumulus clouds.

The detrainment rate,  $D_i$ , and entrainment rate,  $E_i$ , for the  $i$ th subensemble at a certain level are defined as

$$D_i = \frac{\partial M_i}{\partial z} + \rho \frac{\partial \sigma_i}{\partial t} \quad , \quad \text{when} \quad \frac{\partial M_i}{\partial z} + \rho \frac{\partial \sigma_i}{\partial t} < 0 \quad (3.4)$$

and

$$E_i = \frac{\partial M_i}{\partial z} + \rho \frac{\partial \sigma_i}{\partial t} \quad , \quad \text{when} \quad \frac{\partial M_i}{\partial z} + \rho \frac{\partial \sigma_i}{\partial t} > 0 \quad (3.5)$$

where  $\rho$  is the density of the air and depends only on  $z$  under the standard anelastic approximation.

Because only active convective clouds are considered, A-S assumed, as a first approximation, that

$$\sigma_c \ll 1 \quad . \quad (3.6)$$

A consequence of (3.6) is

$$\bar{s} \equiv \tilde{s} \quad \text{and} \quad \bar{q} \equiv \tilde{q} \quad (3.7)$$

where  $s$  and  $q$  are the dry static energy and specific humidity, respectively; the overbar denotes an average over the large-scale area, and a tilde denotes the environment. The total detrainment  $D$  is given by

$$D = \sum_i D_i \quad . \quad (3.8)$$

Using the continuity equation, (3.1) - (3.8), and the hydrostatic equation, and assuming that the detrained liquid water evaporates immediately at the detrainment level, the budget equations for dry static energy and water vapor in the environment are

$$\rho \frac{\partial \bar{s}}{\partial t} = D(\hat{s} - \bar{s} - L\hat{l}) + M_c \frac{\partial \bar{s}}{\partial z} - \rho \bar{\mathbf{v}} \cdot \nabla \bar{s} - \rho \bar{w} \frac{\partial \bar{s}}{\partial z} + \bar{Q}_R \quad , \quad (3.9)$$

where

$$\bar{Q}_R \equiv \tilde{Q}_R + \sum_{dc} Q_{Ri} ,$$

and

$$\rho \frac{\partial \bar{q}}{\partial t} = D(\hat{q}^* + \hat{l} - \bar{q}) + M_c \frac{\partial \bar{q}}{\partial z} - \rho \bar{\mathbf{v}} \cdot \nabla \bar{q} - \rho \bar{w} \frac{\partial \bar{q}}{\partial z} \quad . \quad (3.10)$$

In (3.9) and (3.10),  $\hat{s}$  and  $\hat{q}^*$  are defined as

$$\hat{s} \equiv \bar{s} - \frac{L\varepsilon}{1 + \gamma\varepsilon\delta} [\delta(\bar{q}^* - \bar{q}) - \hat{l}] \quad , \quad (3.11)$$

$$\hat{q}^* \equiv \bar{q}^* - \frac{\varepsilon\gamma}{1 + \gamma\varepsilon\delta} [\delta(\bar{q}^* - \bar{q}) - \hat{l}] \quad , \quad (3.12)$$

where ( )<sup>\*</sup> denotes a saturation value; L is the latent heat per unit mass of water vapor;  $\delta = 0.608$ ;  $\hat{l}$  is the liquid water mixing ratio of the detraining air; and

$$\varepsilon \equiv \frac{c_p T}{L} \quad ; \quad \text{and} \quad \gamma \equiv \frac{L}{C_p} \left( \frac{\partial \bar{q}^*}{\partial \bar{T}} \right)_p \quad .$$

From (3.9) and (3.10), the total amount of detrained air, D, the liquid water content of the detraining air,  $\hat{l}$ , and the total cloud vertical mass flux,  $M_c$ , are needed to estimate the changes of the environmental temperature and moisture fields by cumulus clouds. A spectral cumulus ensemble model is used to determine the vertical distribution of the cloud mass flux and subensemble cloud properties.

### 3.1.2 The spectral cumulus ensemble model

In the A-S spectral cumulus ensemble model, the fractional rate of entrainment,  $\lambda$ , is introduced to characterize a cloud type. Different values of  $\lambda$  correspond to different cloud types with different cloud-top heights, and a larger  $\lambda$  corresponds to a cloud with a lower cloud top. With this definition of  $\lambda$ , the vertical mass flux of the cloud ensemble at level  $z$  can be expressed as

$$\begin{aligned} M_c(z) &= \int_0^{\lambda_{max}} m(z, \lambda) d\lambda \\ &= \int_0^{\lambda_{max}} m_B(\lambda) \eta(z, \lambda) d\lambda \quad , \end{aligned} \quad (3.13)$$

where  $m(z, \lambda) d\lambda$  is the mass flux of the subensemble with fractional entrainment rate  $\lambda$ ;  $m_B(\lambda) = m(z_B, \lambda)$  is the cloud base mass flux of the subensemble; and  $\eta(z, \lambda) \equiv m(z, \lambda) / m_B(\lambda)$  is the normalized subensemble mass flux. A-S assumed that  $\lambda$  is a constant with height for the same cloud type. Then using the definition of  $\lambda$ , i.e.

$$\frac{1}{M_c} \frac{\partial M_c}{\partial z} \equiv \lambda \quad ,$$

and  $\eta(z, \lambda) \equiv m(z, \lambda) / m_B(\lambda)$ , an exponential relationship between the normalized subensemble mass flux and the fractional entrainment rate exists and is given by

$$\begin{aligned} \frac{1}{\eta(\lambda, z)} \frac{\partial \eta(\lambda, z)}{\partial z} &= \lambda \quad , \text{ or} \\ \frac{\partial \eta(\lambda, z)}{\partial z} &= \lambda \eta(\lambda, z) \quad . \end{aligned} \quad (3.14)$$

Considering the budget of the moist static energy,  $h \equiv s + Lq$ , gives

$$\frac{\partial}{\partial z} [\eta(z, \lambda) h_c(z, \lambda)] = \lambda \eta(z, \lambda) \bar{h}(z) \quad , \quad (3.15)$$

where  $h_c(z, \lambda)$  is the moist static energy of the type  $\lambda$  cloud; and  $\bar{h}(z)$  is the environmental moist static energy. The right-hand side of (3.15) represents entrainment effects.

In the A-S parameterization, a well mixed layer of variable depth is used to represent the subcloud layer, and the cloud-base properties are given by the subcloud layer values, i.e.

$$s_c(z_B, \lambda) = s_M \quad , \quad (3.16)$$

$$q_c(z_B, \lambda) = q_M \quad , \quad (3.17)$$

$$h_c(z_B, \lambda) = h_M, \quad (3.18)$$

where the subscript M denotes mixed-layer values. The height of the mixed layer,  $z_B$ , is a prognostic variable of the model. For a given moist static energy at cloud base, the moist static energy at cloud top can be obtained as a function of  $\lambda$  by integrating equation (3.15) with height from cloud base to cloud top. When the virtual temperature effect is neglected, the neutral buoyancy condition at the cloud top is given by

$$h_c(z, \lambda_D) = \bar{h}^*(z), \quad (3.19)$$

where  $\lambda_D(z)$  is the  $\lambda$  of the clouds that lose buoyancy (and detrain) at level  $z$ . Eq. (3.19) is an implicit equation for  $\lambda$  and must be solved iteratively. This iteration can be quite expensive and is sometimes poorly behaved.

After the fractional entrainment rate,  $\lambda$ , has been obtained, the vertical distribution of a subensemble's in-cloud moist static energy and the normalized subensemble mass flux can be determined. Fig. 3.2 shows an example of vertical profiles of  $h$ ,  $h^*$ , and  $h_c(z, \lambda)$  for several values of  $\lambda$ .

Similarly, the moisture budget equation gives

$$\begin{aligned} & \frac{\partial}{\partial z} \{ \eta(z, \lambda) [q_c(z, \lambda) + l(z, \lambda)] \} \\ &= \frac{\partial \eta(z, \lambda)}{\partial z} \bar{q}(z) - \eta(z, \lambda) r(z, \lambda), \end{aligned} \quad (3.20)$$

where  $r(z, \lambda)$  is the precipitation production rate per unit mass flux and per unit height.  $r(z, \lambda)$  and  $l(z, \lambda)$  are assumed to be related by

$$r(z, \lambda) = C_0 l(z, \lambda) \quad (3.21)$$

where  $C_0$  is a constant. The right-hand side of (3.20) represents entrainment and precipitation effects. Using the definition of  $\gamma$ , and assuming that the clouds are saturated, the in-cloud water vapor mixing ratio at each model level can be determined using

$$q_v(z, \lambda) = \bar{q}_v^*(z) + \frac{\gamma(z)}{[1 + \gamma(z)]L} [h_c(z, \lambda) - \bar{h}^*(z)] \quad (3.22)$$

Then, the in-cloud suspended liquid water mixing ratio "before precipitation" is

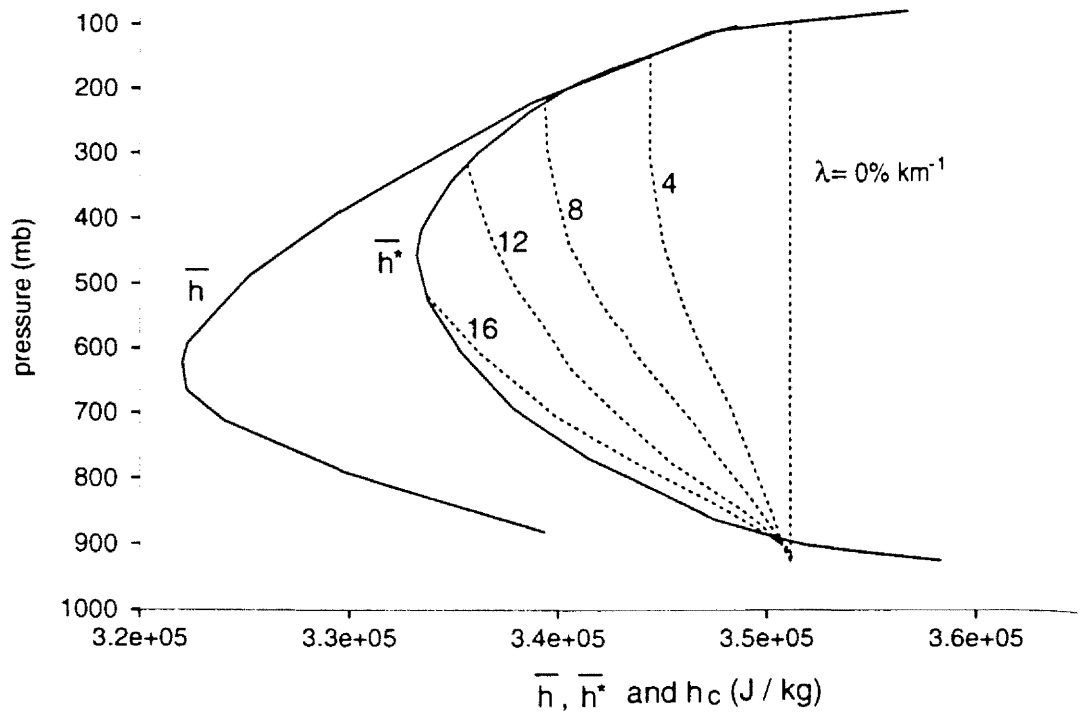


Fig. 3.2 Typical vertical profiles of  $\bar{h}(p)$ ,  $\bar{h}^*(p)$  (solid lines) and  $h_c(p, \lambda)$  (dashed lines).  $h_c(p, \lambda)$  are labeled with value of  $\lambda$  in percent per kilometer (from Arakawa and Schubert, 1974).

$$l(z, \lambda) = q_c(z, \lambda) - q_v(z, \lambda) \quad . \quad (3.23)$$

Using (3.20) – (3.23), and for a given  $\lambda$ , the vertical distribution of in-cloud moisture and the precipitation production rate are determined. Therefore, the thermodynamical properties of the subensemble can be determined.

The spectral cumulus ensemble model used in the A-S parameterization is similar to a stationary, one-dimensional, entraining plume model. As indicated by Arakawa and Cheng (1993), however, the spectral cloud ensemble model describes the average characteristics of a subensemble of clouds which are at various stages of their life cycles. Then the subensemble-average vertical structure may simply reflect the temporal change of rising bubbles, as in the spectral model of Ooyama (1971).

### **3.2 The Quasi-Equilibrium Closure Hypothesis of the A-S Parameterization**

#### **3.2.1 The cloud work function**

If  $K(\lambda) d\lambda$  is defined as the cloud-scale kinetic energy of subensemble clouds with fractional entrainment rate between  $\lambda$  and  $\lambda + d\lambda$ , the budget equation for the cumulus kinetic energy can be written as

$$\frac{d}{dt}K(\lambda) d\lambda = [A(\lambda) - D(\lambda)] M_B(\lambda) d\lambda \quad , \quad (3.24)$$

where  $D(\lambda)$  is the dissipation rate per unit  $M_B(\lambda) d\lambda$ .  $A(\lambda)$  is the cloud work function, which was introduced by the A-S to measure the work done by the buoyancy force per unit mass flux at cloud base. When virtual temperature effects due to the existence of

vapor and liquid are neglected, the cloud work function for type  $\lambda$  clouds is given by

$$A(\lambda) = \int_{z_B}^{z_D(\lambda)} \eta(z, \lambda) g \frac{T_c(z, \lambda) - \bar{T}(z)}{\bar{T}} dz \quad , \quad (3.25)$$

where  $g$  is gravity and  $g \frac{T_c(z, \lambda) - \bar{T}(z)}{\bar{T}}$  is the buoyancy force per unit mass. When  $\lambda$  is given, the subensemble properties can be determined, so the cloud work function depends on the environmental and subcloud mixed-layer thermodynamic properties.

From (3.24), the cloud work function is the rate of generation of cumulus kinetic energy. Therefore,  $A(\lambda)$  is a generalized measure of moist convective instability. A-S showed that the environment must be moist enough in order to have a positive cloud work function, which is necessary for kinetic energy generation. This simply means that conditional instability is not enough to produce convection. That is why it is called “*conditional*” instability! For non-entraining clouds ( $\lambda = 0$ ), the environmental moisture above the boundary layer is not important and  $A(\lambda) > 0$  can be considered as a necessary but not sufficient condition for convection.

The time derivative of the cloud work function can be expressed as a summation of cloud terms and large-scale terms, that is

$$\frac{dA(\lambda)}{dt} = \left[ \frac{dA(\lambda)}{dt} \right]_C + \left[ \frac{dA(\lambda)}{dt} \right]_{LS} \quad , \quad (3.26)$$

where the subscripts C and LS denote convective terms and large-scale terms, respectively. The large-scale terms are called the large-scale forcing and denoted by  $F(\lambda)$ . When  $F(\lambda)$  is positive, large-scale processes tend to increase the cloud work function and so destabilize the atmosphere. A way to calculate the large-scale forcing will be described

later.

The convective terms of the time rate of change of the cloud work function in (3.26) are called the cumulus adjustment terms. Because cumulus convection acts to decrease the cloud work function and stabilize the atmosphere, the convective term of (3.26) is expected to be less than zero. This “cumulus adjustment” term can be written as

$$\left[ \frac{dA(\lambda)}{dt} \right]_C = \int_0^{\lambda^{max}} K(\lambda, \lambda') M_B(\lambda') d\lambda' \quad , \quad (3.27)$$

where  $K(\lambda, \lambda')$  is the mass flux kernel and is the rate of decrease (stabilization) of the cloud work function, for type  $\lambda$  clouds, through the modification of the environment by type  $\lambda'$  clouds. The kernel  $K(\lambda, \lambda')$  is typically negative.

The large scale forcing,  $F(\lambda)$ , was further divided into two parts as

$$F(\lambda) = F_C(\lambda) + F_M(\lambda) \quad , \quad (3.28)$$

where  $F_C(\lambda)$  is the cloud-layer forcing and  $F_M(\lambda)$  is the mixed-layer forcing. The main contributions to the cloud-layer forcing are due to cooling of the environment above the mixed-layer by large-scale processes, including adiabatic cooling due to large-scale upward motion, and radiative cooling. The mixed-layer forcing includes the deepening of the mixed layer by turbulent entrainment and large-scale lifting at the top of the mixed layer, the surface heating and moistening.

The mass flux kernel, which represents interactions among different subensembles, can be divided into three parts as

$$K(\lambda, \lambda') = K_V(\lambda, \lambda') + K_D(\lambda, \lambda') + K_M(\lambda, \lambda') \quad . \quad (3.29)$$

where the subscripts V, D, and M denote the vertical mass flux, detrainment and mixed-layer terms, respectively. The A-S showed that the most dominant effect in the mass flux kernel is the decrease of the cloud work function, for type  $\lambda$  clouds, through adiabatic warming of the environment due to the subsidence induced by type  $\lambda'$  clouds. For the detrainment kernel,  $K_D(\lambda, \lambda')$  is zero when  $\lambda' < \lambda$ , which means that the deep clouds do not affect the shallow clouds through detrainment. The detrainment kernel is always positive when  $\lambda' > \lambda$ . The physical meaning is that shallower clouds increase the cloud work function of deeper clouds by cooling and moistening the environment, by evaporation of the liquid or ice detrained from the shallow clouds.

Based on the above discussion, (3.26) can be written as

$$\frac{dA(\lambda)}{dt} = \int_0^{\lambda_{max}} K(\lambda, \lambda') M_B(\lambda') d\lambda' + F(\lambda) \quad . \quad (3.30)$$

We will use (3.30) to discuss the closure hypothesis of the A-S parameterization in the following section.

### 3.2.2 The quasi-equilibrium hypothesis

Two time scales, the cumulus adjustment time scale,  $\tau_{ADJ}$ , and the large-scale forcing time scale,  $\tau_{LS}$ , were introduced by A-S in order to explain the cloud work function quasi-equilibrium hypothesis.

Suppose that the atmosphere is in a state in which there is no large-scale forcing

and no cumulus convection, but the sounding gives a positive cloud work function  $A(\lambda)$  for certain types of clouds. Under these conditions, a positive cumulus mass flux will be generated and cumulus clouds will grow, provided that there is a triggering mechanism. The cumulus convection, meanwhile, will modify the large-scale environmental sounding, for example, by warming and drying the environment above the mixed layer. This will decrease the buoyancy force as well as the cloud work function, and lead to a decay of the cumulus clouds. Finally, the atmosphere will adjust to a neutral state. The  $e$  folding time needed for this adjustment process is called the adjustment time scale, denoted by  $\tau_{ADJ}$ . If there is a steady large-scale forcing, the adjusted state will be unstable rather than neutral. The unstable equilibrium is characterized by  $A(\lambda) > 0$  and  $dA(\lambda)/dt=0$ . In this case, cumulus convection will be maintained and the stabilization rate by cumulus convection will be equal to the destabilization rate by the large-scale forcing. The adjustment time needed to reach the equilibrium state will be about  $\tau_{ADJ}$ , at least for weak large-scale forcing, as discussed by Arakawa and Schubert (1974).

In the real atmosphere, the large-scale forcing is not steady but changes in time. Therefore, there is a time scale associated with the large-scale forcing, denoted here by  $\tau_{LS}$ . For finite  $\tau_{LS}$ , cumulus convection cannot fully adjust the environment to an equilibrium state and so the present state of the atmosphere always depends on the past history of the large-scale forcing. When the large-scale forcing time scale  $\tau_{LS}$  is much longer than the adjustment time scale  $\tau_{ADJ}$ , cumulus convection can always keep the environment close to an equilibrium with the current large-scale forcing. This “quasi-equilibrium assumption” is used to close the A-S cumulus parameterization.

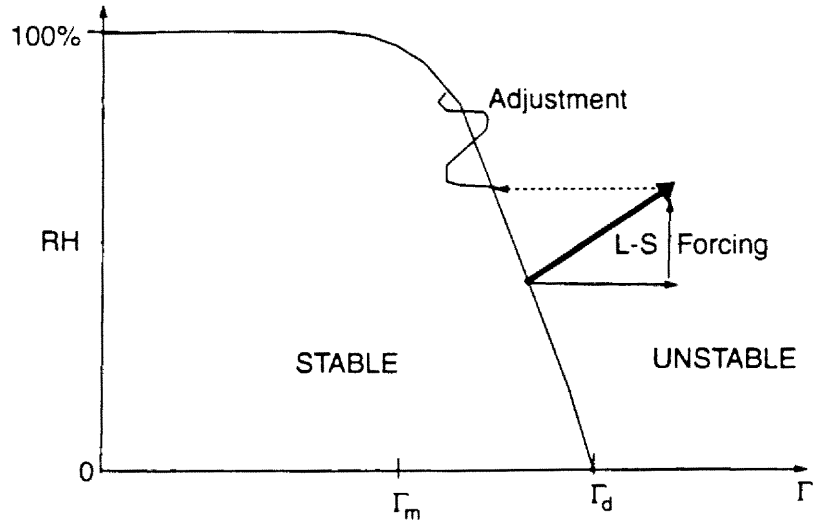


Fig. 3.3. A schematic diagram showing a hypothetical equilibrium curve in the  $\Gamma$ -RH space that separates stable and unstable regions. Large-scale forcing (heavy solid arrow), its components (solid arrows), and the corresponding adjustment (dashed arrow) are shown in the diagram (from Arakawa, 1993).

Arakawa and Chen (1987) and Arakawa and Cheng (1993) demonstrated that the cloud work function depends on atmospheric relative humidity, RH, and lapse rate,  $\Gamma$ , i.e.  $A \equiv A(RH, \Gamma)$ . Therefore, the cumulus adjustment processes can be illustrated as shown in Fig. 3.3. The large-scale forcing tends to make the atmosphere unstable, while cumulus convection adjusts the atmosphere to the “quasi-equilibrium” state by the release of the available potential energy of the mean state.

In equation (3.26), the cloud adjustment term is of order

$$\left[ \left[ \frac{dA(\lambda)}{dt} \right]_C \right] \sim \frac{A(\lambda)}{\tau_{ADJ}} \quad (3.31)$$

The time change of the cloud work function is of order

$$\left| \frac{dA(\lambda)}{dt} \right| \leq \frac{A(\lambda)}{\tau_{LS}} . \quad (3.32)$$

Combining (3.31) and (3.32) gives

$$\left| \frac{dA(\lambda)}{dt} \right| \leq \frac{\tau_{ADJ}}{\tau_{LS}} \left[ \left| \frac{dA(\lambda)}{dt} \right| \right]_C . \quad (3.33)$$

When the time scale of the large-scale forcing,  $\tau_{LS}$ , is much longer than the adjustment time scale  $\tau_{ADJ}$ , the time change of the cloud work function is much smaller than the cumulus adjustment term. Therefore, the left hand side of (3.26) can be neglected. Returning to (3.30), the left-hand side is seen to be negligible. Eq. (3.30) becomes

$$\int_0^{\lambda_{max}} K(\lambda, \lambda') M_B(\lambda') d\lambda' + F(\lambda) \equiv 0 . \quad (3.34)$$

The magnitude of the time rate of change of the cloud work function has been compared with the large-scale forcing, by using observational data, in Arakawa and Schubert (1974). They found that the observed  $dA(\lambda)/dt$  is much smaller than the large-scale forcing term  $F(\lambda)$ . This suggests that (3.34) is a good approximation at least for the data they used.

With the quasi-equilibrium assumption, the cloud-base mass flux can be computed by using (3.34). Then, the cloud model can be used to determine the subensemble cloud properties and vertical cloud mass fluxes. The effects of cumulus convection on the large-scale environment can then be determined. The cumulus parameterization is thus closed.

### 3.3 Observational Tests

#### 3.3.1 Evaluation of the quasi-equilibrium hypothesis

Lord and Arakawa (1980) evaluated the quasi-equilibrium hypothesis proposed by the A-S, by using observations.

In GCMs, the cumulus parameterization is used to determine cumulus cloud effects in order to predict the time evolution of large-scale fields. When a certain variable is chosen to be in an equilibrium in order to apply a quasi-equilibrium hypothesis, this variable must not be one which the GCM is intended to predict. This is the first principle that the closure assumption needs to satisfy. Meanwhile, comprehensive global models must be valid for a variety of synoptic and surface conditions in order to simulate the real climate. This validity must not be destroyed by the choice of the closure assumption used in the cumulus parameterization. This is the second principle which is required to be satisfied by making the closure assumption. Therefore, the closure assumption must satisfy at least two basic principles which are universally valid, and must not lead to a loss of predictability of the large-scale fields, as indicated by Arakawa (1993).

In the A-S parameterization, the closure states that there is a balance between the generation of moist convective instability by the large-scale processes and the destruction of the instability by cumulus convection. Replacing each term of (3.24) by its order of magnitude gives

$$\frac{K(\lambda)}{\tau} - A(\lambda) M_B(\lambda) - \frac{K(\lambda)}{\tau_{DIS}} \quad , \quad (3.35)$$

where  $\tau$  and  $\tau_{DIS}$  are time scales of the time change of the cloud-scale kinetic energy and

the dissipation time scale, respectively. When  $\tau \gg \tau_{DIS}$ , the left-hand side of (3.24) can be neglected. Then (3.24) gives

$$A(\lambda) \approx D(\lambda) \quad . \quad (3.36)$$

This is called “kinetic energy quasi-equilibrium.” Since we tend to predict changes of a cumulus ensemble over the time scale of large-scale disturbances ( $\tau_{LS}$ ), an appropriate choice for  $\tau$  is  $\tau = \tau_{LS}$ . The order of  $\tau_{LS}$  is typically about  $10^5$  s or larger. The order of  $\tau_{DIS}$  is only the time scale of dissipative processes of cumulus clouds, it must be smaller than an actual cloud lifetime. Therefore,  $\tau_{DIS}$  can be estimated to be on the order  $10^2 - 10^3$  s. This shows that  $\tau_{DIS} \ll \tau_{LS}$ , so that kinetic energy quasi-equilibrium is a good approximation.

Since  $D(\lambda)$  is the dissipation rate per unit cloud-base mass flux, it should depend only on the cloud type once the quasi-equilibrium state is reached, no matter what the dissipation mechanism is. In other words,  $D(\lambda)$  can be regarded as an intrinsic subensemble property and is a quasi-constant for each cloud type. Therefore,  $A(\lambda)$  is also a quasi-constant for each cloud type, provided that the quasi-equilibrium state is reached.

After Lord and Arakawa (1980) reached the above conclusions, they used the Marshall Islands data set (Yanai *et al.*, 1973 and Chu, 1976), the VIMHEX data set (Betts and Miller, 1975), the GATE data set (Thompson *et al.*, 1979), and the AMTEX data set (Nitta, 1976) to calculate cloud work functions corresponding to various cloud types. Their results showed that cloud work functions fall into a well-defined narrow range for each subensemble even though the thermodynamical vertical structures of the various data sets

are quite different. Hence, they concluded that the quasi-equilibrium hypothesis is well supported by observations.

### 3.3.2 Observational tests of the A-S parameterization

Lord (1982) used a semi-prognostic approach and GATE data to evaluate the A-S parameterization. In the semi-prognostic method, observed large-scale variables, advective tendencies, surface fluxes and radiative heating are used to calculate the large-scale forcing  $F(\lambda)$  and to predict the cumulus mass flux spectrum. With the cloud ensemble model and the mass flux spectrum, the effects of convection on the large-scale environment can be determined.

The tests of the A-S parameterization showed that the precipitation rate predicted by the A-S scheme is in very good agreement with estimates from the observed large-scale moisture budget and from radar observations. This implies that the major interactions between cumulus convection and large-scale circulation have been captured by the A-S parameterization. The quasi-equilibrium closure assumption is shown to be a very good approximation. Sensitivity experiments showed that this parameterization is rather insensitive to some of its cruder aspects, such as the precipitation parameter  $C_0$  in (3.21). The time-averaged vertical heating and drying profiles were also compared with observational estimates. The predicted heating and drying patterns are quite similar to observations except below 750 mb where the A-S parameterization created an excess drying equivalent to  $\sim 2 \text{ K day}^{-1}$ . The reason may be neglect of 1) cumulus-scale downdrafts, 2) the influence of deep mesoscale circulations associated with stratiform rain areas and/or 3) evaporation and melting in these rain areas. Despite these small disagreements between

predictions and observations, the A-S parameterization has withstood these tests quite well.

### **3.4 Modifications of the A-S Parameterization**

#### **3.4.1 The inclusion of convective downdrafts**

The importance of convective downdrafts has been recognized in many studies (e.g., Telford, 1975; Johnson, 1976; Houze, 1977; Emanuel, 1981). Cheng and Arakawa (1991a, 1991b) incorporated convective downdrafts into the A-S parameterization. Because the weight of rainwater and the cooling of air due to evaporation of raindrops are the two major factors driving the convective-scale downdrafts, the rainwater flux must be estimated for the inclusion of downdrafts in cumulus parameterizations. Cheng (1989) assumed that the raindrops fall with their terminal velocities relative to the surrounding cloud air, rather than falling to ground instantaneously, as in the A-S parameterization. Therefore, the horizontal and vertical components of the updraft air velocity, relative to the cloud, are needed in order to trace the motions of the raindrops. In this case, the tilting of the updraft must be considered and the tilting angle becomes an important factor for estimating the rainwater budget, as in the schematic diagram figure 2.4.

Cheng (1989) used the rainwater budget equations and in-cloud vertical momentum to determine the tilting angle, and a downdraft model to obtain the properties of the downdrafts. Cheng and Arakawa (1993) compared observations with predicted results of the A-S schemes with and without downdraft effects in terms of semi-prognostic tests, using GATE Phase III data. They found that the excess drying of lower layers from the A-S scheme can be drastically reduced by the inclusion of downdraft effects.

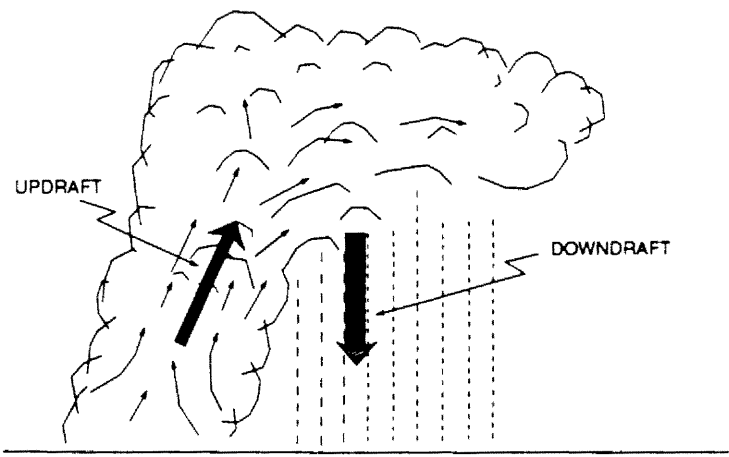


Fig. 3.4 A schematic diagram showing updraft with tilting and downdraft.

### 3.4.2 Prognostic closure

The quasi-equilibrium closure used in the A-S parameterization has received strong support from observations (e.g., Lord and Arakawa, 1980; Lord, 1982; Arakawa and Chen, 1987; Xu and Emanuel, 1989) and numerical simulations (e.g., Kao and Ogura, 1987; Grell et al., 1991), but its practical implementation is relatively difficult. For example, the mass flux kernel matrix and the large-scale forcing term  $F(\lambda)$  must be computed at every time step in order to determine the subensemble cloud base mass flux. Because  $M_B$  is the cloud base mass flux, physically we need

$$M_B \geq 0 . \tag{3.37}$$

In practice, when (3.34) is used to determine cloud base mass flux for each subensemble simultaneously, the solutions often fail to satisfy condition (3.37). This caused difficulties for implementations of the A-S parameterization in GCMs. Although various methods

(e.g., linear programming) have been proposed to find a “best” solution of  $M_B$  which can satisfy (3.37), the uniqueness of such solutions is still questionable (e.g., Moorthi and Suarez, 1992).

In order to simplify the implementation of the A-S parameterization without losing its physical content, Randall and Pan (1993) proposed a prognostic closure assumption by assuming that

$$K = \alpha M_B^2 \quad , \quad (3.38)$$

where  $K$  is the vertically integrated kinetic energy of the subensemble per unit area (hereafter referred as CKE);  $\alpha$  is a parameter; and  $M_B$  is the subensemble cloud base mass flux. By introducing a dissipation time scale, denoted by  $\tau_D$ , and integrating (3.24) for all cloud types, the prognostic equation for CKE can be written as

$$\frac{\partial K}{\partial t} = M_B A - \frac{K}{\tau_D} \quad , \quad (3.39)$$

where  $A$  is cloud work function. Substituting (3.38) into (3.39) gives a linear prognostic equation for  $M_B$ :

$$\frac{\partial M_B}{\partial t} = \frac{A}{2\alpha} - \frac{M_B}{2\tau_D} \quad . \quad (3.40)$$

The cloud-base mass flux can be predicted by using (3.40), or the CKE can be predicted by using (3.39), for given  $A$ ,  $\alpha$ , and  $\tau_D$ . If (3.39) is used to predict the CKE, the cloud base mass flux can then be obtained in terms of (3.38). This is the prognostic closure.

The differences between quasi-equilibrium closure and prognostic closure were

discussed by Randall and Pan. Based on (3.30), the time rate of change of the cloud work function is given by

$$\frac{\partial A}{\partial t} = JM_B + F \quad , \quad (3.41)$$

where  $J$  and  $F$  correspond to the mass flux kernel and large-scale forcing of quasi-equilibrium closure assumption. Combining (3.40) and (3.41) and assuming  $J$  to be independent of time, second-order ordinary differential equations for  $A$  and  $M_B$  can be derived:

$$\ddot{A} + \frac{\dot{A}}{2\tau_D} - \frac{J}{2\alpha}A = \frac{F}{2\tau_D} + \dot{F} \quad , \quad (3.42)$$

and

$$\ddot{M}_B + \frac{\dot{M}_B}{2\tau_D} - \frac{J}{2\alpha}M_B = \frac{F}{2\alpha} \quad . \quad (3.43)$$

Here a ‘‘dot’’ is used to represent a time derivative. Considering the limit  $\tau_D \rightarrow \infty$  , with  $F = 0$  , (3.42) and (3.43) reduce to

$$\ddot{A} - \frac{J}{2\alpha}A = 0 \quad (3.44)$$

and

$$\ddot{M}_B - \frac{J}{2\alpha}M_B = 0 \quad . \quad (3.45)$$

This indicates that the system contains a time scale  $\sqrt{\alpha/|J|}$  . Equations (3.44) and (3.45) have oscillatory solutions. Under the constraints

$$A \geq 0 \quad , \quad M_B \geq 0 \quad , \quad (3.46)$$

the oscillations will halt as soon as  $A$  and  $M_B$  have decreased to zero. Therefore, the time

scale  $\sqrt{\alpha/|J|}$  can be interpreted as the  $\tau_{ADJ}$  discussed by the A-S in connection with the quasi-equilibrium closure. Suppose that

$$\left. \begin{aligned} \ddot{A} &\sim \frac{A_F}{\tau_{LS}^2} , \\ \dot{A} &\sim \frac{A_F}{\tau_{LS}} , \\ \dot{F} &\sim \frac{F}{\tau_{LS}} . \end{aligned} \right\} \quad (3.47)$$

Then if the time scales in the system satisfy

$$\frac{\tau_{ADJ}}{\tau_{LS}} \ll 1 , \quad (3.48)$$

$$\left( \frac{\tau_{ADJ}}{\tau_{LS}} \right) \cdot \left( \frac{\tau_{ADJ}}{\tau_D} \right) \ll 1 , \quad (3.49)$$

and

$$\frac{\tau_D}{\tau_{LS}} \ll 1 , \quad (3.50)$$

equations (3.42) and (3.43) can be approximated by

$$A = -\alpha \frac{F}{J\tau_D} , \quad (3.51)$$

$$M_B = -\frac{F}{J} . \quad (3.52)$$

Under these conditions, the solution based on prognostic closure should closely approxi-

mate the quasi-equilibrium solution.

It should be noticed that even though (3.52) is identical to quasi-equilibrium closure, the cloud base mass flux from prognostic closure is not necessarily the same one that would be obtained from the quasi-equilibrium closure. In the A-S quasi-equilibrium hypothesis, the contributions to the time change of the cloud work function must be grouped into “convective” and “non-convective” components. In practice, however, some processes are difficult to classify as “convective” or “non-convective.” For example, the upper tropospheric stratiform anvil clouds are for the most part produced by detrainment from deep convective clouds. Logically, the stratiform precipitation and radiative processes associated such stratiform clouds should be included as part of the *response* of cumulus convection, rather than part of the large-scale forcing. When some effects of convection-associated stratiform clouds are incorrectly treated as large-scale forcing in the A-S quasi-equilibrium hypothesis, both the large-scale forcing and the mass flux kernel can be incorrectly estimated and the cloud base mass flux,  $M_B$ , can be different from the one from the prognostic closure.

Randall and Pan discussed the physical bases for determining  $\alpha$  and  $\tau_D$ , and presented some simulations using prognostic closure. The prognostic closure can capture most climate features which are captured by quasi-equilibrium, and at the same time, the computational algorithm is drastically simplified. The required computing time for cumulus parameterization can be cut by 50% if the prognostic closure assumption is used. This is a significant improvement because it facilitates further modifications of the A-S parameterization to add more physical content. We take advantage of this flexibility in order to

make the changes discussed in this report.

### **3.5 Simulations with the A-S Parameterization in the CSU GCM**

The A-S parameterization has been implemented in the current Colorado State University (CSU) General Circulation Model (GCM). A brief description of CSU GCM and some simulation results obtained by using the A-S parameterization with the prognostic closure are presented in this section.

#### **3.5.1 Description of CSU GCM**

The CSU GCM has been derived from the UCLA GCM, which was developed at UCLA, beginning in the early 1960s, by Professor A. Arakawa and collaborators. A copy of the UCLA model was brought to the Goddard Laboratory for Atmospheres (GLA) in 1982, and from there to CSU in July 1988. Since the model left UCLA, many changes have been made, including revisions of the solar and terrestrial radiation parameterizations (Harshvardhan *et al.*, 1987), the introduction of a new parameterization of land-surface processes (Sellers *et al.* 1995a, b; Randall *et al.* 1995), cumulus convection parameterization (Randall and Pan, 1994), liquid and ice cloud microphysics (Fowler *et al.*, 1995), and a major enhancement of the diagnostics. Some recent results obtained with the GCM are presented by Harshvardhan *et al.* (1989), Randall *et al.* (1989), Randall *et al.* (1991), Fowler *et al.* (1995), Fowler and Randall (1995) and Randall *et al.* (1995).

##### **i) Vertical coordinate**

The CSU GCM is formulated using a modified sigma coordinate, in which the planetary boundary layer (PBL) top is a coordinate surface, and the PBL itself is the low-

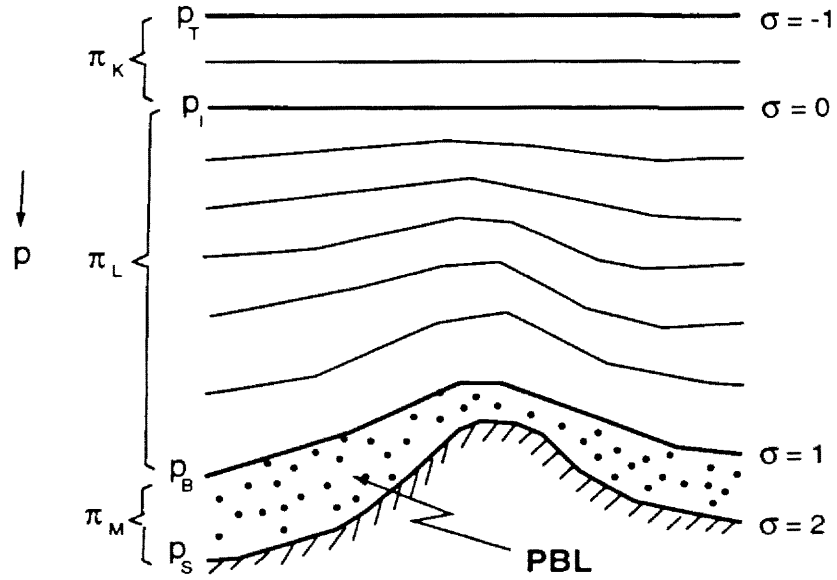


Fig. 3.5 The modified  $\sigma$ -coordinate.  $\sigma = 1$  corresponds to the PBL top and  $\sigma = 2$  to the surface (from Suarez *et al.*, 1983).

est model layer. Fig. 3.5 illustrates the relationship between  $\sigma$  and the pressure,  $p$ . The vertical coordinate is defined by

$$\sigma = \begin{cases} -\left(\frac{p_I - p}{\pi_K}\right), & \text{for } p_I \geq p \geq p_T \\ \left(\frac{p - p_I}{\pi_L}\right), & \text{for } p_B \geq p \geq p_I \\ 1 + \left(\frac{p - p_B}{\pi_{LM}}\right), & \text{for } p_S \geq p \geq p_B \end{cases} \quad (3.53)$$

Here  $p$  is pressure, and the subscripts are defined as follows:  $p_T$  is the constant pressure at the model top;  $p_I$  is a constant pressure roughly at the tropopause, and nominally chosen

as 100 mb; and  $p_B$  and  $p_S$  are the spatially and temporally varying pressures at the PBL top and the earth's surface, respectively. We define

$$\left. \begin{aligned} \pi_K &= p_I - p_T, \\ \pi_L &= p_B - p_I, \\ \pi_M &= p_S - p_B. \end{aligned} \right\} \quad (3.54)$$

as the pressure thicknesses of the "stratosphere," the "troposphere," and the PBL, respectively.

## ii) Prognostic variables

The prognostic variables of the CSU GCM are: the potential temperature; the mixing ratio of water vapor; the horizontal wind components; the surface pressure; the pressure thickness of the free troposphere and the PBL; the turbulence kinetic energy of the PBL; the temperatures of the ground surface and the "deep" soil at land points and the ice temperature at land ice and sea ice points; the depth of both snow and intercepted surface liquid water and the stomatal conductance at land points; the kinetic energy associated with cumulus convection; the cloud microphysical variables, i.e., the mass of water vapor, cloud water, cloud ice, rain and snow.

## iii) Horizontal, vertical and time differencing

The governing equations are finite-difference, using highly conservative schemes (Arakawa and Lamb, 1977, 1981; Arakawa and Suarez, 1983). Fourier filtering of the mass flux and pressure gradient vectors is used to maintain computational stability near

the poles, following Arakawa and Lamb (1977).

The horizontal differencing is based on a regular latitude-longitude grid. The horizontal differencing scheme is of second-order accuracy, except that the inertial terms of the momentum equation correspond to a fourth-order scheme for the advection of vorticity (Takano and Wurtele, 1982), and the horizontal advection schemes used for potential temperature and moisture are of fourth-order accuracy (Arakawa, unpublished).

The atmospheric variables are vertically staggered following the Lorenz scheme, in which potential temperature, the horizontal wind vector, and the mixing ratios of moisture and ozone are defined at “layer centers”, while the diagnostically determined vertical velocity is defined at “layer edges.” Currently only one model layer is permitted inside the PBL.

The model uses a complex time-differencing scheme, which can be summarized as follows. Adiabatic, frictionless processes (advection, pressure gradient force, etc.) use the leapfrog scheme, with a Matsuno step inserted periodically to prevent separation of the solutions. Let  $\Delta t$  be the time step used for these terms, so that leapfrog steps span  $2\Delta t$ , and Matsuno steps span a single  $\Delta t$ . We refer to the Matsuno and leapfrog steps as “short” time steps, and to the intervals between Matsuno steps as “long” time steps. Prior to each Matsuno step, heating, moistening, and cumulus mass fluxes are computed, saved, and added evenly over the succeeding Matsuno and leapfrog steps. The surface fluxes are computed on short time steps, using an implicit differencing scheme. Horizontal diffusion of momentum uses the forward time-differencing scheme, and is added every short time step.

#### iv) Solar radiation and the terrestrial radiation parameterizations

The model's solar radiation and the terrestrial radiation parameterizations are described by Harshvardhan *et al.* (1987). The solar radiation parameterization includes the seasonal cycle through a prescription of the earth-sun geometry as a function of Julian Day, Rayleigh scattering and absorption by water vapor and ozone, as well as the effects of clouds. For the case in which ozone is not predicted by the model, an ozone distribution is prescribed, as a function of latitude, height, and season, based on observations. The terrestrial radiation parameterization includes the effects of water vapor, carbon dioxide, and ozone. Ozone is included as described above for the solar radiation parameterization.

#### v) Planetary boundary layer

The planetary boundary layer is parameterized as a well mixed layer of variable depth. The PBL depth is calculated prognostically from

$$\frac{\partial}{\partial t}(\pi_M) + \nabla \cdot (\int_1^2 \pi_M \mathbf{V} d\sigma) = g(E - M_B) \quad , \quad (3.55)$$

where  $E$  is the rate of turbulent entrainment at the PBL top, and  $M_B$  is the mass flux into the base of cumulus clouds, which is calculated by the cumulus parameterization.

The turbulence kinetic energy (TKE) of the PBL is also predicted, following the method of Randall *et al.* (1987). The TKE varies due to shear production is determined by a closure condition involving dissipation, buoyant consumption, and the rate at which TKE is supplied to make newly entrained air turbulent. The surface fluxes of sensible heat, moisture, and momentum are determined through a simplified version of the method of

Deardorff (1971), which takes into account the effects of stability and surface roughness.

PBL stratocumulus clouds are detected by checking for saturation at the PBL top, using the mixed-layer assumption. The same assumption is used to find the cloud base level, where the predicted PBL mixing ratio equals the saturation mixing ratio. The occurrence of PBL stratus clouds promotes entrainment through concentrated cloud-top radiative cooling and latent heat effects. When the condition for cloud-top entrainment instability is met (Randall, 1980), the PBL is assumed to exchange mass with the GCM layer above until the instability is removed. The PBL depth is assumed to remain unchanged during this process, which is referred to as “layer cloud instability” (LCI). The existence of PBL stratocumulus clouds affects the GCM results in three ways: 1) through the radiation parameterization; 2) by influencing the entrainment rate; 3) through LCI.

vi) Cumulus parameterization and stratiform cloud precipitation

The A-S cumulus parameterization with the prognostic closure (Randall and Pan, 1993), as discussed in previous sections, is used for penetrative cumulus convection. Because A-S only parameterized the effects of cumulus clouds that originate at the PBL top, and it is also possible for cumulus updrafts to originate in the free atmosphere, above the PBL, the current CSU GCM includes a supplementary parameterization for moist convection that originates above the PBL, which is Manabe’s moist convective adjustment scheme. We have indicated that the incidence of the moist convective adjustment is uneven larger than that of cumulus clouds. The moist convective adjustment will be replaced by a generalized cumulus parameterization in Chapter 6.

The stratiform clouds and precipitation are parameterized by the bulk cloud microphysical scheme (Fowler et al., 1995; Fowler and Randall, 1995). The production of rain and snow occur through auto-conversion of cloud water and cloud ice. Rain drops falling through clouds can grow by collecting cloud water, and falling snow can collect both cloud water and cloud ice. These collection processes are formulated using the continuous collection equation. Evaporation of cloud water, cloud ice, rain, and snow are allowed in subsaturated layers. Melting and freezing are considered in the bulk cloud microphysical scheme. Optical and infrared radiative properties of the clouds are parameterized according to the cloud water, cloud ice, and snow paths for grid cells in which the condensate mixing ratio exceeds  $10^{-5} \text{ kg kg}^{-1}$  (less dense condensate is assumed to be radiatively inactive).

vii). Boundary conditions and albedo

The prescribed boundary conditions of the GCM include realistic topography, and the observed climatological seasonally varying global distributions of sea-surface temperature, sea-ice thickness, surface albedo, and surface roughness, as well as seasonally varying morphological and physiological parameters for the land-surface vegetation. The surface albedo of the ocean is zenith-angle dependent, following Briegleb et al. (1986), who used the data of Payne (1972).

The albedo of the vegetated land surface is determined according to the method of Sellers et al. (1986), which includes the effects of snow cover. The fraction of the ground covered by snow is not permitted to exceed 0.8. The albedo of sea ice is 0.8 in the visible, and 0.4 in the near infrared, except that when the temperature of the sea ice is within  $0.05^\circ$

K of the melting point, these values are replaced by 0.48 and 0.24, respectively. The albedo of land ice is 0.8 in the visible and 0.5 in the near infrared.

#### viii). Land-surface processes

For vegetated land points, the surface fluxes of sensible and latent heat are determined using the Simple Biosphere (SiB) parameterization developed by Sellers et al. (1995a). SiB uses eight prognostic variables: the temperatures of the surface soil/ground cover, and the deep soil; the moisture contents of the surface soil, root zone, and deep soil; and the surface moisture stores of the canopy and surface soil/ground cover, which can represent snow or ice variable.

### 3.5.2 Some numerical experiments

In this section, some numerical simulation results from CSU GCM are presented. In this simulation, the A-S parameterization and the moist convective adjustment are used for cumulus clouds originating in the PBL and the free atmosphere, respectively. The horizontal resolution used is  $4^\circ$  of latitude by  $5^\circ$  of longitude. The time-steps used are 10 minutes for the dynamics and 1 hour for the physical parameterizations. A three month run is carried out starting from a 1 May initial condition obtained from an earlier run of the model. Because this simulation uses the model without any modification, we refer to it as the Control Run.

Fig. 3.6 shows the 500 mb geopotential height for July from control-run (a) and the ECMWF data (b). In the Northern Hemisphere, the extended subtropical high belt is clearly seen in both (a) and (b). Synoptic scale troughs appear over the east coasts of North

## July 500 mb Geopotential Height

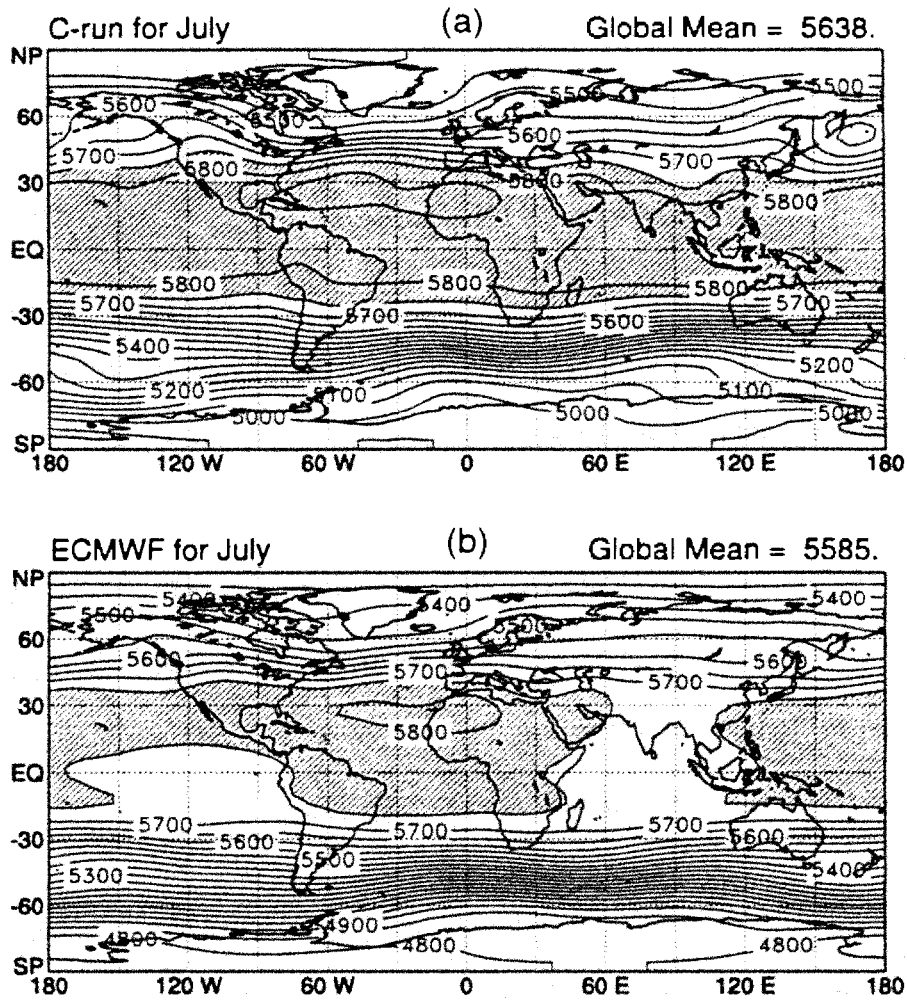


Fig. 3.6 July 500 mb geopotential height from the control run (a); and the ECMWF four year mean (b). Units are in meter. Heavy shading corresponds to values greater than 5750m. Contour intervals are every 50 meters.

America and Asia. In the Southern Hemisphere, the height contours tend to be more steady because there are less topography variations. Generally, the basic patterns have

been simulated by the model. It is also seen that area over 5750 m on map (a) is clearly larger than that on map (b). This means that the model produces higher 500 mb pressure surface than the real atmosphere. The reason is that the warmer atmosphere in tropics has been produced by the model. This can be seen clearly in Fig. 3.7.

Fig. 3.7 shows zonal mean temperature fields from the control-run simulation (a); the ECMWF four year mean data (b); and the difference between the control run simulation and the ECMWF data (c). From the panels (a) and (b), the basic patterns of the temperature fields from the model simulation and observations are very similar, e.g., the warmer atmosphere in tropics and the strong baroclinic instability in the middle latitudes in both Hemispheres (stronger in the Southern Hemisphere). The temperature difference in (c) indicates that the model produces warmer atmosphere in the tropical upper troposphere. In the North Pole and the tropopause, the atmospheric temperature simulated by the model is too low compared with observations.

The July total precipitation from the control run simulation and observations (Legates and Willmott, 1990) are shown in Fig. 3.8. It can be seen that the simulated global mean value is apparently larger than that reported by Legates and Willmott, but the shapes of the simulated and observed geographical distributions of precipitation are in good agreement. The precipitation maxima over the south Asian monsoon region and over the Pacific ocean ITCZ region are well simulated by the model. The maximum region over Atlantic ITCZ branch, however, is somewhat underpredicted. Through the analysis of the cumulus precipitation pattern simulated by the model, we can conclude that the unrealistic strong maximum center of the total precipitation in the western Pacific ocean is caused by

## Temperature

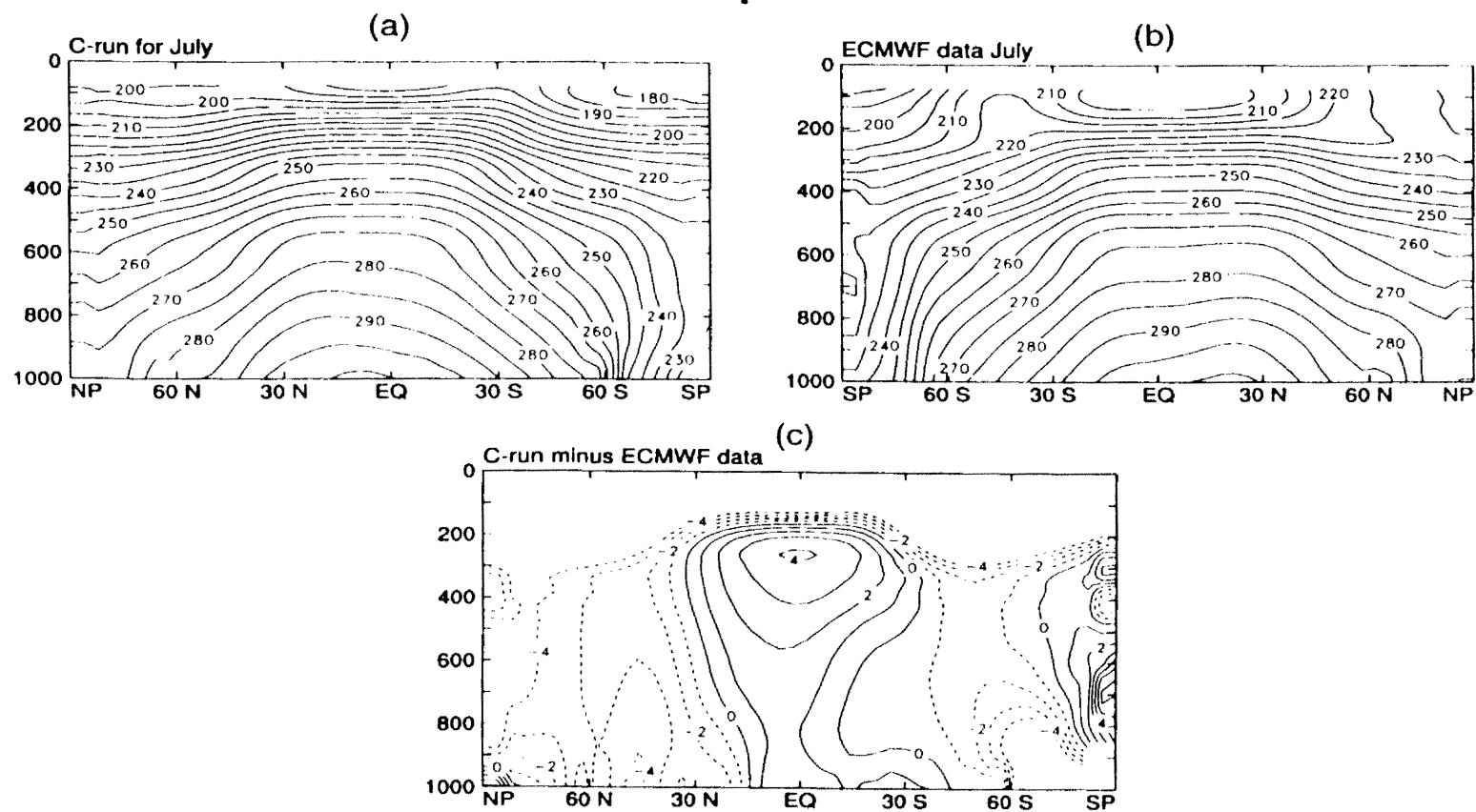


Fig. 3.7 Latitude-pressure temperature distributions from the C-run (a); the ECMWF data (b); and ECMWF data minus the C-run (c). Units are in degree K. Contour intervals are 5 K in (a) and (b); and 1 K in (c).

## July Total Precipitation

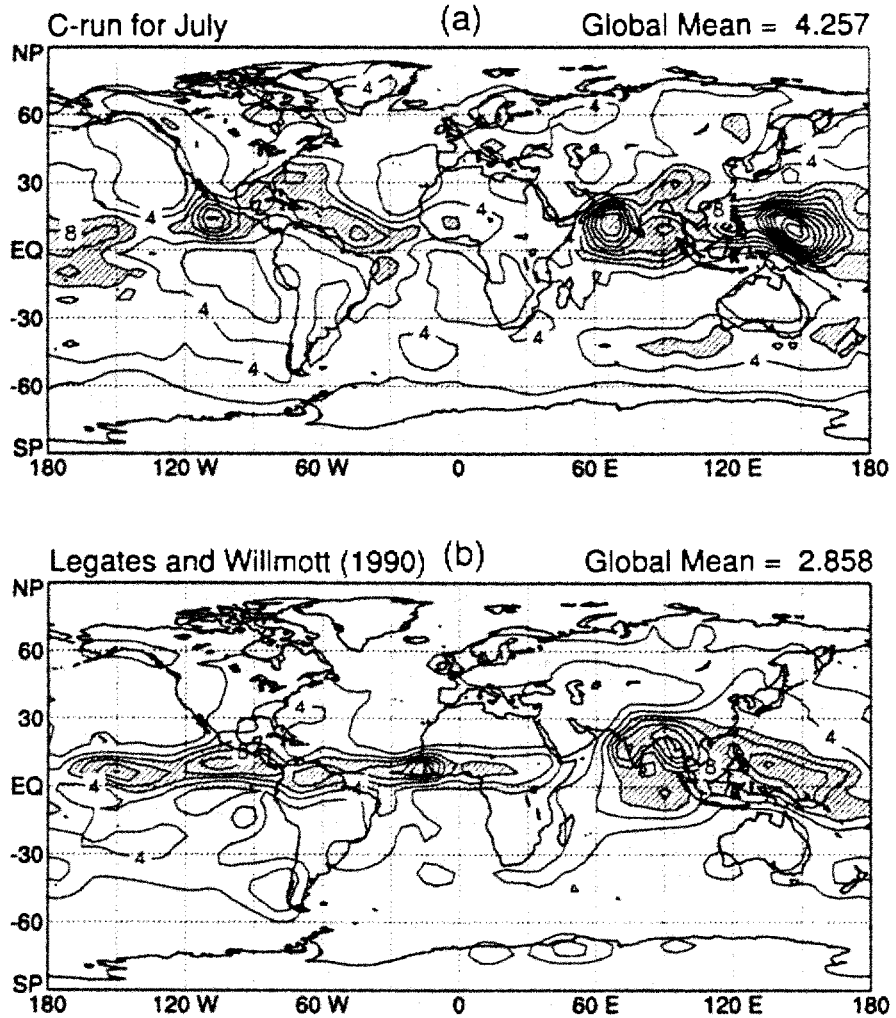


Fig. 3.8 Total July precipitation from (a) the control run simulation, and (b) observations according to Legates and Willmott (1990). Units are in  $\text{mm day}^{-1}$  and contour intervals are  $2 \text{ mm day}^{-1}$ . Values larger than  $6 \text{ mm day}^{-1}$  are shaded.

the strong cumulus precipitation.

The control-run simulated and observed July stream functions of the mean meridional circulation are shown in Fig. 3.9. The strong direct Hadley cell is well simulated by

## Zonal Mean Meridional Circulation

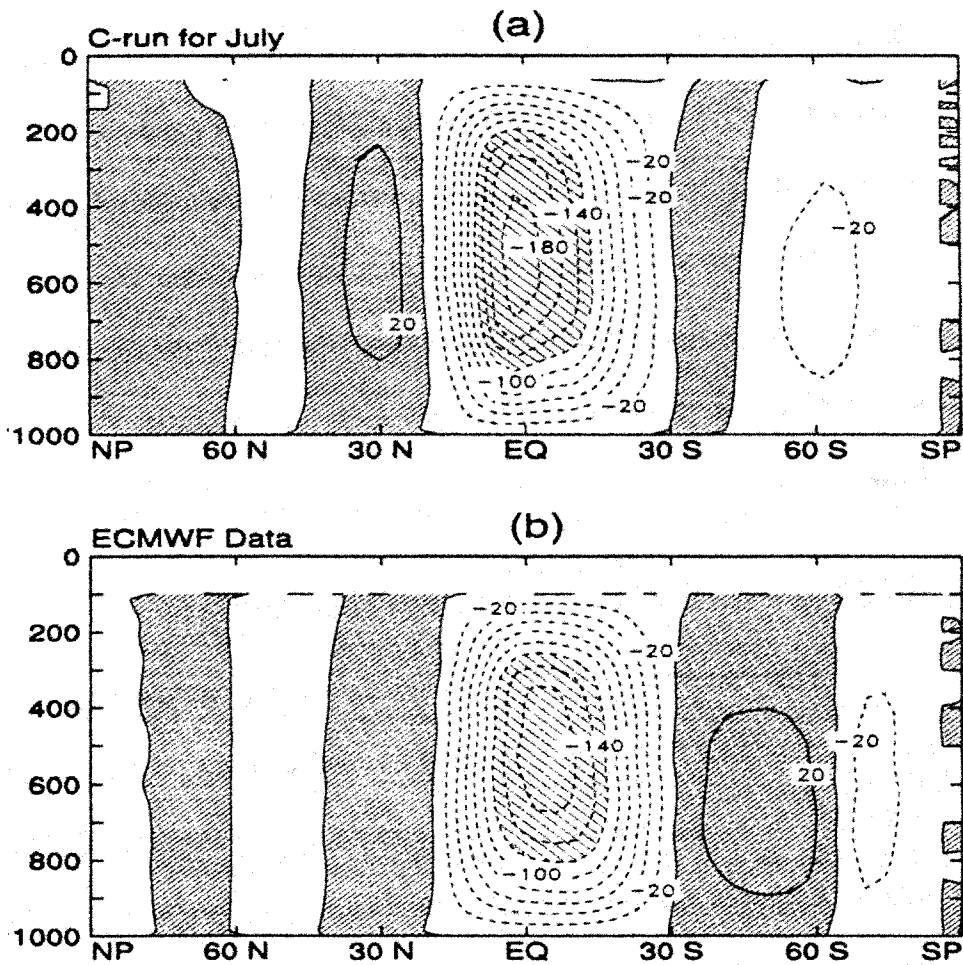


Fig. 3.9 Streamfunction of the control-run simulated (a) and observed (b) mean meridional circulation with units in  $10^9 \text{ kg s}^{-1}$ . Contour intervals are  $20 \times 10^9 \text{ kg s}^{-1}$ . Positive values are heavy shaded and values less than  $-120 \times 10^9 \text{ kg s}^{-1}$  are light shaded.

the model. The location of the Hadley cell generated by the model has good agreements with the observations. The magnitudes of the Hadley cell and the Ferrel cell simulated by the model are stronger than the observations. The observed Southern Hemisphere Ferrel cell is not well simulated.

We have presented some CSU GCM simulation results and compared them with observations. Most climate features can be well captured by the current CSU GCM, e.g., the zonal mean temperature patterns; the global precipitation distributions; and the mean meridional circulation patterns. We have also indicated some difference between the simulation results and observations, e.g., the warmer tropical troposphere created by the model; the unrealistic strong maximum precipitation center over the tropical Western Pacific ocean caused by the cumulus precipitation of the model; the too strong Hadley circulation simulated by the model, etc.. These problems will be further discussed in the following Chapters.

### **3.6 Effects of the MSTADJ in model simulations**

In the current CSU GCM, a modified A-S parameterization (CUP) is implemented for cumulus clouds originated in the PBL and a moist convective adjustment scheme (MSTADJ) is supplemented for moist convection starting from the free atmosphere. In order to further investigate effects of moist convection originating in the free atmosphere and how the effects can be parameterized by using MSTADJ, we do simulation test by turning off the MSTADJ in the CSU GCM.

#### **3.6.1 MSTADJ incidence in the control simulation**

Before the simulation test without MSTADJ is carried out, we look at the frequency of occurrence of MSTADJ in the control run. Fig. 3.10 shows the incidence of cumulus (starting from the PBL) and MSTADJ from the control-run for July. It can be seen that MSTADJ incidence is quite comparable to the cumulus incidence. In the tropics MSTADJ is even larger than CUP. The forcing of MSTADJ may be from stratiform cloud

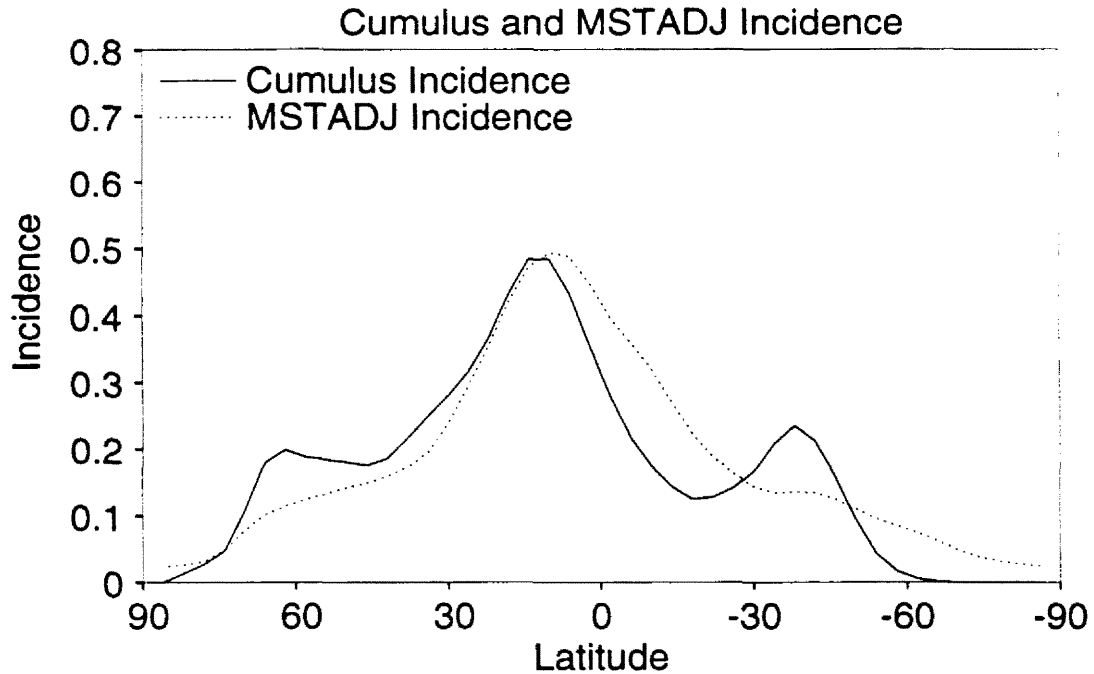


Fig. 3.10 Zonally averaged cumulus Incidence (solid line) and MSTADJ incidence (dotted line) from the C-run for July.

radiative effects, the large-scale motions and the cooling due to evaporation of precipitation generated by deep cumulus clouds and stratiform clouds. Fig. 3.10 indicates that moist convection starting from the free atmosphere may play an important role in the model climate.

Based on above discussion, we performed an experiment in which we kept the entire GCM the same as the control run except that MSTADJ was turned off. We ran the GCM for one month from July 1st to July 31st. This experiment is called the C2-run. The difference between the C2-run and the C-run will show the effects of moist convection originating in the free atmosphere and to what extent these effects are parameterized by MSTADJ.

### 3.6.2 Simulation test without MSTADJ

The zonally averaged temperature difference between the C2-run and the C-run is

shown in Fig. 3.11. Without MSTADJ, the atmosphere above 400 mb in Northern tropics and subtropics, and in the Southern Hemisphere is warmed. The atmosphere below 400 mb in Northern tropics and subtropics is cooled. Because MSTADJ only mixes two neighbor model layers when they are either saturated or moist unstable, its effects are just like dry adiabatic mass mixing which warms below and cools above, as indicated by Randall et al. (1989). When the heating effects of MSTADJ are removed, a phenomenon of cooling below and warming above relative to the control run appears in C2-run, as shown in Fig. 3.11. From the warming layer and cooling layer in Fig. 3.11, MSTADJ occurs mainly in the middle troposphere.

### Zonally Averaged Temperature Difference

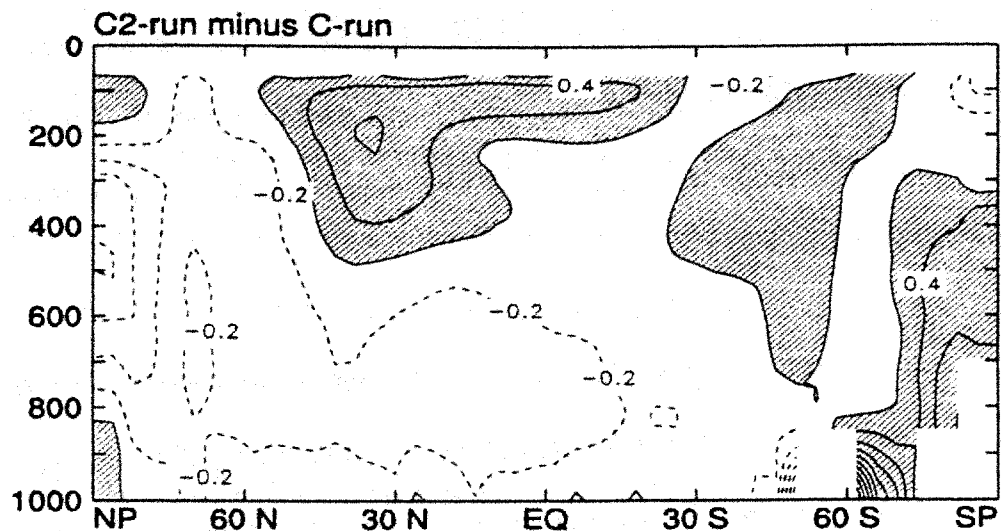


Fig. 3.11 Zonally averaged temperature difference between the C2-run and the C-run for July. Contour intervals are 0.4 K and values larger than zero are shaded.

The cooling in the Northern mid-latitudes relative to the control simulation might

indicate that moist convection starting in the free atmosphere in this region is ignored by the model while the MSTADJ is turned off.

The zonally averaged cumulus, large-scale and total precipitations from the C2-run and the C-run are shown in Fig. 3.12. The cumulus precipitation simulated by the C2-run is smaller than that of the C-run in the Northern tropics and mid-latitudes. Little effect of MSTADJ on the zonally averaged large-scale precipitations can be seen. The model simulations with and without MSTADJ produce very similar zonally averaged precipitation patterns.

We have indicated that MSTADJ is used as a supplementary parameterization for moist convection originating in the free atmosphere. It is natural to believe that the precipitation in the real atmosphere will change when the cumulus clouds starting from the free atmosphere are ignored. Fig. 3.12 implies that effects of moist convection originating in the free atmosphere is not well parameterized by MSTADJ in the model.

Observations (Warner et al., 1980) suggest that cumulus clouds with high cloud bases (>5 km) are often related to deep convective clouds. These deep penetrative cumulus clouds usually detrain ice or liquid water at upper troposphere to form anvil clouds and these optically thick convective anvil clouds have very important radiative effects on the atmosphere (e.g., Harshvardhan et al. 1989; and Randall et al. 1989). The parameterization of moist convection originating in the free atmosphere, therefore, is expected to have prominent influences on the radiative budget of the model results.

Fig. 3.13 displays maps of the out-going long-wave radiation (OLR) and down-

## Zonally Averaged Precipitation

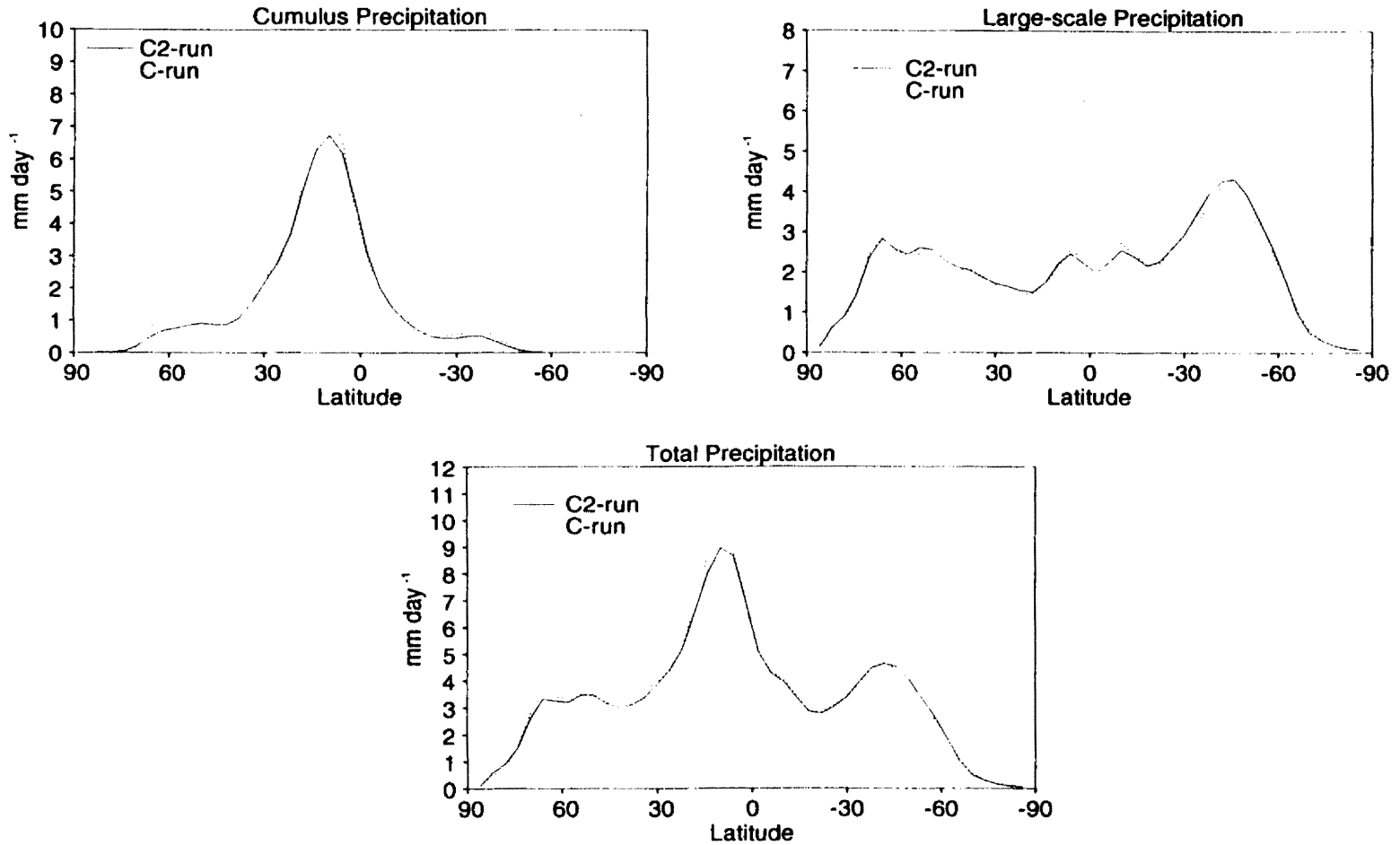
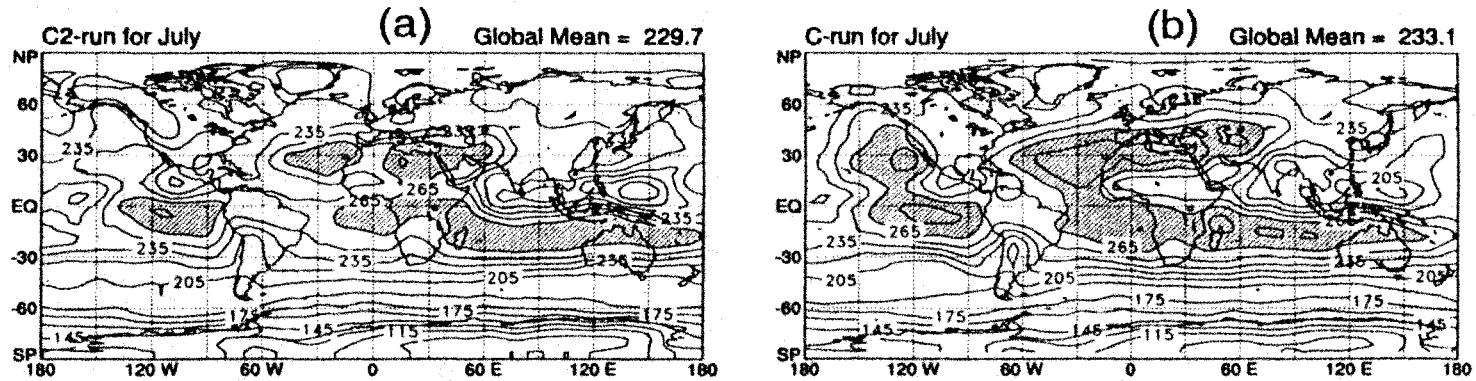


Fig. 3.12 Zonally average cumulus precipitation, large-scale precipitation and total precipitation from the C2-run (solid lines) and the C-run (dotted lines). Units are in  $\text{mm day}^{-1}$ .

## OLR



## Downward Solar Radiation

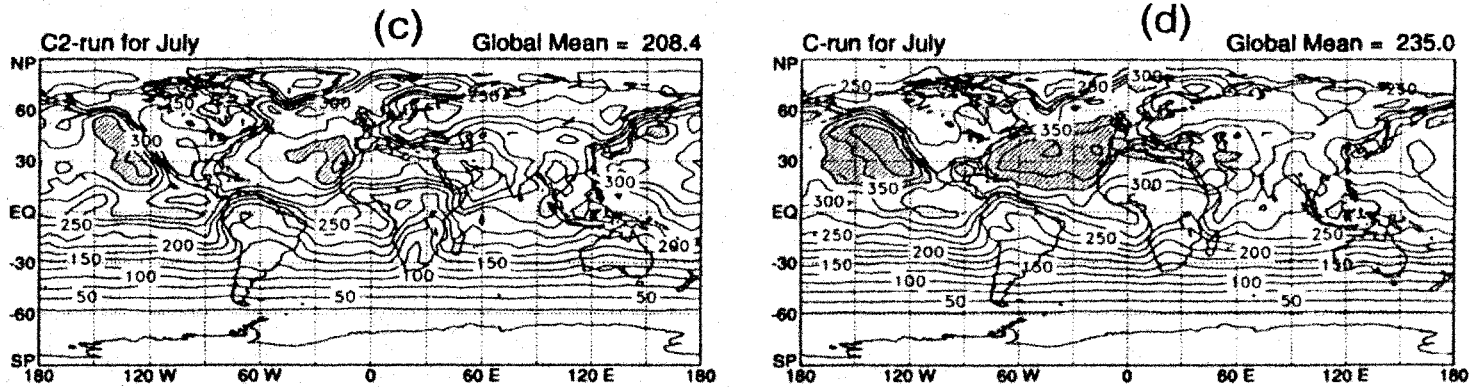


Fig. 3.13 OLR (upper panel) and downward solar radiation (lower panel) at the model top from the C-run and the C2-run for July. Units are in  $\text{W m}^{-2}$ . Values larger than  $265 \text{ W m}^{-2}$  are shaded, and contour intervals are  $15 \text{ W m}^{-2}$  in panels (a) and (b); values larger than  $350 \text{ W m}^{-2}$  are shaded and contour intervals are  $25 \text{ W m}^{-2}$  in panels (c) and (d).

ward short wave radiation at the model top from both the C2-run and the C-run. In the OLR maps, the maxima of OLR are located in the subtropical high regions in the two Hemispheres from both runs. The active convection over the Southern Asian monsoon regions corresponds to minima of OLR because the OLR is reflected back by the upper tropospheric clouds related to the deep convection in this region. Comparing maps (a) and (b), the out-going long-wave radiation decreases in the C2-run results. In other words, more clouds are generated in the model simulation with MSTADJ.

In the downward solar radiation maps, both runs also have very similar features, e.g., the maxima in the subtropical high regions in both Pacific ocean branch and Atlantic ocean branch. Comparing the C-run and the C2-run results, the downward solar radiation apparently decreases in the simulation without MSTADJ. The global mean value decreases from  $235.0 \text{ W m}^{-2}$  in the C-run to  $208.4 \text{ W m}^{-2}$  in the C2-run. This indicates again that too many clouds are generated in the C2-run.

Fig. 3.14 shows zonally averaged OLR and downward solar radiation from the C2-run and the C-run. The decrease of OLR and downward solar radiation in the C2-run can be seen clearly in zonal mean plots.

In general, we found that MSTADJ has a strong effect on the model radiation fields. In other words, the radiative effects of moist convection originating in the free atmosphere cannot be neglected by model simulations.

In this section, we have demonstrated that cumulus clouds starting from the free atmosphere occur very frequently in the model. This is deduced from the high MSTADJ

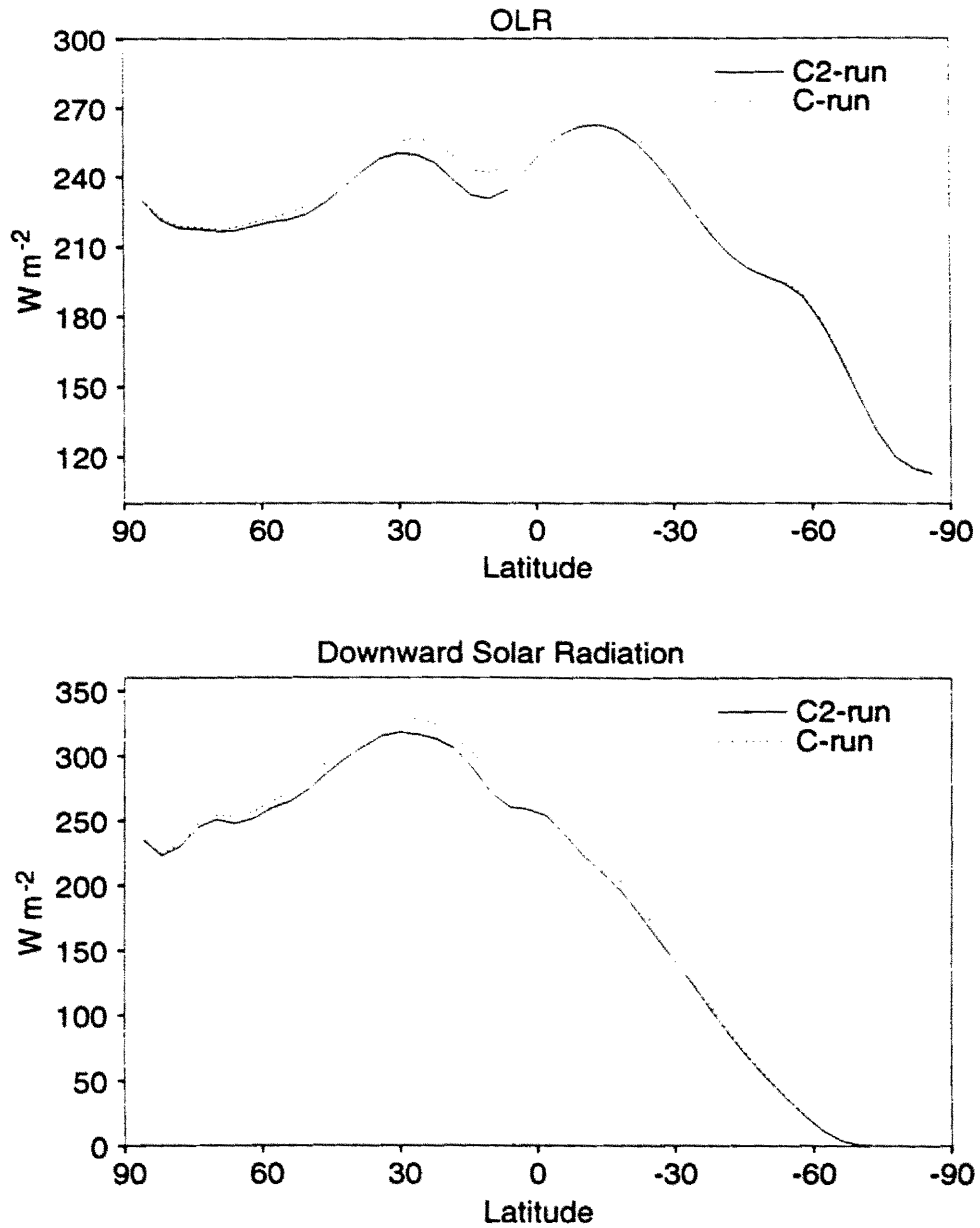


Fig. 3.14 Zonally averaged OLR and downward solar radiation from the C2-run (solid lines) and the C-run (dotted lines). Unit is  $W m^{-2}$ .

incidence. The important effects of these cumulus clouds on the atmospheric circulation can not be ignored in GCMs. It is seen that simulations without MSTADJ as a supplementary cumulus parameterization produce too many clouds and make apparent changes of radiation fields of the model results. Since the MSTADJ only acts to transport heat verti-

cally, many effects of altocumulus clouds can not be parameterized, e.g., the precipitation of altocumulus clouds. This manifests again that to develop a generalized cumulus parameterization which is suitable for all kinds of cumulus clouds is necessary in order to simulate the atmosphere circulations by using GCMs. According to our strategy described in the Chapter 1, we plan to simplify the A-S parameterization as the first step from the next Chapter.

## **Chapter 4**

### **The Linear Mass Flux Profile ( I )**

In many ways, the cumulus entrainment and mixing processes control the growth and decay of cumuli, so it is impossible to develop a proper cloud model for the parameterization of the effects of cumulus convection without knowledge of where and how environmental air is entrained into the cumulus clouds. Various cloud models currently used in cumulus parameterizations emphasize different entrainment processes, e.g., lateral entrainment or cloud top entrainment. It is necessary to have a better understanding of real entrainment processes in order to improve cumulus parameterizations.

As indicated in Chapter 2, one of the shortcomings of the A-S parameterization is the complexity of its implementation in GCMs. As a first step of this report, we need to simplify the A-S parameterization. To this end, the linear mass flux profile assumption is presented in this Chapter, after studies of cumulus entrainment processes have been reviewed.

## 4.1 Entrainment and Cloud Models

### 4.1.1 Jet and plume models

Stommel (1947) hypothesized that cumulus convection is similar to a steady-state entraining jet in which fluid from the environment is incorporated into the main flow through the side of the jet, in a “lateral” entrainment process. He suggested that the surrounding air is laterally entrained into the ascending cloudy column. By using airplane soundings inside and outside the trade-wind cumuli near San Juan, Puerto Rico, he calculated both the upward mass flux and liquid water content within the clouds from his steady-state jet model. The results demonstrated the reality of the entrainment of surrounding air.

Byers and Hull (1949) also did some observational work on the entrainment of environmental air into clouds, during the Thunderstorm Project. They measured the fractional rate of change in area of triangles formed by three balloons, to compute the amount of horizontal inflow into a convective cloud. They found that the horizontal component of the velocity of tracer balloons was directed toward the center of the storm at all levels above cloud base and below the anvil. Byers and Hull concluded that significant lateral entrainment occurred at all stages of cloud growth, regardless of whether the cloudy currents were updrafts or downdrafts. Malkus (1954) presented cross sections through two trade-cumulus clouds made from a slow-flying aircraft, showing the temperature, turbulence, and water-vapor content of the clouds and their nearby environment, the cloud slope, and the external wind profile. The steady-state draft theories were shown to be applicable to the central portions of at least some clouds and to give self-consistent results.

The theory of similarity plumes was developed during the 1960s for studies of cloud entrainment processes. In contrast to the treatment of jets given by Stommel and Malkus, in which the entrainment rate was assumed to be proportional to the vertical velocity and inversely proportional to the radius of the plume, Squires and Turner (1962) proposed a steady-state plume model which depicts cloud growth as depending primarily on the mass flux at the condensation level. The rate of entrainment of environmental air was calculated according to the idea that the inflow velocity at any height is proportional to the upward velocity of the plume. Their model results seemed reasonably consistent with observations, especially in regard to cloud shape. Marwitz *et al.* (1970) applied Squires' and Turner's steady-state plume model to the updraft vaults of hailstorms. In their experiments, the initial conditions for cloud base temperature, height, updraft speed and radius were taken directly from the observations. Comparing model results and observations, they found that the model can predict realistic liquid water contents and updraft speeds, but not the radius of the vault.

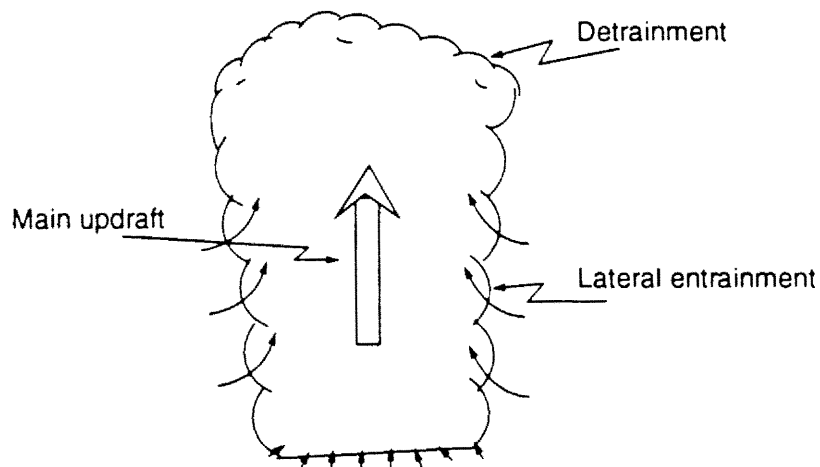


Fig. 4.1 A schematic diagram of plume model.

In general, the jet and the plume models are based on the concept of lateral entrainment, as illustrated in the schematic diagram of Fig. 4.1. In this model, the air movement is similar to that in plumes: the cloud air starts from the condensation level, and ascends to cloud top; meanwhile, environmental air is laterally entrained into the plume and moves upward with the updraft. The cloud air is assumed to be horizontally homogeneous at each level. In other words, the entrained environmental air is assumed to be laterally well mixed with cloud air immediately after entrainment. They suggested that, because of the mixing of the cloud air with the cold dry environmental air, eventually the cloud air loses buoyancy and the clouds cease to grow. Plume models have been successfully applied in cumulus parameterization schemes in some General Circulation Models (GCMs). For example, in the implementation of the AS parameterization, a plume cloud model was used by Lord and Arakawa (1980) and Lord (1982), as discussed in Chapter 3.

#### 4.1.2 Thermal or bubbles

Scorer and Ludlam (1953) proposed the “bubble” theory of convection. They considered the process of convection in terms of bubbles since the ideas of early pilots suggested that the thermals in which they soared were rising bubbles of warm air. In this thermal model, the growth of a cumulus cloud is due to the aggregation of smaller bubbles which are formed by the buoyant air near the ground. These bubbles are steadily eroded as they rise because the environmental air above them is lifted and cooled as the bubble approaches and then drains down, mixing with the bubbles as it passes along their sides. Therefore each bubble ascends into the atmosphere trailing a wake composed of a mixture of material from the bubble and its surroundings. The upper cap of a bubble would continue to shed into the wake until eventually the whole bubble was completely mixed. Some

photographs of evolutions of cumuli were interpreted in terms of bubble structures.

Fankhauser *et al.* (1982) developed a conceptual model of the entrainment processes in developing cumulus towers in the central High Plains. They suggested that as the cloud rises, environmental air from successively higher levels mixes into it through the top. The resulting mixtures move upward or downward until they reach their neutral buoyancy level. From experiments they found that the source of the entrained air often appeared to be close to the observation level.

Blyth *et al.* (1988) proposed a “shedding thermal” model for cumulus entrainment and mixing processes, which has a dynamical structure consistent with the observations. In their schematic model, the simplest picture of a cumulus cloud is a single thermal formed by an undiluted region. The ascent of the thermal ends when either the core region is eroded or it reaches a level where the thermal has negative buoyancy. The internal flow pattern in the thermal core is a toroidal circulation. A trailing wake of material is shed from this rising core, and the wake material remains near or slightly below the level at which mixing with the environment occurred. The entrainment of environmental air occurs on the front (or top) of the thermal as it rises. Then the entrained air moves down around outside of the thermal core, along the toroidal circulation, and into the wake. The mixing process accelerates when the entrained air moves around the outside of the thermal core, so mixtures have already got positive buoyancy before they are carried into the wake. The vertical motion in the wake becomes small because of this continuing active mixing process, and so the wake tends toward neutral buoyancy. The source of the entrained air is close to or slightly higher than the observation level. Blyth *et al.* stated that their schematic

model does not imply that a cumulus cloud is a single thermal. It is likely that the clouds contain multiple thermals.

The schematic diagram of the thermal model is given by Figure 3.2, which illustrates the general ideas of the rising thermal, the entrainment region, and the turbulent wake.

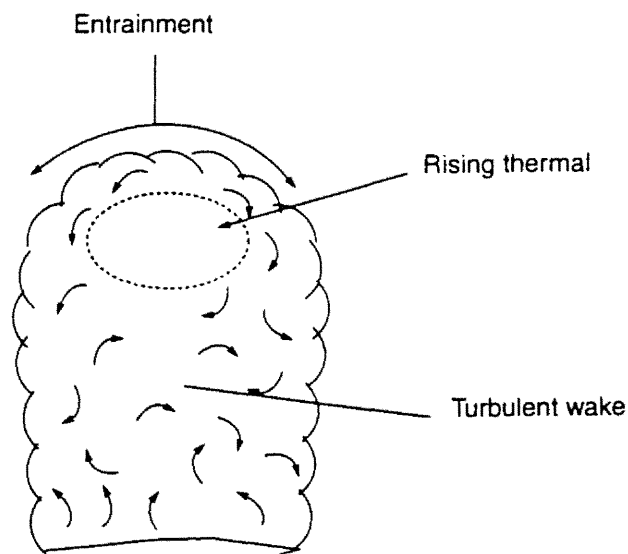


Fig. 4.2 A schematic diagram of thermal model. A cumulus clouds can consist of several thermals.

Two main types of cloud model, jet or plume and thermal or bubble have been described. Squires and Turner (1962) compared these two types of cloud models and concluded that both of them contain features which should be incorporated in a full theory of cloud growth, but that each of them also has shortcomings. For example, the plume theories disregard any development in time of depth or width, and neglect the cloud top entrainment process. The bubble theories, however, ignore the possibility of relatively

steady updrafts driven by continuing sources of buoyancy below cloud base. Squires and Turner finally concluded that different cloud types will correspond to different dominant entrainment and mixing processes. For the shallower cumulus clouds, the cloud's depth is comparable to its diameter, so that cloud top entrainment may be dominant and the thermal model may be most appropriate. For a deep cumulus cloud with a strong updraft, the cloud's depth is much larger than its width. Then lateral entrainment and mixing may be more important and the plume model may represent the entrainment process better than the thermal model. Because the deep clouds have a stronger influence on the large-scale circulation and climate, the plume model may be more useful in simulations of the large-scale atmosphere circulation.

## 4.2 The Linear Mass Flux Profile

### 4.2.1 The linear mass flux profile assumption

Observational and modeling studies have illustrated physical processes of entrainment and mixing related to cumulus convection and its environment. For cumulus parameterization, it is necessary to quantitatively formulate these processes. Simpson *et al.* (1965) and Simpson and Wiggert (1969, 1971) developed a one-dimensional model of the cumulus tower. The fractional rate of entrainment,  $\mu$ , in this model was specified by

$$\mu = \frac{1}{M} \frac{dM}{dz} = \frac{2\alpha}{R} , \quad (4.1)$$

where  $\alpha$  is a constant of proportionality and  $R$  is the radius of the rising cumulus tower. Simpson *et al.* (1965) indicated that  $R$  that is constant with height, in Lagrangian sense, leads to a better agreement with observations than the alternative assumptions of horizon-

tally expanding thermals or plumes.

In the A-S parameterization, the fractional rate of entrainment for the time-averaged mass flux of the cloud is assumed to be approximately constant with height. From Chapter 3, a single positive parameter,  $\lambda$ , is chosen to characterize cloud types in the A-S parameterization. When the constant fractional rate of entrainment is chosen as the parameter  $\lambda$ , the relationship between the normalized subensemble mass flux,  $\eta(z, \lambda)$ , and  $\lambda$  is given by (3.14). Integrating (3.14) with height gives

$$\eta(z, \lambda) = e^{\lambda(z-z_B)}, \text{ when } z_B \leq z \leq z_D(\lambda) \quad (4.2)$$

and

$$\eta(z, \lambda) = 0, \text{ when } z_D(\lambda) < z, \quad (4.3)$$

where  $z_D(\lambda)$  is the detrainment level of the cloud which has  $\lambda$  as its fractional rate of entrainment. Equation (4.2) states that the normalized mass flux of cloud subensembles changes exponentially with height. In other words, the A-S parameterization uses an exponential mass flux profile. The successful implementations of the A-S parameterization proved that the assumption of the exponential mass flux profile is physically acceptable. Computational difficulties arise from this assumption, however. For example, as explained below the fractional entrainment rate  $\lambda$  needs to be computed iteratively, and this iteration consumes a lot of computer time.

If we assume that for cumulus clouds the normalized entrainment mass flux increases with height linearly, the equation (4.2) can be approximately written as

$$\eta(z, \lambda) = 1 + \lambda(z - z_B) \quad (4.4)$$

Because the cloud base mass flux  $\eta(z_B, \lambda)$  is assumed to be one, equation (4.4) is equivalent to  $\eta(z, \lambda) - \eta(z_B, \lambda) = \lambda(z - z_B)$ , or

$$\frac{\partial \eta(z, \lambda)}{\partial z} = \lambda \quad (4.5)$$

Equation (4.5) is the assumption of the linear mass flux profile. Moorthi and Suarez (1992) and Cheng and Arakawa (1993) have used the linear mass flux profile in their modified A-S cumulus parameterization. They found that the results with the linear mass flux profile were very close to those of the original AS parameterization, but that the costly calculations which are needed to find the fractional entrainment rate could be avoided. In Moorthi and Suarez's work, all liquid water in clouds is assumed to be carried to cloud tops, and cumulus precipitation is formed only at cloud tops. In our cloud model, cumulus precipitation and icing can occur at any cloud level.

#### 4.2.2 The linear relation between the entrainment rate and the in-cloud moist static energy

In this section, we will prove that the in-cloud moist static energy of each subensemble has a linear relationship with the fractional entrainment rate  $\lambda$  under the assumption of the linear mass flux profile. This will simplify the calculation of the vertical distribution of the in-cloud moist static energy in our cloud model. We specify model layers as shown in Fig. 4.3. The region bounded by levels  $k-1/2$  and  $k+1/2$  is referred to as "layer  $k$ ." The lowest model layer (shaded),  $k = k_M$ , is the planetary boundary layer (PBL).

Layer kF is the layer just above cloud base.

Based on Fig. 4.3, equation (4.5) can be written as

$$\eta_{k-\frac{1}{2}} = \eta_{k+\frac{1}{2}} + \lambda \Delta z_k, \quad (4.6)$$

where  $k - 1/2$  and  $k + 1/2$  denote the upper and the lower edges of the layer k, respectively, and  $\Delta z_k$  is the thickness of layer k. If a subscript B is used to denote the cloud base level, and if  $\eta_B$ , the normalized cloud base mass flux, is one, we have

$$\eta_{k-\frac{1}{2}} = 1 + \lambda \left( z_{k-\frac{1}{2}} - z_B \right), \quad (4.7)$$

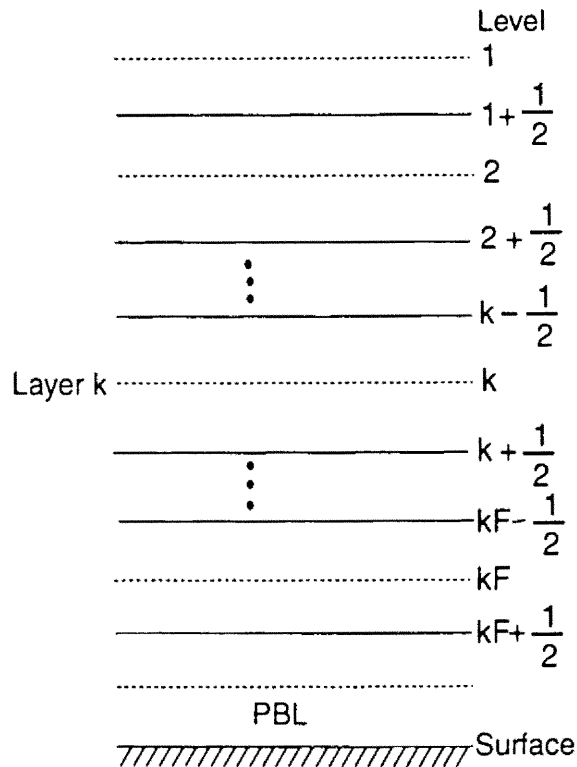


Fig. 4.3 Model layer description (based on Lord *et al.*, 1982).

and

$$\eta_{k+\frac{1}{2}} = 1 + \left( z_{k+\frac{1}{2}} - z_B \right). \quad (4.8)$$

Corresponding to Fig. 4.3, (3.15) has the form

$$(\eta h_c)_{k-\frac{1}{2}} - (\eta h_c)_{k+\frac{1}{2}} = \lambda \bar{h}_k \Delta z_k. \quad (4.9)$$

Again a subscript  $c$  denotes in-cloud values, and a overbar denotes environmental properties. Eq. (4.9) can be further written as

$$\eta_{k-\frac{1}{2}}(h_c)_{k-\frac{1}{2}} - \eta_{k+\frac{1}{2}}(h_c)_{k+\frac{1}{2}} = \lambda \bar{h}_k \Delta z_k. \quad (4.10)$$

Now, substituting (4.7) and (4.8) into (4.10) and rearranging the result, we can show that,

$$(h_c)_{k-\frac{1}{2}} = \frac{\left[ 1 + \lambda \left( z_{k+\frac{1}{2}} - z_B \right) \right] (h_c)_{k+\frac{1}{2}} + \lambda \bar{h}_k \Delta z_k}{1 + \lambda \left( z_{k-\frac{1}{2}} - z_B \right)}. \quad (4.11)$$

Equation (4.11) states that  $(h_c)_{k-\frac{1}{2}}$  depends on  $(h_c)_{k+\frac{1}{2}}$ ,  $\lambda$  and environmental atmospheric characteristics. If  $k + \frac{1}{2}$  is specified to be the cloud base level,  $(h_c)_{k-\frac{1}{2}}$  depends only on  $\lambda$  for given environmental soundings. In other words, the in-cloud moist static energy at each level has a linear relationship with  $\lambda$  when the environmental air properties are specified. It is necessary to demonstrate that this relationship exists in any model levels rather than only  $k - \frac{1}{2}$  level when  $k + \frac{1}{2}$  is specified as the cloud base level. For doing this, we replace index  $k$  by  $k-1$  in (4.11), then

$$(h_c)_{k-\frac{3}{2}} = \frac{\left[1 + \lambda \left(z_{k-\frac{1}{2}} - z_B\right)\right] (h_c)_{k-\frac{1}{2}} + \lambda \bar{h}_{k-1} \Delta z_{k-1}}{1 + \lambda \left(z_{k-\frac{3}{2}} - z_B\right)} \quad (4.12)$$

Rearranging (4.12) gives

$$\begin{aligned} \left[1 + \lambda \left(z_{k-\frac{3}{2}} - z_B\right)\right] (h_c)_{k-\frac{3}{2}} - \left[1 + \lambda \left(z_{k-\frac{1}{2}} - z_B\right)\right] (h_c)_{k-\frac{1}{2}} \\ = \lambda \bar{h}_{k-1} \Delta z_{k-1} \end{aligned} \quad (4.13)$$

After substituting (4.11) into (4.13) to eliminate  $(h_c)_{k-\frac{1}{2}}$ , (4.13) becomes

$$\begin{aligned} \left[1 + \lambda \left(z_{k-\frac{3}{2}} - z_B\right)\right] (h_c)_{k-\frac{3}{2}} - \left[\left[1 + \lambda \left(z_{k+\frac{1}{2}} - z_B\right)\right] (h_c)_{k+\frac{1}{2}} + (\lambda \bar{h}_k \Delta z_k)\right] \\ = \lambda \bar{h}_{k-1} \Delta z_{k-1} \end{aligned} \quad (4.14)$$

From (4.14),  $(h_c)_{k-\frac{3}{2}}$  is still only depends on the cloud base properties, the entrainment rate  $\lambda$ , and the environmental properties. When the environmental soundings are given,  $(h_c)_{k-\frac{3}{2}}$  has a linear relationship with the fractional entrainment rate  $\lambda$ . If replacing index  $k$  by  $k-1$  in (4.14) and repeating above steps, it can be proven that  $(h_c)_{k-\frac{5}{2}}$  still has a linear relationship with the entrainment rate  $\lambda$  when the cloud environmental soundings are specified. Hence, we can conclude that there exists a simple linear relationship between the in-cloud moist static energy and the environmental entrainment rate  $\lambda$ .

Under the assumption of the linear mass flux profile, we can use a simple form to summarize the relationship between  $h_c$  and  $\lambda$ , which is

$$(h_c)_{k-\frac{1}{2}} = \frac{C_1 + \lambda C_2}{1 + \lambda \Delta z} \quad , \quad (4.15)$$

where  $C_1$  and  $C_2$  are two coefficients which can be determined for given environmental soundings; here,  $\Delta z$  denotes the thickness between level  $k - \frac{1}{2}$  and cloud base level.

In (4.15), for  $\lambda = 0$  (non-entraining clouds) we see that

$$(h_c)_{k-\frac{1}{2}} = C_1 \quad . \quad (4.16)$$

For non-entraining clouds, cloud air originates at the cloud base level and is not diluted. In this case, the moist static energy of cloud air is conserved during its ascent which can be considered as a moist adiabatic process. The in-cloud moist static energy is just  $(h_c)_B$ , the moist static energy at cloud base. Therefore, we can show that

$$C_1 = (h_c)_B \quad . \quad (4.17)$$

In our cloud model,  $(h_c)_B$  is equal to the moist static energy in the PBL which is

$$(h_c)_B \equiv \bar{h}(kM) \quad . \quad (4.18)$$

Then, we have

$$C_1 = \bar{h}(kM) \quad (4.19)$$

The determination of  $C_2$  and  $\lambda$  will be discussed in section 4.3. Equation (4.15) can be

used to estimate in-cloud moist static energy provided that  $C_1$ ,  $C_2$  and  $\lambda$  are known.

#### 4.2.3 The linear relation between the entrainment rate and the in-cloud moisture

With the assumption of the linear mass flux profile, the in-cloud moisture has the similar relationship with the entrainment rate  $\lambda$  as the in-cloud moist static energy does.

Replacing  $h_c$  by  $q_c$  in (4.9) and (4.10), the in-cloud moisture budget is given by

$$(q_c)_k = \frac{\left[ 1 + \lambda \left( z_{k+\frac{1}{2}} - z_B \right) \right] (q_c)_{k+\frac{1}{2}} + \lambda \bar{q}_k \Delta z_k}{1 + \lambda \left( z_{k-\frac{1}{2}} - z_B \right)}, \quad (4.20)$$

where  $(q_c)_k$  is used to represent the total cloud water mixing ratio in the layer  $k$  before cloud precipitation processes. If we use  $(q_c)_{k-\frac{1}{2}}$  and  $(P_r)_k$  to denote the total cloud water mixing ratio in the layer  $k$  after cumulus precipitation processes and the cumulus precipitation production rate in layer  $k$ , respectively, the total mixing ratio after precipitation in layer  $k$  should be the difference between the total mixing ratio before the precipitation and the cumulus precipitation production rate in the layer  $k$ , that is

$$(q_c)_{k-\frac{1}{2}} = (q_c)_k - (P_r)_k. \quad (4.21)$$

Following the A-S parameterization, the cumulus precipitation production rate in layer  $k$  can be related to in-cloud liquid water mixing ratio by

$$(P_r)_k = \frac{C_0 \Delta z_k (q_{l,c})_k}{1 + C_0 \Delta z_k}, \quad (4.22)$$

and

$$(q_{l,c})_k = (q_c)_k - (q_{v,c})_{k-\frac{1}{2}} \quad , \quad (4.23)$$

where  $(q_{l,c})_k$  and  $(q_{v,c})_{k-\frac{1}{2}}$  are in-cloud liquid water mixing ratio before cloud precipitation processes and in-cloud water vapor mixing ratio in the layer  $k$ , respectively.  $C_0$  in (4.22) is a constant precipitation conversion rate. The in-cloud water vapor mixing ratio,  $(q_{v,c})_{k-\frac{1}{2}}$ , can be calculated from (following Lord *et al.*, 1982)

$$(q_{v,c})_{k-\frac{1}{2}} = (\bar{q}_v^*)_k + \frac{\gamma_k}{(1+\gamma_k)L} \left[ (h_c)_{k-\frac{1}{2}} - \bar{h}_k^* \right] \quad , \quad (4.24)$$

where  $(\bar{q}_v^*)_k$  and  $\bar{h}_k^*$  are environmental saturated water vapor mixing ratio and moist static energy, respectively;  $L$  is the latent heat per unit mass of water vapor; and  $\gamma$  is defined as

$$\gamma = \frac{L}{c_p} \frac{dq^*}{dT} \quad , \quad (4.25)$$

where  $c_p$  is the specific heat of air under constant pressure. Substituting (4.24) into (4.23) gives

$$(q_{l,c})_k = (q_c)_k - \left[ (\bar{q}_v^*)_k + \frac{\gamma_k}{(1+\gamma_k)L} \left[ (h_c)_{k-\frac{1}{2}} - \bar{h}_k^* \right] \right] \quad . \quad (4.26)$$

Using (4.22) and (4.26), the cumulus precipitation production rate has the form

$$(P_r)_k = \frac{C_0 \Delta z_k}{1 + C_0 \Delta z_k} \left[ (q_c)_k - (\bar{q}_v^*)_k - \frac{\gamma_k}{(1+\gamma_k)L} \left[ (h_c)_{k-\frac{1}{2}} - \bar{h}_k^* \right] \right] \quad . \quad (4.27)$$

In order to find the budget equation for  $(q_c)_{k-\frac{1}{2}}$ , we substitute into (4.21) and using the right hand side of (4.20) for  $(q_c)_k$ , giving

$$(q_c)_{k-\frac{1}{2}} = \frac{\left[1 + \lambda \left(z_{k+\frac{1}{2}} - z_B\right)\right] (q_c)_{k+\frac{1}{2}} + \lambda \bar{q}_k \Delta z_k}{1 + \lambda \left(z_{k-\frac{1}{2}} - z_B\right)} \frac{1}{1 + C_0 \Delta z_k} + \frac{C_0 \Delta z_k}{1 + C_0 \Delta z_k} \left[ (\bar{q}_v^*)_k + \frac{\gamma_k}{(1 + \gamma_k) L} \left[ (h_c)_{k-\frac{1}{2}} - \bar{h}_k^* \right] \right] \quad (4.28)$$

On the right hand side of (4.28),  $(h_c)_{k-\frac{1}{2}}$  appears as a non-environmental variable. Substituting (4.11) into (4.28) to eliminate  $(h_c)_{k-\frac{1}{2}}$ , and rearranging, we obtain

$$\begin{aligned} & \left[ (q_c)_{k-\frac{1}{2}} - \frac{C_0 \Delta z_k}{1 + C_0 \Delta z_k} \left[ (\bar{q}_v^*)_k - \frac{\gamma_k}{(1 + \gamma_k) L} \bar{h}_k^* \right] \right] \left[ 1 + \lambda \left(z_{k-\frac{1}{2}} - z_B\right) \right] \\ &= \left[ \frac{(q_c)_{k+\frac{1}{2}}}{1 + C_0 \Delta z_k} + \frac{C_0 \Delta z_k}{1 + C_0 \Delta z_k} \frac{\gamma_k}{(1 + \gamma_k) L} (h_c)_{k+\frac{1}{2}} \right] \left[ 1 + \lambda \left(z_{k+\frac{1}{2}} - z_B\right) \right] \\ & \quad + \frac{\lambda \Delta z_k}{1 + C_0 \Delta z_k} \left\{ \bar{q}_k + C_0 \Delta z_k \frac{\gamma_k}{(1 + \gamma_k) L} \bar{h}_k \right\} \quad (4.29) \end{aligned}$$

Equation (4.29) shows that the total cloud mixing ratio after the precipitation process,  $(q_c)_{k-\frac{1}{2}}$ , only depends on the entrainment rate  $\lambda$ ; the moisture at cloud base,  $(q_c)_{k+\frac{1}{2}}$  (again, we specify  $k+\frac{1}{2}$  as the cloud base level); and the environmental sounding. Because the cloud-base mixing ratio is assumed to be equal to the mixing ratio of PBL, the in-cloud moisture budget can be estimated for given  $\lambda$  and environmental

soundings. Again, using  $k-1$  to replace  $k$  in (4.29), we get

$$\begin{aligned}
& \left[ (q_c)_{k-\frac{3}{2}} - \frac{C_0 \Delta z_{k-1}}{1 + C_0 \Delta z_{k-1}} \left[ (\bar{q}_v^*)_{k-1} - \frac{\gamma_{k-1}}{(1 + \gamma_{k-1}) L} \bar{h}^*_{k-1} \right] \right] \\
& \cdot \left[ 1 + \lambda \left( z_{k-\frac{3}{2}} - z_B \right) \right] = \\
& \left[ \frac{(q_c)_{k-\frac{1}{2}}}{1 + C_0 \Delta z_{k-1}} + \frac{C_0 \Delta z_{k-1}}{1 + C_0 \Delta z_{k-1}} \frac{\gamma_{k-1}}{(1 + \gamma_{k-1}) L} (h_c)_{k-\frac{1}{2}} \right] \cdot \left[ 1 + \lambda \left( z_{k-\frac{1}{2}} - z_B \right) \right] \\
& + \frac{\lambda \Delta z_{k-1}}{1 + C_0 \Delta z_{k-1}} \left\{ \bar{q}_{k-1} + C_0 \Delta z_{k-1} \frac{\gamma_{k-1}}{(1 + \gamma_{k-1}) L} \bar{h}_{k-1} \right\} \quad . \quad (4.30)
\end{aligned}$$

Substituting (4.11) and (4.29) into (4.30) to eliminate  $(h_c)_{k-\frac{1}{2}}$  and  $(q_c)_{k-\frac{1}{2}}$ , and rearranging, the in-cloud moisture budget equation becomes

$$\begin{aligned}
& \left[ (q_c)_{k-\frac{3}{2}} - \left( \frac{C_0 \Delta z_{k-1}}{1 + C_0 \Delta z_{k-1}} \right) \left[ (\bar{q}_v^*)_{k-1} - \frac{\gamma_{k-1}}{(1 + \gamma_{k-1}) L} \bar{h}^*_{k-1} \right] \right] \\
& \cdot \left[ 1 + \lambda \left( z_{k-\frac{3}{2}} - z_B \right) \right] (1 + C_0 \Delta z_{k-1}) = \frac{C_0 \Delta z_k}{1 + C_0 \Delta z_k} \\
& \cdot \left[ (\bar{q}_v^*)_k - \frac{\gamma_k}{(1 + \gamma_k) L} \bar{h}_k^* \right] \left[ 1 + \lambda \left( z_{k-\frac{1}{2}} - z_B \right) \right] +
\end{aligned}$$

$$\begin{aligned}
& \left[ (q_c)_{k+\frac{1}{2}} + C_0 \Delta z_k \frac{\gamma_k}{(1+\gamma_k)L} (h_c)_{k+\frac{1}{2}} \right] \frac{1 + \lambda \left( z_{k+\frac{1}{2}} - z_B \right)}{1 + C_0 \Delta z_k} \\
& + \frac{\lambda \Delta z_k}{1 + C_0 \Delta z_k} \left\{ \bar{q}_k + C_0 \Delta z_k \frac{\gamma_k}{(1+\gamma_k)L} \bar{h}_k \right\} + C_0 \Delta z_{k-1} \frac{\gamma_{k-1}}{(1+\gamma_{k-1})L} \\
& \cdot \left[ \left[ 1 + \lambda \left( z_{k+\frac{1}{2}} - z_B \right) \right] (h_c)_{k+\frac{1}{2}} + \lambda \bar{h}_k \Delta z_k \right] + \lambda \Delta z_{k-1} \\
& \cdot \left[ \bar{q}_{k-1} + C_0 \Delta z_{k-1} \frac{\gamma_{k-1}}{(1+\gamma_{k-1})L} \bar{h}_{k-1} \right] .
\end{aligned} \tag{4.31}$$

From equation (4.31),  $(q_c)_{k-\frac{3}{2}}$  only depends on  $\lambda$  when cloud environment soundings are specified. The relation between  $(q_c)_{k-\frac{3}{2}}$  and  $\lambda$  is linear because there are no terms involving  $\lambda^2$  in (4.31).

### 4.3 The Determination of the Entrainment Rate with the Consideration of Virtual Temperature

We have demonstrated the linear relationship between in-cloud moist static energy and the cloud entrainment rate  $\lambda$  as well as between in-cloud moisture and  $\lambda$ . In the original A-S parameterization, the cloud-top non-buoyancy condition for cloud type  $k$  is given by  $h_c(k) = \bar{h}^*(k)$ . This gives an implicit equation about  $\lambda$ . An iterative approach has

to be used to determine  $\lambda$ . Using the linear relations, the fractional entrainment rate  $\lambda$  can be determined with the consideration of the virtual temperature. The costly iterative computations for finding  $\lambda$  in the A-S parameterization can be avoided. The procedure for determining  $\lambda$  with the consideration of the virtual temperature and by the use of the linear relationship proven in preceding sections is described in this section.

From (4.25), we can write

$$\gamma c_p dT = Ldq^* \quad \text{, or}$$

$$\gamma(c_p dT + Ldq^*) = (1 + \gamma) Ldq^*$$

Rearranging above two equations gives

$$\gamma dh^* = (1 + \gamma) \gamma c_p dT \quad .$$

where  $h^* = c_p dT + Ldq^*$  is the saturation moist static energy. The above equation can be written as

$$dT = dh^* \frac{1}{c_p (1 + \gamma)} \quad . \quad (4.32)$$

Assuming that the cloud air is saturated and that  $\gamma$  is approximately a constant at a given pressure level, and using (4.32), the in-cloud temperature can be approximated as

$$T_c = \bar{T} + (h_c - \bar{h}^*) \frac{1}{c_p (1 + \gamma)} \quad , \text{ or}$$

$$T_c - \bar{T} \approx (h_c - \bar{h}^*) \frac{1}{c_p(1+\gamma)} \quad . \quad (4.33)$$

From the definition of the virtual temperature,

$$T_v = T(1 + \delta q) \quad , \quad (4.34)$$

where  $\delta = 0.608$  and  $q$  is the mixing ratio of water vapor. The virtual temperature difference between the cloud air and the environmental air at the same pressure level can be written as

$$T_{vc} - \bar{T}_v \equiv (T_c - \bar{T}) + \bar{T}\delta(q_c - \bar{q}) \quad . \quad (4.35)$$

With the assumption that the cloud is saturated, we can write

$$\begin{aligned} q_c - \bar{q} &\equiv q_c^* - \bar{q} \\ &= (q_c^* - \bar{q}^*) + (\bar{q}^* - \bar{q}) \quad . \end{aligned} \quad (4.36)$$

Again, from equation (4.25), we have

$$\begin{aligned} dq^* &= \frac{dh^*}{L} \left( \frac{\gamma}{1+\gamma} \right) \quad , \text{ or} \\ q_c^* - \bar{q}^* &= \frac{(h_c - \bar{h}^*)}{L} \left( \frac{\gamma}{1+\gamma} \right) \quad . \end{aligned} \quad (4.37)$$

Combining (4.36) and (4.37) gives

$$q_c - \bar{q} = \frac{(h_c - \bar{h}^*)}{L} \left( \frac{\gamma}{1 + \gamma} \right) + (\bar{q}^* - \bar{q}) \quad (4.38)$$

Substituting (4.33) and (4.38) into (4.35), and rearranging, the virtual temperature difference between the cloud and its environment is

$$T_{vc} - \bar{T}_v = \frac{(h_c - \bar{h}^*)}{1 + \gamma} \left[ \frac{1}{c_p} + \frac{\delta \bar{T} \gamma}{L} \right] + \delta \bar{T} (\bar{q}^* - \bar{q}) \quad (4.39)$$

In the previous section, it has been proven that the moist static energy  $h_c$  is a linear function of  $\lambda$  provided that the environmental soundings are specified. Referring to equation (4.15), (4.39) can be rewritten as

$$T_{vc} - \bar{T}_v = \frac{\left( \frac{C_1 + \lambda C_2}{1 + \lambda \Delta z} - \bar{h}^* \right)}{1 + \gamma} \left[ \frac{1}{c_p} + \frac{\delta \bar{T} \gamma}{L} \right] + \delta \bar{T} (\bar{q}^* - \bar{q}) \quad (4.40)$$

With the consideration of the effects of moisture on buoyancy (when the virtual temperature is used), the non-buoyancy condition for the cloud becomes

$$T_{vc} = \bar{T}_v \quad (4.41)$$

Using the non-buoyancy condition (4.41) in (4.40), a linear equation for  $\lambda$  can be obtained to express the non-buoyancy condition, i.e.

$$\frac{C_1 + \lambda C_2}{1 + \lambda \Delta z} = \bar{h}^* - \frac{(1 + \gamma) \delta \bar{T} (\bar{q}^* - \bar{q})}{\frac{1}{c_p} + \frac{\delta \bar{T} \gamma}{L}} \quad (4.42)$$

We define

$$h''_c \equiv \bar{h}^* - \frac{(1 + \gamma) \delta \bar{T} (\bar{q}^* - \bar{q})}{\frac{1}{c_p} + \frac{\delta \bar{T} \gamma}{L}} . \quad (4.43)$$

Then  $h''_c$  can be computed by using the large-scale environmental sounding, and equation (4.42) becomes

$$\frac{C_1 + \lambda C_2}{1 + \lambda \Delta z} = h''_c ,$$

or

$$\lambda = \frac{h''_c - C_1}{C_2 + \Delta z h''_c} . \quad (4.44)$$

Using (4.44), we can easily solve for the entrainment rate  $\lambda$ , for each cloud-top level. The problem is reduced to determining the coefficients  $C_1$  and  $C_2$ . In section 3.2.2 we have shown that  $C_1$  is the moist static energy in the PBL. In order to determine  $C_2$ , we rewrite (4.44) as

$$C_2 = \frac{h''_c (1 + \lambda \Delta z) - C_1}{\lambda} . \quad (4.45)$$

Using equation (4.43), we can calculate  $h''_c$  at each level for a given  $\lambda$ . Then, by giving an arbitrary entrainment rate  $\lambda''$ , the coefficient  $C_2$  can be estimated by using equation (4.45).  $C_2$  will depend on the detrainment level. Because the coefficient  $C_2$  solely depends on the large-scale sounding, the vertical profile of  $C_2$  should be unique regardless of the choice of  $\lambda''$ . We have done some tests which showed that the  $C_2$  profile is indeed unique

for various  $\lambda''$  when the large-sounding is specified. After the coefficient  $C_2$  has been obtained,  $\lambda$  can be calculated by using equation (4.44).

We now summarize the steps for finding the entrainment rate  $\lambda$ . For given large-scale soundings,  $h''_c$  can be calculated from (4.43) for each level. The coefficient  $C_1$  is given by the moist static energy of the PBL. The coefficient  $C_2$  at each level can be computed by using (4.45) for a given arbitrary  $\lambda''$ . Finally, (4.44) can be used to calculate the entrainment rate,  $\lambda$ . Compared with the costly iterative calculations for finding  $\lambda$  in the AS parameterization, the above procedure is much more economical and simpler. In the following chapter, it is demonstrated that simulation results are closer to the real climate (compared with the original AS parameterization with the prognostic hypothesis) with this new method for finding  $\lambda$ .

## **Chapter 5**

### **The Linear Mass Flux Profile ( II )**

In the preceding Chapter we have formulated the relations between cumulus entrainment parameter  $\lambda$  and in-cloud moist static energy, as well as the in-cloud moisture profile corresponding to the linear mass flux profile assumption. We now go on to include the cloud-top entrainment process into the new cumulus model, and formulate the ice formation processes in this Chapter. In the last part of this Chapter, we present some simulation results from the CSU GCM with the use of the new linearized cumulus parameterization, and compare the results of the control run presented in Chapter 3.

#### **5.1 Cloud-top entrainment**

##### **5.1.1 Entrainment processes at cloud top**

Squires (1958) reviewed theories of the interaction between cumuli and their environment in the light of observations. He pointed that the region around the top of a growing cloud may be an important source of the dry air which mixes with cloud air. The turbulent mixing of dry environmental air near the tops of clouds may produce negative

buoyancy and lead to penetrative downdrafts. A model of the penetration of top-entrained air into a cloud showed that dry parcels can remain unstaturated while subsiding up to three kilometers. These downdrafts would have the effects of reducing the liquid water content (LWC) and cooling the cloud. This explained why the LWC observed in cumulus clouds is always less than the adiabatic value for that level (Squires, 1955).

The idea of cloud-top entrainment was further explored by Telford (1975). He argued that mixing in clouds is primarily a buoyancy-driven process, and that therefore the cloudy air should usually be near buoyancy equilibrium with the environment. Based on the above argument, Telford assumed that mixing occurs at the cloud top and that the parcels subsequently move vertically to their level of neutral buoyancy. With these assumptions, he was able to obtain agreement between the calculated and the observed distributions of the liquid water content.

Paluch (1979) presented a graphical method for analyzing the properties of cloudy and clear air that provide information about the altitude from which the entrained air originates. Two conserved variables, equivalent potential temperature and total water mixing ratio, were used to deduce the environmental origin of air sampled by gliders inside Colorado cumuli. She found that the source of the entrained air was often up to 2 km above the aircraft penetration level and usually slightly below cloud top. She saw little evidence of lateral entrainment.

Many further studies also indicated the importance of cloud-top entrainment. Raymond and Wilkening (1982) provided observational evidence that the lateral inflow of air in small mountain cumulus in New Mexico is insignificant and that the source altitude of

entrained dry air is close to the cloud-top height. Randall and Huffman (1982) noted the need for a realistic parameterization of cloud-top entrainment in a simple cumulus model. Cooper and Rodi (1982) also suggested that the mixing process is dry air entraining from the cloud top, but the downdraft formed on the edges of the rising core. Based on an observational study of the source region of the entrained air for cumulus clouds of the United States High Plains and Mid-west, Boatman and Auer (1983) found that “entrainment within 20 mb of the cloud top was the source of entrained air in 78 out of 87 cases examined.” Applying Paluch’s method to four fair-weather cumuli in South Dakota, LaMontagne and Telford (1983) concluded that the entrained air originated near the cloud top. All of these studies concluded that cloud-top entrainment is important and should be considered in cumulus parameterizations.

### 5.1.2 The incorporation of cloud-top entrainment into the cloud model

In the AS parameterization, cloud-top entrainment is ignored in its cloud model which is used to determine cloud properties. We have introduced the linear mass flux assumption in the previous chapter. Moorthi and Suarez (1992) mentioned that, for a given  $\lambda$ , a linear mass flux will cause less dilution of cloud air at upper levels and thus results in deeper clouds than when the AS formula is used. In other words, the environmental air entrainment in upper cloud layers (including the cloud-top layer) is reduced when an exponential mass flux profile is replaced by a linear mass flux profile.

Based on the above concerns, the additional amount of entrainment at cloud top has been included in our cloud model. The method is from Cheng and Arakawa (1992). With the linear mass flux assumption, the normalized mass flux at cloud top,  $\eta_T(\lambda)$ , can

be written as

$$\eta_T(\lambda) = 1 + \lambda(z_T - z_B) , \quad (5.1)$$

where  $z_T$  and  $z_B$  are cloud top and cloud base heights of  $\lambda$  cloud, respectively. If cloud-top entrainment is considered, (5.1) can be written as

$$\eta_T(\lambda) = 1 + \lambda(z_T - z_B) + (\Delta\eta)_T , \quad (5.2)$$

where  $(\Delta\eta)_T$  is the amount of entrainment at the cloud top. A ratio,  $v$ , was introduced by Cheng and Arakawa (1992) to measure the amount of the entrainment at cloud top with

$$v \equiv \frac{(\Delta\eta)_T}{\lambda(z_T - z_B)} . \quad (5.3)$$

Then we can write

$$(\Delta\eta)_T = v\lambda(z_T - z_B) . \quad (5.4)$$

From (5.4), the amount of the entrainment at cloud top can be controlled by the ratio  $v$ . For example,  $v = 0$  means that there is no cloud-top entrainment.

With the consideration of the cloud-top entrainment,  $(h_c)_T$ , the in-cloud moist static energy at cloud top, can be written as

$$(h_c)_T = \frac{(h_c)_{T+} [1 + \lambda(z_{T+} - z_B)] + [\lambda\Delta z_T + (\Delta\eta)_T] \bar{h}_T}{1 + \lambda(z_T - z_B) + (\Delta\eta)_T} , \quad (5.5)$$

where subscript  $T+$  is used to represent values at the level immediately below the cloud top level;  $\Delta z_T$  is the thickness between the cloud top level and level  $T+$ ; and  $\bar{h}_T$  is the

moist static energy of the environment of the cloud-top layer (between cloud-top level and the level  $T_+$ ). Substituting (5.4) into (5.5) gives

$$(h_c)_T = \frac{(h_c)_{T_+} [1 + \lambda (z_{T_+} - z_B)] + [\lambda \Delta z_T + v \lambda (z_T - z_B)] \bar{h}_T}{1 + \lambda (z_T - z_B) + v \lambda (z_T - z_B)} \quad (5.6)$$

Equation (5.6) is used in our cloud model to calculate the in-cloud moist static energy at cloud top with the effects of cloud top-entrainment. Similarly, the total moisture inside clouds at cloud tops is given by

$$(q_c)_T = \frac{(q_c)_{T_+} [1 + \lambda (z_{T_+} - z_B)] + [\lambda \Delta z_T + v \lambda (z_T - z_B)] \bar{q}_T}{1 + \lambda (z_T - z_B) + v \lambda (z_T - z_B)} \quad (5.7)$$

Cheng and Arakawa (1992) conducted some tests to determine the ratio  $v$ . They found that  $v = 1$  is a proper choice.

## 5.2 The Ice Phase of Cumulus Clouds

### 5.2.1 The inclusion of the ice phase

Many cumulus cloud tops can reach to heights which are higher than the freezing level, and ice processes in clouds are believed to be among the major mechanisms contributing to precipitation, so the effects of the ice formation and the release of the latent heat of fusion on the buoyancy of cumulus clouds have been investigated in many studies. For example, Simpson and Wiggert (1969, 1971) indicated that there is a sudden growth of cumulus towers under conditions of the silver iodide seeding and subsequent ice formation.

In Chapter 2 we have reviewed that anvil clouds (which are formed from frozen water droplets detrained from cumulonimbi) significantly influence the large-scale radiation budget and provide mesoscale stratiform precipitation which accounted for a substantial fraction of the total rainfall in GATE. It is our primary goal to include the effects of anvil clouds in numerical prediction models. The melting of ice particles in anvil clouds, which increases cooling and strengthens mesoscale downdrafts, is an important characteristic of anvil clouds. In order to parameterize the effects of anvil clouds, we need to determine the ice particle source as the first step. This is another reason to include ice phase in our cloud model.

The approach to introduce the ice phase in our cloud model is based on Lord (1978). As in Chapter 3, for layer  $k$ , we define  $(q_c)_k$  the total moisture inside clouds before precipitation processes;  $(P_r)_k$  the cumulus precipitation production rate;  $(q_c)_{k-\frac{1}{2}}$  the total moisture inside clouds after precipitation processes; and

$$(q_c)_{k-\frac{1}{2}} = (q_c)_k - (P_r)_k \quad (5.8)$$

Equation (5.8) is the same as equation (4.21). With the inclusion of the ice phase, in addition we define that  $(q_{l,c})_k$  the liquid water mixing ratio inside clouds before ice formation processes; and  $(q'_{l,c})_k$  the liquid water mixing ratio inside clouds after ice formation processes.

It is assumed that conversion of supercooled liquid water droplets to ice per unit height in the cloud depends on the cloud temperature and the amount of liquid water in the cloud. The conversion rate of liquid water into ice is given by

$$\mathfrak{R}_k = \frac{T_{cr} - (T_c)_k}{T_{cr} - T_f}, \quad (5.9)$$

where  $T_f = -40^\circ\text{C}$  and  $T_{cr} = -10^\circ$ ; and  $(T_c)_k$  is the cloud temperature of layer  $k$ . It is also assumed that

$$\mathfrak{R}_k = 0, \quad \text{when } (T_c)_k > T_{cr}; \quad (5.10)$$

and

$$\mathfrak{R}_k = 1, \quad \text{when } (T_c)_k < T_f. \quad (5.11)$$

Using above assumptions, the liquid water mixing ratio inside clouds, after ice formation, can be written as

$$\begin{aligned} (q'_{l,c})_k &= (q_{l,c})_k - \mathfrak{R}_k \cdot (q_{l,c})_k \\ &= (1 - \mathfrak{R}_k) (q_{l,c})_k, \end{aligned} \quad (5.12)$$

and, similarly to (4.22), the precipitation production rate,  $(P_r)_k$ , can be written as

$$\begin{aligned} (P_r)_k &= \frac{C_0 \Delta z_k}{1 + C_0 \Delta z_k} (q'_{l,c})_k \\ &= \frac{C_0 \Delta z_k}{1 + C_0 \Delta z_k} (1 - \mathfrak{R}_k) (q_{l,c})_k. \end{aligned} \quad (5.13)$$

If  $(q_{i,c})_k$  is used to represent the ice mixing ratio inside clouds before the ice formation processes in the current layer, or in other words, the ice carried up from lower layer by updrafts and from the environment by entrainment, the water vapor mixing of layer  $k$ ,

$(q_{v,c})_{k-\frac{1}{2}}$ , can be obtained from

$$(q_{v,c})_{k-\frac{1}{2}} = (\bar{q}_v^*)_k + \frac{\gamma_k}{(1+\gamma_k)L} \left[ (h_c)_{k-\frac{1}{2}} - \bar{h}_k^* + L_f(q_{i,c})_k \right], \quad (5.14)$$

where  $L_f$  is the latent of fusion. This is similar to (4.24). Then the liquid water mixing ratio inside clouds, before ice formation, can be obtained by

$$(q_{l,c})_k = (q_c)_k - (q_{i,c})_k - (\bar{q}^*)_k - \frac{\gamma_k}{(1+\gamma_k)L} \left[ (h_c)_{k-\frac{1}{2}} - \bar{h}_k^* + L_f(q_i)_k \right]. \quad (5.15)$$

Substituting (5.15) into (5.13) gives

$$(P_r)_k = \frac{C_0 \Delta z_k}{1 + C_0 \Delta z_k} (1 - \mathfrak{R}_k) \left[ (q_c)_k - (q_{i,c})_k - (\bar{q}^*)_k - \frac{\gamma_k}{(1+\gamma_k)L} (h_c)_{k-\frac{1}{2}} + \frac{\gamma_k}{(1+\gamma_k)L} \bar{h}_k^* - \frac{\gamma_k}{(1+\gamma_k)L} (L_f(q_{i,c})_k) \right]. \quad (5.16)$$

Equation (5.16) gives the precipitation production rate with ice effects. In (5.16),  $(q_{i,c})_k$  is the ice from the lower layer and environment, and is given by

$$(q_{i,c})_k = \frac{\left[ 1 + \lambda \left( z_{k+\frac{1}{2}} - z_B \right) \right] (q_{i,c})_{k+\frac{1}{2}} + \lambda (\bar{q}_i)_k \Delta z_k}{1 + \lambda \left( z_{k-\frac{1}{2}} - z_B \right)}, \quad (5.17)$$

where  $(\bar{q}_i)_k$  is the environmental ice mixing ratio. If we use  $(q_{i,c})_{k-\frac{1}{2}}$  to represent the ice mixing ratio inside clouds after ice formation in the current layer, then

$$(q_{i,c})_{k-\frac{1}{2}} = (q_{i,c})_k + \mathfrak{R}_k \cdot (q_{l,c})_k \quad . \quad (5.18)$$

When (5.17) is used to calculate the ice mixing ratio flux,  $(q_{i,c})_{k+\frac{1}{2}}$ , on the left-hand side of (5.17), should be the ice mixing ratio of the layer after the ice formation and be calculated by using (5.18).

One procedure for determining the in-cloud properties with the linear mass flux assumption and the inclusion of the ice phase can be summarized as follows. For each model layer, equations (4.11), (4.20) and (5.17) are used to calculate  $(h_c)_{k-\frac{1}{2}}$ ,  $(q_c)_k$  and  $(q_{i,c})_k$ . Then, equations (5.14), (5.15) and (5.16) are used to determine  $(q_{v,c})_{k-\frac{1}{2}}$ ,  $(q_l)_k$  and  $(P_r)_k$ . The next step is to use equations (4.21) and (5.18) to obtain  $(q_c)_{k-\frac{1}{2}}$  and  $(q_{i,c})_{k-\frac{1}{2}}$ . Finally, equations (4.11), (4.20) and (5.17) are used repeatedly for the next layer's in-cloud properties.

### 5.2.2 The Linear Relation between the Entrainment Rate and Cloud Moisture with Ice

In Chapter 3, we have proven that there are linear relations of the entrainment rate,  $\lambda$ , with the moist static energy inside, and  $\lambda$  with the moisture without ice inside clouds. In this section, we are going to prove the existence of a similar linear relation between  $\lambda$  and cloud moisture with the inclusion of the ice phase.

Substituting (5.16) into (5.8), the total moisture inside clouds after precipitation and ice formation processed is given by

$$\begin{aligned}
(q_c)_{k-\frac{1}{2}} &= (q_c)_k - \frac{C_0 \Delta z_k}{1 + C_0 \Delta z_k} (1 - \mathfrak{R}_k) \left\{ (q_c)_k - (q_{i,c})_k - (\bar{q}^*)_k \right. \\
&\quad \left. - \frac{\gamma_k}{(1 + \gamma_k)L} (h_c)_{k-\frac{1}{2}} + \frac{\gamma_k}{(1 + \gamma_k)L} \bar{h}^*_k - \frac{\gamma_k}{(1 + \gamma_k)L} L_f (q_{i,c})_k \right\} \\
&= \frac{1 + C_0 \Delta z_k \mathfrak{R}_k}{1 + C_0 \Delta z_k} (q_c)_k + \frac{C_0 \Delta z_k}{1 + C_0 \Delta z_k} (1 - \mathfrak{R}_k) \left[ (\bar{q}^*)_k - \frac{\gamma_k}{(1 + \gamma_k)L} (h_c)_{k-\frac{1}{2}} \right. \\
&\quad \left. - \frac{\gamma_k}{(1 + \gamma_k)L} \bar{h}^*_k + \frac{L + \gamma_k (L + L_f)}{(1 + \gamma_k)L} (q_{i,c})_k \right] . \tag{5.19}
\end{aligned}$$

Substituting (4.20) into (5.19) to replace  $(q_c)_k$ , (5.19) becomes

$$\begin{aligned}
(q_c)_{k-\frac{1}{2}} \left[ 1 + \lambda \left( z_{k-\frac{1}{2}} - z_B \right) \right] &= \frac{1 + C_0 \Delta z_k \mathfrak{R}_k}{1 + C_0 \Delta z_k} \left\{ \left[ 1 + \lambda \left( z_{k+\frac{1}{2}} - z_B \right) \right] \right. \\
&\quad \left. \cdot (q_c)_{k+\frac{1}{2}} + \lambda \bar{q}_k \Delta z_k \right\} + \frac{C_0 \Delta z_k}{1 + C_0 \Delta z_k} (1 - \mathfrak{R}) \left\{ (\bar{q}^*)_k \left[ 1 + \lambda \left( z_{k-\frac{1}{2}} - z_B \right) \right] \right. \\
&\quad \left. + \frac{\gamma_k}{(1 + \gamma_k)L} \left( \left[ 1 + \lambda \left( z_{k+\frac{1}{2}} - z_B \right) \right] (h_c)_{k+\frac{1}{2}} + \lambda \bar{h}_k \right) - \frac{\gamma_k}{(1 + \gamma_k)L} \bar{h}^*_k \right. \\
&\quad \left. \cdot \left[ 1 + \lambda \left( z_{k-\frac{1}{2}} - z_B \right) \right] + \frac{L + \gamma_k (L + L_f)}{(1 + \gamma_k)L} \left[ 1 + \lambda \left( z_{k+\frac{1}{2}} - z_B \right) \right] \right. \\
&\quad \left. \cdot (q_{i,c})_{k+\frac{1}{2}} \right\} . \tag{5.20}
\end{aligned}$$

Rearranging (5.20), a budget equation for the moisture inside clouds is given by

$$\begin{aligned}
& \left[ (q_c)_{k-\frac{1}{2}} - \frac{C_0 \Delta z_k}{1 + C_0 \Delta z_k} (1 - \mathfrak{R}_k) \left[ (\bar{q}^*)_k - \frac{\gamma_k}{(1 + \gamma_k) L} \bar{h}^*_k \right] \right] \\
& \cdot \left[ 1 + \lambda \left( z_{k-\frac{1}{2}} - z_B \right) \right] \\
= & \left[ \frac{1 + C_0 \Delta z_k \mathfrak{R}_k}{1 + C_0 \Delta z_k} (q_c)_{k+\frac{1}{2}} + \frac{C_0 \Delta z_k}{1 + C_0 \Delta z_k} (1 - \mathfrak{R}_k) \left[ \frac{\gamma_k}{(1 + \gamma_k) L} (h_c)_{k+\frac{1}{2}} \right. \right. \\
& \left. \left. + \frac{L + \gamma_k (L + L_f)}{(1 + \gamma_k) L} (q_{i.c})_{k+\frac{1}{2}} \right] \right] \cdot \left[ 1 + \lambda \left( z_{k+\frac{1}{2}} - z_B \right) \right] \\
& + \frac{1 + C_0 \Delta z_k \mathfrak{R}_k}{1 + C_0 \Delta z_k} \cdot \lambda \bar{q}_k \Delta z_k + \frac{C_0 \Delta z_k}{1 + C_0 \Delta z_k} (1 - \mathfrak{R}_k) \frac{\gamma_k}{(1 + \gamma_k) L} \\
& \cdot \lambda \bar{h}_k \Delta z_k . \tag{5.21}
\end{aligned}$$

If we let  $C_0 = 0$  and  $\mathfrak{R} = 0$  in (5.21) (clouds without precipitation and ice phase), we find that

$$(q_c)_{k-\frac{1}{2}} \left[ 1 + \lambda \left( z_{k-\frac{1}{2}} - z_B \right) \right] = \left[ 1 + \lambda \left( z_{k+\frac{1}{2}} - z_B \right) \right] (q_c)_{k+\frac{1}{2}} + \lambda \bar{q}_k \Delta z_k ,$$

which is same as (4.20) except that  $(q_c)_k$  in (4.20) has been replaced by  $(q_c)_{k-\frac{1}{2}}$ . If we let  $C_0 \neq 0$  but  $\mathfrak{R} = 0$  (clouds with precipitation but without ice phase) in (5.21), then,

$$\begin{aligned}
& \left[ (q_c)_{k-\frac{1}{2}} - \frac{C_0 \Delta z_k}{1 + C_0 \Delta z_k} \left[ (\bar{q}_v^*)_{k-\frac{1}{2}} - \frac{\gamma_k}{(1 + \gamma_k) L} \bar{h}_k^* \right] \right] \left[ 1 + \lambda \left( z_{k-\frac{1}{2}} - z_B \right) \right] \\
&= \left[ \frac{(q_c)_{k+\frac{1}{2}}}{1 + C_0 \Delta z_k} + \frac{C_0 \Delta z_k}{1 + C_0 \Delta z_k} \frac{\gamma_k}{(1 + \gamma_k) L} (h_c)_{k+\frac{1}{2}} \right] \left[ 1 + \lambda \left( z_{k+\frac{1}{2}} - z_B \right) \right] \\
&= \left[ \frac{(q_c)_{k+\frac{1}{2}}}{1 + C_0 \Delta z_k} + \frac{C_0 \Delta z_k}{1 + C_0 \Delta z_k} \frac{\gamma_k}{(1 + \gamma_k) L} (h_c)_{k+\frac{1}{2}} \right] \left[ 1 + \lambda \left( z_{k+\frac{1}{2}} - z_B \right) \right] \\
&\quad + \frac{\lambda \Delta z_k}{1 + C_0 \Delta z_k} \left\{ \bar{q}_k + C_0 \Delta z_k \frac{\gamma_k}{(1 + \gamma_k) L} \bar{h}_k \right\} ,
\end{aligned}$$

which is the same as (4.39). Therefore, equation (5.21) is the general form of the cloud moisture budget equation with both precipitation and ice. Looking at (5.21) we see that

$(q_c)_{k-\frac{1}{2}}$  is still a linear function of  $\lambda$ .

In order to further demonstrate the reality of this linear relation, we use  $k-1$  to replace  $k$  in (5.21). The equation becomes

$$\begin{aligned}
& \left[ (q_c)_{k-\frac{3}{2}} - \frac{C_0 \Delta z_{k-1}}{1 + C_0 \Delta z_{k-1}} (1 - \mathfrak{R}_{k-1}) \left[ (\bar{q}^*)_{k-1} - \frac{\gamma_{k-1}}{(1 + \gamma_{k-1}) L} \bar{h}_{k-1}^* \right] \right] \\
&\quad \bullet \left[ 1 + \lambda \left( z_{k-\frac{3}{2}} - z_B \right) \right]
\end{aligned}$$

$$\begin{aligned}
&= \left[ \frac{1 + C_0 \Delta z_{k-1} \mathfrak{R}_{k-1}}{1 + C_0 \Delta z_{k-1}} (q_c)_{k-\frac{1}{2}} + \frac{C_0 \Delta z_{k-1}}{1 + C_0 \Delta z_{k-1}} (1 - \mathfrak{R}_{k-1}) \right. \\
&\quad \cdot \left[ \frac{\gamma_{k-1}}{(1 + \gamma_{k-1}) L} (h_c)_{k-\frac{1}{2}} + \frac{L + \gamma_{k-1} (L + L_f)}{(1 + \gamma_{k-1}) L} (q_{i,c})_{k-\frac{1}{2}} \right] \Bigg] \\
&\quad \cdot \left[ 1 + \lambda \left( z_{k-\frac{1}{2}} - z_B \right) \right] + \frac{1 + C_0 \Delta z_{k-1} \mathfrak{R}_{k-1}}{1 + C_0 \Delta z_{k-1}} \cdot \lambda \bar{q}_{k-1} \Delta z_{k-1} \\
&\quad + \frac{C_0 \Delta z_{k-1}}{1 + C_0 \Delta z_{k-1}} (1 - \mathfrak{R}_{k-1}) \frac{\gamma_{k-1}}{(1 + \gamma_{k-1}) L} \cdot \lambda \bar{h}_{k-1} \Delta z_{k-1} \quad . \quad (5.22)
\end{aligned}$$

Substituting (4.11), (4.29), (5.17) and (5.18) into (5.21), to replace  $(h_c)_{k-\frac{1}{2}}$ ,  $(q_c)_{k-\frac{1}{2}}$ , and  $(q_{i,c})_{k-\frac{1}{2}}$ , and rearranging the equation, (5.21) becomes

$$\begin{aligned}
&\left[ (q_c)_{k-\frac{3}{2}} - \frac{C_0 \Delta z_{k-1}}{1 + C_0 \Delta z_{k-1}} (1 - \mathfrak{R}_{k-1}) \left[ (\bar{q}^*)_{k-1} - \frac{\gamma_{k-1}}{(1 + \gamma_{k-1}) L} \bar{h}^*_{k-1} \right] \right] \\
&\quad \cdot \left[ 1 + \lambda \left( z_{k-\frac{3}{2}} - z_B \right) \right] \\
&= \frac{1 + C_0 \Delta z_{k-1} \mathfrak{R}_{k-1}}{1 + C_0 \Delta z_{k-1}} \cdot \frac{C_0 \Delta z_k}{1 + C_0 \Delta z_k} (1 - \mathfrak{R}_k) \cdot \left[ (\bar{q}^*)_k - \frac{\gamma_k}{(1 + \gamma_k) L} \bar{h}^*_k \right] \\
&\quad \cdot \left[ 1 + \lambda \left( z_{k-\frac{1}{2}} - z_B \right) \right] + \frac{1 + C_0 \Delta z_{k-1} \mathfrak{R}_{k-1}}{1 + C_0 \Delta z_{k-1}} \left( \left[ \frac{1 + C_0 \Delta z_k \mathfrak{R}_k}{1 + C_0 \Delta z_k} (q_c)_{k+\frac{1}{2}} \right. \right.
\end{aligned}$$

$$\begin{aligned}
& + \frac{C_0 \Delta z_k}{1 + C_0 \Delta z_k} (1 - \mathfrak{R}_k) \cdot \left[ \frac{\gamma_k}{(1 + \gamma_k) L} (h_c)_{k + \frac{1}{2}} + \frac{L + \gamma_k (L + L_f)}{(1 + \gamma_k) L} (q_{i,c})_{k + \frac{1}{2}} \right] \Bigg] \\
& \bullet \left[ 1 + \lambda \left( z_{k + \frac{1}{2}} - z_B \right) \right] + \frac{1 + C_0 \Delta z_k \mathfrak{R}}{1 + C_0 \Delta z_k} \cdot \lambda \bar{q}_k \Delta z_k + \frac{C_0 \Delta z_k}{1 + C_0 \Delta z_k} (1 + \mathfrak{R}_k) \\
& \bullet \frac{\gamma_k}{(1 + \gamma_k) L} \lambda \bar{h}_k \Delta z_k \Bigg) + \frac{C_0 \Delta z_{k-1}}{1 + C_0 \Delta z_{k-1}} \cdot (1 - \mathfrak{R}_{k-1}) \frac{\gamma_{k-1}}{(1 + \gamma_{k-1}) L} \\
& \bullet \left[ \left[ 1 + \lambda \left( z_{k + \frac{1}{2}} - z_B \right) \right] \cdot (q_{i,c})_{k + \frac{1}{2}} + \lambda (\bar{q}_i)_k \Delta z_k \right] \\
& + \frac{C_0 \Delta z_{k-1}}{1 + C_0 \Delta z_{k-1}} \cdot (1 - \mathfrak{R}_{k-1}) \frac{1 + \gamma_{k-1} (L + L_f)}{(1 + \gamma_{k-1}) L} \cdot \left\{ \left[ 1 + \lambda \left( z_{k + \frac{1}{2}} - z_B \right) \right] \right. \\
& \cdot (q_{i,c})_{k + \frac{1}{2}} + \mathfrak{R}_k \left[ 1 + \lambda \left( z_{k + \frac{1}{2}} - z_B \right) \right] \cdot (q_c)_{k + \frac{1}{2}} + \lambda \bar{q}_k \Delta z_k \mathfrak{R}_k \\
& \left. - \mathfrak{R}_k \left[ 1 + \lambda \left( z_{k + \frac{1}{2}} - z_B \right) \right] \cdot (q_{i,c})_{k + \frac{1}{2}} - \mathfrak{R}_k (\bar{q}^*)_k \left[ 1 + \lambda \left( z_{k - \frac{1}{2}} - z_B \right) \right] \right\} \\
& - \frac{\gamma_k \mathfrak{R}_k}{(1 + \gamma_k) L} \left[ \left[ 1 + \lambda \left( z_{k + \frac{1}{2}} - z_B \right) \right] \cdot (h_c)_{k + \frac{1}{2}} + \lambda \bar{h}_k \Delta z_k \right]
\end{aligned}$$

$$\begin{aligned}
& -\bar{h}_k^* \left[ 1 + \lambda \left( z_{k-\frac{1}{2}} - z_B \right) \right] + L_f \left[ 1 + \lambda \left( z_{k+\frac{1}{2}} - z_B \right) \right] (q_{i,c})_{k+\frac{1}{2}} \left. \right] \\
& + \frac{1 + C_0 \Delta z_{k-1}}{1 + C_0 \Delta z_{k-1}} \cdot \mathfrak{R}_{k-1} \lambda \bar{q}_{k-1} \Delta z_{k-1} + \frac{C_0 \Delta z_{k-1}}{1 + C_0 \Delta z_{k-1}} \cdot (1 - \mathfrak{R}_k) \\
& \quad \bullet \frac{\gamma_{k-1}}{(1 + \gamma_{k-1}) L} \cdot \lambda \bar{h}_{k-1} \Delta z_{k-1} \quad . \quad (5.23)
\end{aligned}$$

It can be seen that the right-hand side of (5.23) is still a linear function of  $\lambda$  in terms of quantities which can be determined by large-scale observations. Therefore, we can conclude that the linear relation between the cloud moisture and the entrainment rate,  $\lambda$ , can be satisfied with the inclusion of the ice phase in clouds.

### 5.3 Criteria for the Existence of Clouds

In section 3.3 we have discussed the method to determine  $\lambda$  by considering the virtual temperature with the linear mass flux assumption. In our cloud model, for given large-scale soundings at each grid point, entrainment rate,  $\lambda$ , for clouds with tops in each model layer is calculated first. Then we use these entrainment rates to test the existence of clouds. The following are criteria which are used to test cloud existence.

1. For an existing cloud type, it is required that its non-buoyancy entrainment rate must be equal or greater than zero, or

$$\lambda \geq 0 \quad . \quad (5.24)$$

From the definition of  $\lambda$  we know that a negative entrainment rate is physical meaning-

less. When a negative entrainment rate,  $\lambda$ , is obtained, the corresponding cloud type is eliminated immediately.

2. The entrainment rate,  $\lambda$ , must be smaller than its maximum value which is  $1.5 \times 10^{-3} \text{ m}^{-1}$  in our simulation experiments. The value is determined based on cloud experiments (Sloss, 1967).

3. For different cloud types with different cloud top heights, the entrainment rate,  $\lambda$ , of clouds with higher cloud-top heights must be smaller than those  $\lambda$  corresponding to clouds with lower cloud-top heights. Because larger  $\lambda$  means more entrained environmental air, this will dilute cloud air and stop the cloud quicker, and so make clouds with lower cloud-top heights. Based on this criterion, if clouds with larger  $\lambda$ s have higher cloud-top heights than clouds with smaller  $\lambda$ s, the higher clouds are not allowed. In other words,  $\lambda$  must decrease with increasing cloud-top height.

4. The cloud top must be saturated. Because the entrainment rate,  $\lambda$ , is determined under the assumption that clouds are saturated, the cloud-top saturation condition should be satisfied after the calculation of cloud moisture budget. The cloud temperature is given by

$$T_c = \bar{T} + \frac{h_c - \bar{h}^*}{(1 + \gamma) C_p} , \quad (5.25)$$

after we obtained cloud properties. With cloud temperature  $T_c$ , the cloud saturation mixing ratio,  $q_c^*$ , can be determined. Then we can compare cloud-top  $q_c$  and  $q_c^*$ . If  $q_c$  is smaller than  $q_c^*$  for any cloud types, these cloud types do not exist.

5. The cloud work function must be positive. With the cloud temperature, the cloud virtual temperature can be obtained by

$$T_{v,c} = T_c (1 + \delta \cdot q_c) , \quad (5.26)$$

where  $\delta = 0.608$  . Then the cloud work function,  $A(\lambda)$  , is computed by

$$A(\lambda) = \sum_{k=1}^N \left[ \frac{1}{2} \cdot g \left[ \left( \frac{T_{v,c} - \bar{T}_v}{\bar{T}_v} \eta \right)_{k-\frac{1}{2}} + \left( \frac{T_{v,c} - \bar{T}_v}{\bar{T}_v} \eta \right)_{k+\frac{1}{2}} \right] \right] , \quad (5.27)$$

where  $N$  is the total model layers extended by  $\lambda$  clouds,  $\eta$  is normalized mass flux obtained from (4.7). The requirement of positive  $A(\lambda)$  means that when  $A(\lambda)$  calculated from (5.27) is negative, those clouds do not exist.

In our cloud model, the existence of clouds means that these clouds must meet all five of the above criteria. Only the existing clouds are considered to exert feedbacks on the large-scale environment.

#### **5.4 Simulations Using the Cumulus Parameterization with the Linear Mass Flux Profile**

The cumulus parameterization with the linear mass flux profile and cloud top entrainment has been implemented in the CSU GCM. In this section, some simulation results with the linear mass flux profile and the exponential mass flux profile are presented and compared. Descriptions of the CSU GCM and the control simulation have been given in Chapter 3. For the linear mass flux profile run (the L-run), we used the same initial con-

ditions as in the control run (the C-run). Tests indicate that the L-run saves about 15% ~ 20% of the cpu time for the cumulus parameterization compared with the C-run.

#### 5.4.1 Simulated cumulus activity

As discussed in the preceding sections, with the use of the linear mass flux profile in the cumulus parameterization, the methods used to determine cumulus clouds and cloud properties have been greatly simplified. We now investigate how this simplification affects the simulated cumulus activity and the simulated climate.

Fig. 5.1 shows July cumulus incidence maps from the C-run and the L-run. The two versions of the model generate very similar cumulus incidence patterns. Both maps have maxima over Northern Hemisphere tropics, corresponding to the ITCZ branches over oceans, Western Pacific convective regions, and the India monsoon. Minima can be found in subtropical high pressure regions over the oceans in both maps. The global mean value of the control run is a little bit larger than that of the linear version run.

Fig. 5.2 shows the zonally averaged cumulus incidence distributions from the control simulation (solid line) and the linear version simulation (dotted line). The two distributions of cumulus incidence from two simulations agree very well in both patterns and magnitudes although in general the L-run produces slightly less cumulus incidence than the C-run. From Fig. 5.1 and Fig. 5.2 we can conclude that the simplified cumulus parameterization with the linear mass flux profile can reproduce the cumulus incidence of the C-run.

Once the exponential mass flux profile has been replaced by the linear mass flux

## Cumulus Incidence

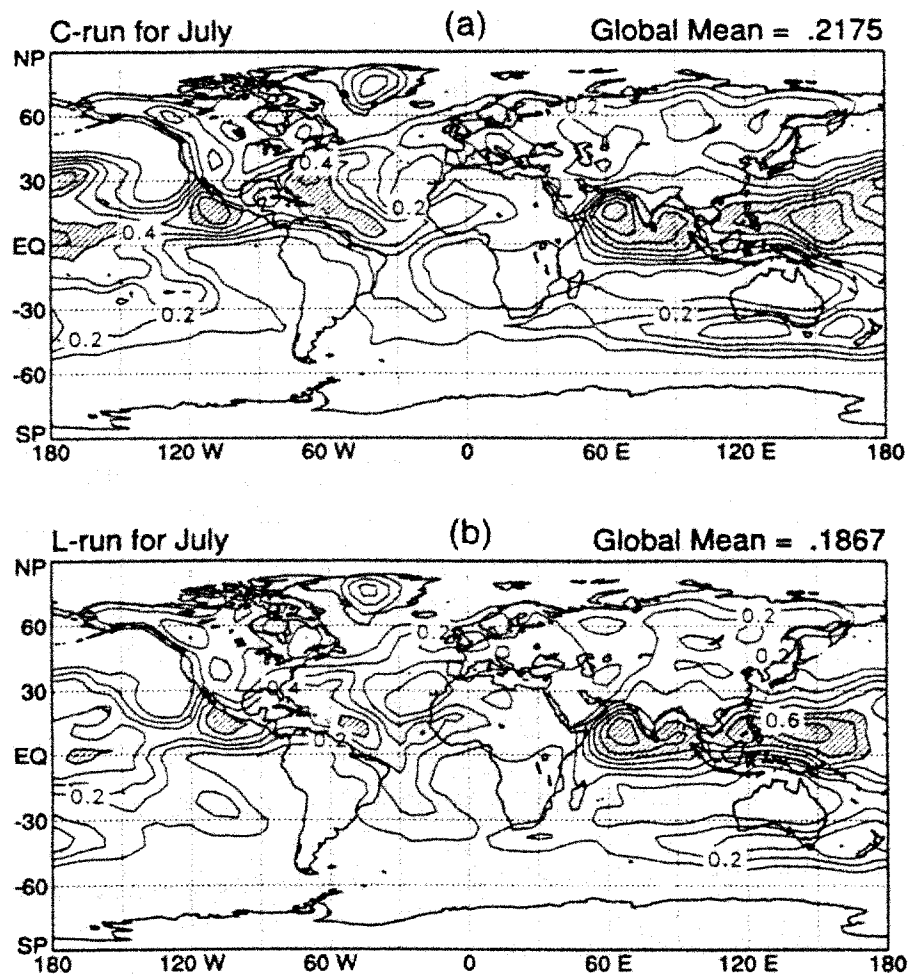


Fig. 5.1 July cumulus incidence from the control run (a) and the linear-version run (b). Contour intervals are 0.1. Values larger than 0.5 are shaded.

profile, the cumulus cloud mass flux (which is detrained at cloud top levels) is expected to be reduced. With the inclusion of the cloud top entrainment, however, the two cumulus parameterization versions actually produced quite similar cumulus cloud mass flux profiles. Fig. 5.3 shows the zonal mean cumulus detrainment intensities from the C-run and the L-run. There is little difference between the two results. Both simulations produce

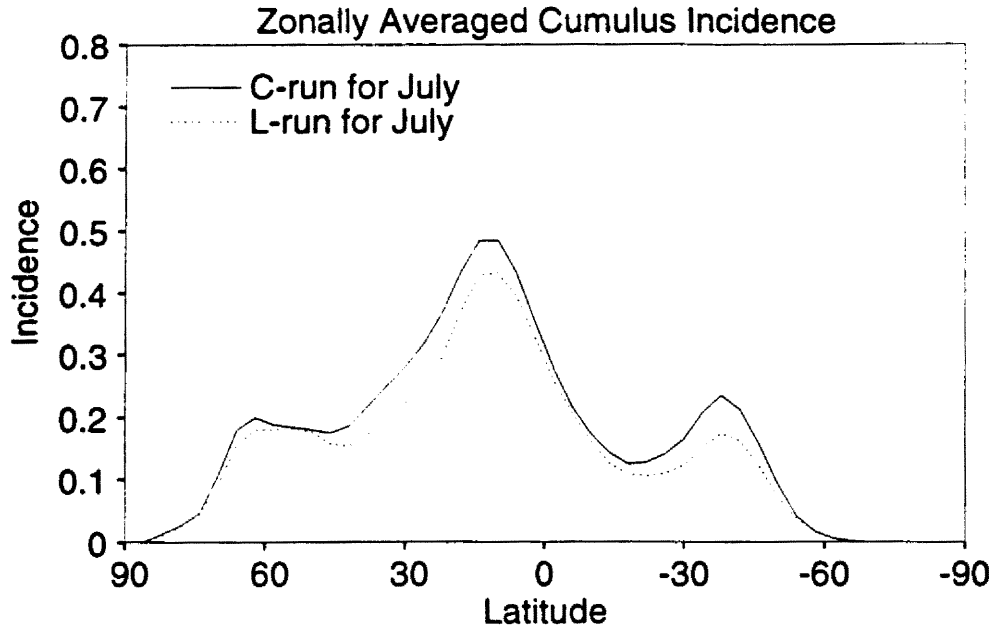


Fig. 5.2 Zonal mean cumulus incidence from control run (solid line) and linear version cumulus parameterization run (dotted line).

maxima in the upper troposphere of the northern tropics and secondary maxima in the middle troposphere in both hemispheres. Because this plot essentially shows where the cumulus clouds have their tops, we can deduce that two parameterizations generate very similar cumulus cloud patterns.

July cumulus precipitation maps from the C-run and the L-run are shown in Fig. 5.4. It is seen that the cumulus precipitation patterns are quite similar. Intense cumulus precipitation occurs over the India monsoon region, the Western Pacific region, and the Pacific ITCZ on both maps. We note that the global mean values from two simulations,  $1.960 \text{ mm} \cdot \text{day}^{-1}$  for the C-run and  $1.806 \text{ mm} \cdot \text{day}^{-1}$  for the L-run, are close. This demonstrates again the similarity of the cumulus activity produced by the two cumulus parameterizations.

## Cumulus Detrainment Mass Flux

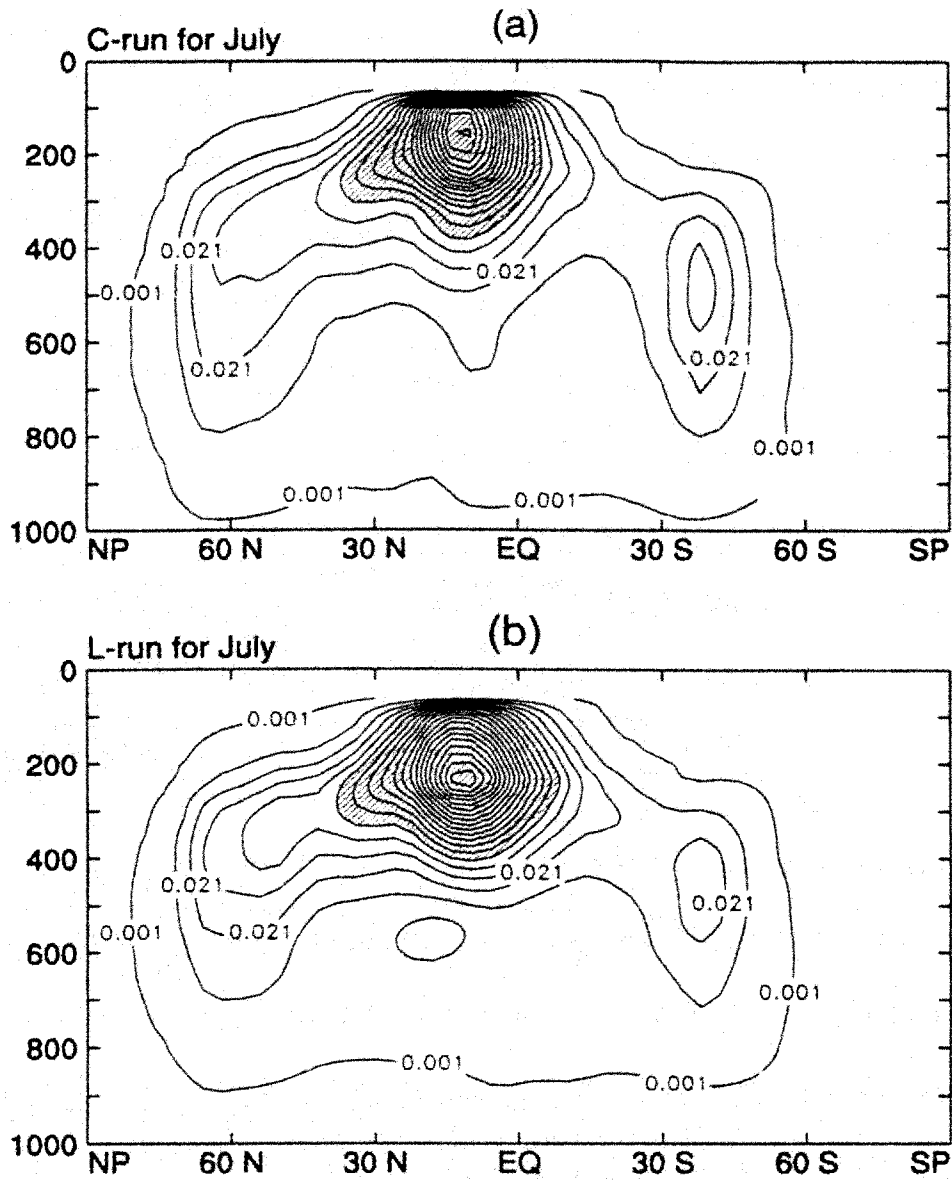


Fig. 5.3 Cumulus detrainment mass flux for July from the control run (a) and the linear version run (b). The unit is inverse hours ( $\text{hour}^{-1}$ ) and values larger than 0.05 are shaded.

The cumulus precipitation maxima from the two simulations are quite different, however. The maximum value is  $24.0 \text{ mm day}^{-1}$  in the C-run and  $17.3 \text{ mm day}^{-1}$  in

## Cumulus Precipitation

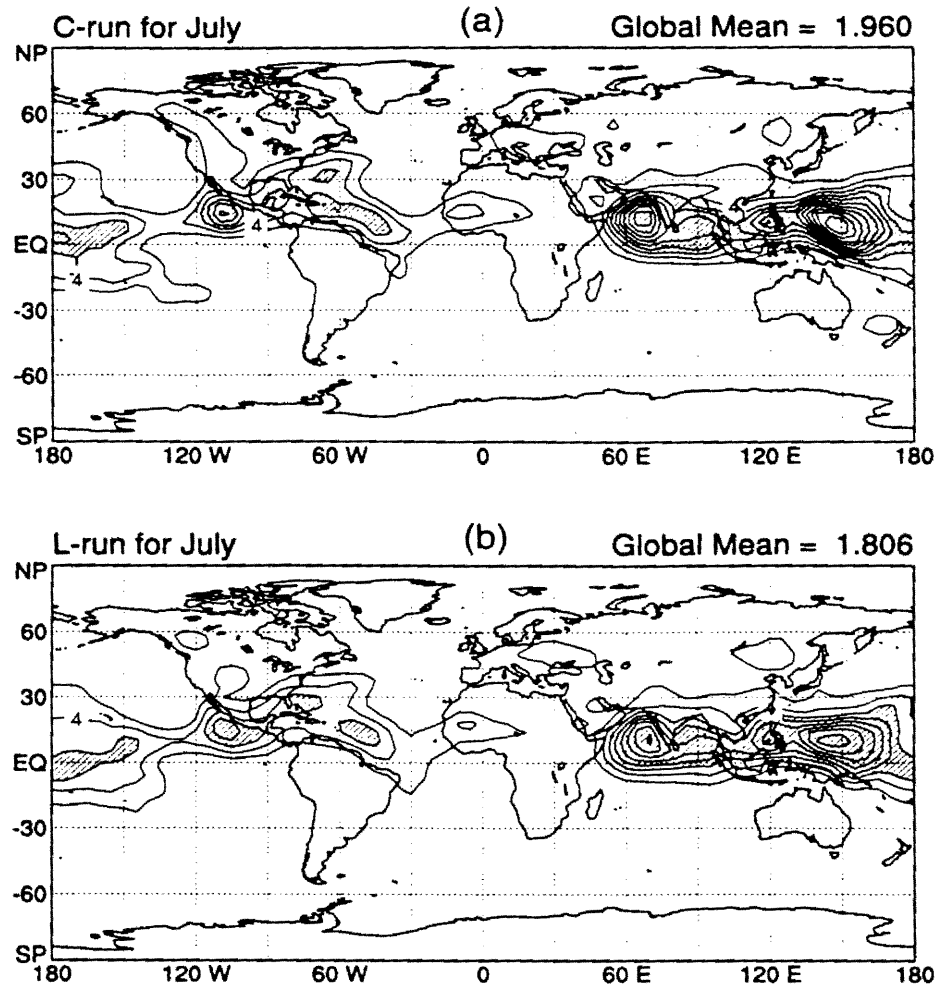


Fig. 5.4 July cumulus precipitation maps from control run (upper panel) and linear version run (lower panel). The unit is  $\text{mm day}^{-1}$  and values larger than  $6 \text{ mm day}^{-1}$  are shaded.

the L-run. The strongest cumulus precipitation occurs in the Western Pacific in both simulations. The intensity of the cumulus precipitation maximum is reduced in the L-run. The weaker cumulus precipitation from the L-run suggests that less deep cumulus convection is generated in the linear version cumulus parameterization. We will see that the reduction

of the maximum cumulus precipitation makes the simulated total precipitation rate closer to observations in the L-run.

Fig. 5.5 shows the July zonally averaged cumulus heating rates from the C-run and the L-run. As shown in the figure, the maximum (about  $3 \text{ K day}^{-1}$ ) cumulus heating occurs at the 400 mb level in the northern tropics, and the area of strong heating extends to the midlatitudes of the northern (summer) Hemisphere. As discussed in Chapter 2 and Chapter 3, the maximum cumulus heating in tropics is interpreted by the large-scale compensation heating corresponding to the strong deep convection. By comparison of (a) and (b) in Fig. 5.5, we see that the two simulations have generated very similar cumulus heating profiles. This indicates again that the cumulus effects generated by the simplified cumulus parameterization agree very well with those produced by the original A-S parameterization.

With the comparisons of model cumulus clouds and their effects from two simulations, we found that the simplified linear version can basically capture all model cumulus features generated by the parameterization with the exponential mass flux profile, e.g., they produced very similar cumulus cloud patterns and types; very similar cumulus precipitation magnitudes and distributions; and almost the same cumulus heating profiles. Because the linear version reduces the cumulus cloud entrainment mass flux and slows the cloud dilution process, deep convection is favored in the linear version. With the inclusion of the cloud top entrainment, however, the model cumulus clouds and their properties from the simplified cumulus parameterization scheme agree well with the current A-S parameterization.

## Cumulus Heating Rate

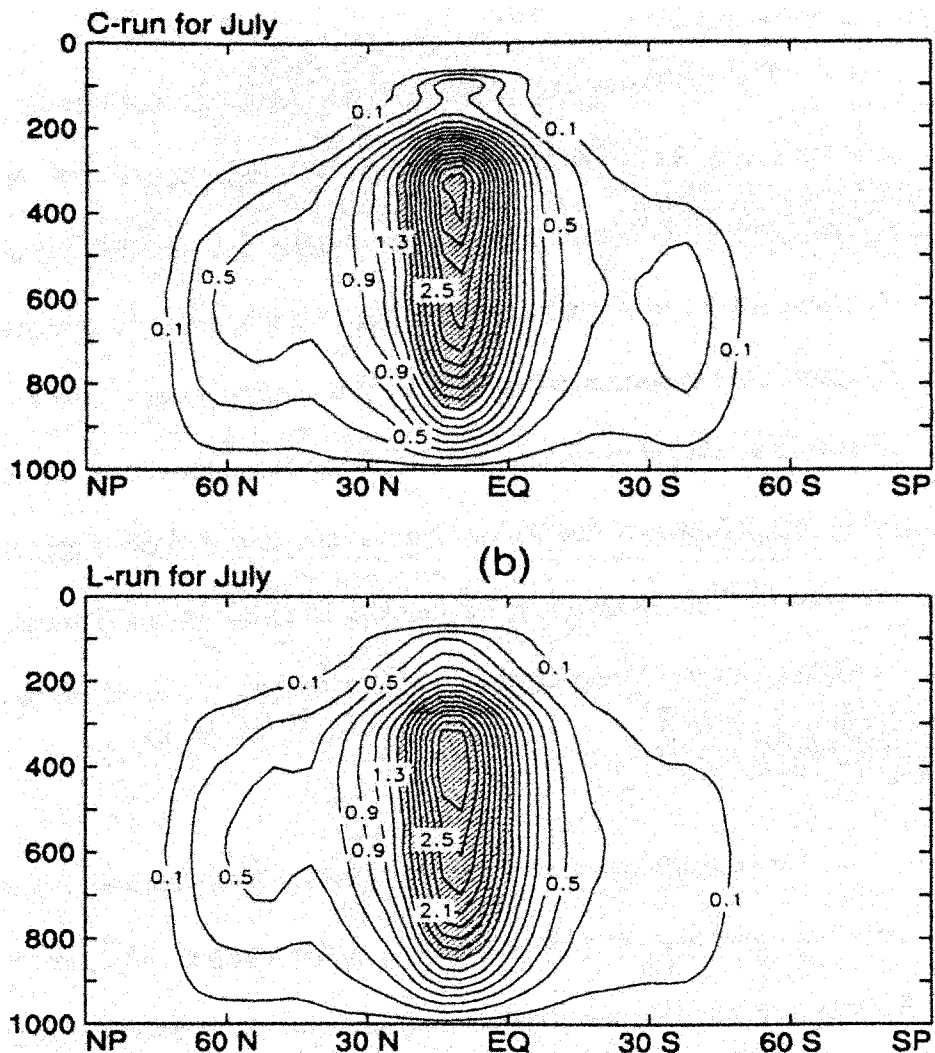


Fig. 5.5 Zonally averaged cumulus heating rates from C-run (a) and L-run (b) for July. Units are in  $\text{K day}^{-1}$ . Contour interval is  $0.2 \text{ K day}^{-1}$ . Values larger than  $1.5 \text{ K day}^{-1}$  are shaded.

### 5.4.2 The simulated climate

In the previous section we have shown that the model with the linear version of the cumulus parameterization can basically reproduce the same cumulus cloud features as the control simulation, even though the linear version is dramatically simple. We therefore

## July 500 mb Geopotential Height

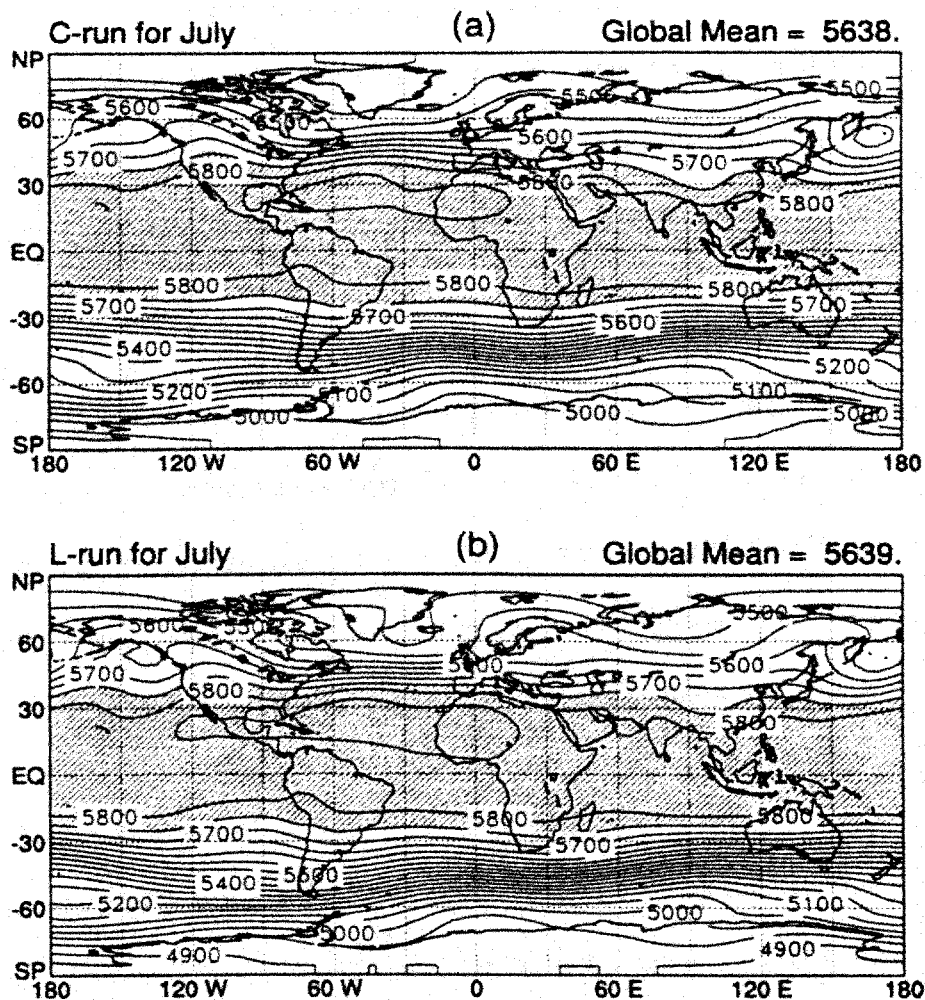


Fig. 5.6 July 500 mb geopotential height fields from the C-run and the L-run. Units are in meter and values larger than 5750 are shaded.

expect that the simplified parameterization can produce the simulated climate similar to that of the control simulation.

Fig. 5.6 shows the 500 mb geopotential height fields from the two simulations. The two simulations are very similar. The shapes of the shaded areas which represent the

pressure surface higher than 5750m from two version simulations also look close to identical. The observed July 500 mb geopotential height based on the European Center for Medium Range Weather Forecasts (ECMWF) data is shown in Fig. 3.6 (b). As shown in these figures, the basic patterns of the July 500 mb geopotential height field have been produced by the model, even though the simulated 500 mb surface is higher than the observed.

The July zonally averaged temperature fields and total precipitation fields simulated from the C-run, the L-run and observations are shown in Fig. 5.7 and Fig. 5.8. The two simulations give quite similar zonal mean temperature fields. There is little significant difference between two temperature plots. The temperature patterns of the simulation results have good agreement with the observations.

For the precipitation maps in Fig. 5.8, the L-run produced smaller precipitation maxima over active convection regions than the C-run. The global mean for the L-run is also slightly less than that in the C-run. The reason is that the L-run generates less deep convection than the C-run. The reduced cumulus precipitation maxima in the L-run contributes to the weak total precipitation rate. The precipitation patterns from the two simulations, however, are quite close. When the simulations are compared with observations, we find that the model reproduces the major precipitation regions. The January simulation results give similar conclusions.

The July zonally averaged specific humidity from the C-run and the L-run are shown in Fig. 5.9. As seen in the figure, the two simulations produce quite similar specific humidity distributions, with maxima near the surface in the northern tropics. The specific

# Temperature

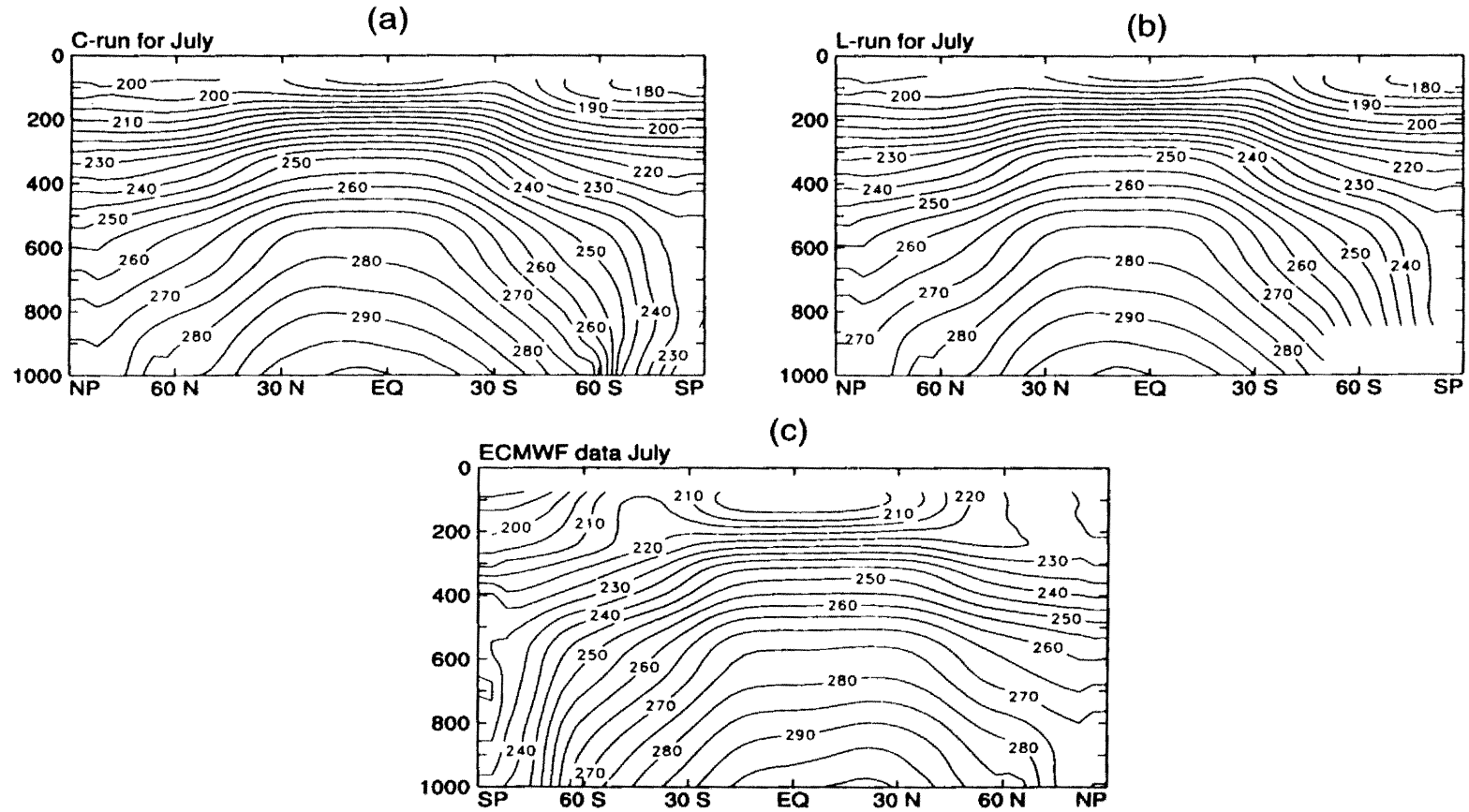


Fig. 5.7 Zonally averaged temperature distributions from the control run (a); the linear version run (b); and the ECMWF analysis (c). Units are in degree K and contour intervals are 5 K.

## July Total Precipitation

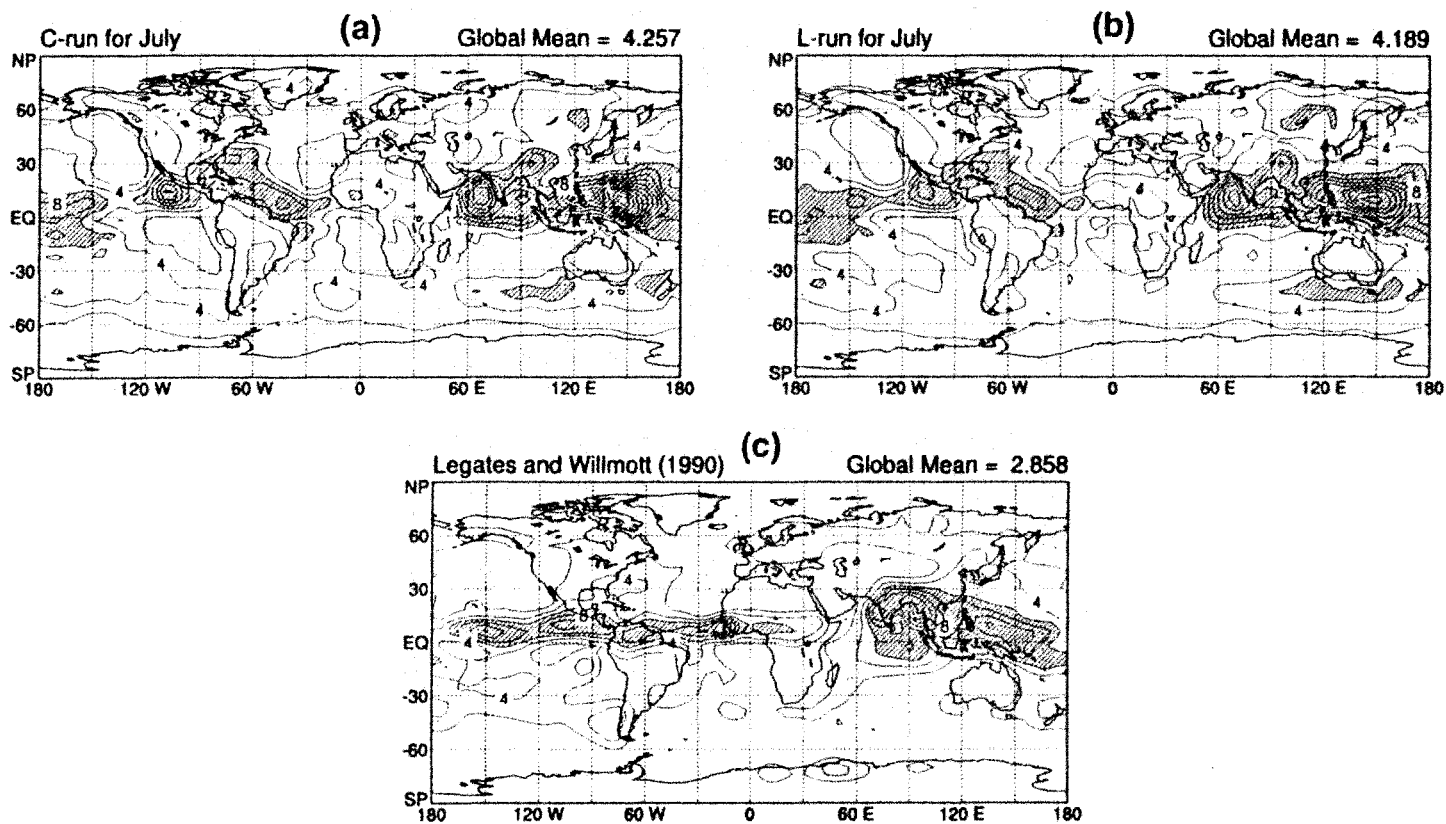


Fig. 5.8 July total precipitation fields from the C-run (a); the L-run (b); and Legates and Willmott (1990). Units are in  $\text{mm day}^{-1}$ . Contour intervals are  $2 \text{ mm day}^{-1}$ . Values larger than  $6 \text{ mm day}^{-1}$  are shaded.

## Specific Humidity

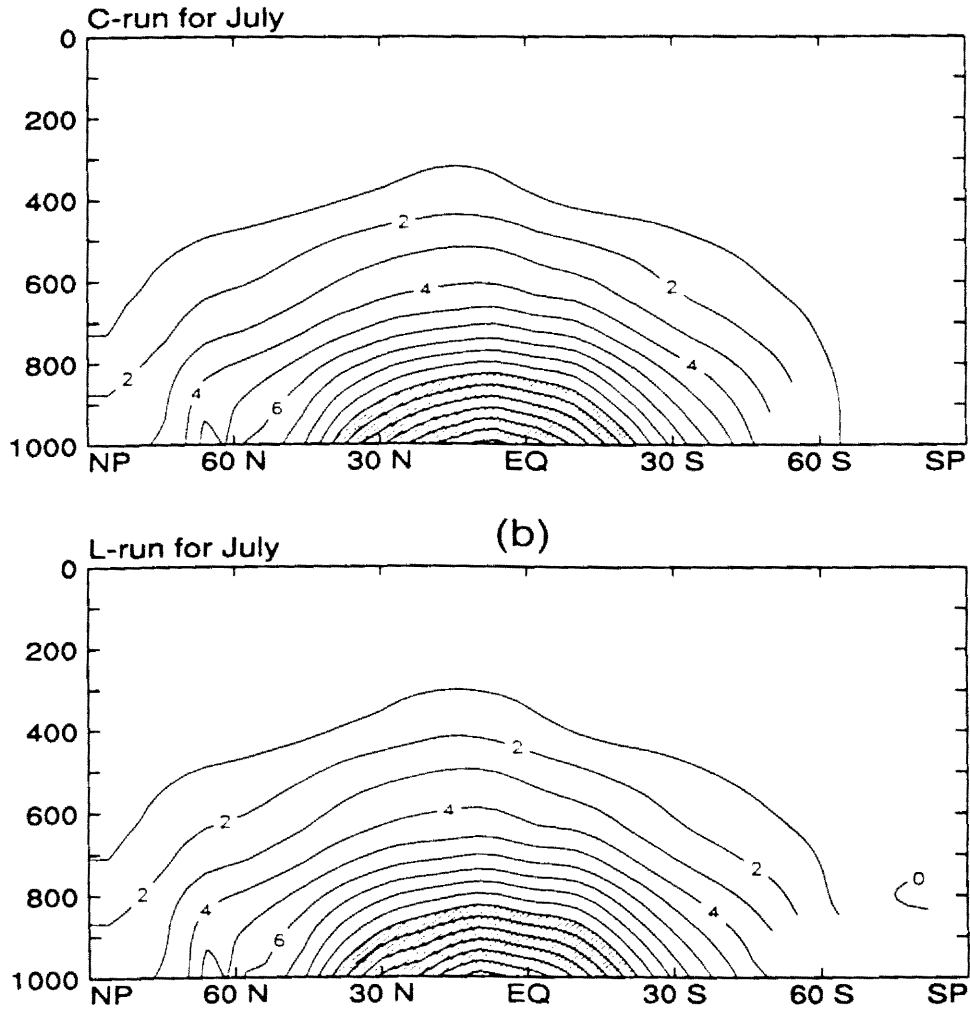


Fig. 5.9 Zonally averaged specific humidity from the C-run and the L-run. Units are in  $\text{g kg}^{-1}$ . Contour intervals are in  $1 \text{ g kg}^{-1}$  and values larger  $10 \text{ g kg}^{-1}$  are shaded.

humidity decreases with height and the summer hemisphere has more moisture than the winter hemisphere. The shaded areas represent specific humidity larger than  $10 \text{ g kg}^{-1}$ . It is seen that there is no significant difference between two shaded areas.

The mean meridional circulations from the C-run and the L-run, shown in Fig. 5.10,

are quite similar. Both the direct Hadley circulation and the indirect Ferrel circulation are very similar in the two runs. By comparing the model results with the ECMWF data, we see that the mean meridional circulations simulated by the model are stronger than observed. This is probably caused by the excessive penetrative convection in the tropics, accompanied by strong cumulus precipitation and related latent heat release.

In general, the two simulations produce very similar 500 mb circulation patterns, atmospheric temperature fields, and the global precipitation patterns. The atmospheric specific humidity distributions and mean meridional circulations from two simulations are also quite similar. In summary, the linear version of the cumulus parameterization with the inclusion of the cloud top entrainment, although relatively simple, can produce the same simulated climate as the current A-S parameterization. This allows us to include more physics in the parameterization without increasing its complexity.

#### 5.4.3 Radiation effects of the linear version cumulus parameterization

Deep cumulus convection often produces optically thick anvil clouds which modify the radiation fields. The radiative effects, meanwhile, play important roles in the generation of cumulus convection. The interactions between moist convection and the radiation are an intricate problem. In this section, we analyze the effects of the simplified cumulus parameterization on the radiation fields.

Fig. 5.11 shows the zonally averaged planetary albedo distributions from the two simulations and the Earth Radiation Budget Experiment (ERBE) data set. Because the planetary albedo,  $\alpha$ , strongly depends on the surface albedo, cloud amount, cloud types, and cloud microphysical properties, it is difficult to accurately simulate the geographical

## Mean Meridional Circulation

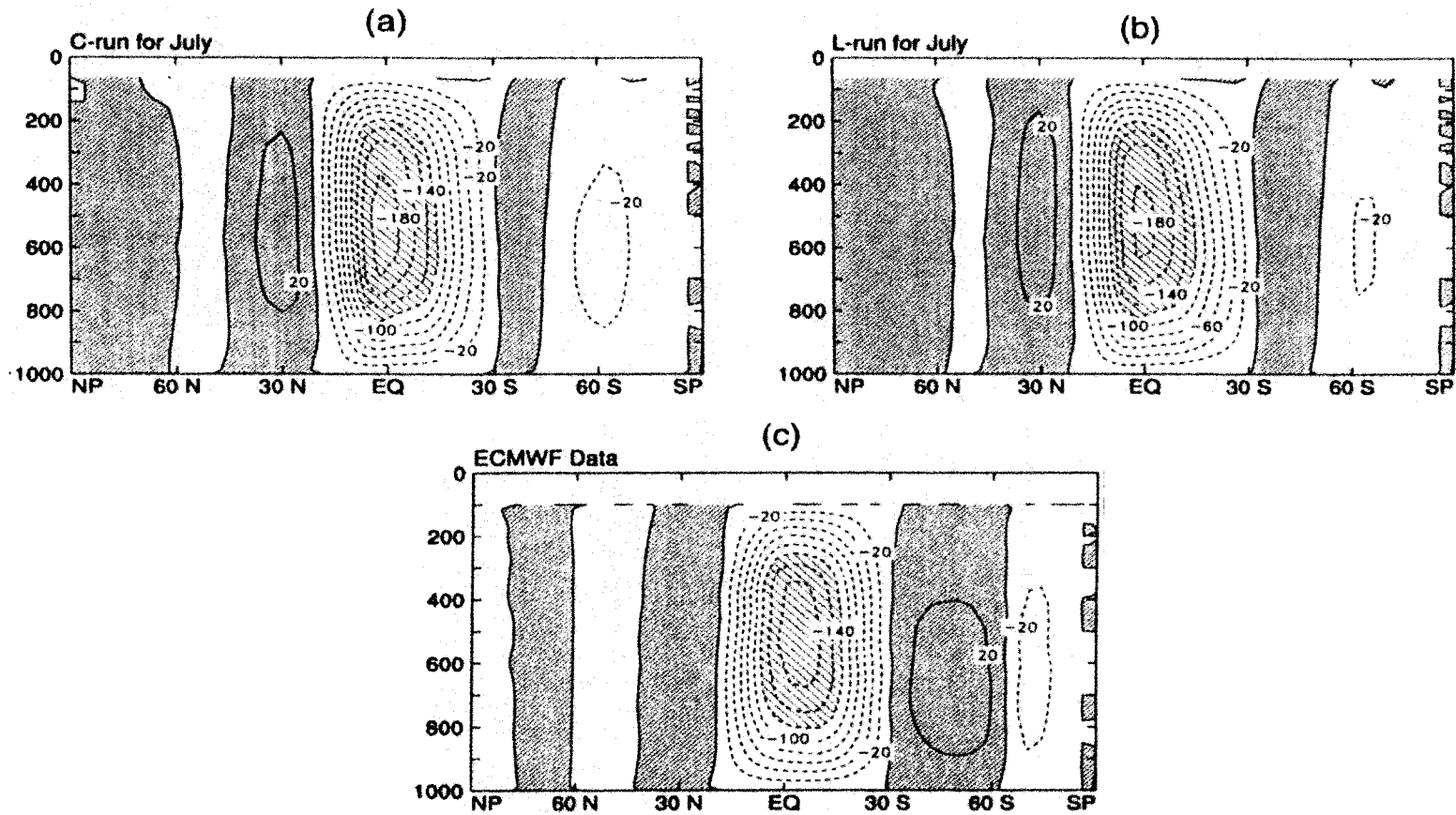


Fig. 5.10 Zonally averaged July mean meridional circulation from the C-run (a); the L-run (b) and observations (c). Units are in  $10^9 \text{ kg s}^{-1}$ . The control intervals are  $20 \times 10^9 \text{ kg s}^{-1}$ . Positive values are heavy shaded and values less than  $-120 \times 10^9$  are light shaded.

distribution of  $\alpha$  in a GCM. From Fig. 5.11, the model generated basically similar zonally averaged  $\alpha$  distributions with the observations, e.g., lower values over subtropical clear sky regions and larger values in high latitudes. It is also seen that the model produced a larger than observed planetary albedo in the tropics. This probably is caused by the excessive deep convection produced by the model in this region. In mid-latitudes, the planetary albedo is under-estimated by the model. The two curves from the model simulations are very close. This is consistent with the previous analysis.

Fig. 5.12 shows maps of the absorbed solar radiation from the C-run, the L-run and the ERBE data. The C-run and the L-run generate quite similar absorbed solar radiation patterns, e.g., the maxima in the subtropical high regions over both the Pacific ocean and the Atlantic ocean in the Northern Hemisphere. It is also seen that strong convection

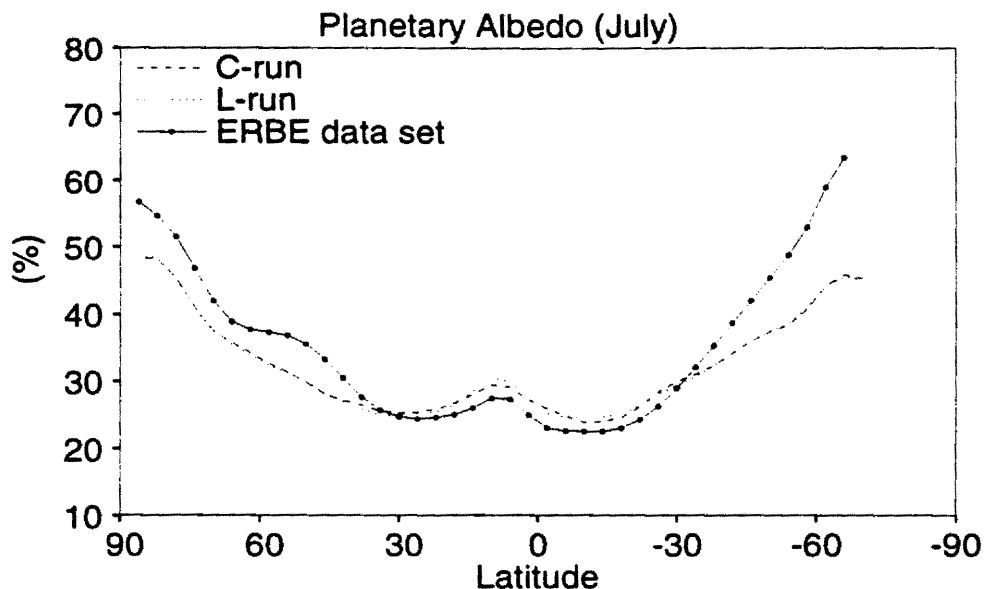


Fig. 5.11 Zonally averaged distributions of planetary albedo simulated from control run and linear version, and derived from the ERBE data set for July. Unit is%.

## Absorbed Solar Radiation

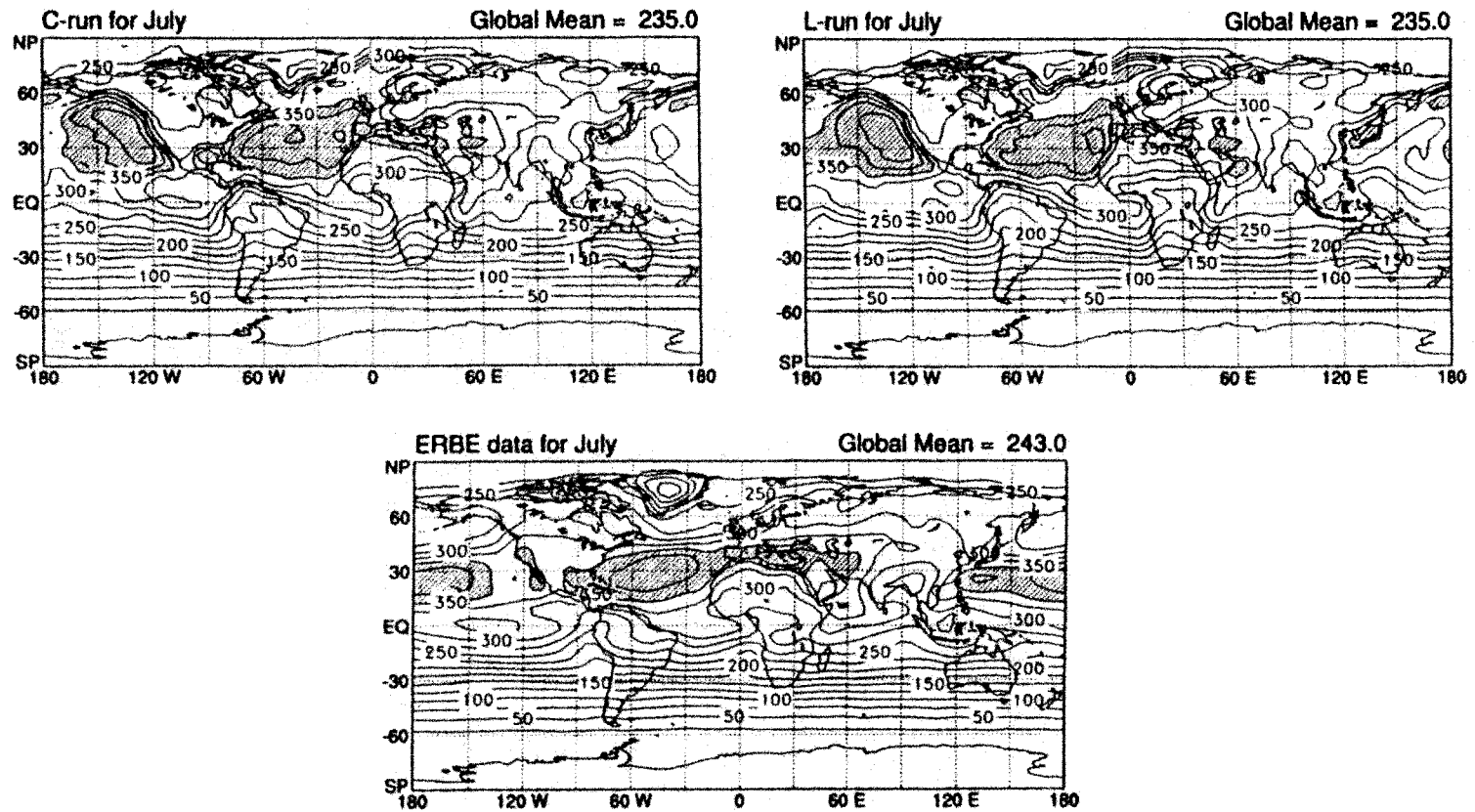


Fig. 5.12 July absorbed solar radiation for the C-run; the L-run; and the ERBE data set. Units are in  $W m^{-1}$ . Contour intervals are  $15 W m^{-1}$ . Values larger than  $265 W m^{-1}$  are shaded.

areas over the India monsoon region, the Western Pacific convective region, and the ITCZ belts correspond to relatively weak absorbed solar radiation, because more solar radiation is reflected by the upper stratiform clouds which are associated with deep convection. The global mean values from the control simulation and the linear version simulation are very close. This again demonstrates that the simplified cumulus parameterization produces the same cloud patterns, cloud amount and cloud distributions as the original A-S parameterization.

When we compare the model output with the ERBE data, the model absorbs less solar radiation than observed. This suggests that the model generates too many or excessively bright clouds. We have mentioned earlier that the model generates unrealistic strong cumulus precipitation. The anvil clouds related to deep convection might help to explain the low absorbed solar radiation in the model.

The outgoing long-wave radiation (OLR) patterns from the C-run, the L-run and the ERBE data set are shown in Fig. 5.13. Again, we obtained very similar OLR distributions and amounts from the two model simulations. The simulated patterns are quite similar to those observed, e.g., the maxima in the subtropical highs and minima over strong convection regions. The global means of OLR from the runs are smaller than observed. This again suggests that the model generates more high level clouds than the real atmosphere.

## **5.5 The summary of the L-run results**

As mentioned in Chapter 1, an important weak point in the A-S parameterization is

## Outgoing Long-Wave Radiation

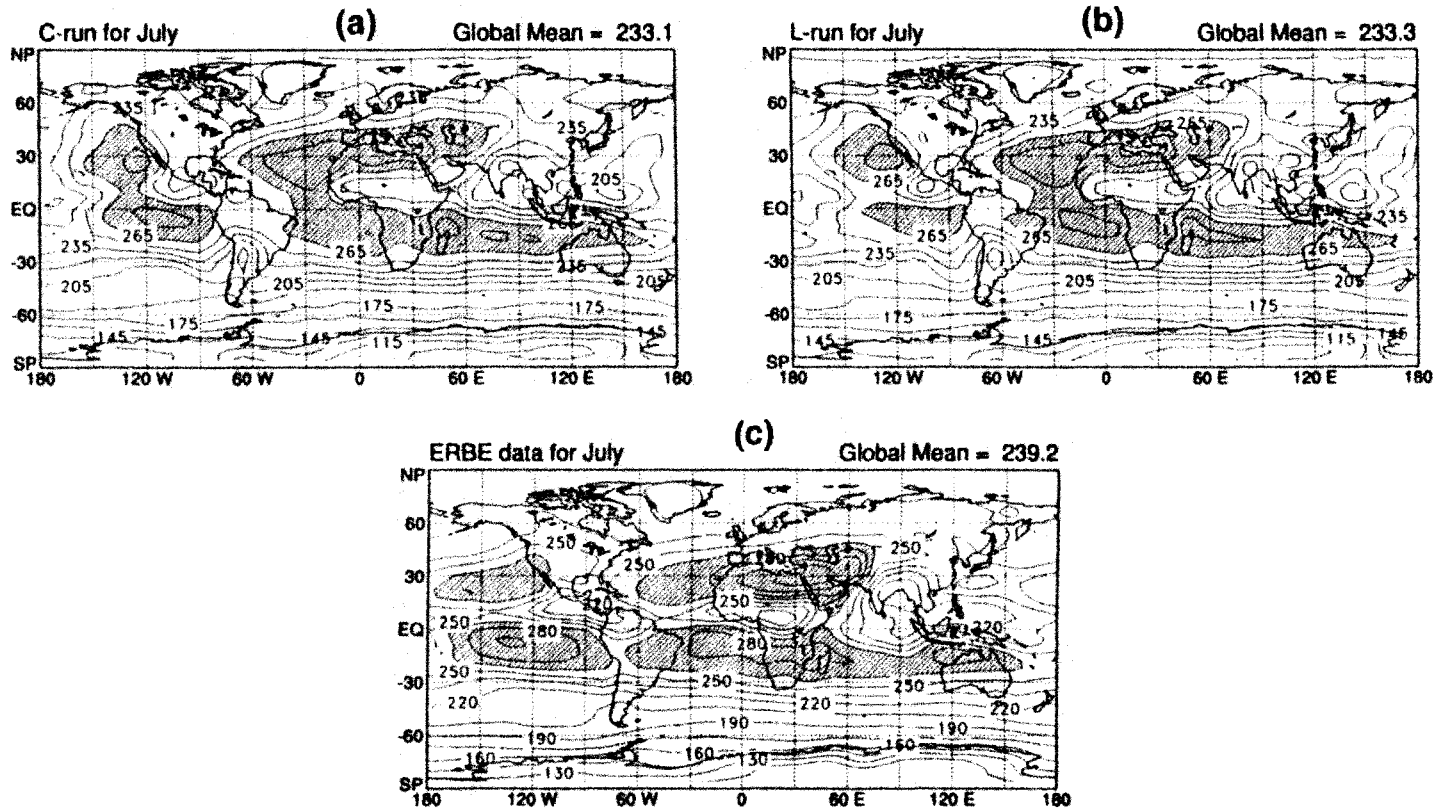


Fig. 5.13 Outgoing long-wave radiation from the control run, the linear version run and the ERBE data. Units are in  $\text{W m}^{-2}$  and values larger than 265  $\text{W m}^{-2}$  are shaded. Contour intervals are 15  $\text{W m}^{-2}$ .

its assumption that all cumulus clouds originate from the PBL. Observational and modeling studies have indicated that it is necessary to include cumulus clouds starting from the free atmosphere. Because the complexity of the A-S parameterization has already made it difficult to implement in GCMs, simplifying the A-S parameterization has been the first step towards adding more physics to it.

Starting from the Chapter 4, we introduced the linear mass flux profile assumption following Moorthi and Suarez (1992) to replace the exponential mass flux profile. The calculations of the cumulus cloud properties are highly simplified under this condition. With the linear mass flux profile, the entrainment parameter  $\lambda$  can be calculated by using an explicit approach which is developed in section 4.3, and the virtual temperature effect is included. This is another major saving of computational expense since the  $\lambda$  calculation was iterative in the original A-S cloud model, and this iteration is a very time consuming process. In order to reduce the differences between the linear and exponential mass flux profile, we added the cloud-top entrainment into the parameterization following Cheng and Arakawa (1992). The ice phase was included, we then developed new cloud existence test criteria. In short, a completely new cloud model has been constructed. The new cloud model not only includes all of the physical processes which are considered in the old model, but also has a linear mass flux profile and include cloud-top entrainment. Importantly, the new cloud model is extremely simple.

The new parameterization has been implemented in the CSU GCM. Some simulation results from the C-run and L-run were presented and compared. We found that the L-run can capture all cloud features and effects obtained by the C-run. The two simulations

generate quite similar cloud types, cloud amounts, cloud distributions and cumulus precipitation. The cloud radiative fields and simulated climate from two simulations are also close to identical. Generally, there are no significant differences between the C-run and the L-run. Since the cumulus parameterization has been dramatically simplified with the linear mass flux profile, it becomes possible to generalize the parameterization to have multiple cloud bases without excessive complexity. The generalized parameterization is presented in the next Chapter.

## **Chapter 6**

# **A Cumulus Parameterization with Multiple Cloud Base Levels**

In the preceding two Chapters, we have developed a simplified cumulus parameterization in which a linear mass flux profile is used to replace the original exponential mass flux profile of the A-S parameterization. A new explicit way to determine the entrainment parameter  $\lambda$  with the consideration of virtual temperature effects has also been formulated, and cloud top entrainment has been included.

In this Chapter, we generalize the parameterization to include cumulus clouds originating from the free atmosphere, and implement the new parameterization in the CSU GCM. The generalized cumulus parameterization with multiple cloud-base levels is introduced in the first section of the Chapter. The effects of the new cumulus parameterization on the simulated patterns of convection are analyzed in the second section. Next, the effects of the new parameterization on the large-scale circulation are presented and discussed. Some individual locations with strong moist convection starting from the free

atmosphere are singled out for further discussion in section 6.4. A discussion of the simulated radiation budget is given in the last section of the Chapter.

## **6.1 A cumulus parameterization with multiple cloud-base levels**

Observational and modeling studies have suggested that moist convection can and does, in reality, originate above the boundary layer in some cases. Cumulus clouds starting from the free atmosphere may have important effects on the global and local climate. It is important to develop a more realistic cumulus parameterization for these alto-cumulus clouds, as indicated by Randall et al. (1989). Based on the modified A-S parameterization, a generalized cumulus parameterization with multiple cloud-base levels has been developed and is described below.

The cloud model for the generalized cumulus parameterization is based on the cloud model of the single-cloud-base parameterization, which has been discussed in Chapters 4 and 5. When cumulus clouds originating from the free atmosphere are included, the number of potential cloud types in the model increases dramatically. The cloud model must be subjected to many changes when cloud base levels become a new “cloud type” index.

### **6.1.1 Conditionally unstable layers**

In the cloud model of the original A-S parameterization, cumulus convection is permitted if the atmosphere is conditionally unstable. When  $\bar{T}$ ,  $\bar{q}$  and  $\bar{q}^*$  are defined at level  $k$ , equation (4.42) can be written as

$$(h_c)_k = \bar{h}_k^* - \frac{(1 + \gamma) \delta \bar{T}_k (\bar{q}_k^* - \bar{q}_k)}{\frac{1}{c_p} + \frac{\delta \bar{T}_k \gamma}{L}} , \quad (6.1)$$

where  $(h_c)_k$  denotes moist static energy at cloud top. If the moist static energy of the PBL is denoted by  $h_B$ , the condition that the atmosphere be conditionally unstable is

$$h_B > (h_c)_k . \quad (6.2)$$

Below we generalize this cloud base condition. Eq. (6.2) insures that the cloud work function is positive for a cloud starting at the PBL and penetrating to layer  $k$ , which is the layer where  $\bar{T}$  and  $\bar{q}$  are defined. In a GCM, the feedbacks of cumulus convection on its environment are exerted only if (6.2) is satisfied.

If we remove the constraint that cumulus clouds can only start from the PBL, so that convection is allowed to start from any layer of the model, the condition (6.2) can be generalized to

$$h_n > (h_c)_k , \quad (6.3)$$

where  $n$  is the even level index of the model below level  $k$ . If  $k_B$  is used for the PBL layer index, we have  $k < n \leq k_B$  , for a cumulus cloud with cloud base at level  $n$  and cloud-top at level  $k$ . It can be seen that the cloud base level becomes a second cloud type index. As discussed in the previous chapters, the number of potential cloud types increases remarkably when moist convection is allowed to start from the free atmosphere. The calculations required to determine the cloud properties and the feedbacks of the clouds on the environ-

ment also increase dramatically. This is part of the motivation to simplify the current cumulus parameterization in the previous Chapters.

### 6.1.2 Entrainment rate and cloud properties

We have seen that the role of the cloud base level as a new cloud type index is a key attribute of the cloud model with multiple cloud base levels. To determine the entrainment parameter characterizing a subensemble,  $\lambda$ , we can still use the approach of the linear mass flux by adding the cloud base index. When multiple cloud base levels are allowed in the cloud model, (4.44) can be changed to

$$\lambda = \frac{h''_c - C_{1n}}{C_2 + \Delta z h''_c} \quad (6.4)$$

Here  $C_{1n}$  represents atmospheric moist static energy at the even level  $n$ , which serves as the cloud base property of cumulus clouds with cloud top at level  $k$  and cloud base at level  $n$ . In this case, the entrainment rate,  $\lambda$ , has two subscripts for each grid column of the model. The first is the cloud base level index and the other is the cloud top level index. In section 4.3, the coefficient  $C_2$  is determined by (4.45). When  $C_1$  is changed to  $C_{1n}$  in the multiple cloud base cumulus parameterization, (4.45) can be changed to

$$C_{2n} = \frac{h''_c (1 + \lambda \Delta z) - C_{1n}}{\lambda} \quad (6.5)$$

Therefore, one more index, the cloud base level, is added to coefficient  $C_2$ , and  $C_2$  is thus changed to  $C_{2n}$ . If we use  $\lambda_{n,k}$  to represent the cumulus entrainment parameter, where  $n$  and  $k$  are used as cloud base and cloud top indexes, the cumulus entrainment parameter in the generalized parameterization is obtained by

$$\lambda_{n,k} = \frac{h''_c - C_{1n}}{C_{2n} + \Delta z h''_c} \quad (6.6)$$

After the cumulus cloud entrainment rates have been determined, we can find the in-cloud properties, such as cloud temperature, moisture, precipitation rate and cloud ice, by using approaches similar to those derived in sections 4.2.2, 4.2.3, 5.2.1, and 5.2.2. These calculations will apply to different cloud types characterized by different cloud bases. For example, to calculate the in-cloud moist static energy, we need to change (4.11) to

$$(h_{cn})_{k-\frac{1}{2}} = \frac{\left[ 1 + \lambda_n \left( z_{k+\frac{1}{2}} - z_{Bn} \right) \right] (h_{cn})_{k+\frac{1}{2}} + \lambda_n \bar{h}_k \Delta z_k}{1 + \lambda_n \left( z_{k-\frac{1}{2}} - z_{Bn} \right)} \quad , \quad (6.7)$$

where the subscript  $n$  is still used as the cloud base index and  $z_{Bn}$  is cloud base height for cumulus clouds with cloud base at model level  $n$ . Similar changes apply to the cloud moisture budget.

### 6.1.3 Cloud work function and cumulus kinetic energy

In the linear version of the A-S parameterization, the normalized mass flux,  $\eta(\lambda)$ , at each level is calculated by (4.7) for an individual cloud. When the cloud base index,  $n$ , is added to  $\lambda$ , the corresponded normalized mass flux can be denoted by  $\eta_n$ . Following (5.27), the cloud work function in the generalized parameterization can be calculated by

$$F_{cn}(\lambda_n) = \sum_{k=1}^N \left[ \frac{1}{2} \cdot g \left[ \left( \frac{T_{v,c,n} - \bar{T}_v}{\bar{T}_v} \eta_n \right)_{k-\frac{1}{2}} + \left( \frac{T_{v,c,n} - \bar{T}_v}{\bar{T}_v} \eta_n \right)_{k+\frac{1}{2}} \right] \right] . \quad (6.8)$$

After the cloud work function has been calculated for each cloud type, the cumulus kinetic energy for each cloud type,  $K_n$ , can be predicted following Randall and Pan (1993) by

$$\frac{\partial K_n}{\partial t} = \sqrt{\frac{K_n}{\alpha}} \cdot F_{cn} - \frac{K_n}{\tau_d} , \quad (6.9)$$

where  $\alpha$  is a constant and  $\tau_d$  is the cumulus dissipation time scale, as discussed in section 3.4.2. In our model simulations, a single  $\tau_d$  is used for all cloud types. If we assume that a single  $\alpha$  can be used for all clouds, the cloud base mass flux at the next time step,  $M_{Bn}$ , can be obtained by

$$M_{Bn} = \sqrt{\frac{K_n}{\alpha}} . \quad (6.10)$$

Because all cumulus clouds in the original A-S parameterization are assumed to start from the PBL, there is one cloud base mass flux at each grid point for each time step in the old cloud model. When the A-S cumulus parameterization is generalized, (6.10) gives the cloud base mass flux at every possible cloud base level.

The cloud existence tests for the linear version of the A-S parameterization have been discussed in section 5.3. We apply all tests discussed in section 5.3 to every cloud type, and all cumulus clouds are required to satisfy these tests in the multiple cloud base

(MCB) parameterization. With the increase of cloud types when multiple cloud bases are considered, the cumulus feedback on the environment is also generated to include the effects of all cloud types.

Our GCM simulation tests with different cumulus parameterizations, such as the standard A-S version, the linear mass flux profile version, and the multiple cloud base version, has been carried out on the Cray-90 in the National Energy Research Supercomputer Center located in Livermore, California. For the 4° latitude by 5° longitude horizontal grid and 17-level version of the CSU GCM, the standard version of the A-S cumulus parameterization uses 0.4476 cpu second for one physical time step (one hour), and the cpu time used by the whole model is 9.7735 seconds. When the linear mass flux profile version is used to replace the original A-S parameterization, the cpu time used by the cumulus parameterization decreases to 0.3821 second for one physical time step. Then, about 14.6% of the cpu time used by cumulus parameterization is saved by the simplifications of the linear version cumulus parameterization and this can probably be further improved. For one time step simulation with the multiple cloud base version, the cumulus parameterization uses 0.6034 second of cpu time. The cpu time used by cumulus parameterization thus increases, when the number of cloud types increases. The memory used by the model, as expected, is 19.28 megawords for the C-run and the L-run, and 22.15 megawords for the MCB-run. The MCB parameterization, thus, needs more memory, as expected.

## **6.2 Simulation experiments with the multiple cloud base cumulus parameterization**

The generalized cumulus parameterization has been implemented in the CSU

GCM. In our numerical experiments, we used the same initial conditions as in the C-run and the L-run discussed in Chapter 5. Starting from the 1st of May, the CSU GCM was run three months to the end of July and the results of July are analyzed in following sections. The simulation with the multiple cloud base version of the cumulus parameterization is called the “MCB simulation” or “MCB run” in the following discussion. The changes in the simulated cumulus clouds and the effects of the generalized cumulus parameterization on the simulated climate are presented and discussed in this section. The change of soundings for individual regions where active altocumulus convection is generated, such as the India monsoon region, the SPCZ, the Sahara desert, etc., will be further analyzed in section 6.4.

### 6.2.1 Cumulus clouds from the generalized parameterization

In the preceding sections, we have indicated that the number of possible cloud types in the model will increase dramatically when cumulus clouds are allowed to start from the free atmosphere. Cumulus populations produced by the generalized multiple cloud base parameterization are presented and compared with those of the control simulation in order to study how the MCB parameterization modify the original A-S parameterization.

Fig. 6.1 shows maps of July cumulus incidence of all cloud types from the control simulation (C-run) (a), the MCB simulation (b), and their difference (c). The global mean values from the C-run (0.2175) and the MCB-run (0.2439) indicate that the cumulus incidence slightly increases in the MCB simulation. An interpretation is that there are many more potential cloud types in the generalized cumulus parameterization with multiple

## Cumulus Incidence

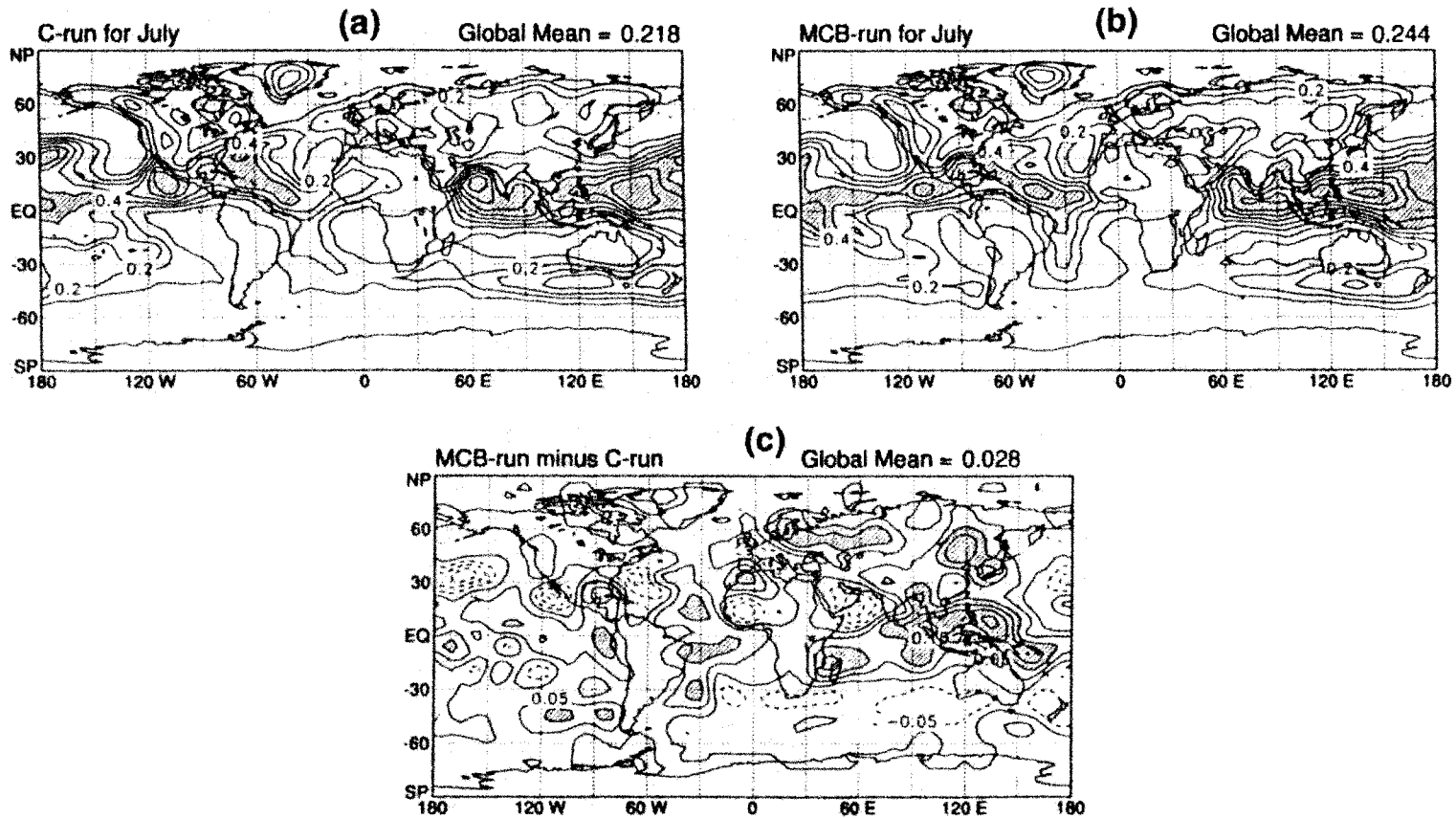
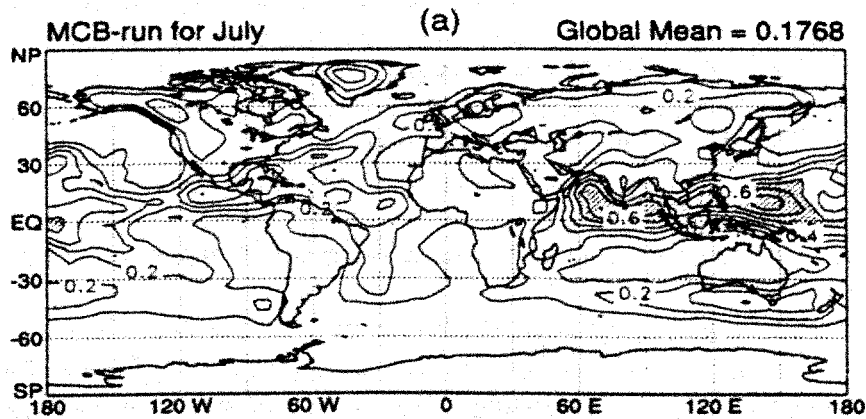


Fig. 6.1 July cumulus incidence from control run (a), multiple cloud base run (b) and their difference (c). Values larger than 0.5 are shaded in (a), (b); values larger than 0.1 are shaded in (c). Contour intervals are 0.1 in (a) and (b), and 0.05 in (c).

cloud bases. The cumulus incidence distributions from two simulations look quite similar, e.g., the maximum cumulus incidence regions occur over the Indian and Southern Asian monsoon regions, ITCZ branches of the Pacific Ocean, and the Western Pacific. Map (c) of Fig. 6.1 shows the cumulus incidence difference between the MCB simulation and the control simulation. The apparent increases of cumulus incidence in the MCB-run are found over active convection areas, such as the Western Pacific, the Bay of Bengal, as well as the North Eastern China and Japan, the European continent. The areas of large increases in map (c) might be indications of active altocumulus convection regions. It is also seen in map (c) that the cumulus incidence over the Pacific subtropical high region and the Eastern Pacific along the central American coast at about 20°N decrease. The results from the MCB and control simulations for some individual regions will be further analyzed and compared in the next section.

In order to investigate cumulus clouds which originate from the free atmosphere, we separate cumulus incidence for clouds starting in and above PBL in the MCB simulation. In Fig. 6.2, the upper map shows cumulus incidence of clouds starting from the PBL, and the lower map shows the difference between the total cumulus incidence and the incidence of clouds starting from the PBL. It can be seen that the basic distribution patterns of the upper map in Fig. 6.2 and the total cumulus incidence (shown by map (b) in Fig. 6.1), as well as the cumulus incidence from the control simulation (shown by map (a) in Fig. 6.1) are very similar. This similarity implies that cumulus clouds originating from the PBL dominate the global cumulus cloud population, as expected. The difference map in Fig. 6.2 gives an indication of where the model produces many cumulus clouds starting from the free atmosphere. Again, it can be seen that the large differences appear over the West-

## Cumulus Incidence for Clouds Starting at the PBL Top



## Difference between Total Cumulus Incidence and Map (a)

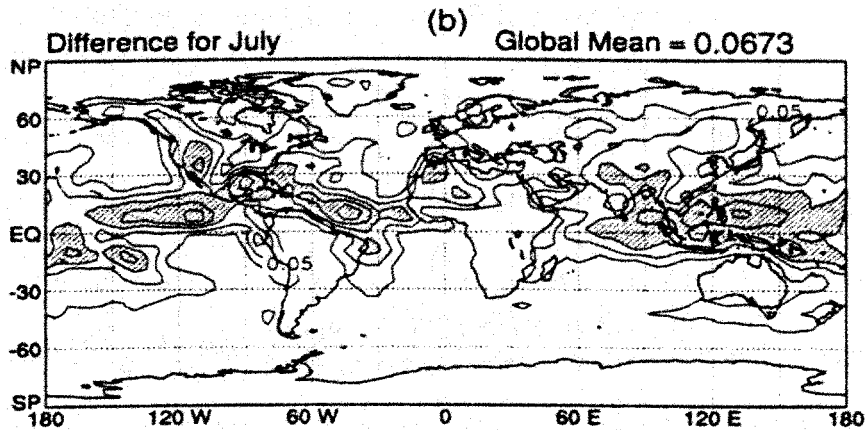


Fig. 6.2 July cumulus incidence from MCB simulation. The upper map shows incidence of cumulus clouds which only start from the PBL. The lower map shows the difference between the total cumulus incidence of MCB-run and the upper map. In (a), values larger than 0.5 are shaded and the contour interval is 0.1. In (b), values larger than 0.15 are shaded and the contour interval is 0.05.

ern Pacific, the Rocky Mountains, the Sahara Desert, and the eastern tropical Pacific. We present more detailed analyses of these regions later. The difference maps from both Fig. 6.1 and Fig. 6.2 indicate that many cumulus clouds with cloud bases at the free atmosphere in the mid-latitudes and other regions are produced in the MCB simulation. Obser-

vations suggest that altocumulus clouds often occur in frontal regions (Colman, 1983) and they are very important to the large-scale atmospheric circulation. This is the first time that this kind of convection has been parameterized completely in a GCM by a physically comprehensive cumulus parameterization.

### MSTADJ Incidence

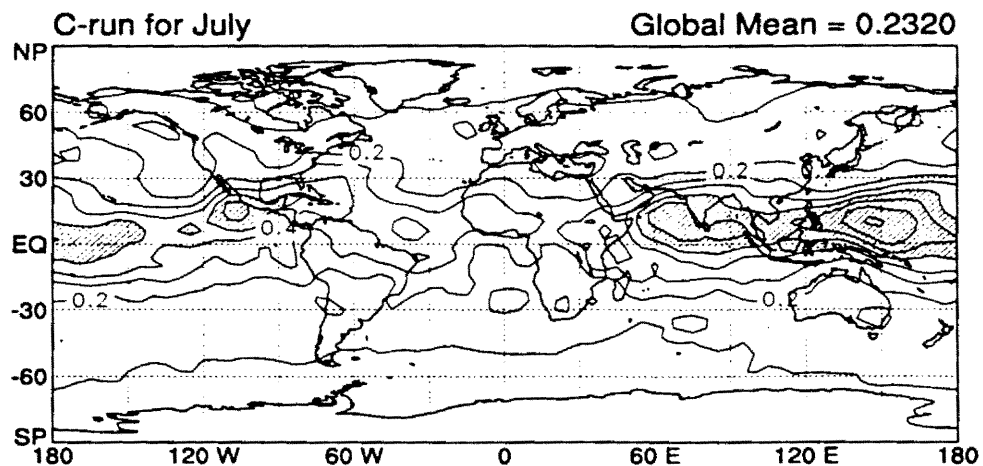


Fig. 6.3 July MSTADJ incidence for C-run. The contour interval is 0.05. Values larger than 0.4 are shaded.

As indicated in Chapter 3, in the control simulation the effects of cumulus convection starting in the free atmosphere are parameterized by using MSTADJ. The July MSTADJ incidence from the C-run is shown in Fig. 6.3. Comparing Fig. 6.3 with Fig. 6.2b, it can be seen that all maxima of MSTADJ incidence correspond to maxima of altocumulus incidence. On the other hand, in some regions, like the Rocky Mountains and the tropical Western Atlantic, there is large altocumulus incidence, but a relatively small MSTADJ incidence. This suggests that MSTADJ can not represent all altocumulus clouds and the MCB parameterization is needed to better parameterize cumulus convection starting in the

free atmosphere.

In order to analyze the cloud type distribution in more detail, a 10-day test run has been made starting from the end of July as a continuation of the MCB-simulation. In this test run, cloud numbers for all kinds of cloud types in the model and their corresponding cloud base mass fluxes have been accumulated. The average cloud numbers and cloud base mass flux per simulated hour, for all cloud types, are shown in Tables 6.1 and 6.2, respectively. Cumulus clouds starting at the PBL top dominate. Cumulus clouds originating from the free atmosphere, meanwhile, are also important. From Table 6.1, we see that many cumulus clouds have their bases in the free atmosphere.

Table 6.1 also shows that most cumulus clouds with high tops start from the PBL and other relatively low model levels. For example, most cumulus clouds with tops at levels 4 and 3 have bases at levels 17 and 16. There are many clouds with tops at level 3 and bases at level 4 or tops at level 4 and bases at level 5. We have found that these high-level shallow convective clouds are located in the Western Pacific, Southern Asia, the tropical Atlantic and the tropical Eastern Pacific. Except in Southern Asia, most of these high-level shallow convective clouds do not occur together with deep convective clouds. They might be cirro-cumulus. In Table 6.1, the cumulus clouds most actively simulated in our model are low-level shallow clouds with tops at levels 14 or 15 and bases at the PBL.

The MSTADJ which is used to replace altocumulus convection in the original A-S parameterization represents one-layer altocumulus clouds of this model. For example, clouds have bases at level  $k$  and tops at level  $k-1$ . In Table 6.1, most these one-layer clouds occur at high levels. In overall, these one-layer clouds are only a portion of total altocumu-

**Table 6.1: Average cumulus cloud incidence per simulated hour for various cloud types from the 10-day test run**

Base level														
4	--	--	--	--	--	--	--	--	--	--	--	--	--	27.3
5	--	--	--	--	--	--	--	--	--	--	--	--	37.7	14.0
6	--	--	--	--	--	--	--	--	--	--	--	24.0	10.1	4.16
7	--	--	--	--	--	--	--	--	--	--	6.96	4.57	2.13	1.53
8	--	--	--	--	--	--	--	--	--	3.51	1.27	0.62	0.70	0.88
9	--	--	--	--	--	--	--	--	3.34	0.53	0.91	0.63	0.61	0.56
10	--	--	--	--	--	--	--	2.31	0.34	0.55	0.43	0.31	0.23	0.32
11	--	--	--	--	--	--	0.81	0.53	0.57	0.43	0.22	0.13	0.07	0.08
12	--	--	--	--	--	0.16	1.58	3.14	1.53	0.67	0.31	0.21	0.22	0.11
13	--	--	--	--	0.07	1.63	3.13	3.29	1.41	0.86	0.58	0.28	0.16	0.16
14	--	--	--	0.13	1.99	4.20	2.88	2.47	1.77	1.18	0.68	0.71	0.43	0.25
15	--	--	0.4	6.55	12.9	14.4	15.7	14.5	11.4	9.65	6.52	6.92	6.65	6.28
16	--	1.91	21.2	39.6	38.8	45.8	48.7	43.4	35.2	26.8	23.8	26.6	25.9	23.2
17	2.55	125.7	106.5	80.1	73.1	81.4	97.5	88.6	67.3	43.4	30.2	28.5	27.9	22.1
Top Level	16	15	14	13	12	11	10	9	8	7	6	5	4	3

**Table 6.2: Average cloud base mass flux per simulated hour for various cloud types from the 10-day test run (Units are  $10^{-2}$  kg m<sup>-2</sup> hour<sup>-1</sup>)**

Base level															
4	--	--	--	--	--	--	--	--	--	--	--	--	--	--	1.40
5	--	--	--	--	--	--	--	--	--	--	--	--	--	1.92	0.72
6	--	--	--	--	--	--	--	--	--	--	--	1.22	0.52	0.24	
7	--	--	--	--	--	--	--	--	--	--	0.36	0.24	0.12	0.10	
8	--	--	--	--	--	--	--	--	--	0.18	0.06	0.04	0.04	0.10	
9	--	--	--	--	--	--	--	--	0.18	0.02	0.08	0.10	0.16	0.18	
10	--	--	--	--	--	--	--	0.12	0.02	0.06	0.06	0.12	0.10	0.28	
11	--	--	--	--	--	--	0.04	0.02	0.06	0.10	0.04	0.04	0.02	0.02	
12	--	--	--	--	--	.0	0.12	0.76	0.54	0.38	0.24	0.10	0.16	0.06	
13	--	--	--	--	.0	0.07	0.78	1.00	0.78	0.94	0.68	0.30	0.14	0.18	
14	--	--	--	.0	0.14	0.46	1.40	2.46	2.30	1.60	0.94	0.92	0.58	0.34	
15	--	--	0.02	0.6	3.40	4.16	14.8	17.6	16.2	15.8	10.5	11.8	11.8	11.6	
16	--	0.10	1.62	9.94	18.5	17.9	51.6	57.8	51.8	41.8	39.0	44.6	44.6	40.2	
17	0.14	10.7	21.4	29.2	35.4	23.5	68.4	75.8	67.2	49.2	36.6	37.6	39.8	32.2	
Top Level	16	15	14	13	12	11	10	9	8	7	6	5	4	3	

lus clouds. It is impossible to replace entire effects of altocumulus convection by MST-ADJ. Table 6.2 shows the average cloud base mass flux for various cloud types corresponding to Table 6.1. The magnitudes of the average cloud base mass flux depend on both cloud incidence and cloud types. Basically, the cloud base mass flux distribution is consistent with the cloud incidence distribution in Table 6.1. The one-layer altocumulus clouds contribute even less in Table 6.2. Again, this indicates that the MCB-parameterization is needed.

Table 6.2 also shows that altocumulus clouds with bases at level 16 and tops at levels 12 to 3 are very active. Since level 16 is just above the PBL, the many clouds starting at this level indicate that atmosphere immediately above the PBL is moist and unstable. It is interesting to further study the effects of the PBL on the generation of these altocumulus clouds.

### 6.2.2 Precipitation

One important criterion for judging the success of physical parameterizations in a GCM is how well precipitation patterns are simulated by the model. Total precipitation rates in the CSU GCM consists of the sum of large-scale precipitation and cumulus precipitation. We compare precipitation patterns from the control simulation, the MCB simulation, and observations in this section, in order to investigate modifications of model results by the MCB parameterization.

Fig. 6.4 shows July total precipitation patterns from C-run (a); MCB-run (b); observations (Legates and Willmott, 1990); and the MCB-run minus the C-run (d). The simulated global means are larger than that reported by Legates and Willmott, and the

## Total July Precipitation

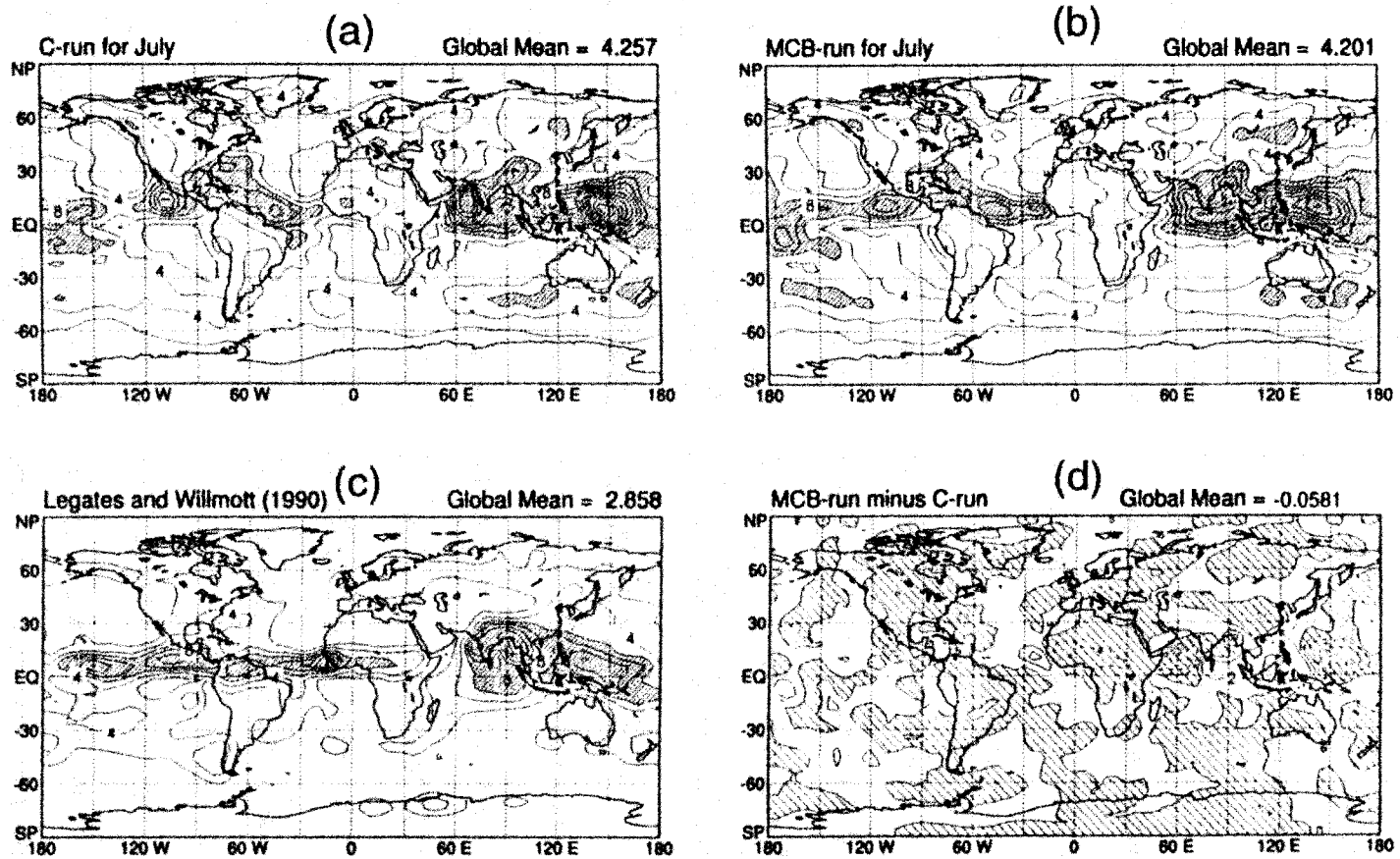


Fig. 6.4 Total July precipitation from control simulation (a); MCB simulation (b); Legates and Willmott (1990); and MCB-run minus C-run (d). Units are in  $\text{mm day}^{-1}$ . The contour interval is 2 and values larger than 6 are shaded in (a), (b), and (c); values less than zero are lightly shaded in (d).

MCB simulation produces a similar global mean ( $4.201 \text{ mm day}^{-1}$ ) to that of the C-run ( $4.257 \text{ mm day}^{-1}$ ). The main patterns of the precipitation geographical distributions, however, are in good agreement between model simulations and observations. In general, the model successfully produces precipitation maxima of the ITCZ branches over the Pacific and Atlantic oceans, the India monsoon region, the South Pacific Convergence Zone, the Central America, and the Western Pacific convective region. From these three precipitation maps, the over estimation of the precipitation in the control simulation over the Western Pacific convective region in the control simulation has apparently been improved in the MCB simulation. We will see that the improvement is due to the modification of the cumulus precipitation. The precipitation rate over central America is also improved in the MCB simulation, especially in the Eastern tropical Atlantic ocean in the Northern Hemisphere. The precipitation rate over tropical Africa is still under-estimated in the simulations, compared with the analyses of Legates and Willmott (1990), but the MCB run produces a better shape in overall. Panel (d) shows that the MCB simulation produces a smaller precipitation rate in most regions, especially in the Western Pacific and the Indian Ocean. In the tropical Atlantic and the tropical Eastern Pacific, however, the MCB simulation produces a larger precipitation rate. This makes the precipitation patterns produced by the simulation closer to observations.

The zonal mean precipitation distribution for July (b) is shown in Fig. 6.5. It is seen that the simulations produced larger precipitation rates over mid-latitudes and tropics, in both Hemispheres, compared with the analyses of Legates and Willmott. The MCB simulation produces slightly smaller precipitation rates over the northern tropics than the control simulation. We will show later that this is because the strong deep convection in

### Zonal Mean Precipitation of July

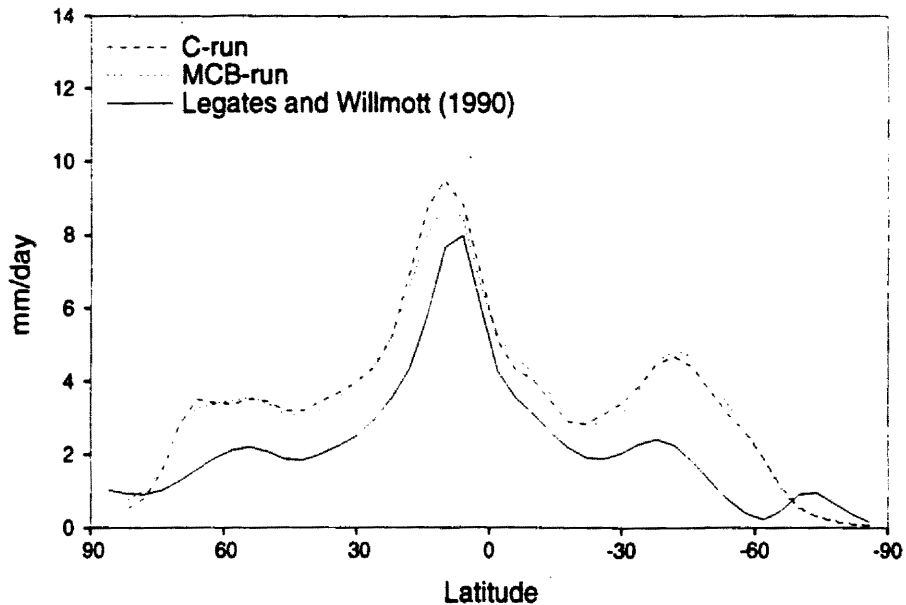


Fig. 6.5 Zonal mean total precipitation rates for July from the C-run, the MCB-run and observations. Unit is  $\text{mm day}^{-1}$ .

the Western Pacific Ocean in the control simulation is reduced by the MCB parameterization.

From Fig. 6.4, we have seen that the simulated total precipitation patterns are improved in the MCB run, e.g., the unrealistic strong precipitation rate over the Western Pacific is reduced in the MCB simulation. This can also be seen in Fig. 6.5. We now compare cumulus precipitation distributions from two runs and analyze contributions of the improvement.

Fig. 6.6 shows cumulus precipitation distributions from the MCB simulation (a) and cumulus precipitation differences between the MCB simulation and the control (b). As discussed in the previous section, cumulus incidence increases when the MCB parame-

## Cumulus Precipitation

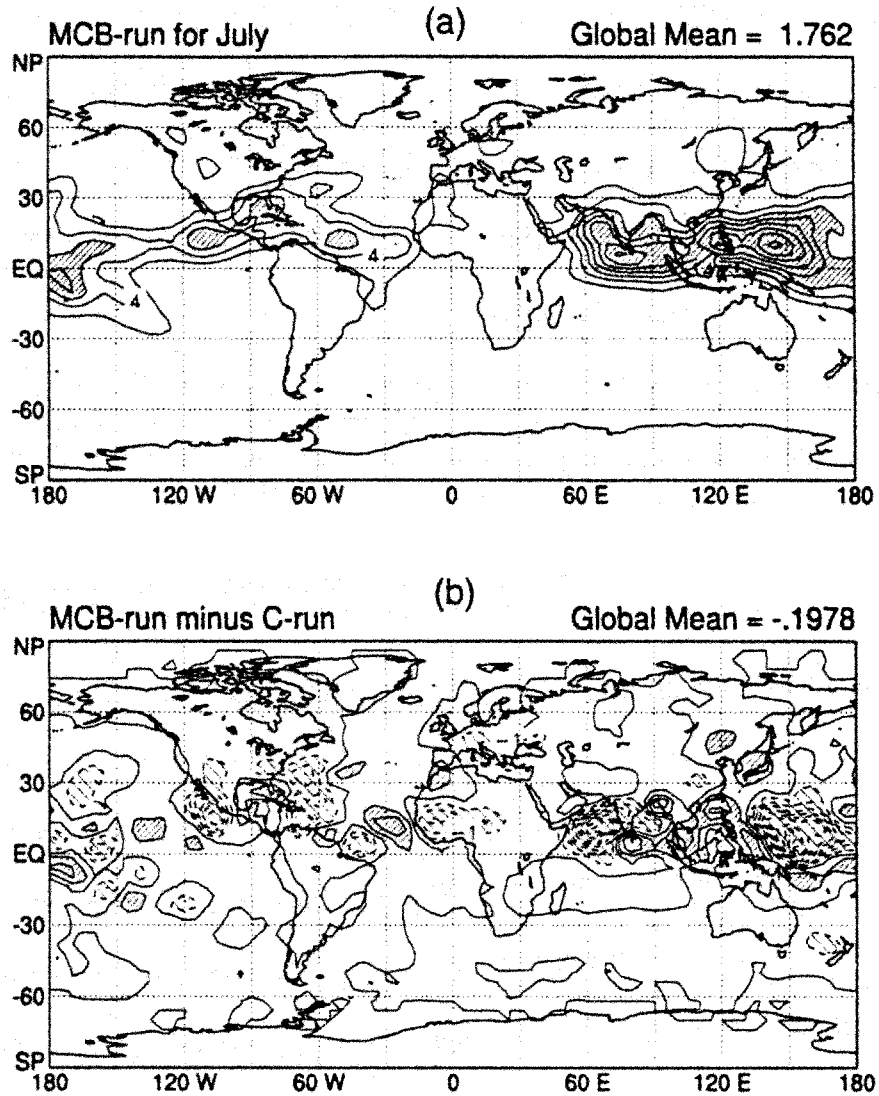


Fig. 6.6 July cumulus precipitation from MCB simulation (a), and the difference between MCB simulation and control simulation (b). Unit is  $\text{mm day}^{-1}$ . Values larger than  $6 \text{ mm day}^{-1}$  are shaded in map (a), and values larger than  $1 \text{ mm day}^{-1}$  are heavy shaded; smaller than  $-1 \text{ mm day}^{-1}$  are light shaded in (b). Contour interval is  $2 \text{ mm day}^{-1}$  in (a), and  $1 \text{ mm day}^{-1}$  in (b).

terization is implemented in the model. From Fig. 5.4 and Fig. 6.6, the global mean cumulus precipitation from the MCB simulation is  $1.762 \text{ mm day}^{-1}$ , which is slightly less than that ( $1.960 \text{ mm day}^{-1}$ ) from the control simulation. Therefore, the increased cumulus incidence in the MCB parameterization does not increase the cumulus precipitation globally. As discussed above, with more cumulus cloud types produced in the MCB simulation, cumulus precipitation patterns are expected to change from the control simulation. Comparing cumulus precipitation patterns from the control simulation in Fig. 5.4 and map (a) in Fig. 6.6, we see that the two model simulations produced similar cumulus precipitation patterns, e.g., maxima over the Southern Asian monsoon and Indian monsoon strong convective regions, the Western Pacific, as well as the central America, the regions of the SPCZ. In the control simulation, cumulus precipitation is concentrated in several intensely convective regions. In the MCB simulation, unrealistically strong deep convection in some regions, in the C-run, has been reduced, and areas of strong cumulus precipitation are broader and the precipitation pattern is smoother. This is because the altocumulus clouds weaken the deeper cumulus clouds in some strong convective regions, and increase cumulus activity in some convection-free regions of the C-run. This can be seen in panel (c) of Fig. 6.1. The MCB simulation increases cumulus incidence in latitudes  $30^\circ \sim 60^\circ\text{N}$  and  $0^\circ \sim 30^\circ\text{S}$ , which are regions of small cumulus incidence in the C-run; and meanwhile the MCB simulation decreases the cumulus incidence in latitudes  $0^\circ \sim 30^\circ\text{N}$  which are strong cumulus incidence regions.

Differences of cumulus precipitation between the two simulations are shown in map (b) of Fig. 6.6. It is clearly seen that although the MCB simulation produces more cumulus cloud types and more cumulus incidence globally, the intensities of some strong

cumulus precipitation regions, such as the Western Pacific, the Arabian sea and eastern Central America, are less in the MCB simulation than in the control simulation. We have indicated in Chapter 3 that the model produces unrealistically strong precipitation over the Western Pacific, which is related to the excessive deep convection produced by the current version of the A-S parameterization. The reduction of the maximum cumulus precipitation over Western Pacific convective regions by the MCB simulation definitely makes the model precipitation closer to reality, as shown in Fig. 6.4 and Fig. 6.5.

This result can be interpreted in two ways: i) cumulus clouds with higher cloud base levels compete for convective available potential energy (CAPE) and moisture with the deep penetrative cumulus clouds starting from the PBL, which contribute most of the cumulus precipitation, so that the cumulus precipitation maximum weakens when the amount and intensity of deep penetrative cumulus clouds starting from the PBL decrease; ii) the deep cumulus clouds originating in the free atmosphere produce less precipitation because less moisture is available at their cloud base levels. Finally, when more realistic cloud types and cloud amounts are produced by the generalized cumulus parameterization, a more realistic cumulus precipitation pattern is generated.

The zonal mean cumulus precipitation and the differences between the control simulation and the MCB simulation are shown in Fig. 6.7. Again, the two simulations generate very similar zonal mean cumulus precipitation patterns. The decrease of cumulus precipitation in the MCB simulation in the northern tropics corresponds to the weakened maxima over the Western Pacific Ocean, the Arabian sea, and Central America. There is no significant cumulus precipitation difference at mid-latitudes between the control and

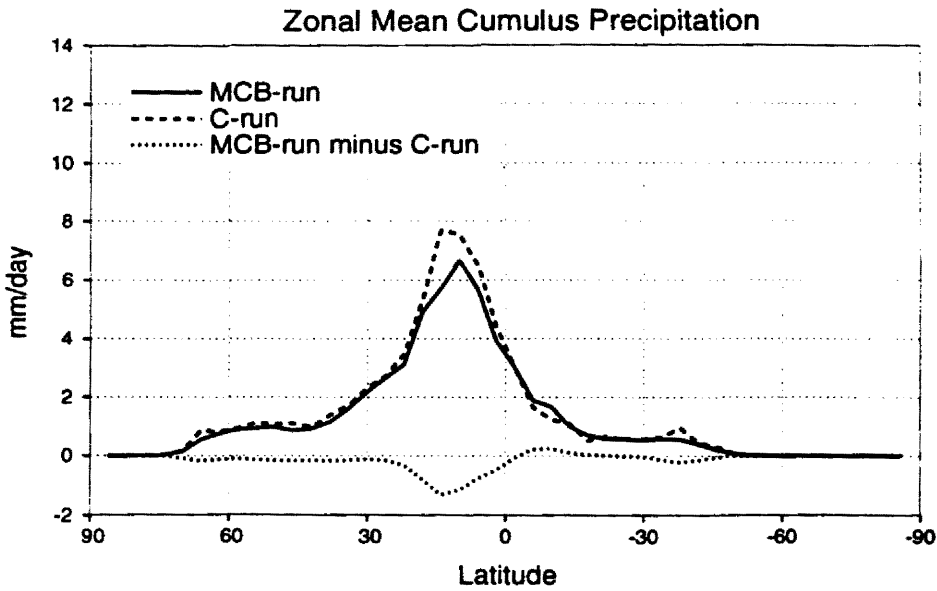


Fig. 6.7 July zonal mean cumulus precipitation from the MCB simulation (solid curve), control simulation (dotted curve) and their difference (dashed curve). Unit is mm day<sup>-1</sup>.

the MCB simulations.

In summary, the MCB simulation produces more realistic cumulus cloud types and cloud distributions. This leads to improvements in the cumulus precipitation patterns produced by the model. Through comparisons of the cumulus precipitation patterns produced by the MCB simulation and the control simulation, we find that although the MCB simulation produces more cloud types and cumulus incidence compared with the control simulation, the global cumulus precipitation rate is not increased in the MCB run. Smoother cumulus precipitation patterns are produced, and the unrealistically strong cumulus precipitation maxima over the Western Pacific Ocean and the Arabian sea are reduced by the MCB parameterization. The improvement of cumulus precipitation pattern leads to the improvement of the simulated total precipitation pattern.

### 6.2.3 Cumulus mass flux detrainment, cumulus heating and cumulus moistening

Cumulus clouds transport moisture and moist static energy vertically from lower layers to upper layers. The large-scale moisture and temperature fields can be modified through cumulus-induced subsidence and cumulus cloud-top detrainment. Cumulus-induced subsidence in the environment causes large-scale warming and drying; and cloud top detrainment of liquid and cloud ice particles causes large-scale cooling and moistening. In this section, we analyze the effects of the MCB parameterization on the detrainment processes, cumulus heating and cumulus moistening.

Fig. 6.8 shows the zonally averaged cumulus detrainment mass flux from the C-run (a), the MCB-run (b), and their difference (c), as functions of latitude and pressure. This plot essentially shows where cloud tops are and how strong the cumulus activity is. The general patterns shown in (a) and (b) are similar. The maximum over the tropics from 200 mb to 300 mb corresponds to strong deep convection in this area. The detrainment mass flux intensity in the C-run over the tropics is stronger than that in the MCB-run, however. This can be clearly seen in the difference plot (c). Therefore, the MCB parameterization reduces the intensity of tropical deep cumulus convection. This means that cumulus clouds starting from the free atmosphere retard the development of deep convection to some degree. This is an improvement over the original A-S parameterization which produces excessively strong convection in the tropics. This is also consistent with the cumulus precipitation changes analyzed in the previous section. The larger detrainment rates in mid-latitudes and high-latitudes of the MCB-run are effects of altocumulus clouds, which are ignored in the original A-S parameterization.

### Cumulus Detrainment Mass Flux

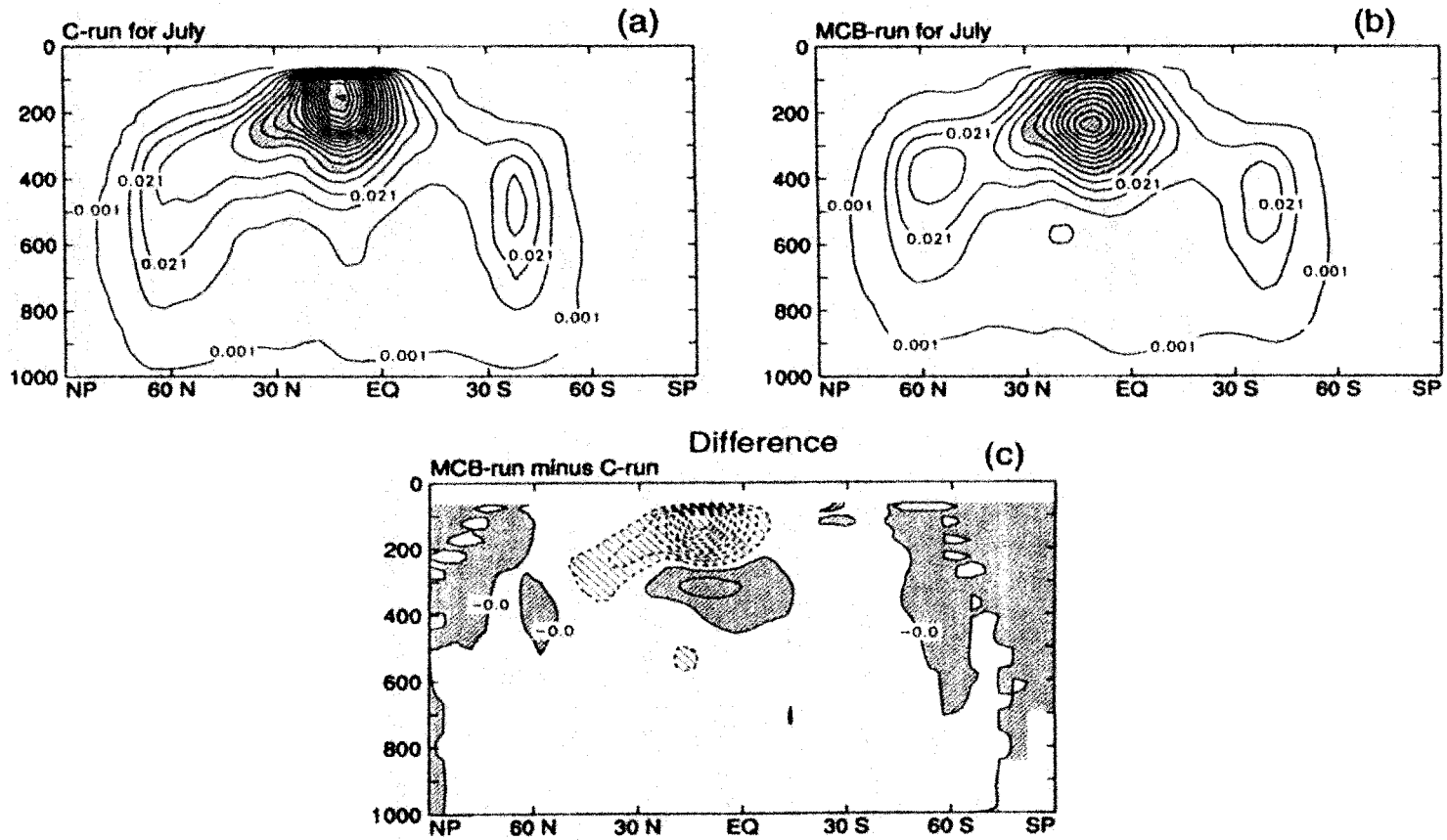


Fig. 6.8 Zonal mean July cumulus detrainment from C-run (a), MCB-run (b) and MCB-run minus C-run (c). Units are in  $\text{hour}^{-1}$ . Values larger than 0.05 are shaded in (a) and (b); values larger than zero are shaded in (c).

The zonally averaged cumulus heating profile from the C-run, the MCB-run and their difference are shown in Fig. 6.9. The MCB and control simulations produce very similar zonally averaged cumulus heating profiles. A tropical maximum of about  $3 \text{ K day}^{-1}$  near 400 mb appears in both the C-run and the MCB-run. In the difference map (c), we find that when the MCB parameterization is used to replace the original A-S parameterization and the MSTADJ, the intensity of moist convection (especially deep convection) in the model tropics has been reduced. In the adjacent subtropics, however, the MCB-run produces more cumulus heating than the C-run in the middle troposphere

The moistening effects of altocumulus clouds are shown in Fig. 6.10. The upper level moistening and lower level drying are consequences of upward moisture transport by cumulus convection. Once altocumulus clouds are involved in this moisture transport process, the MCB simulation has stronger upper level moistening and low level drying than the control simulation. In other words, more moisture is vertically transported in the MCB parameterization, although it produces less cumulus precipitation. This is consistent with the previous results that the overall cumulus activity is enhanced in the MCB simulation.

### **6.3 The simulated climate**

We have discussed cumulus cloud type distributions, total and cumulus precipitation rates, as well as cumulus detrainment mass flux profile and cumulus heating, moistening profiles with the implementation of the MCB parameterization. The important effects of cumulus convection on the large-scale atmospheric circulation have been discussed in Chapters 1 and 2. The main purpose for improving the cumulus parameterization is to improve the model's performance in simulations of large-scale circulation. In this section

### Cumulus Heating Rate

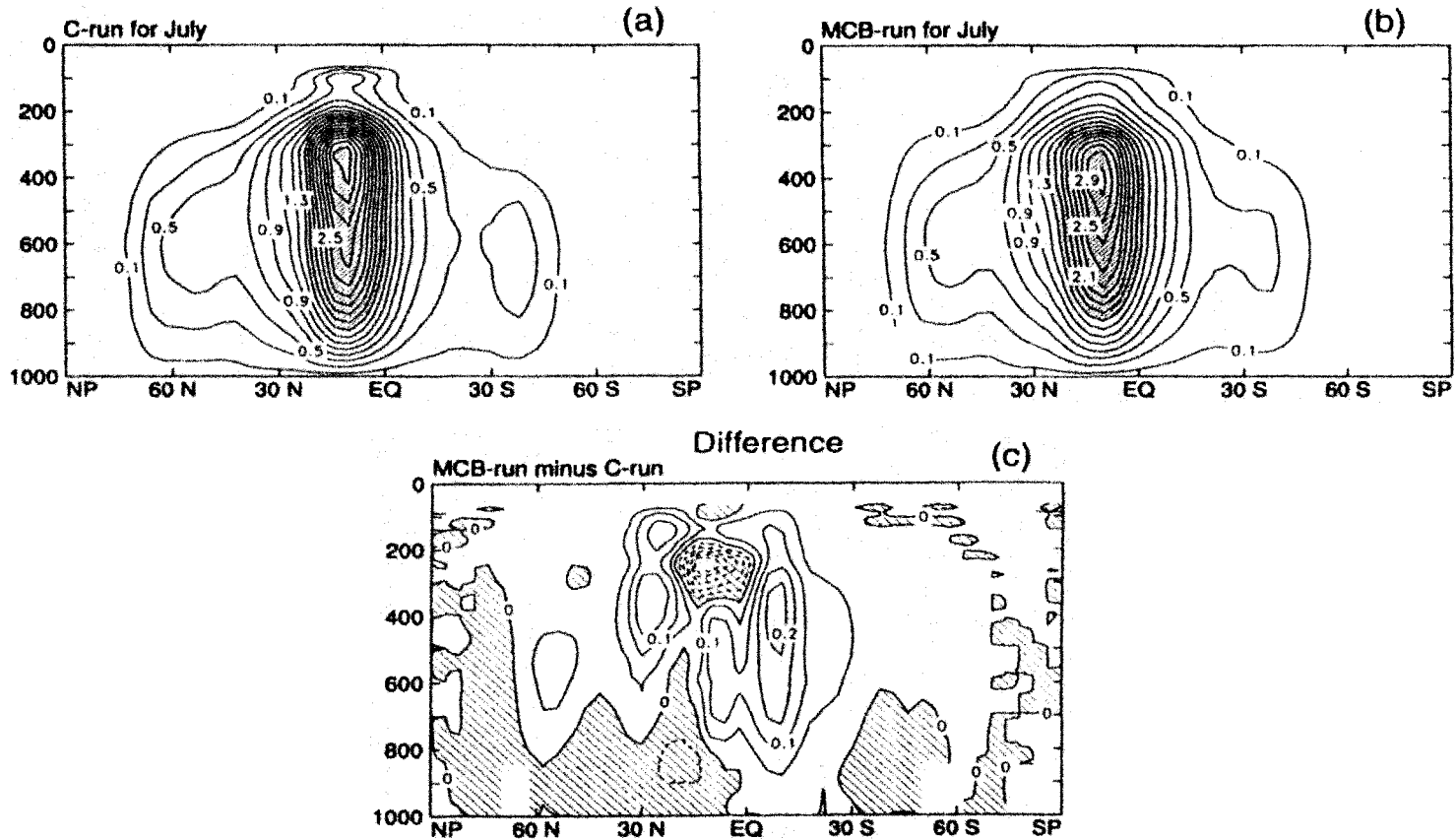


Fig. 6.9 Zonal mean July Cumulus heating rate from C-run (a), MCB-run (b), and MCB-run minus C-run (c). Units are in  $\text{K day}^{-1}$ . Values larger than  $1.5 \text{ K day}^{-1}$  are shaded in (a) and (b). Negative values are shaded in (c).

### Cumulus Moistening

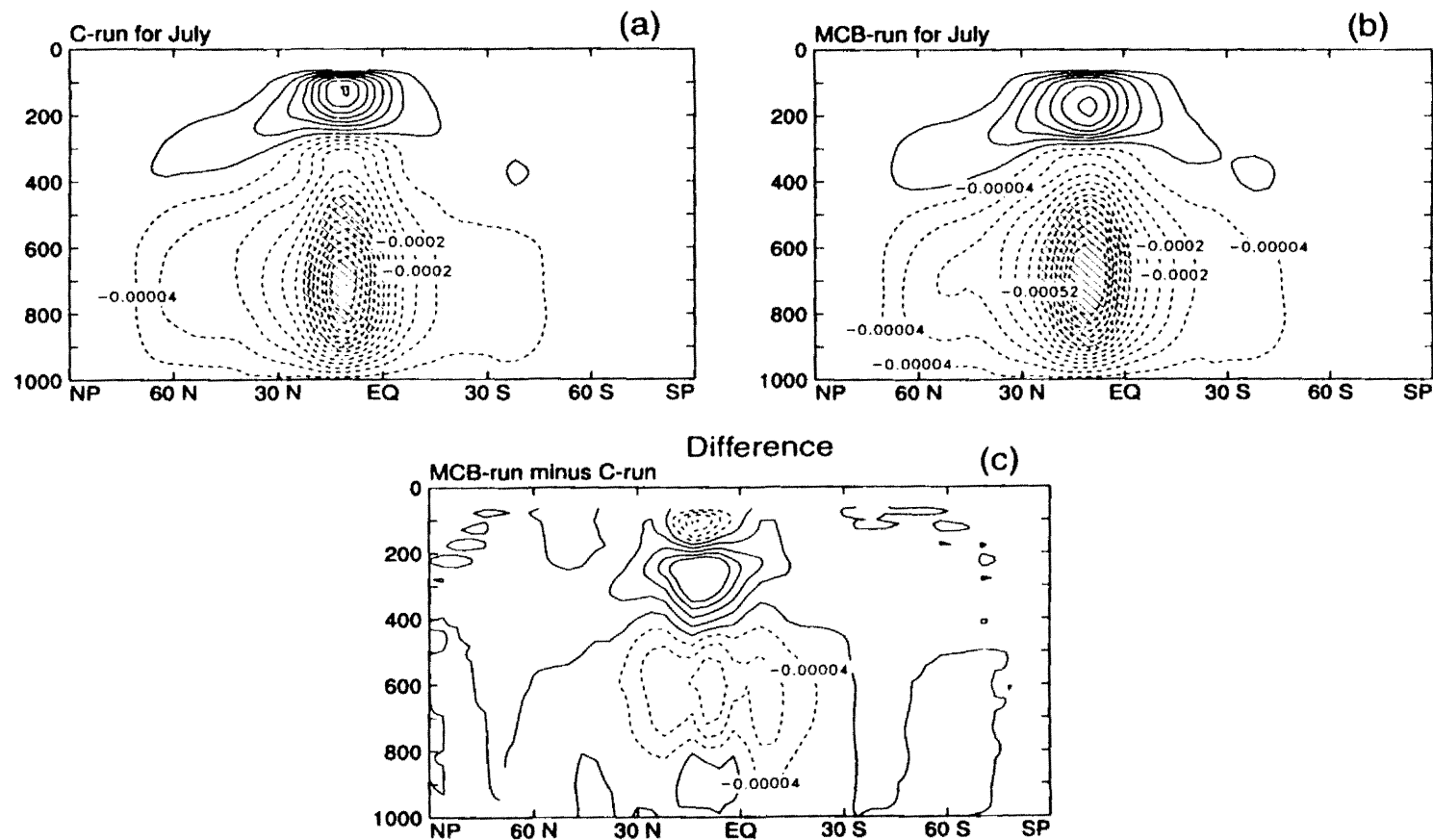


Fig. 6.10 Zonal mean July cumulus moistening rate from C-run (a), MCB-run (b), and MCB-run minus C-run (c). Unit is  $\text{g kg}^{-1} \text{day}^{-1}$ . Values less than  $-0.0005$  are shaded. The contour interval is  $0.00008 \text{ g kg}^{-1} \text{day}^{-1}$ .

the simulated climate with the MCB parameterization is discussed and compared with results of the C-run and with observations.

### 6.3.1 Simulated 500 mb geopotential height fields

Fig. 6.11 shows 500 mb geopotential height fields from the C-run (a), the MCB-run (b), and the ECMWF observations (c). The C-run and the MCB-run produce quite similar 500 mb geopotential heights. Compared with observations in the map (c), the model has successfully simulated observed basic patterns of 500 mb geopotential height field, e.g., the extended subtropical high belts. From these maps, the model produces relatively higher 500 mb surface, especially in tropics. This implies that the atmospheric temperature from the model simulations is warmer than observed. From maps (a) and (b), there is no significant difference of 500 mb geopotential heights between the C-run and the MCB-run.

### 6.3.2 The temperature and moisture fields

The simulated July zonal mean temperature distributions and their differences from observations are shown in Fig. 6.12. The latitude-pressure sections of temperature distributions from (a) and (b) indicate that there is little difference in the temperature fields between the control simulation and the MCB simulation. The strongest vertical temperature gradients are found in the tropical upper troposphere. The strong horizontal temperature gradients in the middle and lower troposphere over mid-latitudes indicate the baroclinicity of the atmosphere. Panels (c) and (d) show that the model produces an excessively warm middle and upper troposphere in the tropics and subtropics. The difference between the C-run and observations in the upper troposphere is very similar to the differ-

### July 500 mb Geopotential Height

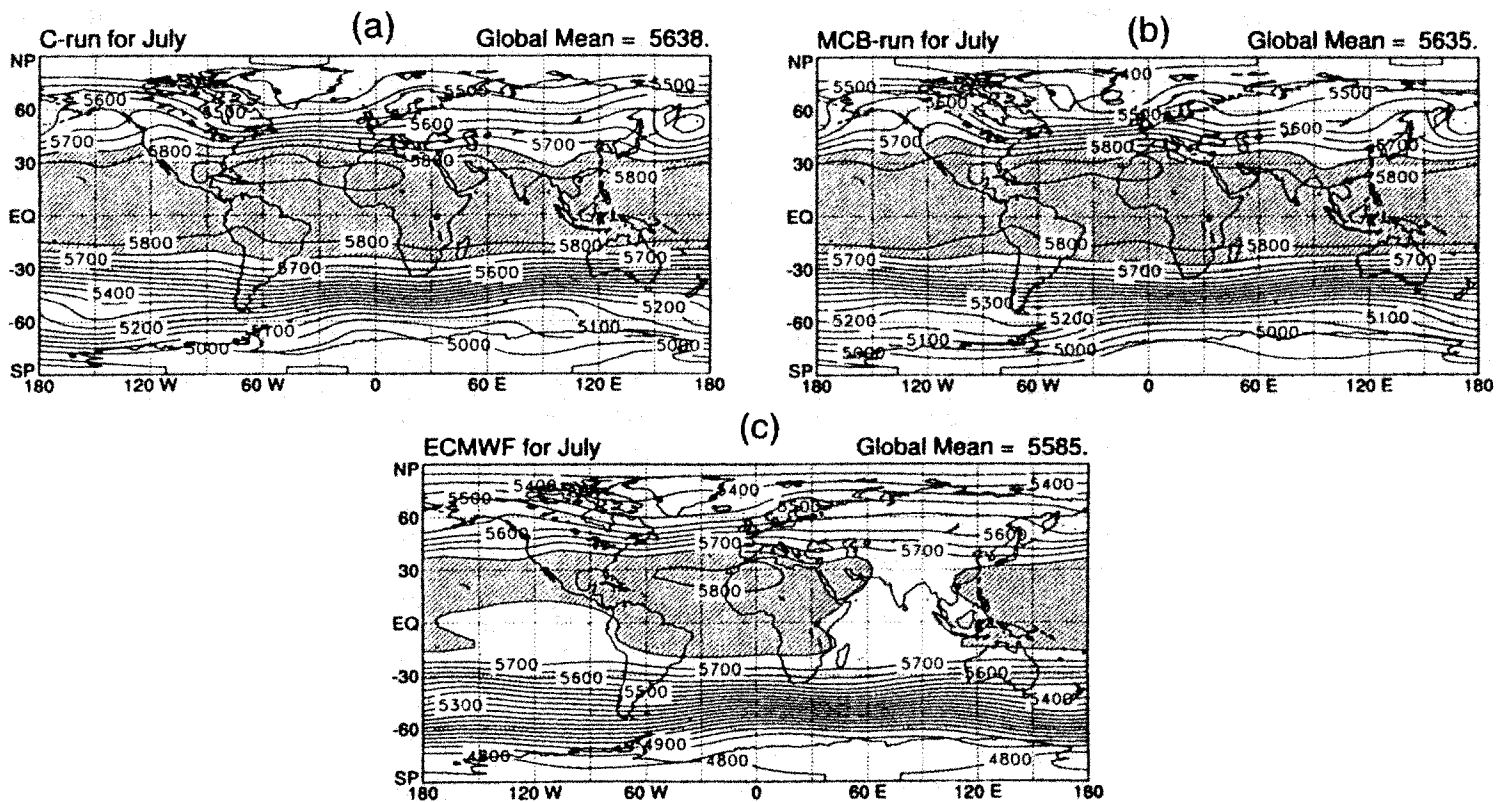


Fig. 6.11 July 500mb geopotential height fields from the C-run (a), the MCB-run (b), and ECMWF data (c). The unit is in meter and values larger than 5750 are shaded. The contour interval is 50 meters.

## Zonal Mean Temperature

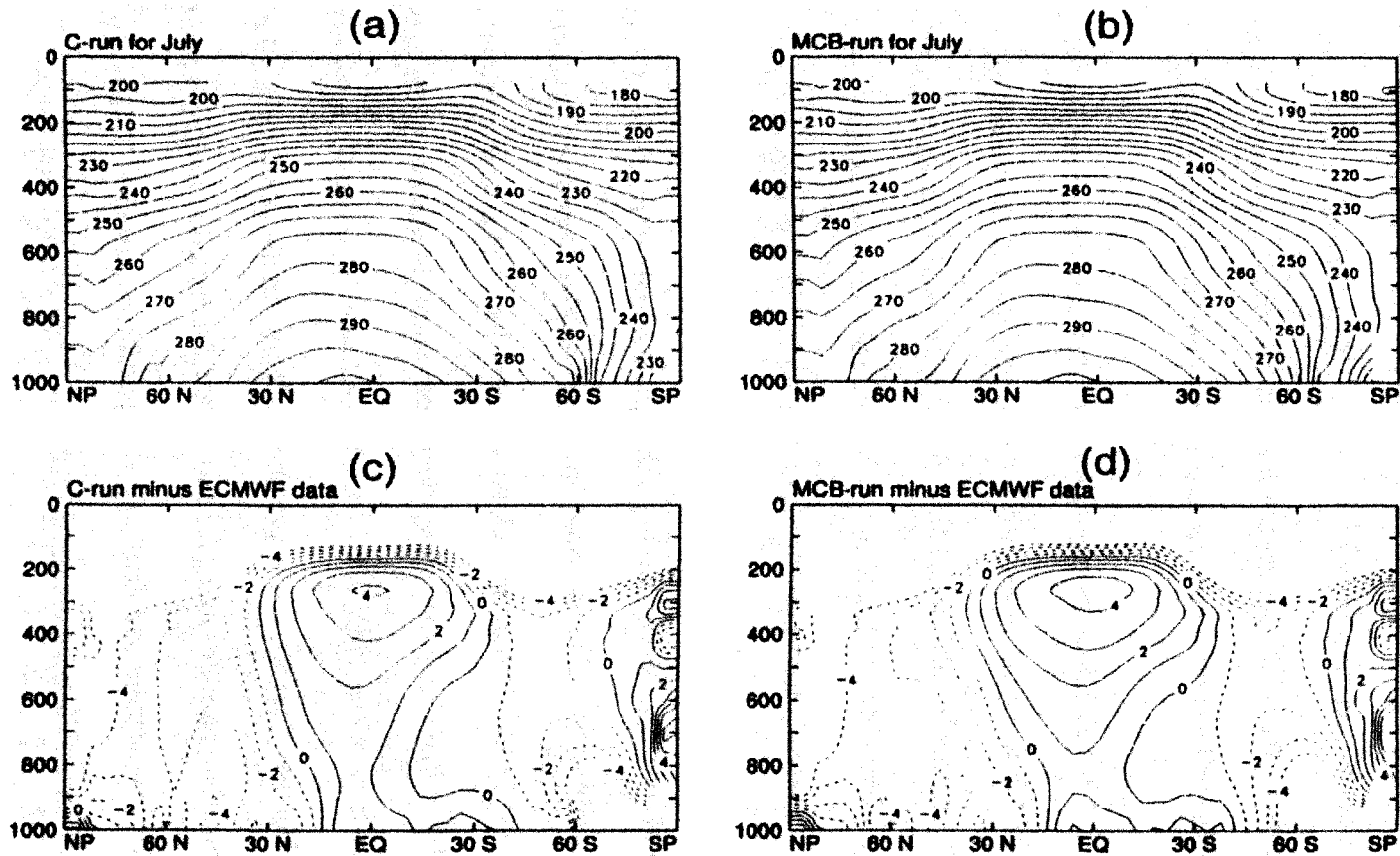


Fig. 6.12 Latitude-pressure temperature distributions from the C-run (a); the MCB-run (b); and the temperature difference with observations (c) and (d). The unit is K. Contour intervals are 5 in (a), (b); and 2 in (c), (d).

ence of the MCB-run and observations.

Fig. 6.12 illustrates that the general atmosphere temperature features have been reasonably reproduced by the model. The modification of the atmospheric temperature fields by the MCB parameterization is not significant without including the evaporation cooling effects by convective downdrafts and the cumulus rainfall.

Zonal mean relative humidity distributions from model simulations and the ECMWF four year mean (1985~1988) analysis are shown in Fig. 6.13. The observations indicate that in July humid air is found near the surface. In the middle troposphere, larger relative humidity is found in tropics and mid-latitudes, where convection and frontal systems vertically transport moisture. Dry air is found in the subtropics of the middle troposphere, in association with subtropical highs. The model basically produces moist surface and lower troposphere; and dry subtropical middle troposphere. The tropical upper troposphere from model simulations has larger relative humidity than observed. This is probably due to the detrainment cloud air from the strong deep convection predicted by the model. Meanwhile, the strong deep convection produced by the model makes tropical lower troposphere drier than observations since it vertically transport moisture upward. The MCB-run and the C-run produce basically similar zonal mean relative humidity distributions. The panel (c) indicates that the MCB simulation produces a more moist lower and middle troposphere and drier upper troposphere in tropics. This is also due to the reduction of the strong deep convection relative to the control simulation.

### 6.3.3 The atmospheric circulation

The effects of the MCB parameterization on the simulated precipitation, tempera-

## Zonal Mean Relative Humidity

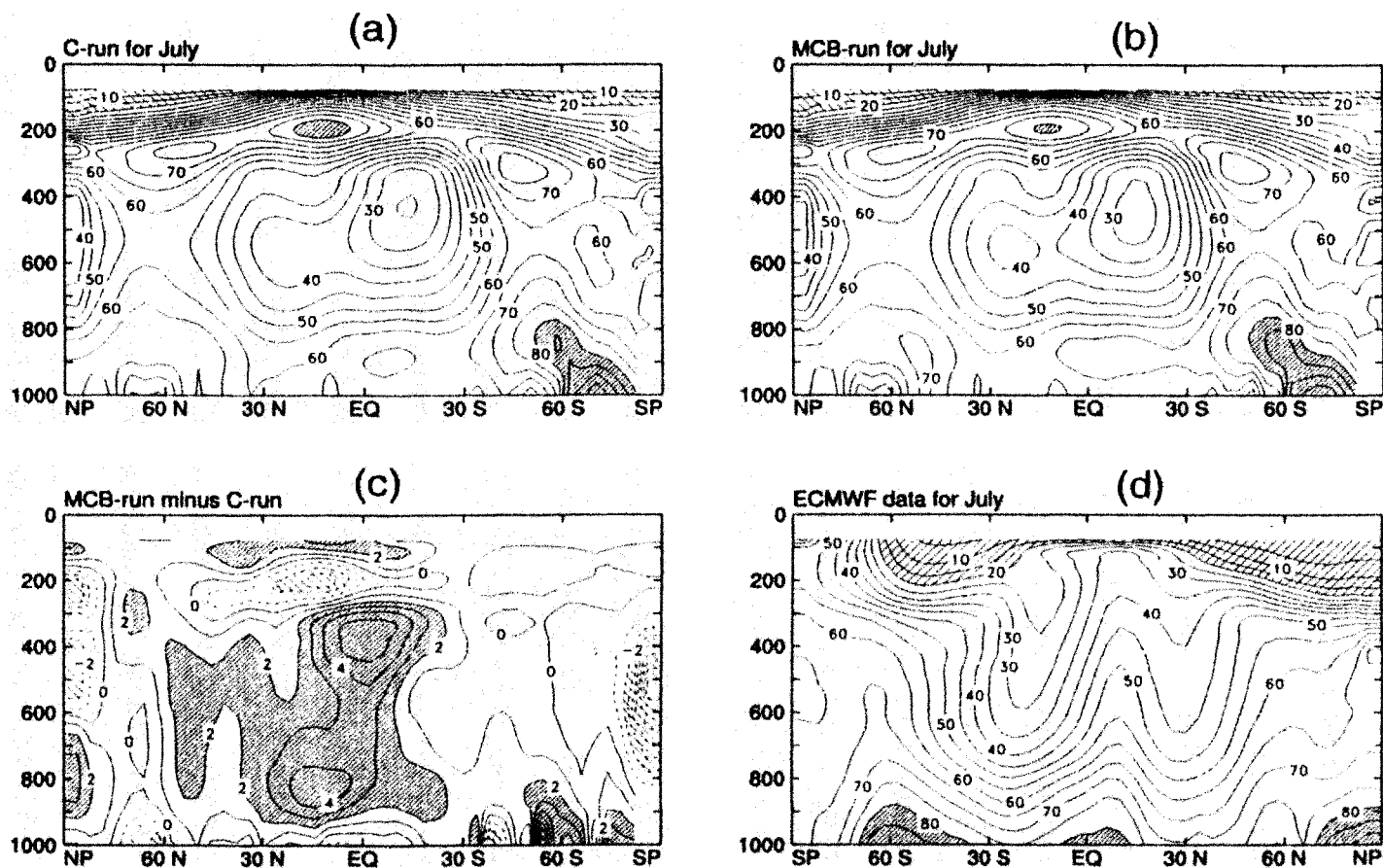


Fig. 6.13 Zonal mean July relative humidity from C-run (a), MCB-run (b), MCB-run minus C-run (c), and ECMWF data (d). Values larger than 80% are dark shaded; and values smaller than 20% are light shaded in panels (a), (b), and (d); Values larger than 2% are dark shaded; and values smaller than -2% are light shaded in the panel (c).

ture, and moisture fields have been presented. The simulations of the zonal wind and mean meridional circulation are discussed in this section.

Fig. 6.14 shows the July zonal mean zonal wind profiles from simulations of the C-run, the MCB-run, and observations. As seen in Fig. 6.14, the model produces strong polar jet in the Southern (winter) Hemisphere and a weaker subtropical jet in the Northern (summer) hemisphere. From Fig. 6.12, the unrealistically strong polar jet in the Southern Hemisphere corresponds to the increased horizontal temperature gradient in the simulations. The simulated zonally averaged tropical easterlies are too weak compared with observations. The observed weak polar easterlies are well simulated by the model. In general, as for the 500 mb geopotential height and temperature fields, the zonally averaged zonal wind profiles from the C-run and the MCB-run have no significant differences.

The latitude-pressure cross sections of the mean meridional circulations obtained from C-run, MCB-run and observations are displayed in Fig. 6.15. In both model simulations, the strong direct Hadley cell in the tropics and the indirect Ferrel cells at northern mid-latitudes are well seen. As for the intensity of the Hadley cell, the MCB simulation produces weaker Hadley circulation than the control simulation, and is in better agreement with observations. This is consistent with our earlier results that the MCB simulation produces weaker penetrative cumulus convection in the tropics, in conjunction with the decreased latent heating and cumulus precipitation there.

The Ferrel circulation in the Southern Hemisphere is clearly seen in the observations, but it is very weak in the control simulation. The MCB run, however, produces a clear Ferrel circulation in the Southern Hemisphere, which is in much better agreement

### Zonal Mean Zonal Wind

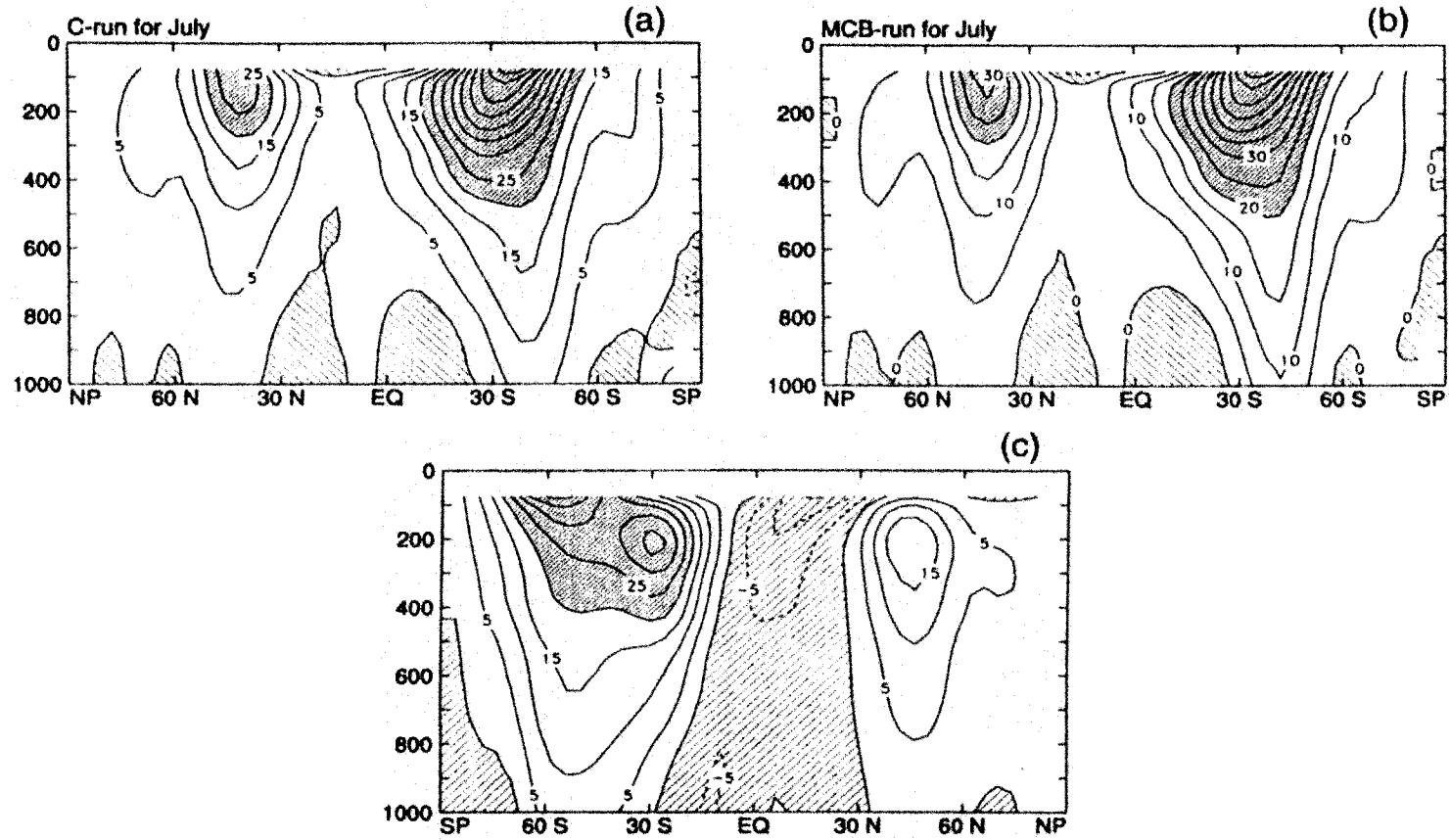


Fig. 6.14 July zonal mean zonal wind from C-run (a), MCB run (b), and ECMWF data. Unit is  $\text{m s}^{-1}$ . The contour interval is  $5 \text{ m s}^{-1}$ . Heavy shading corresponds to values larger than  $20 \text{ m s}^{-1}$ , and light shading corresponds to values less than zero.

## Mean Meridional Circulation

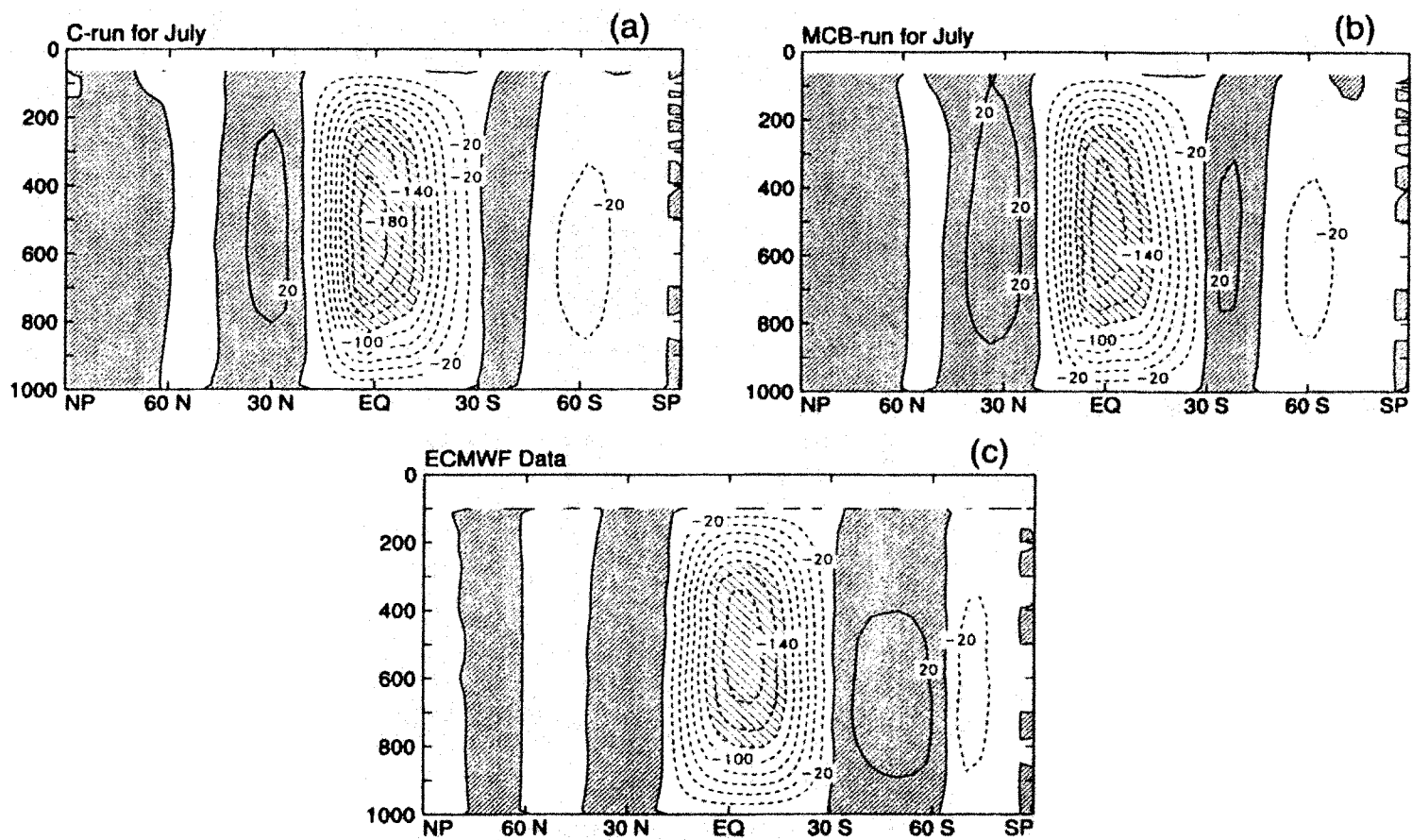


Fig. 6.15 July streamfunction of the mean meridional circulation from C-run (a), MCB-run (b), and observations. Units are in  $10^9 \text{ kg s}^{-1}$ . The control interval is  $20 \times 10^9 \text{ kg s}^{-1}$ . Positive values are heavily shaded and values less than  $-120 \times 10^9 \text{ kg s}^{-1}$  are lightly shaded.

with observations than the control run. From the Fig. 6.15 we conclude that the mean meridional circulation produced by the MCB simulation is in much better agreement with observations in both pattern and magnitudes than the control simulation.

#### 6.4 Effects of altocumulus convection on soundings at some individual locations

As indicated in sections 6.2.1 and 6.2.2, the MCB parameterization has strong effects in some of vigorous convection active regions, like the Western Pacific and Indian monsoon region, and some mid-latitude areas, such as the Rocky Mountains. In this section, we focus on these individual locations to compare results of the MCB simulation and the control simulation.

**Table 6.3: Individual Location List**

Symbol	Grid points and latitude, longitude	Area description
SN1	(64.25); 6°N, 137°E	Western Pacific
SN2	(52.28); 18°N, 77°E	Indian Monsoon area
SN3	(14.33); 38°N, 112°W	Rocky Mountains
SN4	(36,28); 18°N, 2°W	Sahara desert
SN5	(4,18); 22°S, 167°W	Southern Pacific Convergence Zone (SPCZ)
SN6	(14,26); 10°N, 112°W	Eastern Pacific
SN7	(54,31); 30°N, 87°E	Tibet Plateau
SN8	(20,20); 12°S, 82°W	Eastern South American Coast

The selection of individual locations has been based on the distributions of altocumulus incidence. We are interested by places where large altocumulus incidence occurs.

Eight locations have been selected for analysis. Their grid numbers, latitudes and longitudes, and location descriptions are listed in Table 6.3.

The July monthly mean temperature and specific humidity vertical profiles and their differences between the MCB simulation and the control simulation in individual locations SN1 ~ SN8 are shown in Fig. 6.16 through Fig. 6.21. In these figures, solid lines are used for the results of the C-run and dashed lines are used for the results of the MCB-run.

As seen in Fig. 6.16, Fig. 6.17, Fig. 6.19 and Fig. 6.20, the temperature and specific humidity vertical profiles from the C-run and the MCB-run show basically similar features, even though differences in some degrees can be seen in these eight locations. Because all these locations have large altocumulus incidence, we conclude that the MCB parameterization does not change much the characteristics of model simulated soundings. This conclusion is consistent with our preceding analysis of the model simulated climate, which indicates that the model simulated climate has no significant difference between the MCB simulation and the control simulation. Meanwhile, Fig. 6.18 and Fig. 6.21 show that the MCB simulation produces warmer middle and upper troposphere, and cooler lower troposphere, compared to the control simulation. In other words, the MCB parameterization increases the stability of the atmosphere. The increase of temperature in the middle and upper troposphere might be due to the weakening of deep convection by the MCB parameterization, which decreases cumulus detrainment at upper levels and its related evaporation cooling effects.

Fig. 6.18 and Fig. 6.21 also show that changes of temperature profiles due to altoc-

# Temperature

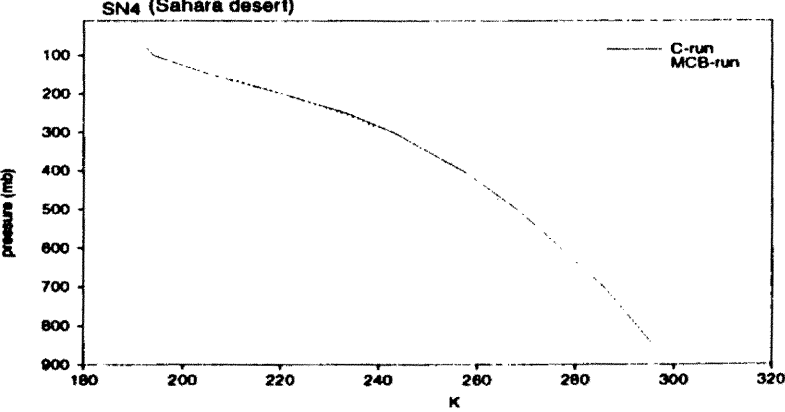
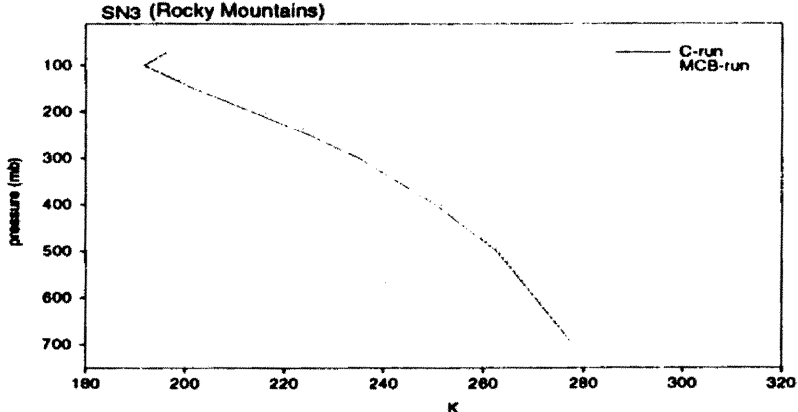
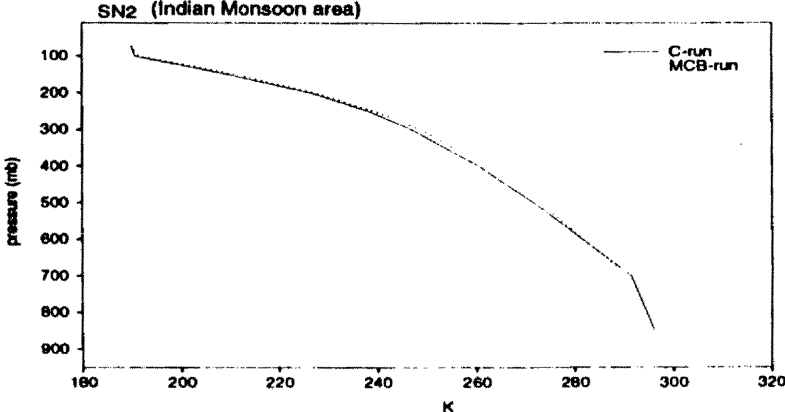
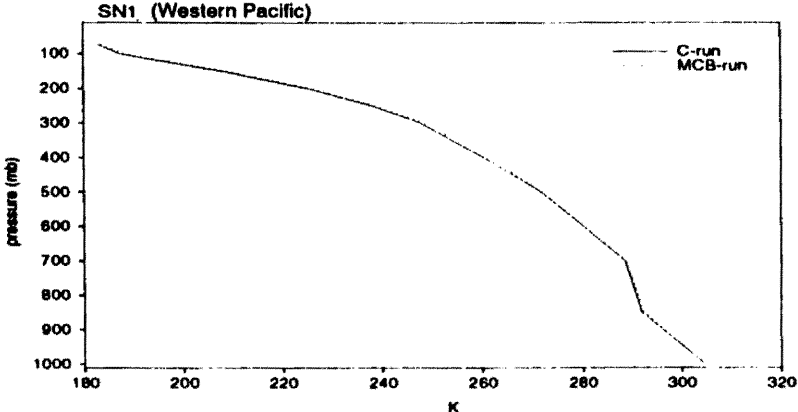


Fig. 6.16 July simulated monthly mean temperature vertical profiles from C-run (solid lines) and MCB-run (dashed lines) for SN1 ~ SN4.

# Specific Humidity

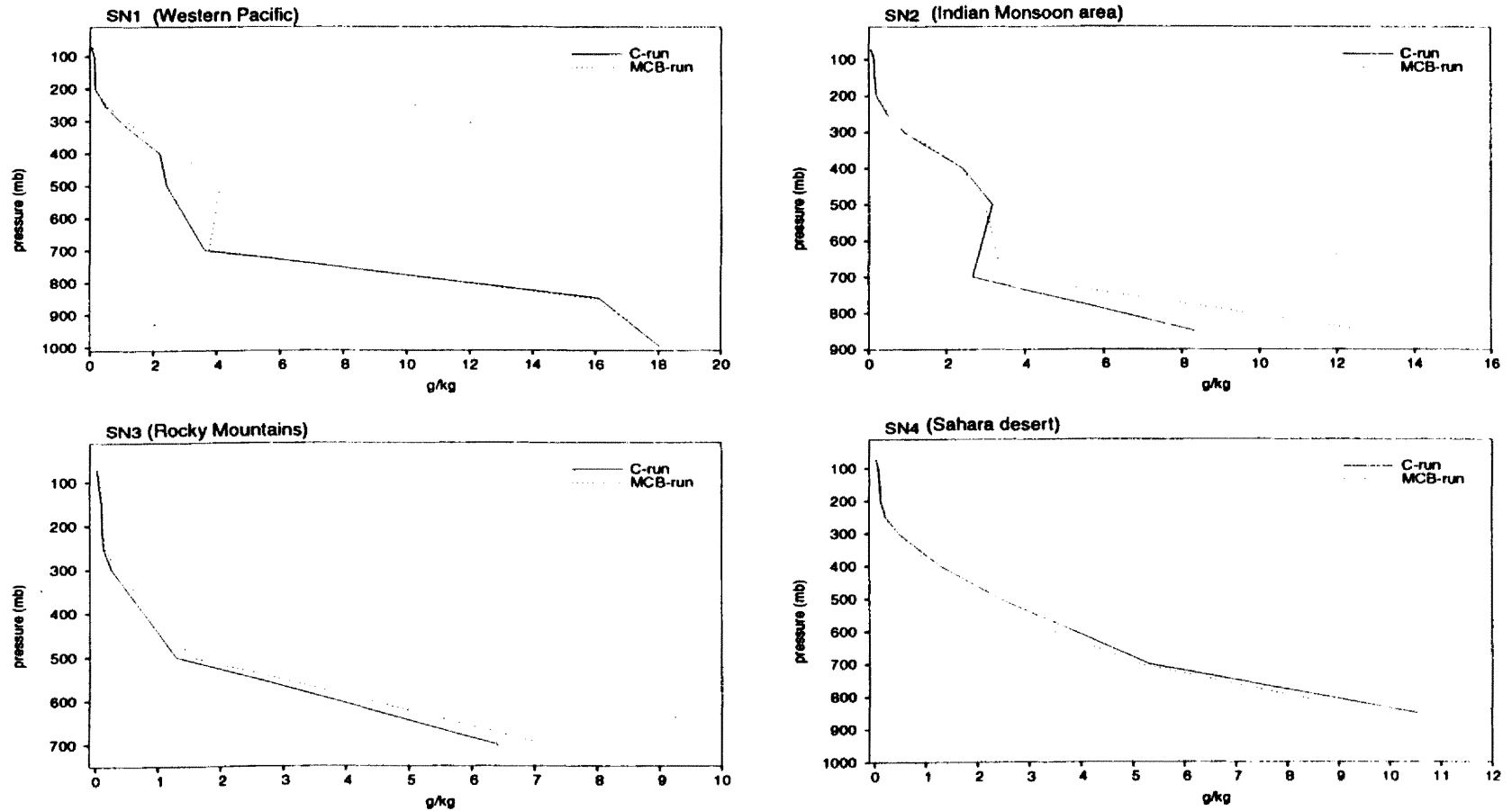


Fig. 6.17 Same as Fig. 6.16, except for specific humidity.

## Temperature and Specific Humidity Difference (MCB-run minus C-run)

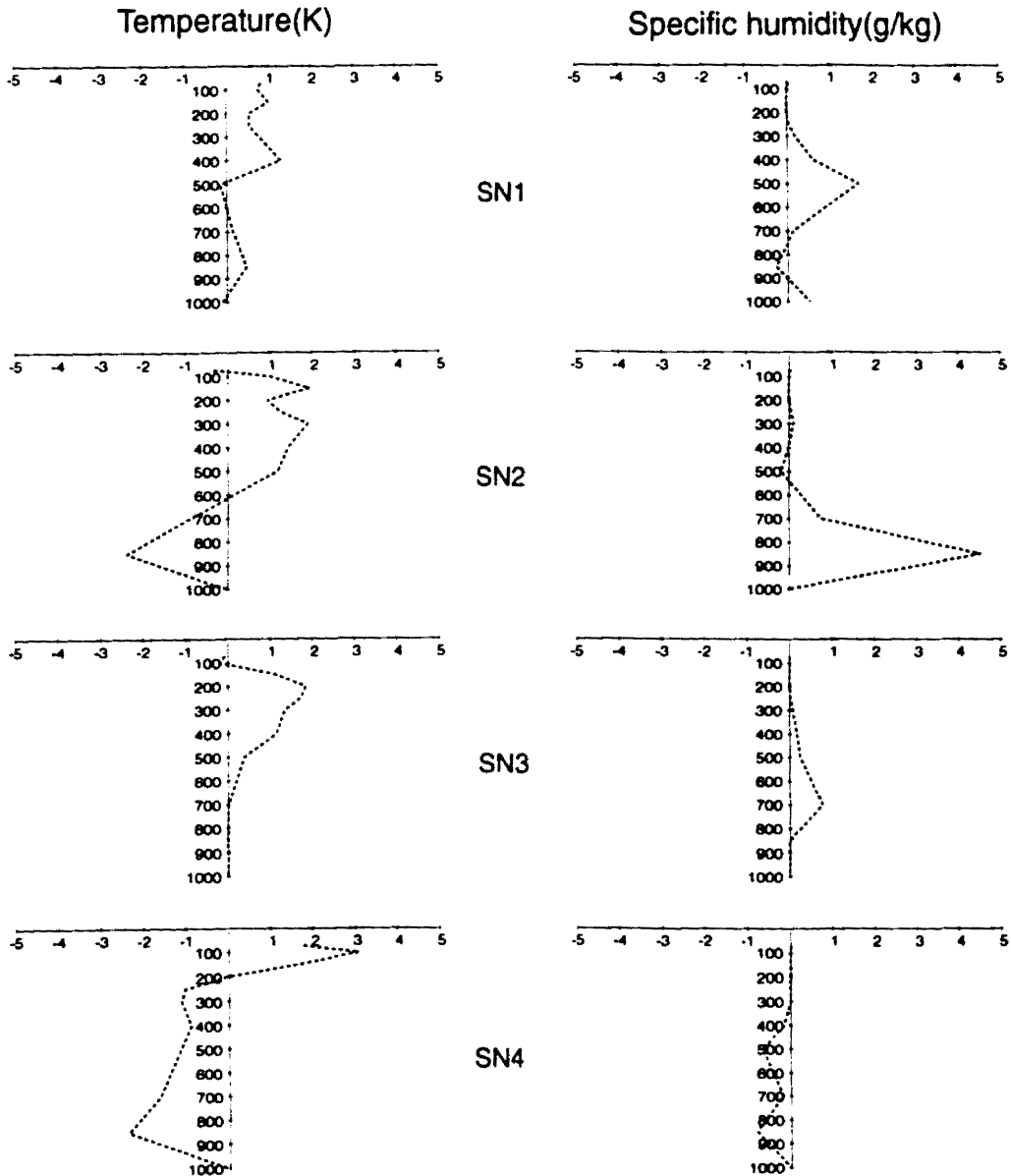


Fig. 6.18 Temperature and specific humidity difference at SN1 to SN4 between the MCB simulation and the control simulation. The vertical coordinate is pressure in mb.

# Temperature

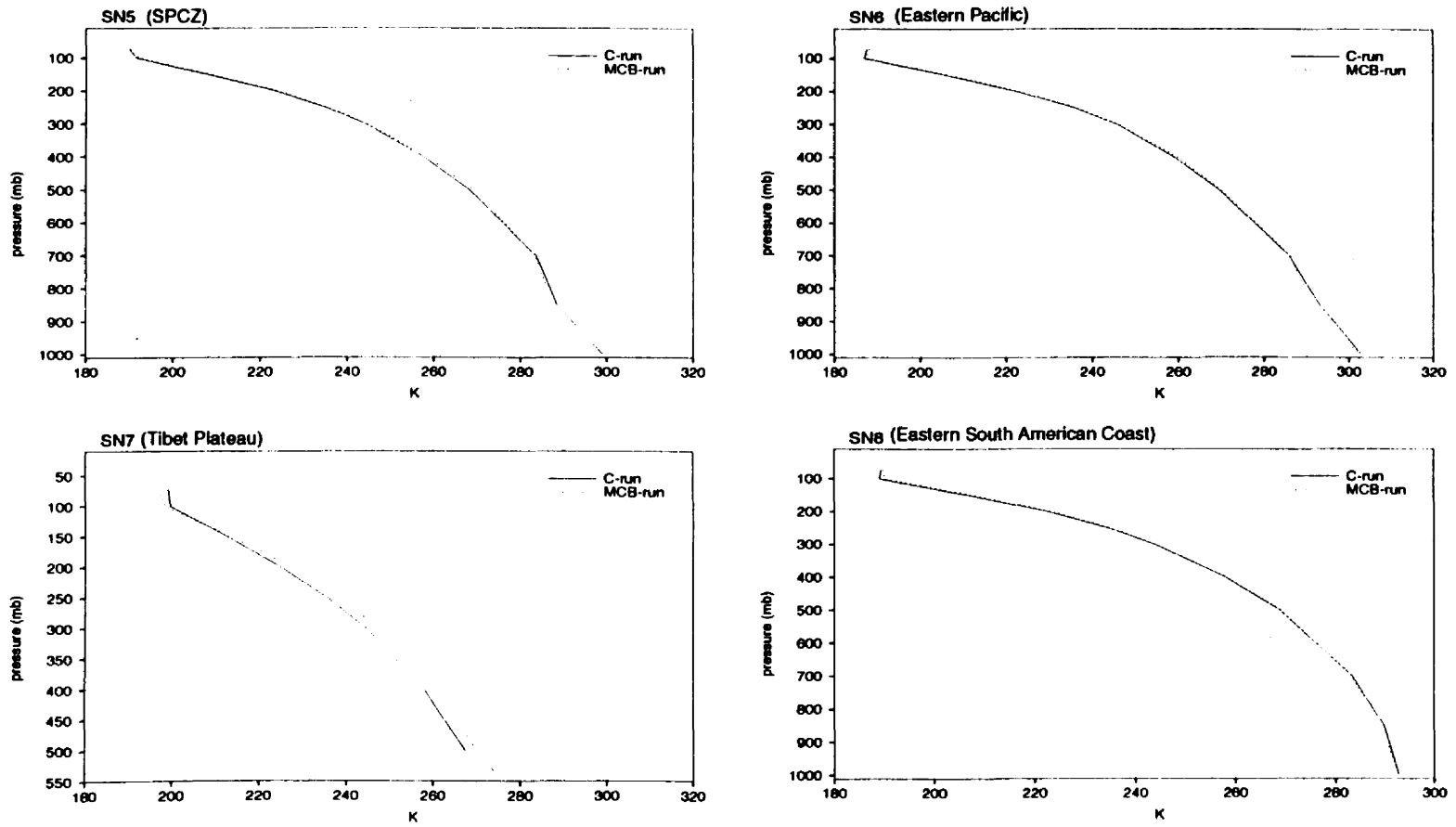


Fig. 6.19 Same as Fig. 6.16, except for SN5 ~ SN8.

# Specific Humidity

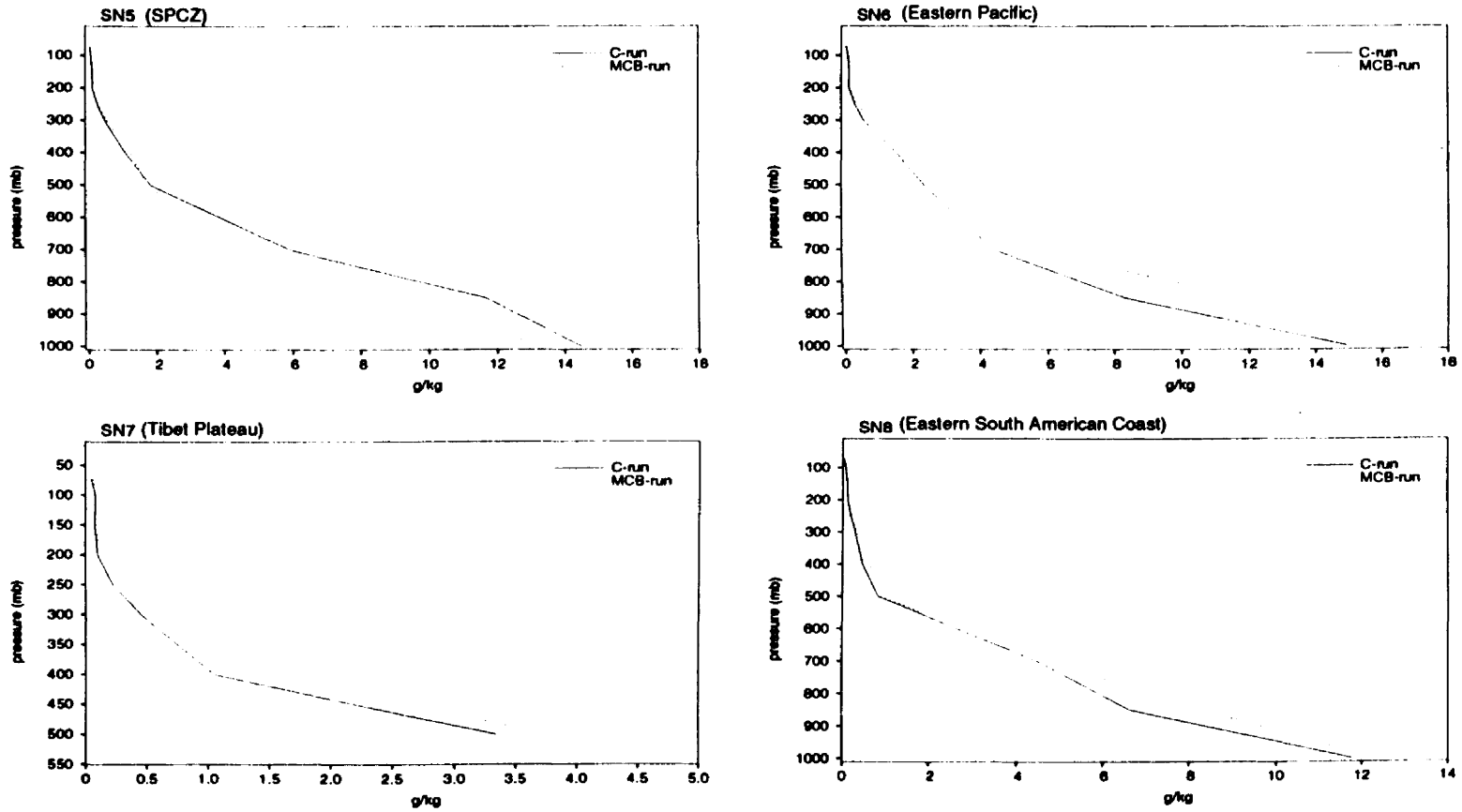


Fig. 6.20 Same as Fig. 6.17, except for SN5 ~ SN8.

# Temperature and Specific Humidity Difference (MCB-run minus C-run)

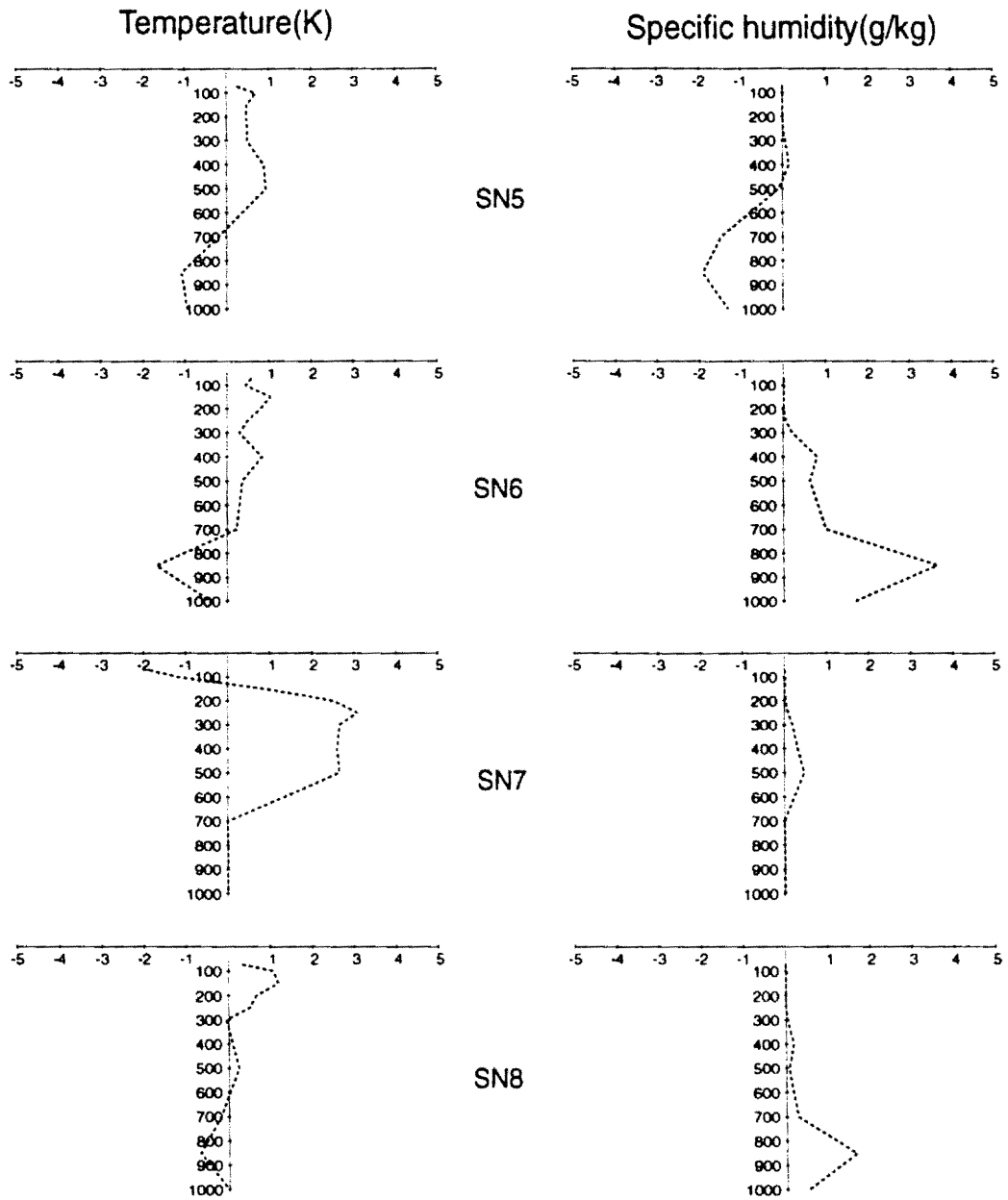


Fig. 6.21 Same as Fig. 6.18, except for SN5 ~ SN8.

umulus clouds are larger over lands than over oceans, e.g., in the Indian Monsoon area (SN2), the Rocky Mountains (SN3), and the Tibet Plateau (SN7), the temperature increases at middle and upper levels in the MCB run are apparently larger than that from ocean locations. In the Sahara Desert (SN4), the strong lower troposphere heating causes penetrative altocumulus convection, which transports heat to very high levels. The temperature is about 2.5 K lower at 800 mb and 3 K warmer at 150 mb from the MCB-run compared to the C-run.

The changes of vertical moisture profiles from the C-run to the MCB-run are also shown in Fig. 6.18 and Fig. 6.21 for these locations. The MCB simulation produces a more moist middle or lower troposphere in most locations, except in the Sahara Desert (SN4) and the SPCZ region (SN5). For example, over the Western Pacific (SN1), the MCB simulation produces a more moist middle troposphere (300 mb ~ 700 mb). It can be concluded that more cumulus clouds with tops higher than 700 mb occur and transport more moisture to upper troposphere. The moisture in low levels is compensated by the increased low level convergence. In the Sahara Desert, the specific humidity at middle and low levels decreases in the MCB-run. An explanation is that there is not enough surface moisture convergence to compensate for the increased moisture vertical transport by enhanced cumulus activities.

The specific humidity at 800 mb apparently increases in the MCB-run over the Indian monsoon region (SN2) and the tropical Eastern Pacific Ocean (SN6). From the cumulus incidence maps, cumulus clouds, both cumulus starting in the PBL and altocumulus, are very active over the regions. There is also large cumulus precipitation in the

locations. The increase of the specific humidity is related to the enhanced cumulus activity which increases the moisture convergence. The increased cumulus precipitation also intensifies low level evaporation which can moisten the atmosphere.

## 6.5 Radiation Budget

In the preceding sections we have shown that the implementation of the generalized cumulus parameterization causes changes of cumulus cloud population and cloud types. These changes have made improvements in the simulated cumulus precipitation patterns and the mean meridional circulation. It is well known that high level stratiform clouds related to deep convection have effects on the Earth's radiation budget and affect the atmospheric general circulation. Of course, stratiform clouds have the strongest effects on the radiation budget. The radiative effects corresponding to changes of the cumulus parameterization, however, can not be ignored in the model. We analyze the simulated radiation budgets from the C-run and the MCB-run in this section.

### 6.5.1 Planetary albedo

Fig. 6.22 shows planetary albedo distributions from the control simulation, the MCB simulation, and the ERBE data set. From the map (a) and (b), the model reproduces basic geographical distributions of the observed planetary albedo, e.g., lower albedo (less than 25%) in clear-sky regions over the subtropical oceans and high albedo (larger than 30%) over the major desert regions due to the higher reflections of the land surface. Over the tropical active convection regions, both simulations produce a high planetary albedo because of the unrealistically strong deep convection produced by cumulus parameterizations. There is no significant improvement on the over estimates of the planetary albedo in

## Planetary Albedo

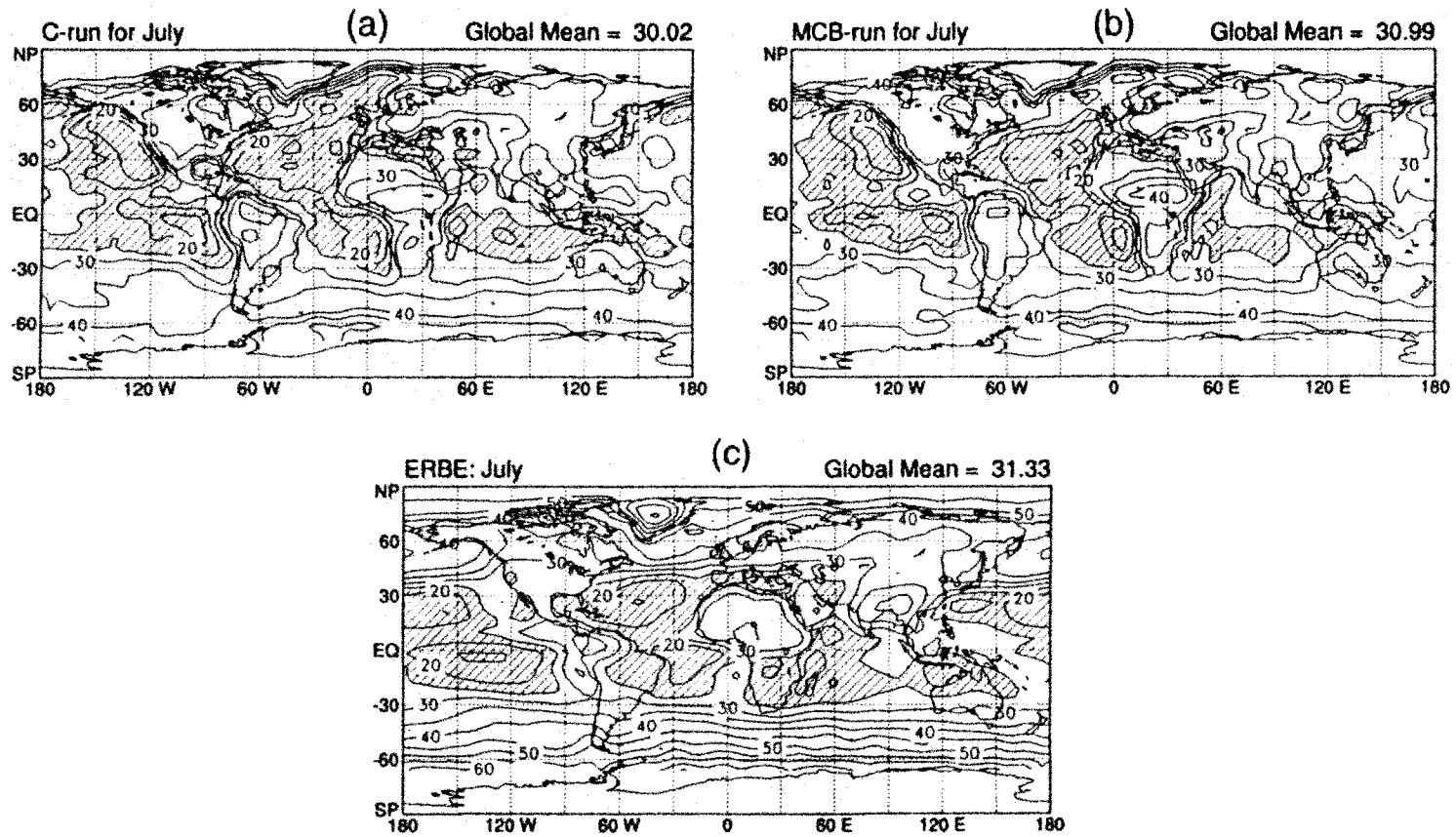


Fig. 6.22 July planetary albedo from control simulation (a); MCB simulation (b); and ERBE data (c). Units are in%. Values smaller than 25 are shaded. The contour interval is 5.

the MCB simulation since the overall intensity of moist convection is enhanced by the generalized cumulus parameterization. The underestimates of the planetary albedo in the Northern Hemisphere  $30^{\circ} \sim 60^{\circ}\text{N}$  in the control simulation, however, are improved in the MCB simulation. This is clearly seen in Fig. 6.23 which shows zonally averaged planetary albedo for July. The global mean of the planetary albedo from the MCB simulation is slightly closer to the observed value than that from the control simulation.

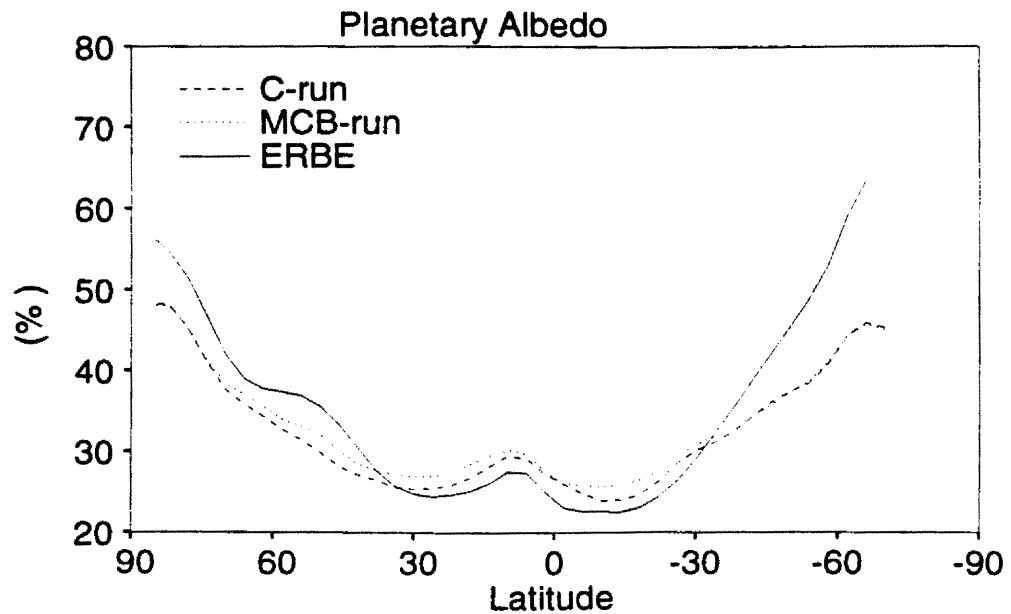


Fig. 6.23 Zonally averaged planetary albedo from the C-run (dashed line); the MCB-run (dotted line); and the ERBE data set for July. Units are in %.

### 6.5.2 OLR and absorbed solar radiation

The global maps of July outgoing longwave radiation (OLR) from the control simulation, the MCB simulation and ERBE are shown in Fig. 6.24. The MCB simulation and the control simulation have produced very similar OLR global distributions. Maps (a) and (b) have quite similar geographical patterns, e.g., the maxima of OLR over the subtropical

## Outgoing Longwave Radiation

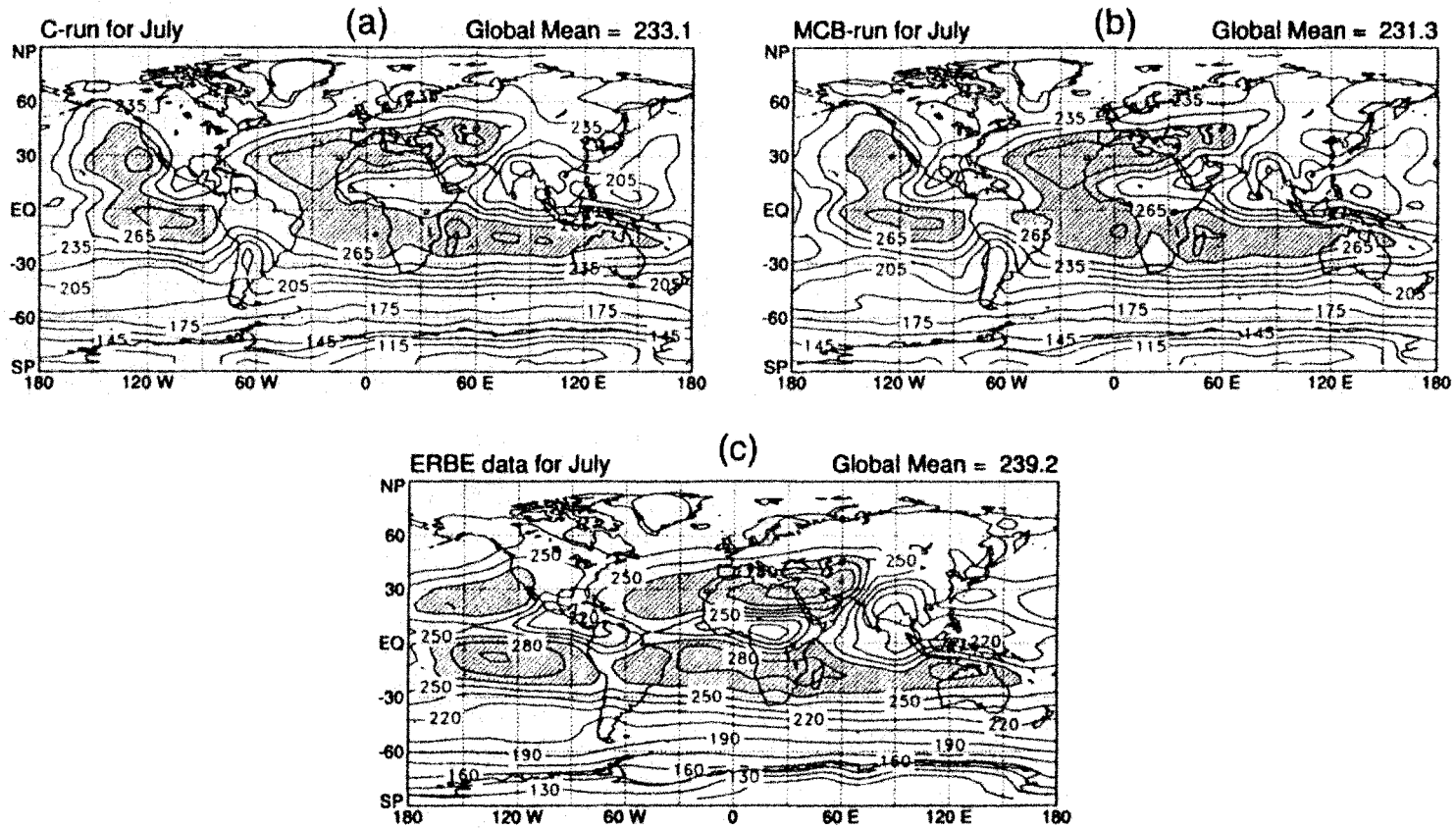


Fig. 6.24 July outgoing longwave radiation maps from the control simulation (a); the MCB simulation (b); and ERBE data (c). Units are in  $\text{W m}^{-2}$ . The contour interval is 15  $\text{W m}^{-2}$ . Values larger than 265  $\text{W m}^{-2}$  are shaded.

oceans; and minima over the Western Pacific, India monsoon and central America. The simulated OLR patterns are in good agreement with the observations shown in the map (c). However, there are some differences in OLR magnitudes between the model simulations and observations. The simulated OLR over the Western Pacific is too small compared with ERBE data. This may be caused by excessively strong cumulus convection.

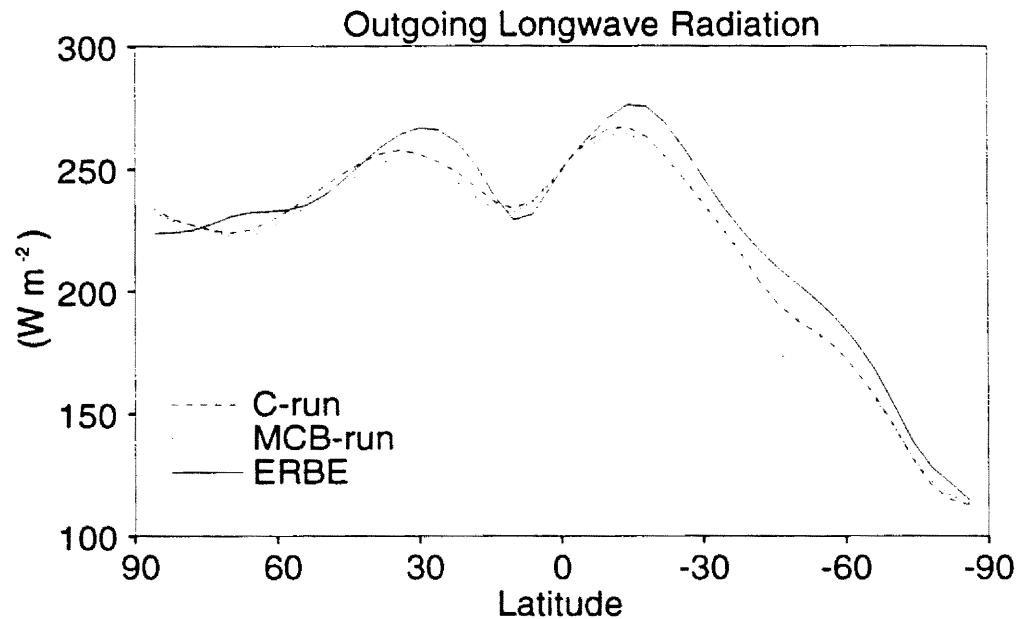


Fig. 6.25 Zonally averaged outgoing longwave radiation from the C-run (dashed line); the MCB run (dotted line); and the ERBE data set for July. Units are in  $W m^{-2}$ .)

The zonally averaged OLR distribution in the simulations and the ERBE observations are shown in Fig. 6.25. It is seen that the simulations produce zonally averaged OLR patterns that are similar to the observation, but smaller, except in the northern tropics. There is no significant difference between the MCB simulation and the control simulation.

Fig. 6.26 shows July absorbed solar radiation distributions from the control simu-

## Absorbed Solar Radiation

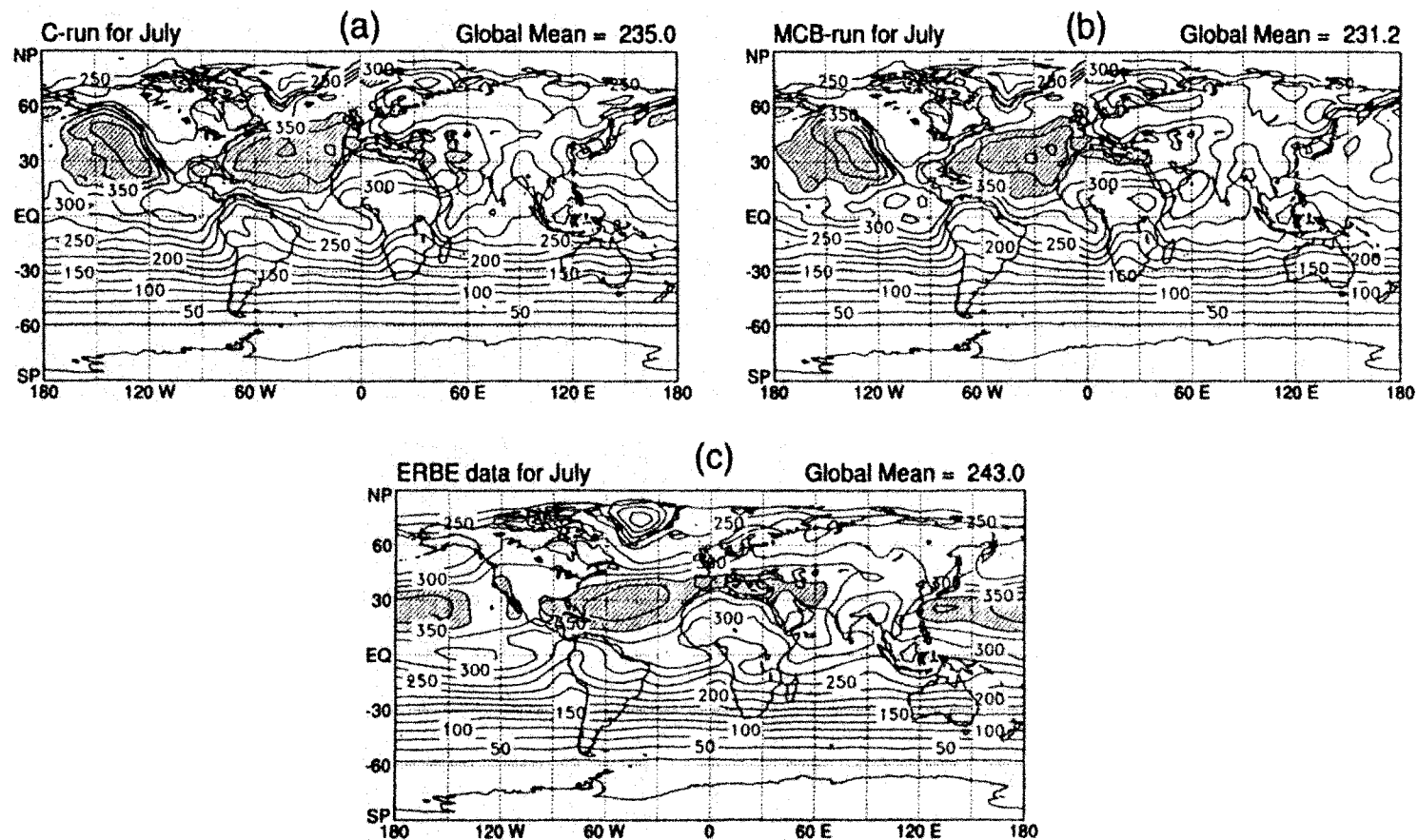


Fig. 6.26 July absorbed solar radiation from control simulation (a); MCB simulation (b); and ERBE data (c). Units are in  $\text{W m}^{-2}$  and values larger than  $350 \text{ W m}^{-2}$  are shaded.

lation, the MCB simulation, and the ERBE data set. The simulations have reproduced global absorbed solar radiation patterns similar to the observations, e.g., maxima of absorbed solar radiation over the subtropical oceans and the zonal distribution in the Southern Hemisphere. The MCB simulation and the control simulation produce similar absorbed solar radiation patterns. The zonally averaged absorbed solar radiation distributions shown

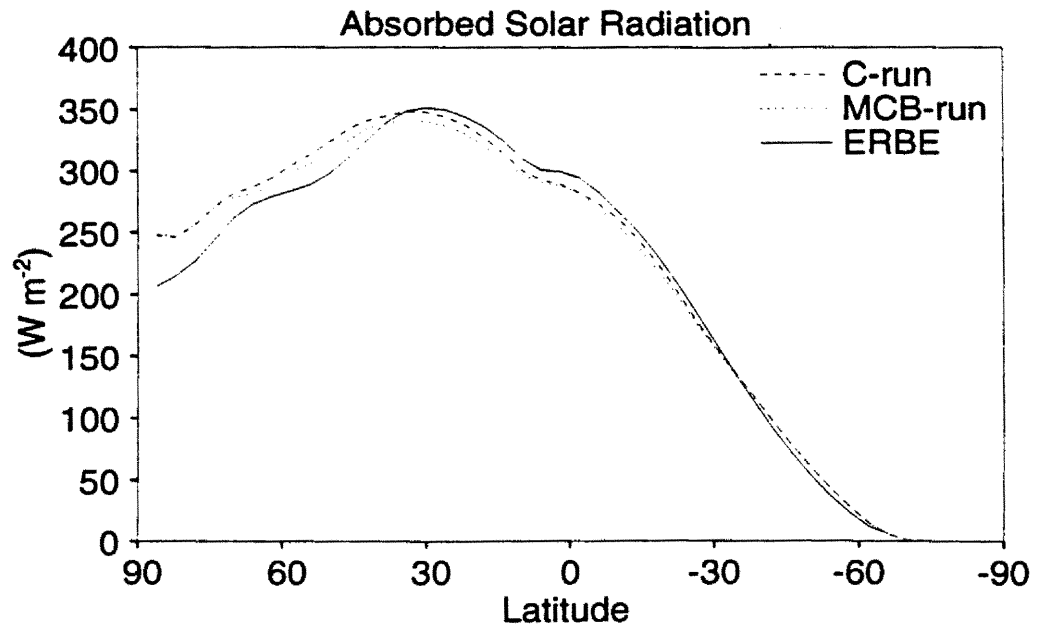


Fig. 6.27 Zonally averaged absorbed solar radiation from the C-run (dashed line); the MCB run (dotted line); and the ERBE data set for July. Units are in  $W m^{-2}$ .)

in Fig. 6.27 confirm that the two simulations give similar results.

As discussed earlier, the change of the cumulus activity in the MCB simulation leads to improvements in the model results, such as the simulated total precipitation patterns and the mean meridional circulation. In this section we have seen that the modifications of the simulated radiation budget by the MCB parameterization are not significant.

## **Chapter 7**

### **Tests of the MCB-Parameterization with Evaporation of Cumulus Rainfall below Cloud Base**

It is well known that in the real atmosphere evaporation can occur when falling raindrops reach unsaturated layers. The evaporation of falling raindrops can reduce the net precipitation reaching the ground surface and cools and moistens the atmosphere. Theoretical and experimental studies of the physical behavior of freely falling waterdrops have been carried out in many ways (Kinzer and Gunn 1951; Watts 1971; Beard and Pruppacher 1971). The evaporation of precipitation has been incorporated into GCMs in large-scale precipitation parameterizations (Sud and Walker, 1993; Fowler et al., 1994).

In the original A-S cumulus parameterization, cumulus precipitation is assumed to occur inside cumulus clouds because all cumulus clouds are assumed to have their cloud bases at the PBL top. In this case, the evaporation efficiency of cumulus precipitation is relatively very small and the evaporation of cumulus precipitation are ignored. Once the original A-S parameterization is generalized to the MCB parameterization, cumulus

clouds can originate from the free atmosphere. For the precipitation of altocumulus clouds, raindrops can fall great distances below cloud base before reaching the surface, and so evaporation is more likely to occur. In this section, we include evaporation of altocumulus precipitation when raindrops fall out cumulus clouds using the scheme by Fowler et al. (1994), and discuss the evaporation effects.

### 7.1 A cumulus rainfall evaporation scheme

In the MCB cumulus parameterization, cumulus clouds originating from both the PBL and the free atmosphere contribute to cumulus precipitation. In order to study effects of the evaporation of cumulus precipitation, we separate cumulus precipitations into two parts: CPB and CPF, where CPB for cumulus precipitation from cumulus clouds starting in the PBL and CPF for cumulus precipitation from cumulus clouds originating from the free atmosphere. We assume that the evaporation of CPB is very small and can be ignored because the subcloud layer corresponding to CPB is shallow. For the CPF, we assume that evaporation may occur when raindrops fall below cloud base.

Following Fowler et al. (1994), the continuous growth equation from Byers (1965) may be written as

$$\frac{d}{dt}M(D_R) = \frac{2\pi D_R (S_W - 1) F}{A' + B'} , \quad (7.1)$$

where

$$A' = \frac{L_v}{K_a T} \left( \frac{L_v M_w}{R^* T} - 1 \right) , \quad (7.2)$$

and

$$B' = \frac{R^* T}{\chi M_w e_{sw}} \quad (7.3)$$

All variables and constants appearing in above and following equations are defined in Table 7.1. The values of  $A'$  and  $B'$  given by Pruppacher and Klett (1978) are used in our precipitation evaporation scheme. In (7.1),  $F$  is a “ventilation factor” which may be written as (Beard and Pruppacher, 1971)

$$F = 0.78 + 0.31 S_c^{1/3} R_e^{1/2} \quad (7.4)$$

If raindrop sizes are assumed to be distributed continuously according to an inverse exponential distribution, the size distribution function for rain derived by Marshall and Palmer (1948) is

$$N_{DR} = N_{0R} \exp(-\lambda_R D_R) dD_R \quad (7.5)$$

where  $\lambda_R$  is the slope factor of the size distribution for rain and is given by

$$\lambda_R = \left( \frac{\pi \rho_L N_{0R}}{\rho q_r} \right) \quad (7.6)$$

Now, substituting (7.4) into (7.1), multiplying (7.1) by (7.5), and integrating over all drop sizes, the total evaporation rate of CPF below cloud base levels (CPF EVP) is then given by

$$\text{CPF EVP} = \frac{2\pi N_{0R} (S_w - 1)}{\rho (A' + B')} \cdot \left[ \frac{0.78}{\lambda_R^2} + 0.31 \frac{\left(a' \frac{\rho}{\mu}\right)^{1/2}}{\lambda_R^3} \Gamma(3) \left(\frac{P_0}{P}\right)^{0.2} \right] \quad (7.7)$$

The above equation can be simply expressed as a function of  $S_w$  and  $q_r$  by

$$\text{CPFEVP} = \text{FRV} \cdot (S_w - 1) \cdot q_r, \quad (7.8)$$

where

$$\text{FRV} = \frac{2}{\rho_L (A' + B')} \cdot \left[ 0.78 \lambda_R^2 + 0.31 \left( a' \frac{\rho}{\mu} \right)^{1/2} \lambda_R \Gamma(3) \left( \frac{p_0}{p} \right)^{0.2} \right]. \quad (7.9)$$

**Table 7.1: List of Symbols**

Symbol	Description	Value	Units
$\rho_L$	Density of water	$10^3$	$\text{kg m}^{-3}$
$\rho$	Density of air		$\text{kg m}^{-3}$
$V_R(D_R)$	Fallspeed of raindrop of diameter $D_R$		$\text{m s}^{-1}$
$D_R$	Raindrop diameter		m
$a'$	Constant in linear fallspeed relation for rain	$3 \times 10^3$	$\text{s}^{-1}$
$\mu$	Dynamic viscosity of air	$1.718 \times 10^{-5}$	$\text{kg m}^{-1} \text{s}^{-1}$
$P_o$	Pressure at the reference level	$10^5$	$\text{N m}^{-2}$
$L_v$	Latent heat of vaporization	$2.5 \times 10^6$	$\text{J kg}^{-1}$
$M_w$	Molecular weight of water	18.0160	
$K_a$	Thermal conductivity of air	$2.43 \times 10^{-2}$	$\text{J m}^{-1} \text{s}^{-1} \text{K}^{-1}$
$T$	Temperature		K
$R^*$	Universal gas constant	$8.314 \times 10^3$	$\text{J kmol}^{-1} \text{K}^{-1}$
$\chi$	Diffusivity of water vapor in air	$2.26 \times 10^{-5}$	$\text{m}^2 \text{s}^{-2}$
$e_{sw}$	Saturation vapor pressure over water		$\text{N m}^{-2}$
$N_{OR}$	Intercept value in raindrop size distribution	$8 \times 10^6$	$\text{m}^{-4}$
$q_r$	Mixing ratio of rain		$\text{kg kg}^{-1}$

To make the integration more manageable, it has been assumed that  $V_R(D_R) = a'D_R$  in the above derivations.

From equations (7.8) and (7.9), the efficiency of precipitation evaporation depends on the relative humidity, the density, the temperature and the pressure of the air below cloud base, the raindrop size distribution, and the terminal velocity of the raindrops. In the next section, we implement the cumulus precipitation evaporation scheme into the MCB cumulus parameterization, and compare simulation results with the MCB-run results discussed in the previous chapter.

## 7.2 Simulation test results

A one-month simulation test has been made with the CSU GCM using the MCB parameterization and the cumulus precipitation evaporation parameterization described above. The initial condition of the simulation test is from the MCB-run and starts from the end of June. The simulation test is denoted by MCBEVP-run in the following discussion. We compare and discuss the results from the MCB-run and the MCBEVP-run in this section.

### 7.2.1 Total precipitation rate

Fig. 7.1 shows total July precipitation maps from the MCB-run, the MCBEVP-run and their difference (MCBEVP minus MCB). In the MCBEVP run, since altocumulus precipitation below cloud base is allowed to evaporate, the total precipitation rate might be expected to be less than that of the MCB simulation. In the maps (a) and (b), the global mean of the MCBEVP simulation is  $4.19 \text{ mm day}^{-1}$ , which is slightly less than the global mean of the MCB simulation,  $4.20 \text{ mm day}^{-1}$ . Because the difference of the global means

## Total July Precipitation

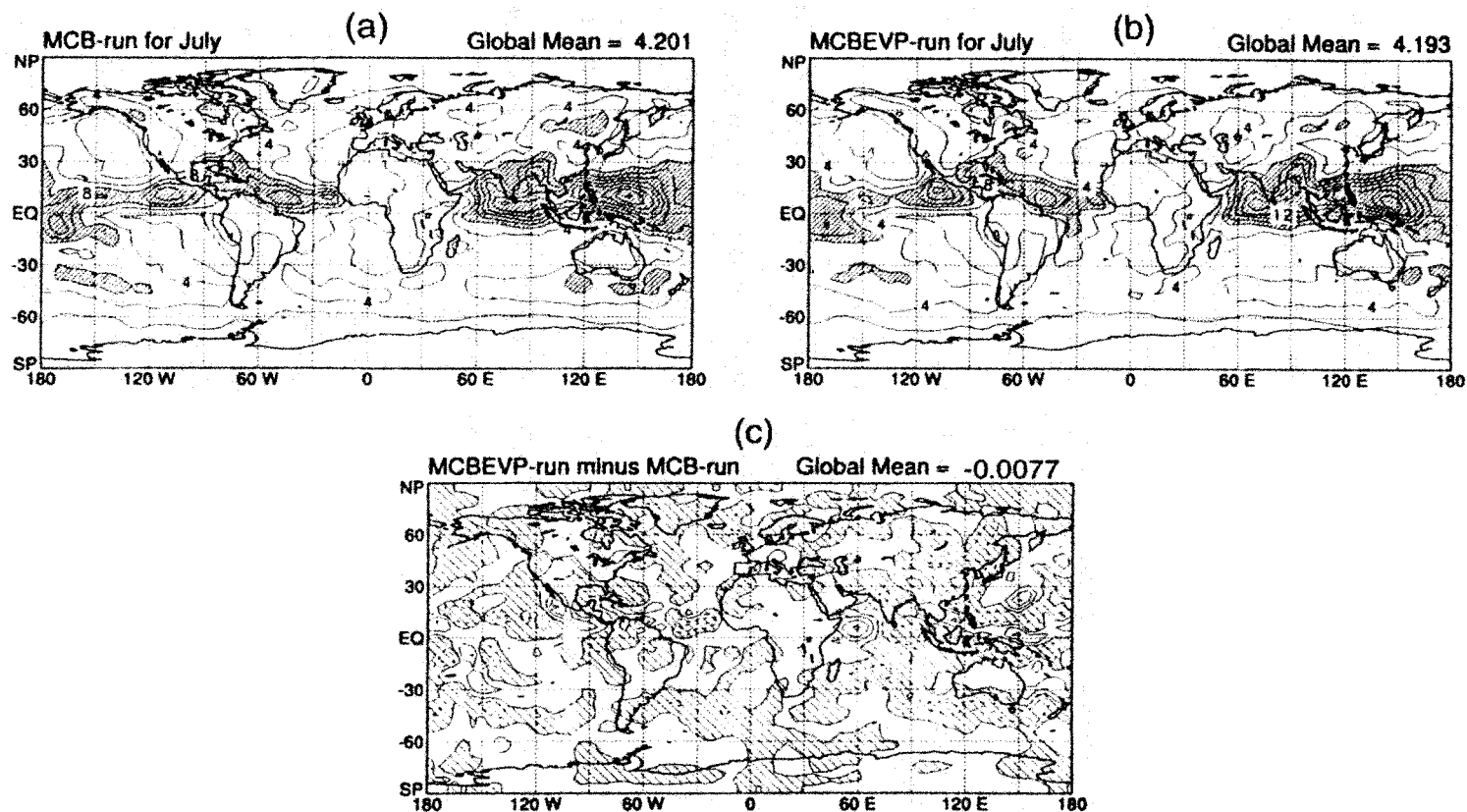


Fig. 7.1 Total July precipitation from the MCB simulation (a); the MCBEVP simulation (b); and their difference (c). Units are in  $\text{mm day}^{-1}$ . Contour intervals are 2 in (a) and (b), and 1 in (c). Values larger than 6 are shaded in (a) and (b), and values less than zero are shaded in (c).

between the MCBEVP -run and the MCB-run is very small ( $-0.01 \text{ mm day}^{-1}$ ), the evaporation effects of the altocumulus precipitation below cloud base might not be significant.

Comparing the maps (a) and (b), it can be seen that the MCBEVP simulation produces total July precipitation patterns quite similar to those of the MCB simulation, except that the maximum precipitation rate is smaller in the Western Pacific. In other words, the evaporation of altocumulus precipitation below cloud base does not change the total precipitation pattern significantly, because of the amount of evaporation is small. The difference map (c) indicates that precipitation decreases in most of areas in the MCBEVP simulation. The precipitation differences are not significant, however.

Tables 6.1 and 6.2 have shown that altocumulus clouds which have cloud bases at relative low levels (model levels 16 and 15 in the 17 vertical layer GCM) dominate the altocumulus population. Most altocumulus precipitation is from these cloud types, because of their moist cloud base condition. Since the altocumulus clouds which contribute most altocumulus precipitation have low cloud bases, i.e., there are only one or two layers between cloud base levels and the PBL, and the relative humidity might be high in these layers (so clouds can start from these layers), it is understandable that the evaporation of altocumulus precipitation below cloud base is not significant. This is the reason that the difference of the global mean total precipitation between the MCBEVP-run and the MCB-run is very small.

### 7.2.2 Comparisons of the moisture and temperature fields

The zonal mean specific humidity of the MCB-run, the MCBEVP-run, and their difference are shown in Fig. 7.2. The basic patterns of the specific humidity from the two

## Specific Humidity

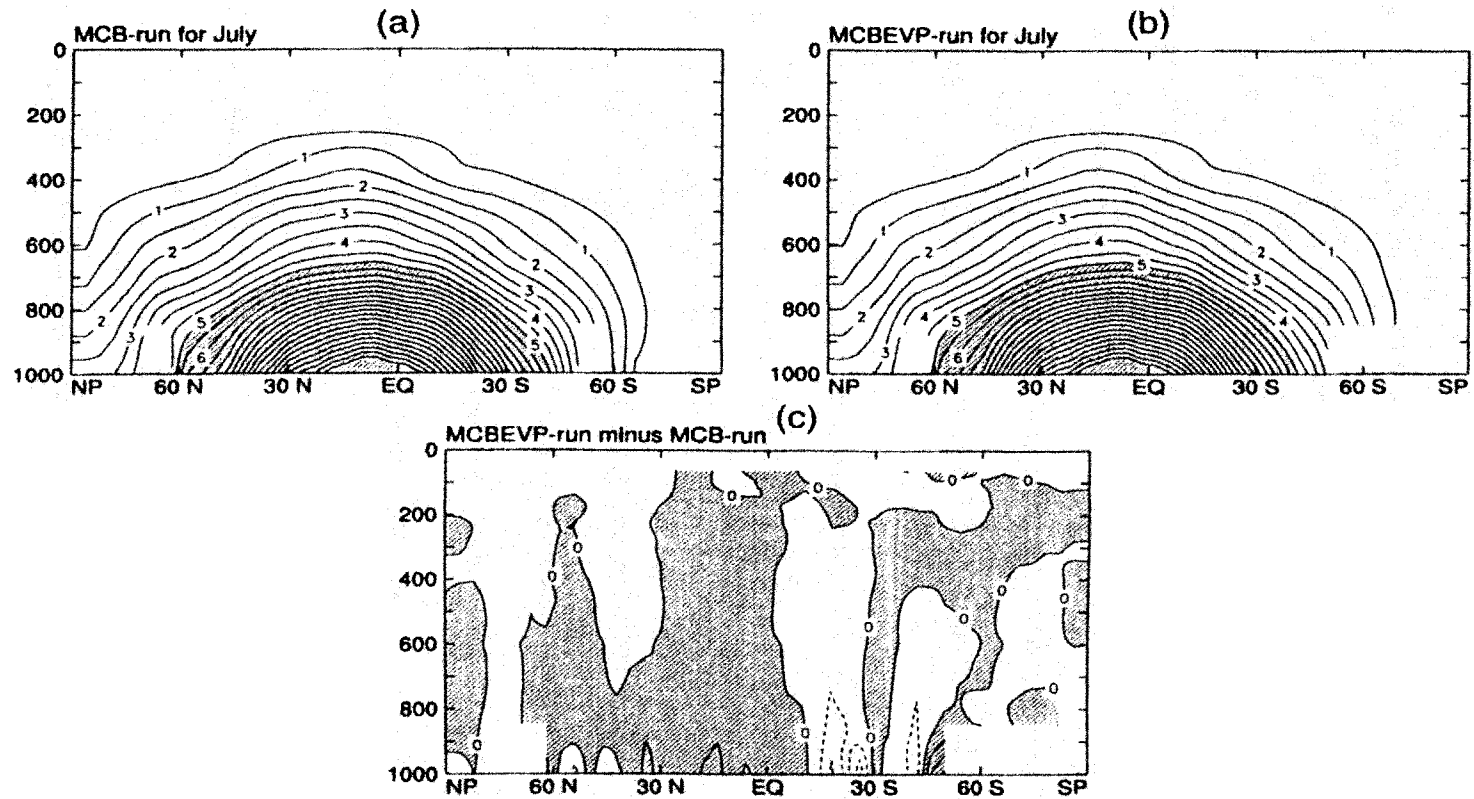


Fig. 7.2 Zonal mean specific humidity from the MCB-run (a); the MCBEVP-run (b); and the MCBEVP-run minus the MCB-run (c). Units are in  $\text{g kg}^{-1}$ . Intervals are 0.5 in the maps (a) and (b) and 0.1 in (c). Values larger than 5 are shaded in (a) and (b). Values larger than zero are shaded in (c).

## Temperature

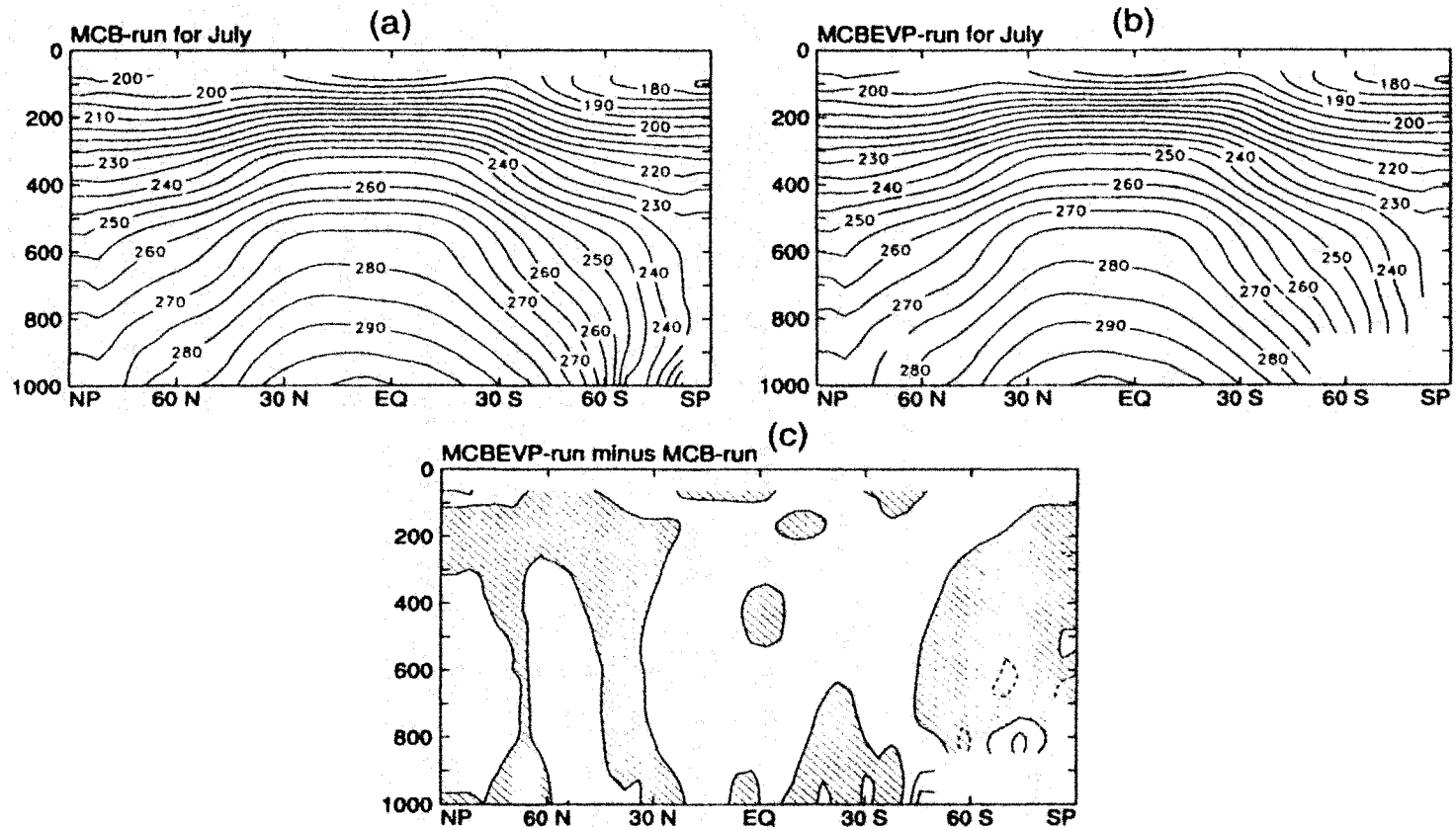


Fig. 7.3 Latitude-pressure temperature distributions from the MCB-run (a); the MCBEVP-run (b); and the differences of MCBEVP and the MCB simulations. The units are in degree K. Contour intervals are 5 K in (a) and (b); and 0.2 K in (c).

simulations are quite similar, e.g., the specific humidity maxima are located at tropics near the surface and decreases upward and poleward. Since the evaporation effects are not significant, as indicated in the last section, the specific humidity differences between two runs in (c) are small. Most of the differences are less than  $0.1 \text{ g kg}^{-1}$  in panel (c). The relatively larger differences are seen in the lower levels in the northern tropics and subtropics. The many altocumulus clouds with bases at model levels 15 and 16 in these regions may account for the maximum in the difference map (c). The comparisons of the specific humidity fields indicate again that the evaporation of altocumulus precipitation below cloud base has no significant influence on the simulation.

Fig. 7.3 shows the zonal mean temperature fields of the MCB-run, the MCBEVP-run and their differences. From the maps (a) and (b), the zonal mean temperature patterns of the MCB and the MCBEVP simulations are quite similar. The temperature difference between the runs is very small.

### 7.2.3 Mean meridional circulation

The mean meridional circulations of the MCB and the MCBEVP simulations are shown in Fig. 7.4. The MCB run and the MCBEVP run produce similar mean meridional circulations although slight differences can be seen in the maps (a) and (b) of Fig. 7.4 in the Southern Hemisphere. Similar results are expected for the reasons mentioned above. Compared with the control simulation and observations (shown in Fig. 6.15), the mean meridional circulations of both the MCB run and the MCBEVP run agree better with observations than that from the control simulation.

## Mean Meridional Circulation

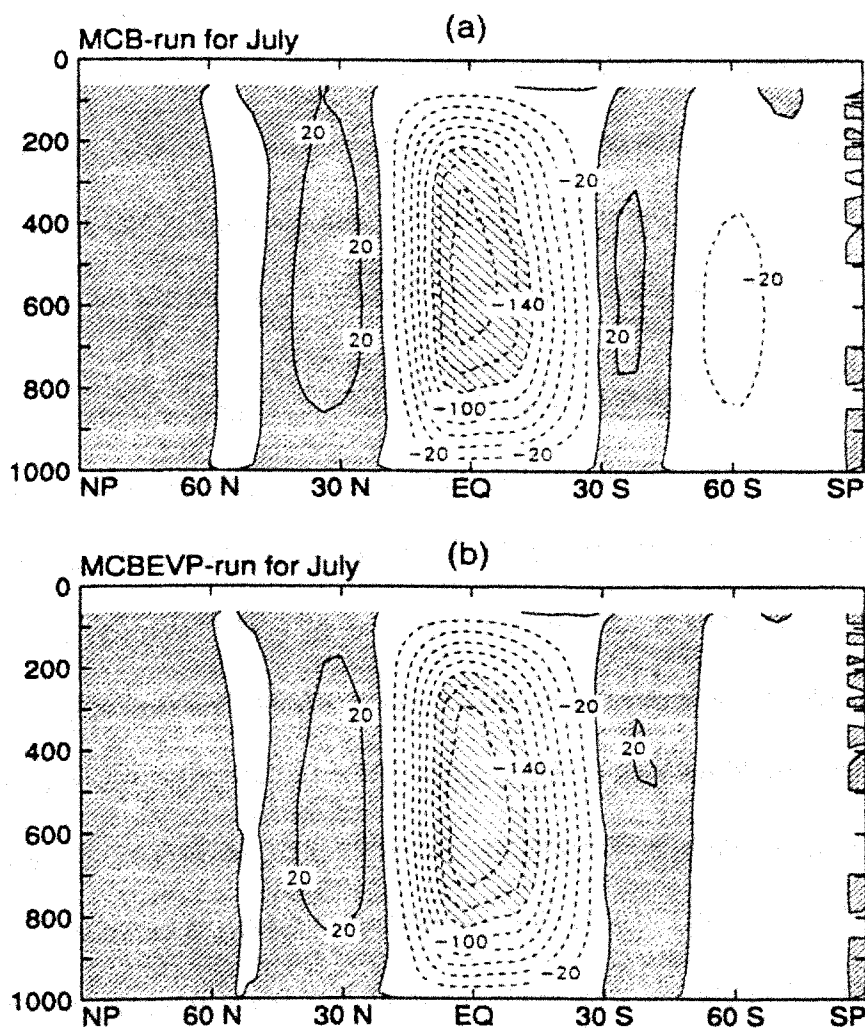


Fig. 7.4 July streamfunction of the mean meridional circulation from the MCB-run (a) and the MCBEVP-run (b). Units are in  $10^9 \text{ kg s}^{-1}$ . The control interval is  $20 \times 10^9 \text{ kg s}^{-1}$ . Positive values are heavy shaded and values less than  $-120 \times 10^9$  are light shaded.

### 7.3 Summary

The evaporation of falling raindrops can affect the atmospheric temperature and moisture fields and the surface precipitation rate. Evaporative cooling can also affect the atmospheric stability. The evaporation of stratiform precipitation has been incorporated

into GCMs in many ways, in various “large-scale precipitation” parameterizations. Since convective precipitation is usually very strong and concentrated in small areas, its corresponding evaporation efficiency is assumed very small. In the original A-S cumulus parameterization, cumulus clouds are assumed to start from the PBL and cumulus precipitation is assumed to occur inside the cumulus clouds. The subcloud layer is thin. In this case, it is reasonable to ignore the evaporation of cumulus precipitation.

In the MCB parameterization, cumulus clouds can start from any level of a GCM. The raindrops fall outside the cumulus clouds, below cloud base. In this case, evaporation of convective precipitation should be considered. In this chapter, we incorporate the raindrop evaporation scheme from Fowler et al. (1994) into the MCB parameterization and carry out a one-month MCBEVP test. Some test results, such as the total precipitation field, the moisture and the temperature fields, and the mean meridional circulation, are compared with the corresponding MCB results. We find that the results of the MCBEVP test show no significant changes relative to the MCB simulation. In Chapter 6 we have shown that most of altocumulus clouds have cloud bases at model levels 15 and 16 for the 17-level GCM. This means that the falling path of raindrops from cloud base height to the ground surface is short and so the evaporation efficiency of altocumulus clouds below cloud bases can be small. The test results indicate that the evaporation of altocumulus precipitation below cloud base levels is not significant.

# Chapter 8

## An Experiment with Revised Cloud base Conditions

### 8.1 Design of the experiment

As reviewed in Chapter 4, in many convection studies (Scorer and Ludlam 1953; Fankhauser et al. 1982; Blyth et al. 1988) cumulus clouds are considered as rising thermal bubbles. A thermal bubble consists of warm and moist air. A cumulus parameterization proposed by Ooyama (1971) uses the assumption that cumulus clouds can be represented as non-interacting spherical bubbles.

In the MCB parameterization, we assume that clouds can exist once they satisfy the five cloud existence criteria, and also that the cloud base properties are the same as the environmental air of the cloud base layer. For example, if  $h_{CB}(k)$  and  $q_{CB}(k)$  are cloud base moist static energy and total water mixture ratio, respectively, and the cloud base is in layer  $k$  of the model, then

$$h_{CB}(k) = \bar{h}_k, \quad (8.1)$$

and

$$q_{CB}(k) = \bar{q}_k, \quad (8.2)$$

where  $\bar{h}_k$  and  $\bar{q}_k$  are the moist static energy and the total water mixing ratio of the environmental air in layer  $k$  of the model, respectively.

According to the bubble theory, cumulus clouds usually originate in places where the air is locally warm and moist. In our experiment with enhanced cloud base moisture, we assume that the cloud base moisture is 5% greater than that of the environment. For example, if the cloud base is in layer  $k$  of the model, the above assumption can be written as

$$q_{CB}(k) = 1.05\bar{q}_k. \quad (8.3)$$

The cloud base moist static energy in the experiment is calculated corresponding to the revised cloud base moisture condition, assuming no cloud-base dry static energy perturbation

In the next section, some results of the experiment are discussed and compared with the MCB run results.

## 8.2 Results and discussions

A one month experiment using the revised cloud base moisture conditions in the MCB parameterization has been carried out using the CSU GCM. The run starts from July 1st. The initial conditions used in the experiment are from the MCB run. The experiment

is called MCBRVC run in the following discussion.

### 8.2.1 Simulated cumulus activity

Corresponding to the cloud type analysis in Chapter 6, a 10-day extended run continuing the MCBRVC run has been made. Cumulus cloud incidence for various cloud types and their corresponding cloud base mass fluxes have been accumulated. Differences of cumulus incidence and cloud base mass flux for various cloud types between the MCBRVC run and the MCB run are shown in Tables 8.1 and 8.2.

From Table 8.1, we see that there are considerable changes in the cumulus incidence distribution in response to the enhanced cloud base moisture. The incidence of altocumulus clouds in middle and lower troposphere, e.g., clouds with bases at levels 12 ~ 16 of the model, increases significantly. Meanwhile, the incidence of altocumulus clouds in the upper troposphere, e.g., clouds with bases at levels 4 ~ 7 of the model, apparently decreases. The incidence of cumulus clouds starting in the PBL decreases slightly. The changes of the cumulus incidence distribution implies that altocumulus clouds, especially shallow altocumulus, at low levels are greatly intensified with moistened cloud base. Table 8.2 shows the changes of cloud base mass flux in response to the enhanced cloud base moisture condition. We see that for most of the clouds with cloud bases in the middle and lower troposphere (including the PBL), the cloud base mass flux is apparently increased in response to the revised cloud base moisture conditions, although the cloud incidence may slightly decrease. Cloud base mass flux of some upper level altocumulus is reduced.

We have found that the largest cumulus incidence in the MCBRVC run is for clouds with bases at the PBL and tops at level 15, which is same as the MCB run (see

**Table 8.1: Differences of average cumulus cloud incidence between the MCBRVC run and the MCB run for various cloud types**

Base level														
4	--	--	--	--	--	--	--	--	--	--	--	--	--	-27.1
5	--	--	--	--	--	--	--	--	--	--	--	--	-36.9	-3.8
6	--	--	--	--	--	--	--	--	--	--	--	-22.9	-8.04	-2.04
7	--	--	--	--	--	--	--	--	--	--	-6.45	-2.83	-0.28	0.46
8	--	--	--	--	--	--	--	--	--	-3.3	-0.54	0.1	0.0	-0.12
9	--	--	--	--	--	--	--	--	-3.13	-0.14	0.3	0.05	-0.19	-0.18
10	--	--	--	--	--	--	--	-2.23	0.15	0.27	0.07	0.02	0.13	-0.09
11	--	--	--	--	--	--	-0.58	0.54	0.71	0.05	-0.03	-0.02	0.06	0.03
12	--	--	--	--	--	0.84	2.02	1.35	1.17	0.74	0.38	0.33	0.26	0.12
13	--	--	--	--	0.88	1.57	1.64	0.38	0.82	0.78	0.32	0.54	0.53	0.35
14	--	--	--	1.51	2.06	1.9	2.3	1.67	0.9	0.92	1.01	0.61	0.38	0.38
15	--	--	3.9	5.15	4.0	0.6	0.4	0.4	0.4	-0.17	1.37	0.31	0.14	-1.04
16	--	10.6	11.2	1.6	-1.5	-5.9	-7.3	-6.1	-6.0	-2.8	-3.2	-6.5	-6.9	-6.5
17	-2.03	-22.7	-7.80	-6.20	-3.7	-6.2	-7.2	-2.5	-1.3	0.7	0.0	-0.3	-1.6	-3.2
Top Level	16	15	14	13	12	11	10	9	8	7	6	5	4	3

**Table 8.2: Differences of average cloud base mass flux between the MCBRVC run and the MCB run for various cloud types (Units are  $10^{-2}$  kg m<sup>-2</sup> hour<sup>-1</sup>)**

Base level															
4	--	--	--	--	--	--	--	--	--	--	--	--	--	--	-1.39
5	--	--	--	--	--	--	--	--	--	--	--	--	--	-1.86	0.04
6	--	--	--	--	--	--	--	--	--	--	--	-1.15	-0.37	-0.08	
7	--	--	--	--	--	--	--	--	--	--	-0.32	-0.12	0.04	0.14	
8	--	--	--	--	--	--	--	--	--	-0.17	-0.01	0.02	0.04	0.04	
9	--	--	--	--	--	--	--	--	-0.17	0.01	0.01	0.06	-0.02	0.01	
10	--	--	--	--	--	--	--	-0.11	0.02	0.08	0.10	0.04	0.13	-0.12	
11	--	--	--	--	--	--	-0.02	0.08	0.29	0.11	0.04	0.04	0.08	0.09	
12	--	--	--	--	--	0.07	0.35	0.92	1.20	0.92	0.52	0.60	0.52	0.32	
13	--	--	--	--	0.07	0.28	1.11	2.15	2.16	1.69	0.77	1.34	1.23	0.73	
14	--	--	--	0.12	0.35	1.52	2.77	3.21	2.26	2.69	2.81	2.13	1.24	1.13	
15	--	--	0.29	1.17	3.82	3.46	6.06	8.19	8.4	5.08	7.52	5.09	4.49	1.1	
16	--	0.79	2.69	5.79	8.19	11.4	12.6	14.1	10.7	12.2	8.8	2.99	0.65	-0.17	
17	-0.03	1.97	7.22	5.98	9.61	9.80	11.4	19.0	15.8	11.1	6.66	7.39	7.33	1.32	
Top Level	16	15	14	13	12	11	10	9	8	7	6	5	4	3	

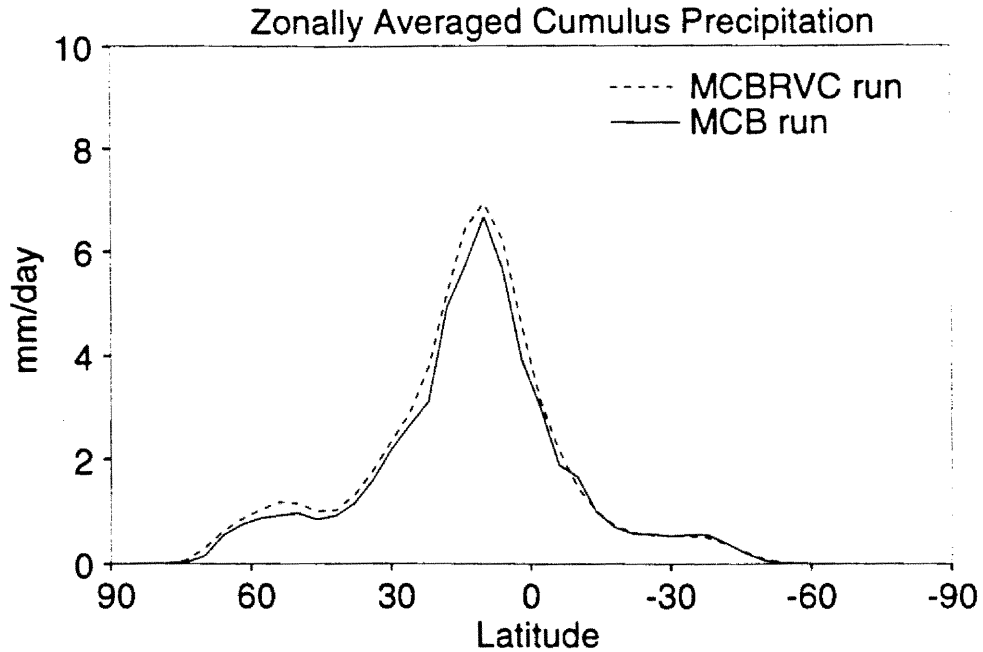


Fig. 8.1 July zonally averaged cumulus precipitation rates from the MCBRVC run (dashed line) and the MCB run (solid line). Units are  $\text{mm day}^{-1}$ .

Table 6.1). In the real atmosphere, we often see that most of the cumulus clouds start at the PBL and have tops just above the PBL. We have conducted an short test to study this phenomenon by using a low resolution GCM. In the test, we assumed that there is no entrainment for cumulus starting at the PBL. The results show that the Lifting Condensation Level (LCL) of PBL air is higher than the layer adjacent to the PBL. This strongly suggests that the LCL is too high in the model. This could be caused by a too warm PBL, or a too dry PBL, or both. Fig. 6.13 shows that the model produces a drier PBL than observed and Fig. 3.12 shows that a warmer tropical surface layer is produced by the model. Further studies of the problem is needed.

### 8.2.2 Precipitation

In view of the changes of the cumulus activity from the MCB run to the MCBRVC

run, we expect differences of the cumulus precipitation rates between the two runs. The zonally averaged cumulus precipitation rates from the two runs are shown in Fig. 8.1. We see that the cumulus precipitation rate of the MCBRVC run is larger than that of the MCB run, as expected, for almost all latitudes. The increment is small, however.

Fig. 8.2 shows the zonally averaged total precipitation rates from the MCBRVC run, the MCB run, and Legates and Willmott (1990). The MCBRVC run produces zonally averaged total precipitation similar to that of the MCB run. Both of them are larger than observed. In the northern tropics, the total precipitation rate of the MCBRVC run is slightly larger than the MCB run, which is caused by the larger cumulus precipitation of the MCBRVC run.

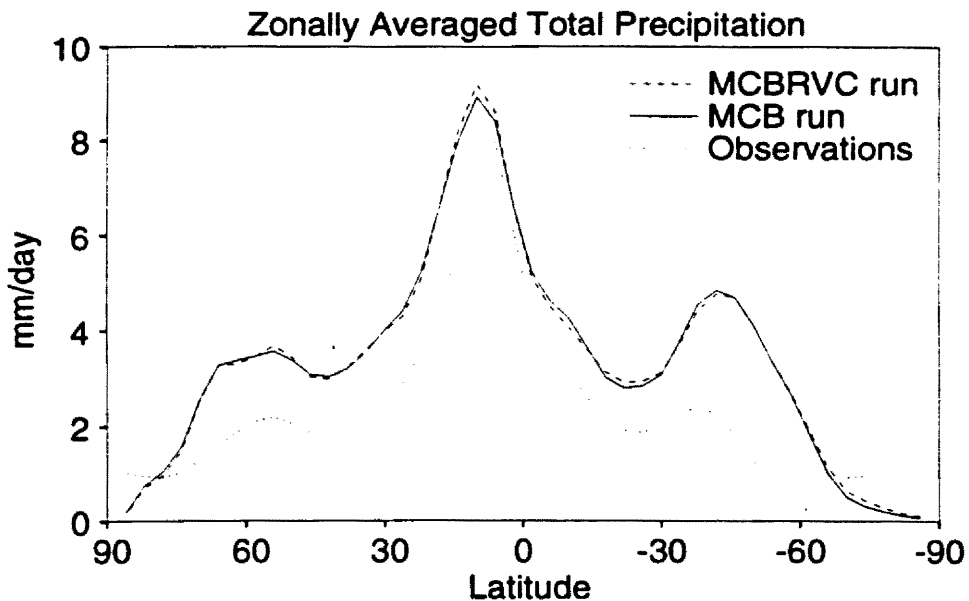


Fig. 8.2 July zonally averaged total precipitation rates from the MCBRVC run (dashed line); the MCB run (solid line); and observations (from Legates and Willmott, 1990) (dotted line). Units are  $\text{mm day}^{-1}$ .

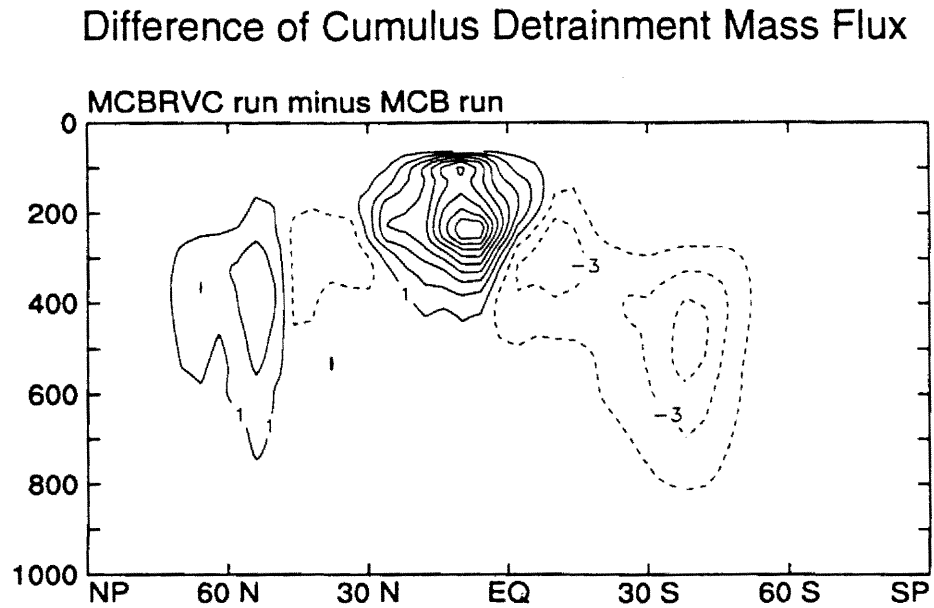


Fig. 8.3 Latitude-pressure cross section of cumulus mass flux difference between the MCBRVC run and the MCB run. Unit is  $10^{-3}$  hour<sup>-1</sup>. The contour interval is  $2 \times 10^{-3}$  hour<sup>-1</sup>.

### 8.2.3 Cumulus detrainment mass flux and specific humidity

Fig. 8.3 shows latitude-pressure cross section of cumulus mass flux difference between the MCBRVC run and the MCB run. The cumulus detrainment mass flux increases in the upper troposphere, and decrease in the middle troposphere in the MCBRVC run compared with the MCB run. The changes of the cumulus detrainment mass flux distribution suggest that cumulus clouds with tops at upper levels are enhanced, and cumulus clouds with tops at middle levels are reduced.

The latitude-pressure cross section of the specific humidity difference between the MCBRVC run and the MCB run is shown Fig. 8.4. In the northern tropics, enhanced shallow and deep cumulus clouds with bases at low levels have drying effects on the environ-

## Specific Humidity Difference

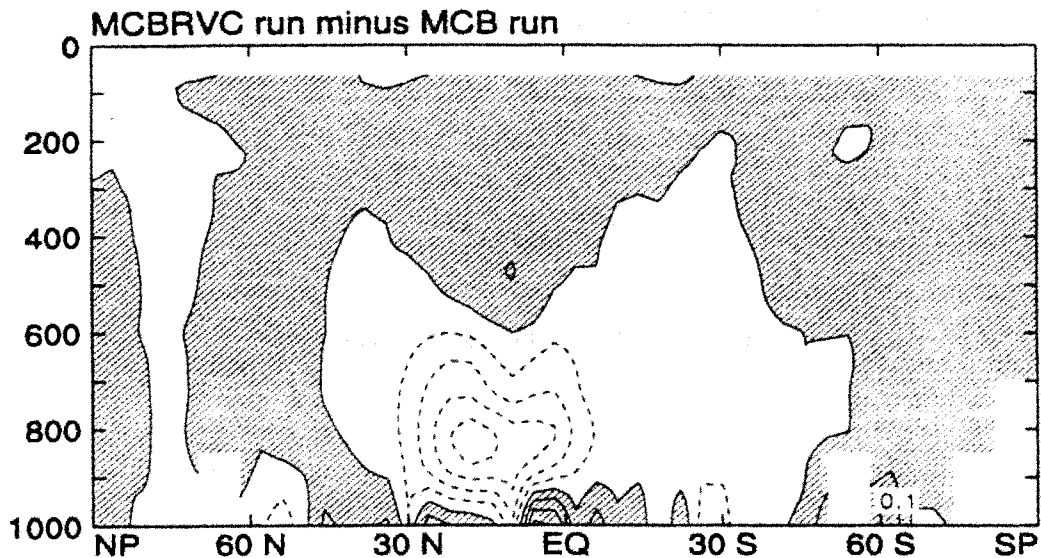


Fig. 8.4 Latitude-pressure cross section of specific humidity difference between the MCBRVC run and the MCB run. Unit is  $\text{g kg}^{-1}$ . The contour interval is  $0.1 \text{ g kg}^{-1}$ . Positive values are shaded.

ment. The MCBRVC run produces smaller specific humidity than the MCB run in lower layers. The wetter upper troposphere in the MCBRVC run is caused by the increased upward moisture transport corresponding to the enhanced cumulus clouds with cloud tops at upper levels. This is consistent with the changes of the cumulus detrainment mass flux distribution. The temperature and circulation patterns of the MCBRVC run (not shown) are very similar to those of the MCB run.

In summary, the MCBRVC experiment shows that the simulated cumulus activity is sensitive to the cloud base conditions. The enhanced cloud base moisture condition can intensify both shallow and deep cumulus clouds originating at low levels. To improve the simulated climate, more realistic cloud base conditions are needed.

By analyzing the cloud type distribution and conducting a non-entraining cloud experiment, we conclude that the simulated PBL is too warm and too dry. The too warm and too dry tropical layer has been seen in Fig. 6.12 and Fig. 6.13. It is necessary to study the reasons for this.

## **Chapter 9**

# **Summary and Conclusions**

### **9.1 Summary**

Cumulus convection plays important roles in the atmospheric general circulation. Cumulus parameterizations are designed to predict the statistical effects of cumulus clouds on their large-scale environment, by using large-scale variables. The A-S parameterization is a comprehensive theory of interactions between cumulus convection and its environment, as well as the PBL. The A-S parameterization uses the assumption that all cumulus clouds start from the PBL top. MSTADJ has been used as a supplementary parameterization to represent moist convection that originates in the free atmosphere.

Some observational studies indicate that in the real atmosphere cumulus clouds, including deep clouds, can originate above the PBL. Numerical simulations also show that the MSTADJ incidence can be comparable to the cumulus incidence for clouds starting in the PBL. In order to understand the effects of altocumulus clouds, a simulation experiment has been made using the CSU GCM, in which MSTADJ is turned off. The results of the

experiment are significantly different with the control run (the C-run). This means that MSTADJ has important effects on the results. In other words, moist convection originating in the free atmosphere should not be ignored in a GCM. Since MSTADJ is designed only to eliminate moist instability between two adjacent model layers, it is not sufficiently general. Based on both observational and modeling studies, a more general cumulus parameterization is needed for simulating large-scale circulations. The main goal of this report is to develop and test a more general cumulus parameterization which can represent all cumulus cloud types in a GCM.

The A-S parameterization is complex and difficult to implement in a GCM. In order to avoid further increasing its complexity. As the first step, we simplify the A-S parameterization.

Starting from Chapter 4, a linear mass flux profile is introduced to replace the exponential mass flux profile in the original A-S parameterization. For a given height above cloud base, linear relationships between entrainment and the in-cloud moist static energy and in-cloud moisture are demonstrated mathematically. A simplified cloud model, which can be used to calculate in-cloud soundings, cloud liquid water, and cumulus precipitation production rates in different model layers, has been developed by using the linear mass flux assumption. The ice phase is included in the linear version of the cloud model. To reduce differences between the linear cloud model and the original one, cloud-top entrainment has been added in the simplified cloud model. In the original A-S parameterization, an iterative method is used to determine the entrainment rate. This is very time consuming and complicated. In the revised parameterization, we have derived a much sim-

pler method to determine the entrainment rate, as shown in Eq. (4.4). To complete the simplified cloud model, five criteria are introduced for cloud existence.

A three month simulation experiment starting, from May 1st, has been carried out using the linearized cumulus parameterization. The experiment is called the L-run. The initial conditions of the L-run are taken from a previous long-term model run, and are the same as ones used in the C-run. The L-run results for July are compared with those of the C-run. The comparisons show that the L-run can produce cumulus activity quite similar to that of the C-run, including similar cumulus incidence and cumulus precipitation patterns, and similar cumulus heating and moistening patterns. The simulated climate of the L-run is also quite similar to that of the C-run, e.g., similar temperature, moisture fields and total precipitation patterns, as well as atmospheric circulations and radiation fields. About 15% of the cpu time for cumulus parameterization is saved in the L-run compared to the C-run, and this can be further improved. The simulation experiments indicate that the linearized cumulus parameterization with cloud-top entrainment can replace the original A-S parameterization with good model performance and less computation. The simplified parameterization allows us to include more physics.

A generalized cumulus parameterization with multiple cloud base levels has been developed in Chapter 6, starting from the simplified single cloud-base parameterization. The main characteristic of the multiple cloud base parameterization is that the cloud base level becomes a new “cloud type” index in the corresponding cloud model. One more “cloud type” index in the cloud model means that the number of potential cloud types increases dramatically. Major changes have been made to incorporate the new “cloud

type” index in the cloud model for calculations of the entrainment, the cloud work function, the cumulus kinetic energy, cloud existence tests, in-cloud properties, and the feedbacks of cumulus clouds on the environment.

We have incorporated the multiple cloud base cumulus parameterization into the CSU GCM. A three-month simulation experiment has been made starting from May 1st, using the same initial conditions as in the C-run and the L-run. The experiment is called the MCB run. The results of the MCB run, including the cumulus activity in the model, the cumulus effects on the environment, the simulated climate, the atmospheric circulation, and radiation budget, have been analyzed and compared with the C-run and observations. In the MCB run, cumulus incidence increases because of the increased number of potential “cloud types.” The cloud type distribution shows that compared with the C-run cumulus clouds with tops in the middle and lower troposphere increase; deep cumulus clouds with bases at the PBL and tops in the upper troposphere decrease, however. The reason is that altocumulus clouds retard the growth of deep convection by competing CAPE and moisture.

In the cloud type distribution of the MCB run, cumulus clouds originating in the PBL still dominate the global cumulus cloud population. With more shallow clouds and fewer deep clouds, the MCB run produces a smoother cumulus precipitation pattern than that of the C-run. As a result, the simulated total precipitation of the MCB run agrees better with observations than the C-run. Both runs produce a warmer tropical troposphere than observed. Due to the reduction of deep convection, a more moist lower and middle troposphere is produced by the MCB run. With the weaker penetrative cumulus convec-

tion in the tropics, in conjunction with the decreased cumulus precipitation and latent heating, the MCB run produces a weaker Hadley cell and a clearly stronger Ferrel circulation in the Southern Hemisphere, which is in much better agreement with observations.

The effects of altocumulus clouds on soundings at some individual locations are also analyzed in regions where altocumulus clouds are active. It is seen that the MCB simulation produces warmer middle and upper troposphere, and cooler lower troposphere, compared with the C-run in these regions.

The radiation budgets produced by the MCB run and the C-run are also compared in Chapter 6. The modifications of the simulated radiation budget by the MCB parameterization are not significant.

When the multiple cloud base cumulus parameterization is used in the model, precipitation from altocumulus clouds can fall through unsaturated air below cloud base before reaching the surface. A one month simulation has been made with the incorporation of an altocumulus rainfall evaporation scheme. The experiment is called MCBEVP run. The simulation results of MCBEVP run have been analyzed and compared with those of the MCB run. Since most of altocumulus clouds have bases at model levels 15 and 16, the falling path of raindrops below cloud base is short. Therefore the evaporation efficiency is small. The test results show that the evaporation of altocumulus precipitation below cloud bases is not significant.

In the original A-S parameterization, it is assumed that the cloud base has the same properties as the environmental air in the same layer. In reality, the cloud base conditions

usually are different with the environmental air. An experiment with the revised cloud base moisture condition has been conducted. The results show that the simulated cumulus activity is sensitive to cloud base conditions and more realistic cloud base conditions are needed to improve the model results. Meanwhile, a test has been conducted to investigate why shallow cumulus clouds do not stop in the layer immediately above the PBL. The results show that unsaturated cloud tops are the major reason. This means that the LCL of the PBL air is too high.

## 9.2 Conclusions

Major conclusions of this study are:

- The A-S cumulus parameterization can be greatly simplified by the linear mass flux profile assumption with the inclusion of cloud-top entrainment. The L-run produces quite similar cumulus activity and simulated climate as the C-run. The simplification of the A-S parameterization allows further improvement by adding more physics.
- A generalized multiple cloud base cumulus parameterization has been developed and implemented in the CSU GCM. In the MCB run, cumulus cloud types are increased by adding altocumulus clouds. The altocumulus clouds suppress deep convection by competing for CAPE. Deep convection is reduced in the MCB run.
- With increased cloud types and reduced deep convection, a wider and smoother cumulus precipitation pattern is produced by the MCB parameterization. This makes to the total precipitation pattern in the MCB run agree better with observations than the control run does.

- The MCB run produces a more realistic meridional circulation pattern than the control run. The excessively strong Hadley cell of the C-run has been weakened due to the weaker penetrative cumulus convection in the tropics of the MCB run. A clear Ferrel cell in the Southern Hemisphere is seen in the MCB run, which agrees with observations.

- Altocumulus clouds tend to warm the middle and upper troposphere, and cool below in some active altocumulus regions. The effects of the MCB parameterization on the global radiation budget are not significant.

- The evaporation efficiency of altocumulus precipitation below cloud base is small because most of altocumulus clouds produced by the model have relatively low cloud bases and so the falling path of raindrops is short.

- Cumulus activity is sensitive to cloud base conditions. More realistic cloud base conditions can improve the cumulus parameterization.

- The tropical PBL of the model is too dry and too warm. This causes the LCL of the PBL air is too high. This problem needs to be solved to improve the model's performance.

### **9.3 Future work**

The importance of convective downdrafts has been recognized in many studies (e.g., Johnson, 1976; Cheng and Arakawa, 1991a,b; etc.). The effects of cumulus downdrafts have been included in the CSU GCM by Chen and Randall (1995) for the single cloud base parameterization. It would be useful to include the downdraft effects of altocu-

mulus clouds in the future.

Cumulus activity is very sensitive to cloud base conditions. The best way to revise the cloud base conditions is an open question. For cumulus clouds starting from different heights, their cloud base conditions may have different controls. Further coupled observational and modeling studies of cloud base properties are needed in order to improve the cumulus parameterization.

In our experiment on the evaporation of altocumulus precipitation, evaporation in the PBL is not included. We have shown that the tropical PBL simulated by the model is too warm and too dry. Precipitation evaporation in the PBL may help to solve this problem.

Finally, the MCB parameterization has raised a computational problem. When both the cloud base and top are cloud type indexes, the number of cloud types will increase exponentially as the number of model layers increases. A more efficient algorithm is needed.

## References

- Ackerman, T. P., K.-N. Liou, F. P. J. Valero and L. Pfister, 1988: Heating rates in tropical anvils. *J. Atmos. Sci.*, **54**, 1606-1623.
- Albrecht, B., and S. K. Cox, 1975: The large-scale response of the tropical atmosphere to cloud modulated infrared heating. *J. Atmos. Sci.*, **32**, 16-24.
- Anthes, R. A., 1977: A cumulus parameterization scheme utilizing a one-dimensional cloud model. *Mon. Wea. Rev.*, **105**, 270-286.
- Arakawa, A., 1969: Parameterization of cumulus convection. *Proc. WMO/IUGG Symp. Numerical Weather Prediction*, Tokyo, 26 November-4 December, 1968, Japan Meteor. Agency, IV, 8, 1-6.
- Arakawa, A., and W. H. Schubert, 1974: The interaction of a cumulus cloud ensemble with the large-scale environment, Part I. *J. Atmos. Sci.*, **31**, 674-701.
- Arakawa, A., and V. R. Lamb, 1977: Computational design of the basic dynamical processes of the UCLA general circulation model. *Methods in Computational Physics*, **17**,

Academic Press, New York, 173-265

Arakawa, A., and V. R. Lamb, 1981: A potential enstrophy and energy conserving scheme for the shallow water equations. *Monthly Weather Review*, **109**, 18-36.

Arakawa, A., and M. J. Suarez, 1983: Vertical differencing of the primitive equations in sigma coordinates. *Mon. Wea. Rev.*, **111**, 34-45.

Arakawa, A., and J.-M Chen, 1987: Closure assumption in the cumulus parameterization problem. *Short- and Medium-range Numerical Prediction*, Collection of Papers at the WMO/IUGG NWP Symposium, Tokyo, 4-8 August, 1986, 107-131.

Arakawa, A., and J.-M Chen, 1993: The Arakawa-Schubert cumulus parameterization. *The Representation of Cumulus Convection in Numerical Models of the Atmosphere*. K. A. Emanuel and D. J. Raymond, Eds., Meteor. Monogr., Vol. 24, No. 46.

Arakawa, A., 1993: Closure Assumptions in the cumulus parameterization problem. *The Representation of Cumulus Convection in Numerical Models of the Atmosphere*. K. A. Emanuel and D. J. Raymond, Eds., Meteor. Monogr., Vol. 24, No. 46.

Baik, J. J., M. DeMaria, and S. Raman, 1990: Tropical cyclone simulations with the Betts convective adjustment scheme. Part II: Sensitivity experiments. *Mon. Wea. Rev.*, **118**, 529-541.

Betts, A. K., 1986: A new convective adjustment scheme. Part I: Observational and theoretical basis. *Quart. J. Roy. Meteor. Soc.*, **112**, 677-691.

- Betts, A. K., and M. J. Miller, 1975: VIMHEX-1972 rawinsonde data. *Atmos. Sci. Report*, Colorado State University.
- Betts, A. K., and M. J. Miller, 1986: A new convective adjustment scheme. Part II: Single column tests using GATE wave, BOMEX, ATEX and arctic air-mass data sets. *Quart. J. Roy. Meteor. Soc.*, **112**, 693-709.
- Betts, A. K., and M. J. Miller, 1993: Closure Assumptions in the cumulus parameterization problem. *The Representation of Cumulus Convection in Numerical Models of the Atmosphere*. K. A. Emanuel and D. J. Raymond, Eds., Meteor. Monogr., Vol. 24, No. 46.
- Blyth, A. M., W. A. Cooper, and J. B. Jensen, 1988: A study of the source of entrained air in Montana cumuli. *J. Atmos. Sci.*, **45**, 3944-3964.
- Briegleb, B. P., P. Minnis, V. Ramanathan, and E. Harrison, 1986: Comparison of regional clear-sky albedos inferred from satellite observations and model computations. *J. Clim. Appl. Meteor.*, **25**, 214-226.
- Byers, H. R., and E. C. Hull, 1949: Inflow patterns of thunderstorms as shown by winds aloft. *Bull. Amer. Meteor. Soc.*, **30**, 90-96.
- Chang, C.-P., 1970: Westward-propagating cloud patterns in the tropical Pacific as seen from time-composite satellite photographs. *J. Atmos. Sci.*, **27**, 133-138.
- Charney, J. G., and A. Eliassen, 1964: On the growth of the hurricane depression. *J.*

*Atmos. Sci.*, **21**, 68-75.

Chen, C.-H. and D. A. Randall, 1995: Modeling the effects of convective downdrafts on the global circulation of the atmosphere. In preparation for *J. Geophys. Res.*

Cheng, M.-D., and A. Arakawa, 1990: Inclusion of convective downdrafts in the Arakawa-Schubert cumulus parameterization. Tech. Rep., Department of Atmospheric Sciences, University of California, Los Angeles, 69 pp.

Cheng, M.-D., and A. Arakawa, 1991a: Inclusion of convective downdrafts in the Arakawa-Schubert cumulus parameterization. *Nineteenth Conf. on Hurricane and Tropical Meteorology*, May 6-10, 1991, Fla., Amer. Meteor. Soc., 395-300.

Cheng, M.-D., and A. Arakawa, 1991b: Inclusion of rainwater budget and convective downdrafts in a cumulus parameterization. *Ninth Conference on Numerical Weather Prediction*, October 14-18, 1991, Denver, Colorado, Amer. Meteor. Soc., 4 pp.

Cheng, M.-D., and A. Arakawa, 1992: A cumulus parameterization with rainwater budget and convective downdrafts.

Cho, H. R., 1975: Cumulus cloud population and its parameterization. *Pure and Appl. Geophys.*, **113**, 837-849.

Cho, H.-R., L. Cheng and R. M. Bloxam, 1979: The representation of cumulus cloud effects in the large-scale vorticity equation. *J. Atmos. Sci.*, **36**, 127-139.

- Cho, H.-R., and L. Cheng, 1980: Parameterization of horizontal transport of vorticity by cumulus convection. *J. Atmos. Sci.*, **37**, 812-826.
- Chu, J.-H., 1976: Vorticity in maritime cumulus clouds and its effects on the large-scale budget of vorticity in the tropics. Ph.D. thesis, UCLA, 123pp.
- Chu, J.-H., M. Yanai and C.-H. Sui, 1981: Effects of cumulus convection on the vorticity field in the tropics. Part I: The large-scale budget. *J. Meteor. Soc., Japan*, **59**, 535-546.
- Cotton, W. R., and R. A. Anthes, 1989: Storm and Cloud Dynamics. Academic Press Inc., San Diego. International Geophysics Series, Vol 44., 883 pp.
- Emanuel, K. A., 1981: A similarity theory for unsaturated downdrafts within clouds. *J. Atmos. Sci.*, **38**, 1541-1557.
- Emanuel, K. A., 1991: A scheme for representing cumulus convection in large-scale models. *J. Atmos. Sci.*, **38**, 1541-1557.
- Emanuel, K. A., J. D. Neelin, and C. S. Bretherton, 1994: On the large-scale circulation of the convecting atmospheres. *Quart. J. Roy. Meteor. Soc.*, **120**, 1111-1143.
- Esbensen, S. K., E. I. Tollerud and J.-H. Chu, 1982: Cloud-cluster-scale circulations and the vorticity budget of synoptic-scale waves over the eastern Atlantic intertropical convergence zone. *Mon. Wea. Rev.*, **110**, 1677-1692.
- Fankhauser, J. C., I. R. Paluch, W. A. Cooper, D. W. Breed and R. E. Rinehart, 1982: *Hail-*

*storms of the Central High Plains, Vol. I: The National Hail Research Experiment.*  
Colorado Associated University Press, 95-149.

Fowler L. D., D. A. Randall, and S. A. Rutledge, 1995: Liquid and ice cloud microphysics in the CSU general circulation model. Part I: Model description and results of a baseline simulation. Submitted to *J. Climate*.

Fowler L. D., and D. A. Randall, 1995: Liquid and ice cloud microphysics in the CSU general circulation model. Part II: Impact on cloudiness, the Earth's radiation budget, and general circulation of the atmosphere. Submitted to *J. Climate*.

Frank, N. L., 1970: Atlantic tropical systems of 1969. *Mon. Wea. Rev.*, **98**, 307-314.

Frank, W. M., 1983: The cumulus parameterization problem. *Mon. Wea. Rev.*, **111**, 1859-1871.

Frank, W. M., and C. Cohen, 1987: Simulation of tropical convective systems. Part I: A cumulus parameterization. *J. Atmos. Sci.*, **44**, 3787-3799.

Frank, W. M., and J. Molinari, 1993: Convective adjustment. *The Representation of Cumulus Convection in Numerical Models of the Atmosphere*. K. A. Emanuel and D. J. Raymond, Eds., Meteor. Monogr., Vol. 24, No. 46.

Fritsch, J. M., C. F. Chappell and L. R. Hoxit, 1976: The use of large-scale budgets for convective parameterization. *Mon. Wea. Rev.*, **104**, 1408-1418.

- Fritsch, J. M., and C. F. Chappel, 1980: Numerical prediction of convectively driven mesoscale pressure systems. Part I: Convective parameterization. *J. Atmos. Sci.*, **37**, 1722-1733.
- Gass, S., 1975: *Linear Programming, Methods and Applications*. McGraw-Hill, 406 pp.
- Gray, W. M., 1973: Cumulus convection and large scale circulations, I, Broadscale and mesoscale considerations. *Mon. Wea. Rev.*, **101**, 839-855.
- Grell, G. A., Y.-H. Kuo, and R. J. Pasch, 1991: Semi-prognostic tests of cumulus parameterization schemes in the middle latitude. *Mon. Wea. Rev.*, **119**, 5-31.
- Harshvardhan, R. Davies, D. A. Randall, and T. G. Corsetti, 1987: A fast radiation parameterization for general circulation models. *J. Geophys. Res.*, **92**, 1009-1016.
- Harshvardhan, D. A. Randall, T. G. Corsetti and D. A. Dazlich, 1989: Earth radiation budget and cloudiness simulations with a General Circulation Model. *J. Atmos. Sci.*, **46**, 1922-1942.
- Heckley, W. A., M. J. Miller, and A. K. Betts, 1987: An example of hurricane tracking and forecasting with a global analysis-forecasting system. *Bull. Amer. Meteor. Soc.*, **68**, 226-229.
- Herman, G. F., M.-L. C. Wu, and W. T. Johnson, 1980: The effects of clouds on the earth's solar and infrared radiation budgets. *J. Atmos. Sci.*, **37**, 1251-1261.
- Holle, R. L., J. Simpson, and S. W. Leavitt, 1979: GATE B-scale cloudiness from whole-

- sky cameras on four U.S. ships. *Mon. Wea. Rev.*, **107**, 874-895.
- Houze, R. A., Jr., and A. K. Betts, 1981: Convection in GATE. *Rev. Geophys. Space Phys.*, **19**, 541-576.
- Joint Organizing Committee, GARP, 1970: Report on the first session of the JOC Study Group on Tropical Disturbances, 1968, Appendix 1. *GARP Publ. Ser.*, No. 4.
- Johnson, R. H., 1976: The role of convective-scale precipitation downdrafts in cumulus and synoptic-scale interactions. *J. Atmos. Sci.*, **33**, 1890-1910.
- Kao, C.-Y. J., and Y. Ogura, 1987: Response of cumulus clouds to large-scale forcing using the Arakawa-Schubert cumulus parameterization. *J. Atmos. Sci.*, **44**, 2437-2548.
- Keenan, T. D., and S. A. Rutledge, 1993: Mesoscale characteristics of monsoonal convection and associated stratiform precipitation. *Mon. Wea. Rev.*, **121**, 352-374.
- Kiladis, G. N., and K. M. Weickmann, 1992: Circulation anomalies associated with tropical convection during Northern winter. *Mon. Wea. Rev.*, **120**, 1900-1923.
- Kiladis, G. N., and K. M. Weickmann, 1992: Extratropical forcing of tropical Pacific convection during Northern winter. *Mon. Wea. Rev.*, **120**, 1924-1938.
- Kinzer, G. D., and R. Gunn, 1951: The evaporation, temperature and thermal relaxation-time of freely falling waterdrops. *J. Meteor.*, **8**, 71-83.

- Kreizberg, C. W., and D. Perkey, 1976: Release of potential instability. Part I: A sequential plume model within a hydrostatic primitive equation model. *J. Atmos. Sci.*, **33**, 456-475.
- Krishnamurti, T. N., and W. J. Moxim, 1971: On parameterization of convective and non-convective latent heat release. *J. Appl. Meteor.*, **10**, 3-13.
- Krishnamurti, T. N., M. Kanamitsu, R. Godbole, C. B. Chang, F. Carr, and J. Chow, 1976: Study of a monsoon depression (II): Dynamical structure. *J. Meteor. Soc. Japan*, **54**, 208-225.
- Krishnamurti, T. N., H.-L. Pan, R. J. Pasch, and J. Molinari, 1980: Cumulus parameterization and rainfall rates I. *Mon. Wea. Rev.*, **108**, 465-472.
- Krishnamurti, T. N., S.-L. Nam, and R. Pasch, 1983: Cumulus parameterization and rainfall rates II. *Mon. Wea. Rev.*, **111**, 815-828.
- Krishnamurti, T. N., H. S. Bedi, 1988: Cumulus parameterization and rainfall rates: Part III. *Mon. Wea. Rev.*, **116**, 583-599.
- Kuo, H. L., 1965: On formation and intensification of tropical cyclones through latent heat release by cumulus convection. *J. Atmos. Sci.*, **22**, 40-63.
- Kuo, H. L., 1974: Further studies of the parameterization of the influence of cumulus convection on large-scale flow. *J. Atmos. Sci.*, **31**, 1232-1240.

- Kurihara, Y., 1973: A scheme of moist convective adjustment. *Mon. Wea. Rev.*, **101**, 547-553.
- Leary, C. A., and R. A. Houze, Jr., 1979b: Melting and evaporation of hydrometeors in precipitation from the anvil clouds of deep tropical convection. *J. Atmos. Sci.*, **36**, 669-679.
- Lord, S. J., 1978: Development and observational verification of a cumulus cloud parameterization. Ph.D. dissertation, UCLA, 359 pp.
- Lord, S. J., and A. Arakawa, 1980: Interaction of a cumulus cloud ensemble with the large-scale environment. Part II. *J. Atmos. Sci.*, **37**, 2677-2692.
- Lord, S. J., 1982: Interaction of a cumulus cloud ensemble with the large-scale environment. Part III: Semi-prognostic test of the Arakawa-Schubert cumulus parameterization. *J. Atmos. Sci.* **39**, 88-103.
- Lord, S. J., W. C. Chao and A. Arakawa, 1982: Interaction of a cumulus cloud ensemble with the large-scale environment. Part IV: The discrete model. *J. Atmos. Sci.* **39**, 104-113.
- Machado, L. A. T., M. Desbois, and J.-Ph. Duvel, 1992: Structural characteristics of deep convective systems over tropical Africa and the Atlantic ocean. *Mon. Wea. Rev.*, **120**, 392-406.
- Malkus, J. S., 1954: Some results of a trade-cumulus cloud investigation. *J. Meteor.*, **12**,

43-57.

Malkus, J. S., and H. Riehl, 1960: On the dynamics and energy transformation in steady state hurricanes. *Tellus*, **12**, 1-20.

Manabe, S., J. Smagorinsky, and R. F. Strickler, 1965: Simulated climatology of a general circulation model with a hydrological cycle. *Mon. Wea. Rev.*, **93**, 769-798.

Manabe, S., and J. Smagorinsky, 1967: Simulated climatology of a general circulation model with hydrologic cycle. II: Analysis of the tropical atmosphere. *Mon. Wea. Rev.*, **95**, 155-169.

Manabe, S., J. L. Holloway, Jr., and H. M. Stone, 1970: Tropical circulation in a time-integration of a global model of the atmosphere. *J. Atmos. Sci.* **27**, 580-613.

Mapes, B. E., 1993: Gregarious tropical convection. *J. Atmos. Sci.* **50**, 2026-2037.

Martin, D. W., and V. E. Suomi, 1972: A satellite study of cloud clusters over the tropical North Atlantic ocean. *Bull. Amer. Meteor. Soc.*, **53**, 135-156.

Marwitz, J. D., J. R. Middleton, A. H. Auer, Jr. and D. L. Veal, 1970: The dynamics of updraft vaults in hailstorms as inferred from the entraining jet model. *J. Atmos. Sci.* **27**, 1099-1102.

Miyakoda, K., J. Smagorinsky, R. F. Strickler, and G. D. Hembree, 1969: Experimental extended predictions with a nine-level hemispheric model. *Mon. Wea. Rev.*, **97**, 1-76.

- Molinari, J., 1982: A method for calculating the effects of deep cumulus convection in numerical models. *Mon. Wea. Rev.*, **11**, 1527-1534.
- Moorthi, S., and M. J. Suarez, 1992: Relaxed Arakawa-Schubert: A parameterization of moist convection for general circulation models. *Mon. Wea. Rev.*, **120**, 978-76
- Nitta, T., 1975: Observational determination of cloud mass flux distributions. *J. Atmos. Sci.* **32**, 73-91.
- Nitta, T., 1976: Large-scale heat and moisture budgets for the Air Mass Transformation Experiment. *J. Meteor. Soc. Japan*, **54**, 1-14.
- Ogura, Y., and H. -R. Cho, 1973: Diagnostic determination of cumulus cloud populations from observed large-scale variables. *J. Atmos. Sci.* **30**, 1276-1286.
- Ooyama, K., 1964: A dynamical model for the study of tropical cyclone development. *Geofis. Intern.*, **4**, 187-198.
- Ooyama, V. K., 1971: A theory on parameterization of cumulus convection. *J. Meteor. Soc. Japan*, **49**, 744-756.
- Ooyama, V. K., 1982: Conceptual evolution of the theory and modeling of the tropical cyclone. *J. Meteor. Soc. Japan*, **60**, 369-380.
- Payne, R. E., 1972: Albedo of the sea surface. *J. Atmos. Sci.* **29**, 959-970.

- Ramanathan, V., E. J. Pitcher, R. C. Malone and M. L. Blackmon, 1983: The response of a spectral general circulation model to refinements in radiative processes. *J. Atmos. Sci.* **40**, 605-630.
- Randall, D. A., J. A. Abeles and T. G. Corsett, 1985: Seasonal simulations of the planetary boundary-layer stratocumulus clouds with a General Circulation Model. *J. Atmos. Sci.* **42**, 641-676.
- Randall, D. A., Harshvardhan, D. A. Dazlich, and T. G. Corsetti, 1989: Interactions among radiation, convection, and large-scale dynamics in a general circulation model. *J. Atmos. Sci.* **46**, 1943-1970.
- Randall, D. A., and D.-M. Pan, 1993: Implementation of the Arakawa-Schubert cumulus parameterization with a prognostic closure. *The Representation of Cumulus Convection in Numerical Models of the Atmosphere*. K. A. Emanuel and D. J. Raymond, Eds., Meteor. Monogr., Vol. 24, No. 46.
- Reed, R. J., and E. E. Recker, 1971: Structure and properties of synoptic-scale wave disturbances in the equatorial western Pacific. *J. Atmos. Sci.* **28**, 1117-1133.
- Riehl, H., and J. S. Malkus, 1958: On the heat balance in the equatorial trough zone. *Geophysica*, **6**, 503-538.
- Riehl, H., and J. S. Malkus, 1961: Some aspects of hurricane Daisy, 1958. *Tellus*, **13**, 181-213.

- Scorer, R. S., and F. H. Ludlam, 1953: Bubble theory of penetrative convection. *Quart. J. Roy. Meteor. Soc.*, **79**, 94-103.
- Sellers, P. J., Y. Mintz, Y. C. Sud, and A. Dalcher, 1986: A simple biosphere model (SiB) for use within general circulation models. *J. Atmos. Sci.*, **43**, 505-531.
- Sheu, R.-S., and J. A. Curry, 1992: Interactions between North Atlantic clouds and the large-scale environment. *Mon. Wea. Rev.*, **120**, 261-278.
- Simpson, J., 1971: On cumulus entrainment and one-dimensional models. *J. Atmos. Sci.* **28**, 449-455.
- Simpson, J., R. H. Simpson, D. A. Andrews and M. A. Eaton, 1965: Experimental cumulus dynamics. *Rev. Geophys.*, **3**, 387-431.
- Simpson, J., and V. Wiggert, 1969: Models of precipitating cumulus towers. *Mon. Wea. Rev.*, **97**, 471-489.
- Sloss, P. W., 1967: An empirical examination of cumulus entrainment. *J. Appl. Meteor.*, **9**, 878-881.
- Squires, P., and J. S. Turner, 1962: An entraining jet model for cumulonimbus updraughts. *Tells*, **14**, 422-434.
- Stephens, G. L., and P. J. Webster, 1979: Sensitivity of radiative forcing to variable cloud and moisture. *J. Atmos. Sci.* **36**, 1542-1556.

- Stevens, D. E., 1979: Vorticity, momentum and divergence budgets of synoptic-scale wave disturbances in the tropical eastern Atlantic. *Mon. Wea. Rev.*, **107**, 535-550.
- Stommel, H., 1947: Entrainment of air into a cumulus cloud. *J. Meteor.*, **4**, 91-94.
- Takano, K. and M. G. Wurtele, 1982: A fourth-order energy and potential enstrophy conserving difference scheme. *Air Force Geophysics Laboratory Report*, AFGL-TR-82-0205, 85 pp.
- Telford, J. W., 1975: Turbulence, entrainment, and mixing in cloud dynamics. *Pure Appl. Geophys.*, **113**, 1067-1084.
- Thompson, R. M., Jr., S. W. Payne, E. E. Recker and R. J. Reed, 1979: Structure and properties of synoptic-scale wave disturbances in the intertropical convergence zone of the eastern Atlantic. *J. Atmos. Sci.* **36**, 53-72.
- Tiedtke, M., 1989: A comprehensive mass flux scheme for cumulus parameterization in large-scale models. *Mon. Wea. Rev.*, **117**, 1779-1800.
- Tollerud, I. E., and S. K. Esbensen, 1983: An observational study of the upper-tropospheric vorticity fields in GATE cloud clusters. *Mon. Wea. Rev.*, **111**, 2161-2175.
- Warner, C., J. Simpon, G. Van Helvoirt, D. W. Marth, D. Suchman and G. L. Austin, 1980: Deep convection on Day 261 of GATE. *Mon. Wea. Rev.*, **108**, 169-194.
- Warner, C., and R. H. Grumm, 1984: Cloud distributions in a Bay of Bengal monsoon

depression. *Mon. Wea. Rev.*, **112**, 153-172.

Watts, R. G., 1971: Relaxation time and steady evaporation rate of freely falling rain drops. *J. Atmos. Sci.* **28**, 219-225.

Webster, P. J., and G. L. Stephens, 1980: Tropical upper tropospheric extended clouds: Inferences from Winter MONEX. *J. Atmos. Sci.* **37**, 1521-1541.

Xu, K.-M., and K. A. Emanuel, 1989: Is the tropical atmosphere conditionally unstable? *Mon. Wea. Rev.*, **117**, 1471-1479.

Yanai, M., 1961a: A detailed analysis of typhoon formation. *J. Meteor. Soc. Japan*, **39**, 187-214.

Yanai, M., 1961b: Dynamical aspects of typhoon formation. *J. Meteor. Soc. Japan*, **39**, 283-309.

Yanai, M., S. K. Esbensen, and J.-H. Chu, 1973: Determination of bulk properties of tropical cloud clusters from large-scale heat and moisture budgets. *J. Atmos. Sci.* **30**, 611-627.

Yanai, M., and R. H. Johnson, 1993: Impacts of cumulus convection on thermodynamic fields. *The Representation of Cumulus Convection in Numerical Models of the Atmosphere*. K. A. Emanuel and D. J. Raymond, Eds., Meteor. Monogr., Vol. 24, No. 46.